

RICE UNIVERSITY

Tunable Interaction in Quantum Degenerate Lithium

by

Kevin Edwin Strecker

A THESIS SUBMITTED
IN PARTIAL FULFILLMENT OF THE
REQUIREMENTS FOR THE DEGREE

Doctor of Philosophy

APPROVED, THESIS COMMITTEE:

Randall G. Hulet, Chairman
Fayez Sarofim Professor of Physics and
Astronomy

Thomas C. Killian
Assistant Professor of Physics and
Astronomy

Frank K. Tittel
J.S. Abercrombie Professor of Electrical
and Computer Engineering

Houston, Texas

April, 2004

ABSTRACT

Tunable Interaction in Quantum Degenerate Lithium

by

Kevin Edwin Strecker

We have designed and constructed an apparatus capable of simultaneously creating both a quantum degenerate Bose and Fermi gas of the two stable isotopes of lithium, ^7Li and ^6Li , respectively. This apparatus has the capability of optically confining pre-cooled samples of atoms, and applying an arbitrary magnetic bias field between zero and 1000 G. The optical confinement allows us to work with any spin state or mixture, of ^6Li or ^7Li . The applied external field can tune the atoms through atom-atom scattering resonances, known as Feshbach resonances. These resonance change the effective coupling between atoms, allowing us to study the behavior of the atoms in both the weak and strong coupling limits. With this tool we have been able to produce large lithium Bose-Einstein condensates, stable attractive Bose-Einstein condensates in one dimension, coherent Fermi mixtures, strongly interacting Fermi mixtures, and have induced the formation of bosonic molecules from an interacting Fermi mixture.

Acknowledgments

No project of this magnitude and complexity can be accomplished by one person. With out the help of several remarkable individuals and the support of countless others we never could have completed these ground breaking experiments.

There have been several amazing people that have helped me along the way. The most credit goes to my advisor, Randy, he not only is responsible for the ideas behind the experiments in this thesis, getting the necessary funding, teaching me the physics behind our experiments, but he even periodically comes and helps collect data. Following in Randy's footsteps, comes the two people that have assisted me in these experiments, Andrew and Guthrie. These two have provided me with countless hours upon hours of crazy banter concerning the wild theories that I come up with at 2 am attempting to explain what the the experiment is doing. As far as the people working directly on the apparatus, there are three others that have made unique contributions. Ian, a fellow graduate student, was the first to attempt to build the apparatus with help from Bita who designed vacuum system and the imaging system, and Dean who designed and constructed our first electromagnetic trap.

There have been many other graduate students that have helped me along the way with ideas, advice, and friendship. I particularly want to thank Cass, Jordan, and Mark for their help.

I also want to thank the post-docs that have worked in the lab. The first post-doc I worked with, Mark Welling, taught me the most useful thing for working in a laser lab, how to align lasers. Marin and Dimitry for their help in the lab, particularly, dealing with the pesky spectra laser. Finally, Michael for answering all my stupid questions while I was writing this thesis.

Of the people outside the lab (a place I did not often visit), I would like to thank my wife most of all. Michelle put up with me not coming home for days on end,

working until the early morning hours, and never being around for dinner. I want to thank her for her support and kindness over these last several years. I also want to thank my parents. Mom and dad have been a constant source of encouragement, not just during my graduate career but for my entire life. I also want to thank my mom-and-dad-inlaw, I appreciate the support and understanding they have shown me over late several years. All my family has been so supportive, putting up with me even though I hardly call or write. I want to thank all the friends that I have made here in Houston. In particular, Jen and Purvez are so accepting and kind. There are so many more friends, scattered all over the world, that have encouraged me over the years, and I am thankful for each one of them.

Contents

Abstract	iii
Acknowledgments	iv
List of Figures	ix
1 Introduction	1
1.1 Overview	1
1.2 Lithium	3
1.3 Feshbach Resonance	8
2 Apparatus	13
2.1 MOT	14
2.1.1 Magnetic Fields	14
2.1.2 Dual-MOT	16
2.1.3 Transfer	18
2.2 Electro-Magnetic Trap	28
2.2.1 Clover Leaf Trap	28
2.2.2 Coil Construction	29
2.2.3 The Switch	37
2.2.4 High Field Control	40
2.3 Optical Trap	48
2.3.1 FORT	48
2.3.2 End Caps	51
2.3.3 Cross Beam Trap	54
2.3.4 Optical Trap Loss Rates	56
2.3.5 Aligning and Transferring	65
2.4 Imaging	70

2.4.1	Overview	70
2.4.2	Imaging System Performance	72
2.4.3	Dispersive and Non-dispersive Imaging	75
2.4.4	Imaging Analysis	77
3	Experiments	80
3.1	Bosons	81
3.1.1	Optical Trapping	81
3.1.2	^7Li Feshbach Resonance	87
3.1.3	Large Lithium Bose Einstein Condensate	89
3.1.4	Bright Matter Wave Solitons	91
3.2	Boson-Fermion Mixtures	108
3.2.1	Dual Evaporation	110
3.2.2	Optimized Evaporation	111
3.2.3	Large Degenerate Fermi Gas	117
3.3	Fermi-Fermi Mixtures	122
3.3.1	Producing a Spin Mixture	124
3.3.2	Long Lived Coherence	126
3.3.3	Microwave Spectroscopy	131
3.3.4	^6Li Feshbach Resonance	137
3.3.5	Formation of ${}^6\text{Li}_2$ Dimers	140
3.3.6	Direct Detection of Molecules	151
4	Conclusion	152
4.1	Trouble Shooting	153
4.2	Improvements	154
5	Appendix	156
5.1	EMRTAP Control	156

5.2	EMTRAP coil design	161
5.3	Image Analysis	169

References	173
-------------------	------------

List of Figures

1.1	Optical transitions	4
1.2	Transition Strengths	4
1.3	Li ground states	6
1.4	Origin of the Feshbach resonance	11
1.5	Sample resonance	12
2.1	MOT switch	15
2.2	^7Li and ^6Li Zeeman structure	18
2.3	Compressed MOT	19
2.4	Compression and cooling ramps.	21
2.5	MOT time-of-flight.	24
2.6	^7Li energy levels	25
2.7	Optical pumping	27
2.8	Electro magnetic trap coils	30
2.9	Bias-curvature coils	31
2.10	Quadrupole wrapping diagram	32
2.11	Quadrupole coils	34
2.12	Assembled coils	35
2.13	Axial trap frequency	36
2.14	Electro Magnetic Trap switch	38
2.15	Energizing bias-curvature coils	39
2.16	Energizing quadrupole coils	39
2.17	Energizing bias-curvature coils with V_{limit} too high.	40
2.18	Magnetic trap turn off.	41
2.19	Timing diagram for Sideways cage.	43

2.20 J1 remote programming connector for EMI supply	43
2.21 Energizing the high field	44
2.22 Block diagram for DG419	45
2.23 Diagram for high field control.	45
2.24 Linear ramp circuit	46
2.25 Danfysik Feedback circuit.	47
2.26 Radial optical potential from a single beam	51
2.27 Axial optical potential from a single beam	52
2.28 Diagram of the beam separator cube.	53
2.29 The optical layout of the endcaps.	53
2.30 The endcap potential	54
2.31 The cross trap potential	55
2.32 Image of ^7Li atoms in the cross trap	56
2.33 Schematic of the optical trap setup	57
2.34 Radial IPG intensity noise spectrum.	60
2.35 Axial IPG intensity noise spectrum.	60
2.36 Radial IPG pointing noise spectrum.	62
2.37 Axial IPG pointing noise spectrum.	62
2.38 Radial IPG pointing noise spectrum.	63
2.39 IPG fiber mounts.	64
2.40 Optical trap heating rate.	65
2.41 Return loss for Crystal Technology Model 3110-125	68
2.42 Control setup for Crystal Technology Model 3110-125	69
2.43 Imaging system	70
2.44 Compound lens system	71
2.45 Zoomed image of a matter-wave soliton	73
2.46 Cross section of USAF test target	74

2.47	Cross section of a single mode optical fiber	74
2.48	Plot of the phase and optical density	76
3.1	Alignment stages of axial beam	82
3.2	Axial beam after 40 ms	83
3.3	One green beam	84
3.4	Completely aligned optical trap	84
3.5	Lifetime of ${}^7\text{Li}$ in optical trap	86
3.6	$F = 1, m_F = 1$ Feshbach resonance	87
3.7	Sample lifetime near a Feshbach resonance	88
3.8	Loss rate determination of Feshbach resonance.	89
3.9	YAG timing diagram.	90
3.10	BEC picture.	91
3.11	High field timing diagram.	94
3.12	Shifted ${}^7\text{Li}$ Feshbach resonance	95
3.13	Magnetic field sweep	96
3.14	Calibration of bias field	97
3.15	Solitons vs. ending field	98
3.16	Solitons size vs. ending field	99
3.17	Experimental setup	99
3.18	Observation of solitons	100
3.19	Observation of soliton interactions	101
3.20	Timing for soliton release	102
3.21	Number of solitons vs. time	103
3.22	Oscillating solitons	105
3.23	Motion of two solitons	106
3.24	Difference frequency	111
3.25	Empirical trajectory.	112

3.26 Evaporation	116
3.27 Varying α	118
3.28 Optimized trajectories	119
3.29 Dual degeneracy	120
3.30 ${}^6\text{Li}$ $2S_{\frac{1}{2}}$ zeeman structure.	122
3.31 ${}^6\text{Li}$ Feshbach Resonance.	123
3.32 $6 \leftrightarrow 1$ transfer frequency.	124
3.33 ${}^6\text{Li}$ high field diagram.	125
3.34 $1 \leftrightarrow 2$ transfer frequency.	126
3.35 Calculation of Rabi oscillations.	127
3.36 Rabi oscillations at 530 G.	128
3.37 Rabi oscillations at 903.25 G.	129
3.38 More Rabi oscillations at 903.25 G.	130
3.39 Trap lifetime at 530 G.	130
3.40 Lifetime at 903 G.	131
3.41 Microwave diagram.	132
3.42 ${}^6\text{Li}$ Feshbach resonances.	133
3.43 567 G spectrum.	135
3.44 551G spectrum.	136
3.45 552 G long hold spectrum.	137
3.46 Little ${}^6\text{Li}$ resonance.	138
3.47 Lifetime near little ${}^6\text{Li}$ resonance.	139
3.48 Loss rate near ${}^6\text{Li}$ resonance.	140
3.49 Atom molecule coupling.	141
3.50 Avoided crossing.	142
3.51 Inverse sweep rate.	143
3.52 Ending field dependance.	145

3.53 First molecular lifetime.	147
3.54 Molecular lifetime ramp.	148
3.55 Molecular lifetime.	149
3.56 Molecular lifetime.	150
5.1 TTL layout	157
5.2 Re-entrant setup	161
5.3 Bias coil	162
5.4 Quadrupole coils	163
5.5 Lid for the coils	164
5.6 Assembled coils	165
5.7 Coil holder	166
5.8 Standoffs	167

Chapter 1

Introduction

During the last eight years, since the first observations of Bose Einstein condensation (BEC) in trapped alkali gasses [1–3], many amazing experiments have been performed that have illuminated the quantum nature of matter. These experiments have shown the coherence of matter, matter interfering, and even the invention of matter-wave lasers. However, even before the interest in bosons grew, there was interest in studying ultra-cold Fermi gases, in order to explore the BCS (Bardeen, Cooper, and Schrieffer) phase transition in dilute atomic gas [4]. Due to experimental difficulties that arose from the fermionic nature of the atoms under study, it took nearly four years before the first two fermion experiments were able to achieve quantum degeneracy in a Fermi system [5, 6].

Along the way, a new feature in alkali atoms was discovered: Feshbach resonances [7, 8]. This resonance gave experimentalist a “knob” by which to tune the atom-atom interactions, allowing them to explore the various regimes of coupling between the atoms. Feshbach resonances have allowed us to study coupling strengths large enough to form bare molecules [9] down to small negative scattering lengths where matter-wave bright solitons are formed [10]. Feshbach resonances give us the ability to truly control and manipulate the atom-atom interactions, making these dilute atomic gases the ultimate vessels for exploring the frontiers of quantum physics.

1.1 Overview

The purpose of this overview is two-fold: the first is to explain the organization of this thesis for the reader, and the second is to justify that organization. Hopefully the two purposes will be simultaneously met. The principle behind the organization of this thesis is to separate out the engineering, development, and troubleshooting from

the experimental results. This is an attempt to make the thesis a useful reference for fixing, repairing, or reproducing different parts of the apparatus, without having to sort through the entire thesis.

The thesis is broken down into five chapters. First is the introduction, which provides an overview for working with Li and an introduction to Feshbach resonances. The introduction reviews a few concepts that are pervasive throughout the thesis, so that the reader is well acquainted with the key concepts prior to addressing the details of the experiments. The second chapter is about apparatus, and is dedicated to discussing the construction and general operation of the apparatus. It includes the design and construction of the electro-magnetic trap, the MOT, the optical trap, and the imaging system, along with how to operate and control each of these elements. The second chapter also deals with the theory behind each device and its operation. The third chapter discusses the experiments. It is sub-divided into three sections: bosons, Bose-Fermi mixtures, and Fermi-Fermi mixtures. The boson sub-section covers our first optical trapping of ${}^7\text{Li}$, the creation of a large ${}^7\text{Li}$ BEC using a Feshbach resonance, and the formation of matter-wave bright solitons. The Bose-Fermi mixture sub-section covers the new implementation of dual-evaporation and the ensuing results. The Fermi-Fermi sub-section covers spectroscopy of a Fermi-Fermi mixture, the observed long coherence times, the observation of the narrow Feshbach resonance, and the production of ${}^6\text{Li}_2$ molecules using a Feshbach resonance. The fourth chapter is the conclusion. The conclusion consists of a general summary, a sub-section dedicated to improving the troubleshooting ability of the apparatus, and a sub-section on improvements to the apparatus. The fifth chapter is the appendixes. They contain detailed information to support discussions from the text.

Lithium Numbers		
Parameter	Symbol	Value
Wavelength	λ	671 nm
Linewidth	Γ	5.9 MHz
Saturation Intensity	I_{sat}	5.1 mW/cm ²
Doppler Velocity	$V_{Doppler}$	41 cm/s
Doppler temperature	$T_{Doppler}$	141 μ K
Recoil Limit	T_r	6 μ K
Bohr magneton	μ_B	1.40 MHz/G
Boltzmann constant	k_B	20.84 kHz/ μ K

Table 1.1 Several useful parameters and numbers. These numbers are used throughout this thesis, typically with these units.

1.2 Lithium

The experiments in this thesis are performed using lithium (Li), Li has two stable isotopes, ⁶Li, a composite fermion, and ⁷Li a composite boson. ⁶Li and ⁷Li differ by only 1 neutron. Several of the parameters important to laser cooling and trapping are given in table 1.1.

The optical transitions for ⁶Li and ⁷Li are very similar, however, there is a shift between their energies from the “isotope shift”. The isotope shift is partly from the difference in mass, which is $7(6) \cdot 1.67 \cdot 10^{-24} g$, and partly from a volume effect [11]. Figure 1.1 shows the energy levels for ⁶Li and ⁷Li. One important thing to note is that the isotope shift is on the order of 10 GHz, which is nearly equal to the difference between the $2P_{1/2}$ and $2P_{3/2}$ levels. The result is that the $2S_{1/2} \rightarrow 2P_{3/2}$ ⁶Li transitions are within 100 MHz of the ⁷Li $2S_{1/2} \rightarrow 2P_{1/2}$ transitions [12]. The proximity of their energies leads to cross talk between the ⁶Li MOT and the ⁷Li MOT. The solution to this problem will be discussed later, and is also covered in references [12, 13].

Figure 1.2 shows the σ^+ transitions and their relative strength for the ⁶Li $2S_{1/2} \rightarrow 2P_{3/2}$. The cycling transition needed for the MOT is the $F = 3/2, m_F = 3/2$ state to the $F = 5/2, m_F = 5/2$ state. Figure 1.1 shows the major difficulties in working with

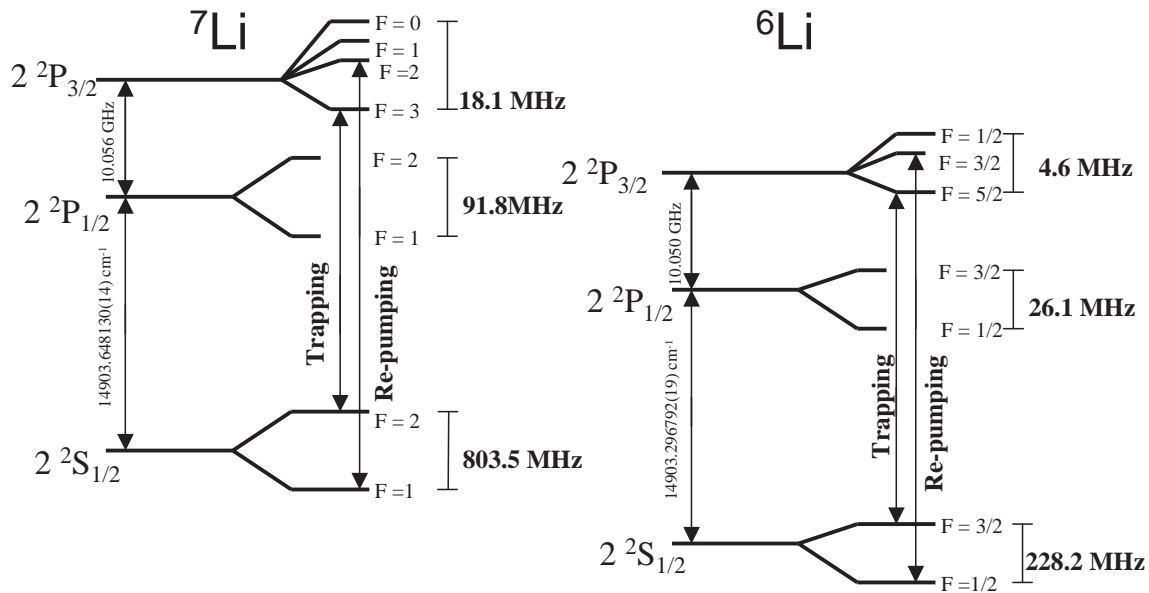


Figure 1.1 Optical transitions for ${}^6\text{Li}$ and ${}^7\text{Li}$.

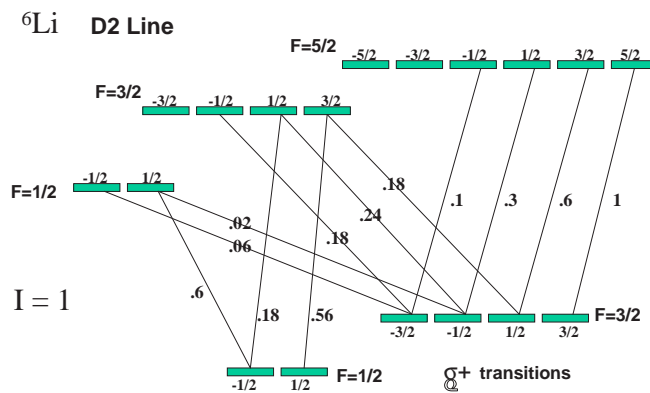


Figure 1.2 Diagram of the σ^+ transitions for the D2 line of ${}^6\text{Li}$. The transition strengths are normalized to the strongest transition. The figure is based on appendix D in reference [14].

Li, which is the frequency separation, at low field, between the $2\ ^2P_{3/2}$ $F = 5/2$, $F = 3/2$, and $F = 1/2$ levels is only 4.6 MHz in ^6Li (and only 18.1 MHz in ^7Li), compared to the linewidth of 5.9 MHz. The result is that for a standard MOT with a detuning of approximately 6Γ , the laser light driving the cycling transition ($F = 3/2 \rightarrow F = 5/2$ in ^6Li) has a high probability of driving non-cycling transitions that will allow the atoms to decay to the other ground state. Most MOTs for other alkali atoms like rubidium and cesium, benefit from a single re-pumping laser beam that pumps atoms lost from the cycling transition back into the correct state. Because of the high probability of losing atoms from the cycling transition in Li, it is necessary for the re-pumping laser to be in MOT configuration (6 beams), for the MOT to work. For this reason, it is best to think of both frequencies as being trapping frequencies, however, for convention we will continue to refer to the $2S_{1/2}$, $F = 3/2$ (2) to the $2P_{3/2}$, $F = 5/2$ (3) transition as the trapping transition and the $2S_{1/2}$, $F = 1/2$ (1) to the $2P_{3/2}$, $F = 3/2$ (2) as the repumping transition, as depicted in Fig. 1.1.

The other major effect of the small separation in the upper state, is to limit absorption imaging. When resonant light falls onto the atoms, they will at best scatter around four photons on the cycling transition before being pumped into a dark state. Unless a second re-pumping beam is used during imaging, the amount of light intensity, detuning, and pulse duration should be limited to only allow fewer than 4 scattered photons per atom. Although four photons per atom can still give a large signal, analysis of the absorbtion signals is complicated by this effect.

After the MOT there are two other types of traps that are used to catch the atoms: a magnetic trap and an optical trap. It turns out that only certain m_F projections of the atoms can be magnetically confined, which are known as low-field seekers. They are attracted to magnetic field minima, like the one produced by magnetic traps. High-field seeking atoms are expelled from a magnetic trap. Figure 1.3 shows the ground states of ^6Li and ^7Li . The high-field seeking states have a downward

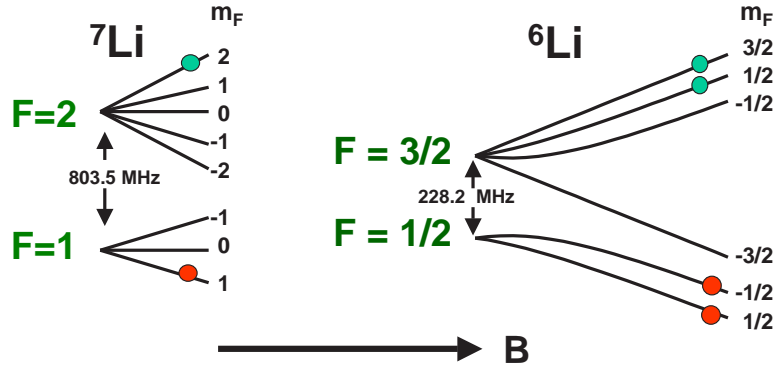


Figure 1.3 Illustration of the Li ground states in a magnetic field. The circles indicate states of interest for the experiments contained in this thesis.

curvature, while the low-field seeking states have an upward curvature.

As can be seen from Fig. 1.3, there are several states that can be magnetically trapped. As a result, we must consider a type of loss from inelastic collisions called spin exchange [15]. In these collisions, two particles come together in different m_F projections. During the collision, the total m_F must be conserved but the individual projections can change, such that $m_{F1} + m_{F2} \mapsto m_{F3} + m_{F4}$, and that $m_{F1} + m_{F2} = m_{F3} + m_{F4}$. An example would be two ${}^7\text{Li}$ atoms both in the $F = 2$, $m_F = 1$ state colliding. This combination has total $m_F = 2$, so it can produce a combination like $F = 2$, $m_F = 2 + F = 1$, $m_F = 0$. The only other rule governing the combinations formed is they must have less internal energy than the initial pair. The excess energy after the collision becomes kinetic energy, resulting in the atoms being lost from the trap. Spin exchange has two effects. The first effect is beneficial: the gas will spin polarize itself, and this guarantees spin purity. The second effect, however, is detrimental. Because spin exchange collisions are density dependant, the atoms are lost preferentially from the highest density portion of the cloud, which decreases the total phase space density of the sample.

Of interest to our experiments are: the spin exchange rates, elastic scattering cross sections, and whether a scattering resonance exists between different combinations of

	${}^6\text{Li}$ $\frac{3}{2}, \frac{3}{2}$	${}^6\text{Li}$ $\frac{1}{2}, \frac{1}{2}$	${}^6\text{Li}$ $\frac{1}{2}, -\frac{1}{2}$	${}^7\text{Li}$ $2, 2$	${}^7\text{Li}$ $1, 1$
${}^6\text{Li}$ $\frac{3}{2}, \frac{3}{2}$	a is Forbidden g is Forbidden None	$a = 25.7 a_0$ $g = 0$ $\text{FB} \sim 8700 \text{ G}$	$a = -1900 a_0$ $g \sim 10^{-11}$ $\text{FB} \sim 8750 \text{ G}$	$a = 40.9 a_0$ $g = 0$ None	$a = 33.5 a_0$ $g = 0$ None
${}^6\text{Li}$ $\frac{1}{2}, \frac{1}{2}$		a is Forbidden g is Forbidden None	$a = 0 a_0$ $g = 0$ $\text{FB} = 836 \text{ G}, 543 \text{ G}$	$a = 28.1 a_0$ $g = 7 \cdot 10^{-11}$ $\text{FB} \sim 600 \text{ G}$	$a = 38.2 a_0$ $g = 0$ $\text{FB} \sim 4000 \text{ G}$
${}^6\text{Li}$ $\frac{1}{2}, -\frac{1}{2}$			a is Forbidden g is Forbidden None	$a = 35 a_0$ $g = 2 \cdot 10^{-11}$ $\text{FB} \sim 200 \text{ G}$	$a = 37.1 a_0$ $g = 1 \cdot 10^{-15}$ $\text{FB} \sim 4000 \text{ G}$
${}^7\text{Li}$ $2, 2$				$a = -27.7 a_0$ $g = 0$ None	$a = -27.7 a_0$ $g = 0$ None
${}^7\text{Li}$ $1, 1$					$a = 7.7 a_0$ $g = 0$ $\text{FB} = 725 \text{ G}$

Table 1.2 Calculated scattering length, spin-exchange rate, and Feshbach resonances for different hyperfine combinations.

${}^6\text{Li}$ and ${}^7\text{Li}$. Looking at these factors illuminates which spin mixtures are of greatest experimental interest. For the purpose of this thesis, we shall only concentrate on select hyperfine states, which were indicated by the round circles in Fig. 1.3. The results of the aforementioned atomic characteristics are summarized in Table 1.2

which gives the scattering length a in terms of the Bohr radius a_0 , the spin exchange rate g is given in units of s^{-1} , and the best known locations of any Feshbach resonances (FB) are given in Gauss. The empty boxes are simply to avoid repeating information. “Forbidden” refers to interactions that are excluded due to the fermionic nature of the atoms.

1.3 Feshbach Resonance

The Feshbach resonance is a scattering resonance between pairs of colliding free atoms and a bound molecular state. The physical upshot of the resonance is that a parameter called the scattering cross section becomes large. The scattering cross section is given by σ , whose value is determined from $\sigma = 4\pi a^2$ ($8\pi a^2$ for a Bose gas). The scattering length is termed “ a ”, and is the parameter of interest for the experiments in this thesis, since it determines the nature of the atom-atom interactions. Since the scattering length is an important concept for the work presented in this thesis, we will dedicate the few paragraphs to a brief discussion of its origin.

Scattering length

The scattering length is a parameter that characterizes low energy collisions. The derivation of the scattering length is a result of general scattering theory and has been discussed in great detail not only in McAlexander’s thesis [15], and Sackett’s thesis [16], but also in most quantum mechanic text books [17].

To get an idea of what the scattering length is, we need to consider two particles that interact via a potential $V(r)$, where r is the coordinate describing the separation between the two particles. The wave function of the colliding particles is then given by the Schrödinger equation

$$\left[-\frac{\hbar^2 \nabla^2}{m} + V(r) \right] \phi(r) = E \cdot \phi(r), \quad (1.1)$$

where E is the center of mass energy and m is the atomic mass. In this collision, if $E > 0$, the particles elastically scatter, and if $E < 0$, the particles form a bound state of $V(r)$. As the separation between the two particles becomes large ($r \rightarrow \infty$) the wave function for the collision can be written as

$$\phi(r) \sim A \cdot \exp(ikz) + f(\vec{k}, \vec{k}') \cdot \frac{ik'r}{r}, \quad (1.2)$$

where the first term is an incident plane wave with amplitude A , and the second term is a scattered spherical wave with amplitude $f(\vec{k}, \vec{k}')$, which is defined to be the scattering amplitude.

The standard treatment is to expand both the wave function and the scattering amplitude in terms Legendre polynomials, $P_l \cdot \cos(\theta)$ [18]. The scattering amplitude is then given by

$$f(\vec{k}, \vec{k}') = \sum_{l=0}^{\infty} f_l(k) P_l \cos(\theta), \quad (1.3)$$

while the wavefunction is given by

$$\phi = R(r) \cdot P_l \cos(\theta). \quad (1.4)$$

Here the wavefunction has been written in terms of both a radial component, $R(r)$ and an angular component. The radial function $R(r) \cdot r = u(r)$ must satisfy the radial Schrödinger equation [19]

$$\frac{-\hbar^2}{2m} \frac{\partial u^2}{\partial r^2} + [V(r) + \frac{\hbar^2}{2m} \frac{l(l+1)}{r^2}]u = Eu. \quad (1.5)$$

Using Eq. 1.2 for the boundary condition, solutions can be found for scattering amplitudes with any given value of l .

A further simplification can be made since we are dealing with ultra-cold collisions. For ultra-cold collisions, $k \rightarrow 0$ and the colliding atoms will not have enough energy to penetrate the centrifugal potential barrier created by having $l \neq 0$. Setting $l = 0$, the scattering amplitude is then given by

$$f(k) = 1/(k \cdot \cot(\delta(k)) - ik), \quad (1.6)$$

where δ is the phase shift, defined to be the difference in phase between the scattered wave in the presence of a potential $V(r)$ versus when $V(r) = 0$ [17]. The s-wave scattering length is defined by the asymptotic behavior of Eq. 1.2 in the limit of low energy collisions, where $f(k) \rightarrow \text{constant}$. In this limit $\phi = 1 - \frac{a}{r}$ [20]. More formally,

a is given by $f(k = 0) = -a$, and [21]

$$a \stackrel{\lim_{k \rightarrow 0}}{=} 1/(k \cdot \cot(\delta) - ik) \quad (1.7)$$

From the definition of the scattering length, we can see that whenever δ approaches $\pi/2$, the scattering length goes through a resonance.

Feshbach Resonance

The Feshbach resonance is a scattering resonance that occurs when the energy of two colliding atoms is equal to the energy of a vibrational level of the molecule. The origin of the Feshbach resonance comes from the hyperfine interaction E_{HF} , which mixes the singlet and triplet states. The hyperfine energy is given by

$$E_{HF} = \frac{\alpha_{HF}}{\hbar^2} \mathbf{I} \cdot \mathbf{S}, \quad (1.8)$$

where \mathbf{I} is the nuclear spin and \mathbf{S} is the electronic spin. The addition of an external magnetic field will change the energies of different hyperfine levels in the atoms by virtue of the Zeeman shift. For example, the energy of a pair of atoms in a triplet state can be tuned relative to a singlet molecular level. As the external magnetic field is increased, the energy of the free colliding atoms comes into resonance with a bound molecular state, resulting in a scattering resonance. Figure 1.4 illustrates a collision between two atoms. If the atoms have energy E greater than the bound state, $a > 0$ corresponding to repulsive interactions. If the atoms have energy E less than the bound state, $a < 0$ and the atom-atom interaction is attractive.

The locations and strengths of the Feshbach resonances can be calculated if the molecular potentials are known. For Li the potentials have been experimentally measured through photo-association [22–25]. The Feshbach resonances are calculated using a coupled channel method which takes two colliding atoms and all the different possible collisional channels between them, then calculates both the elastic and inelastic scattering rates. When these results are tabulated as a function of magnetic

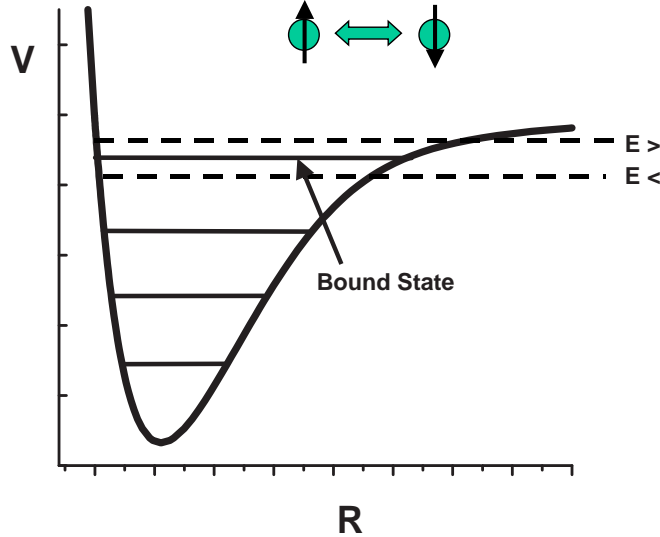


Figure 1.4 Diagram of the origin of the Feshbach resonance. The collision between two particles is described by a molecular potential. External magnetic fields can shift the energy to be near a bound state. The bound state is labelled. The energy of the colliding atoms is either $E >$, or $E <$ depending on whether their energy is greater or less than the bound state energy.

field, the resonance is identified by the elastic scattering rate, parameterized by a , going through a singularity from positive to negative infinity. The coupled channels code used to predict the resonances observed in this thesis was written by W.I. McAlexander and is explained, in detail, in his thesis [15].

A typical resonance is shown in Fig. 1.5. For $a > 0$, the interactions are repulsive and attractive for $a < 0$. The Feshbach resonance can be described by a simple model equation where the scattering length is given by

$$a = a_{bg} \cdot \left(1 - \frac{\Delta B}{B - B_0}\right), \quad (1.9)$$

where a_{bg} is the background scattering length far from the resonance, ΔB is the width of the resonance, and B_0 is the center of the resonance. The calculation is shown in Fig. 1.5, with $\Delta B = 25$ G, $B_0 = 200$ G, and $a_{bg} = 10 a_0$.

With this understanding, we are able to search all possible hyperfine mixtures of ${}^6\text{Li}$, ${}^7\text{Li}$, and ${}^6\text{Li}$ on ${}^7\text{Li}$ to predict the existence and location of Feshbach resonances.

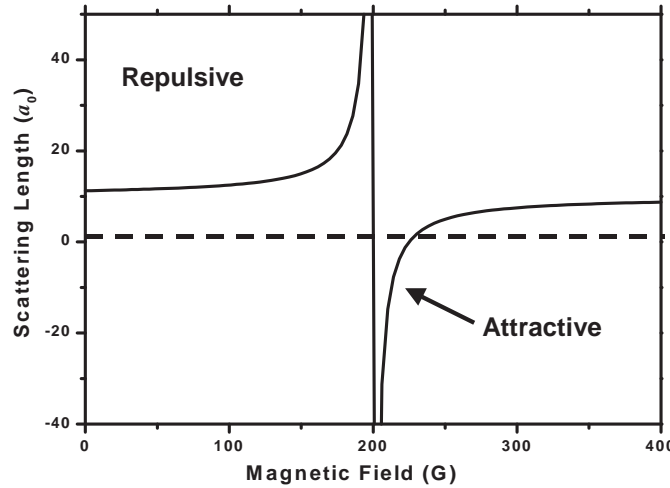


Figure 1.5 A sample Feshbach resonance calculated using the Eq. 1.9. The center is located at 200 G, the width is 25 G, and the background scattering length is $10 a_0$. The region with $a > 0$ is labelled “repulsive”, and “attractive” for $a < 0$.

The results are recorded in an internal lab document, the “orange book”. The results are subdivided by isotope and total m_F projection. The coupled channel code for producing the plots is located in `/source/iancode/cc_c2/`. The file is called “bat” and there are several pre-complied versions with varying step sizes. For example bat01, would have 0.1 G resolution while bat5 would have 5 G resolution. The details are given in reference [15].

Chapter 2

Apparatus

The goal of this chapter is to describe the EMtrap apparatus in such a way that the motivation behind the complexities of the apparatus are made clear. This chapter covers the general construction and operation of the EMTrap apparatus.

Most of the constituent parts have been described elsewhere [12, 13, 15]. The main vacuum system is described in McAlexander’s Ph.D. [15], along with the general design of the electro-magnetic trap. The remainder of the apparatus and the ^7Li laser system is described in Strecker’s masters thesis [12], while the dual ($^6\text{Li}, ^7\text{Li}$) MOT laser setup is described in Partridge’s masters thesis [13].

For completeness and solidarity, we will briefly review all the aforementioned except the vacuum system. We will focus on the new additions and improvements made to the apparatus since they were last discussed, as well as offer a sort of “users manual” for each of the various components.

2.1 MOT

The magneto-optical trap, or MOT, is simply an elaborate configuration of laser beams and magnetic field that are used to damp the motion of the atoms and localize them in space. In our experiments, the MOT is set up to damp and localize two different isotopes of lithium, ^6Li and ^7Li . This configuration is known as a “dual-MOT”. The dual-MOT has been covered in Partridge’s masters thesis [13]. Here we will cover the optical layout, magnetic fields, and switching referring to reference [13] for a full discussion on the laser system requirements.

2.1.1 Magnetic Fields

The magnetic field and the MOT switch are described in [13], but will be briefly discussed here. The anti-Helmholtz MOT coils are made from refrigerator tubing, and each coil has four turns of $\frac{1}{8}$ " tubing wrapped in a generic fiberglass insulation bought from Newark. The coils are wrapped around a set of stand-offs behind the electro-magnetic coils. At a current of 280 Amps we get a field with a nearly 30 G/cm gradient. As will be discussed later, the MOT traps all m_F state, and since we only want one m_F state in the magnetic trap, we must optically pump the atoms into the desired m_F state. This requires the MOT field to be off and an external bias field to be present to define the spin axis. Atoms trapped in the MOT have a temperature of nearly 1 mK, which means that the atoms average speed is nearly 2 mm/ms. Due to the inductance of the external bias coils, they take over 10 ms to energize them. The atoms then travel over 2 cm before they can be optically pumped. To avoid this problem, the external bias cage is kept on while the MOT is on. The external field displaces the center of the MOT from the center of the magnetic trap. A small 0.078 Ohm resistor shunts current from one of the MOT coils, pushing the MOT back into the center of the trapping region.

The MOT switch diagram is adapted from [13] and shown in Fig. 2.1. The

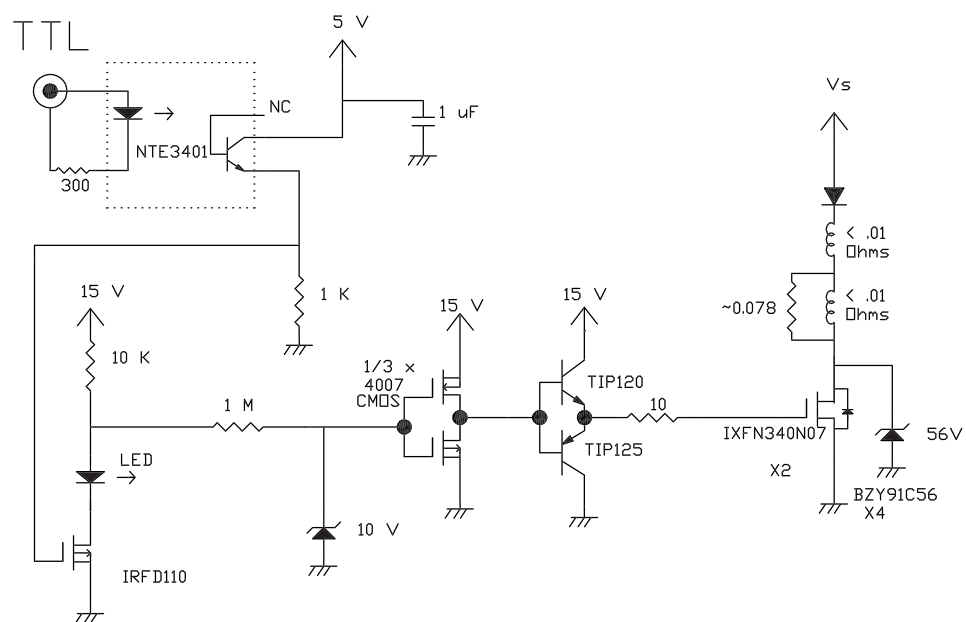


Figure 2.1 Schematic diagrams for the MOT switch. The TTL comes in through a optical isolation chip, NTE3401. The signal is inverted and fed into a 4007 CMOS buffer. The CMOS buffer drives a push-pull transistor pair that controls the gate of the high current FET. The push-pull pair are used to overcome the gate-source capacitance of the FET.

	${}^6\text{Li}$	${}^7\text{Li}$
W_0	1.25 cm	1.75 cm
P_T	30 mW	50 mW
P_r	12 mW	25 mW
I_T	2.03 mW/cm ²	2.165 mW/cm ²
I_r	0.815 mW/cm ²	1.08 mW/cm ²
Δ_T	4.5 Γ	6.5 Γ
Δ_r	4.5 Γ	4.5 Γ

Table 2.1 Typical MOT parameters for ${}^6\text{Li}$ and ${}^7\text{Li}$. W_0 is the $1/e^2$ beam waist, P_T is the total trapping power, P_r is the total repump power, I_T is the per-beam trapping intensity, I_r is the per-beam repump intensity, Δ_T is the trapping laser detuning, and Δ_r is the repump laser detuning.

schematic shows the placement of the shunt resistor, and a rough estimate of the resistance of the coils. The power supply is a Sorensen DLM8-350E, which we typically run at 280 amps and 6.99V. The majority of the voltage drop is due to the protection diode on the output of the supply and resistance on the cables and connectors hooking the supply to the coils. In addition, the supply must be run in voltage limit mode, since it has an internal protection against suddenly spiking into voltage limit. In this instance, the supply goes into a protection mode and stops putting out current or voltage until it is manually reset.

2.1.2 Dual-MOT

The magneto optical trap (MOT) has been extensively discussed in several theses [12, 13, 15]. Table 2.1 summarized the typical optical parameters for the MOTs. There is one facet which deserves repeating, which is the need for the trap depths of ${}^7\text{Li}$ and

${}^6\text{Li}$ MOTs to be similar. It has been experimentally demonstrated that the ${}^6\text{Li}$ MOT can be formed with as little as 10 mW trapping and 6 mW repumping, however, the addition of the ${}^7\text{Li}$ cleans out the ${}^6\text{Li}$ trap. As the trapping light in the ${}^6\text{Li}$ MOT is increased to around 20 mW, with 12 mW in the repump, there is a digital turn-on of the survival of the ${}^6\text{Li}$ in the presence of the ${}^7\text{Li}$. There are two possible explanations. The first is that when ${}^6\text{Li}$ thermalizes with the ${}^7\text{Li}$ MOT, the ${}^6\text{Li}$ is hotter than the capture velocity of the ${}^6\text{Li}$ MOT. The second possibility is ${}^6\text{Li}$ on ${}^7\text{Li}$ fine-structure-changing collisions as seen in a ${}^7\text{Li}$ MOT [26], and they studied the effects of fine-structure-changing collisions as a function of MOT trap depth. Here they give the trap depth of a MOT as,

$$E_T = \frac{1}{2}mv_{max}^2 \quad (2.1)$$

where v_{max} is the highest velocity an atom can have and remain trapped. Further, they estimate the energy gained by a fine-structure-changing collision as $E_{FS} = 480$ mK [26]. This suggest that the observed losses are due to fine-structure-changing collisions rather then temperature imbalances between the ${}^6\text{Li}$ and ${}^7\text{Li}$ MOTs, since the temperature difference is less then 1 mK and the fine-structure-changing collision are nearly 500 times more energetic.

In order to eliminate fine-structure-changing collision $E_T > E_{FS}$ [26]. We utilize a combination of laser intensity and detuning to accomplish this. The current incarnation of the MOT uses the Coherent 699 ring dye laser to produce the ${}^7\text{Li}$ MOT. The MOT beams are fiber coupled with a $1/e^2$ Gaussian beam radius of 1.75 cm. The total intensity in all six beams is approximately 19.47 mW/cm², at a detuning of 6.5Γ , where $\Gamma = 5.9$ MHz. The ${}^6\text{Li}$ MOT is produced using a Spectra-Physics 380-D ring dye laser for the ${}^2\text{S}_{\frac{1}{2}}$, $F = 3/2$ to ${}^2\text{P}_{\frac{3}{2}}$, $F = 5/2$ trapping transition, and a laser diode driving the ${}^2\text{S}_{\frac{1}{2}}$, $F = 1/2$ to the ${}^2\text{P}_{\frac{1}{2}}$, $F = 3/2$ repumping transition. The beams are spatially filtered and have a final beam waist of 1.25 cm, giving the intensity in all six beams at 17 mW/cm², with a detuning of approximately 4.5Γ .

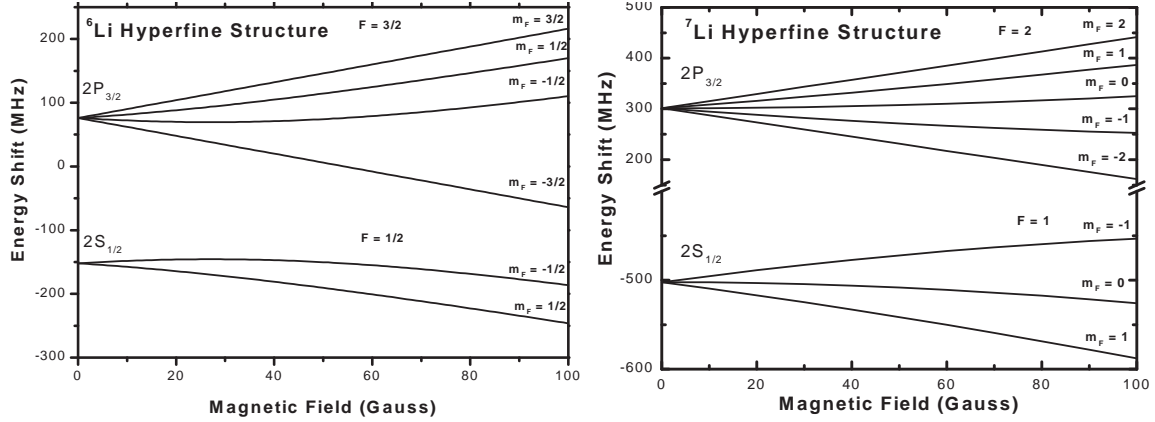


Figure 2.2 Calculation of the zeeman splitting of the ground state hyperfine structure for both ${}^6\text{Li}$ and ${}^7\text{Li}$.

Extrapolating from the data presented in [26], we see that in this condition, the dual MOT trap depth should be sufficient to suppress the fine-structure-changing collisions. However, if a minor (6 mW) decrease in the ${}^6\text{Li}$ trapping power occurs, the fine-structure-changing collisional loss will become significant.

Further detail of the ${}^6\text{Li}$ MOT laser setup is given in [13], while the details of the ${}^7\text{Li}$ MOT, including frequency generation and optical beam layouts, are given in [12].

2.1.3 Transfer

There are two steps in transferring atoms from the MOT into the magnetic trap. The first step is the compression and cooling; the second is the optical pumping. The goal of the compression and cooling stage is to increase the initial density and provide some optical cooling to the gas. Specifically, the aim is to produce the highest initial phase space density possible. The optical pumping serves to get as many atoms as possible into the desired F, m_F state for the magnetic trap, which is the $F = 2, m_F = 2$ state for ${}^7\text{Li}$ and the $F = 3/2, m_F = 3/2$ state for ${}^6\text{Li}$. Figure 2.2 shows the ground state m_F levels for both ${}^6\text{Li}$ and ${}^7\text{Li}$.

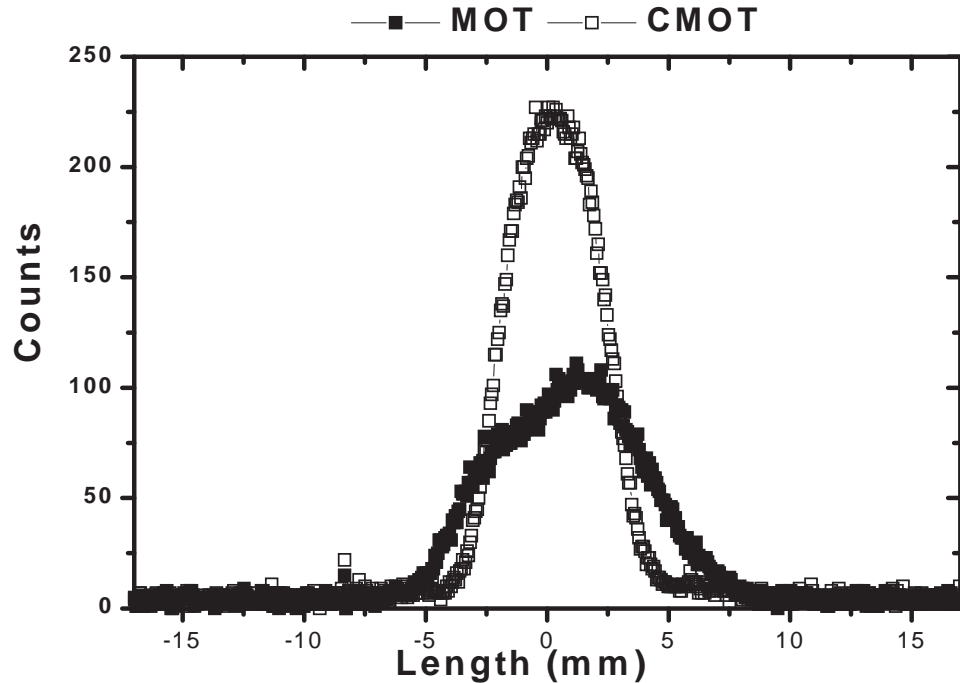


Figure 2.3 Fluorescence images of a steady state MOT and a compressed MOT. The images were taken using the Spectra-380D in MOT configuration for the probe with a detuning of $\sim 6 \Gamma$.

Compression and Cooling

The idea behind the compression and cooling stage is that in steady state operation, the density of a MOT gets limited by two main factors: the re-radiation pressure, and the column density. When the density of the MOT becomes large, a spontaneously radiated photon can be re-absorbed by another atom. Because the photon is radiated spontaneously it can have a random direction, and the net result is a pressure that limits the peak density of the MOT. In this case as more atoms are loaded into the MOT, the MOT becomes “flat-topped” and only grows in size, loosing its gaussian shape (see Fig. 2.3). The second effect is due to the column density of the MOT. As the density and size of the MOT grow, the cloud becomes optically thick, and attenuates the light penetrating to the center of the cloud. As this occurs, the trapping force in the center of the MOT decreases, limiting the maximum achievable

density.

Reference [27] discusses this problem for sodium, and offers some solutions based on a simple model of the MOT. In the model, the trapping force F_{MOT} is given by,

$$F_{MOT} = -\kappa p r \hat{r} \quad (2.2)$$

where κ is the spring constant p is the probability for an atom to be in a bright hyperfine state. The repulsive force F_{rep} is given by,

$$F_{rep} = \kappa \frac{n}{n_0} p^2 r \hat{r} \quad (2.3)$$

where n is the local density and n_0 is the peak density. The repulsive force depends on p^2 because it requires two photon scatters. For stability $|F_{MOT}| > |F_{rep}|$, implying the condition that $n > \frac{n_0}{p}$. This condition suggests that by trapping atoms in a dark state where $p \ll 1$, the peak density of the MOT can be increased significantly. The drawback is that the MOT spring constant κ depends on p , and the fewer photons that are scattered, the lower the MOT spring constant. If p becomes too small, the MOT's trapping frequency will decrease, lowering the density.

A solution suggested for the sodium MOT is directly applicable to lithium: the temporal dark MOT [27]. This concept is paramount to our compression and cooling stage. It consists of reducing the intensity of the repumping light by nearly a factor of 100. In our model, this makes p for the repumping transition approximately .01 of the p for our steady state MOT, greatly increasing the density of atoms in the lower hyperfine state, $F=1$, and $m_F = 1, 0, -1$ for ${}^7\text{Li}$. This gives us our compression.

To cool the gas one needs to look at basic Doppler theory on how the temperature scales with the MOT parameters [14]. There are two rates to compare, the heating rate and the cooling rate. If we consider atoms in a MOT with a fixed detuning Δ , the atoms will absorb photons and randomly emit them. The randomness causes the atoms to undergo a random walk, which heats the atoms. The increase in energy is proportional to the square root of the number of scatters. The cooling rate is

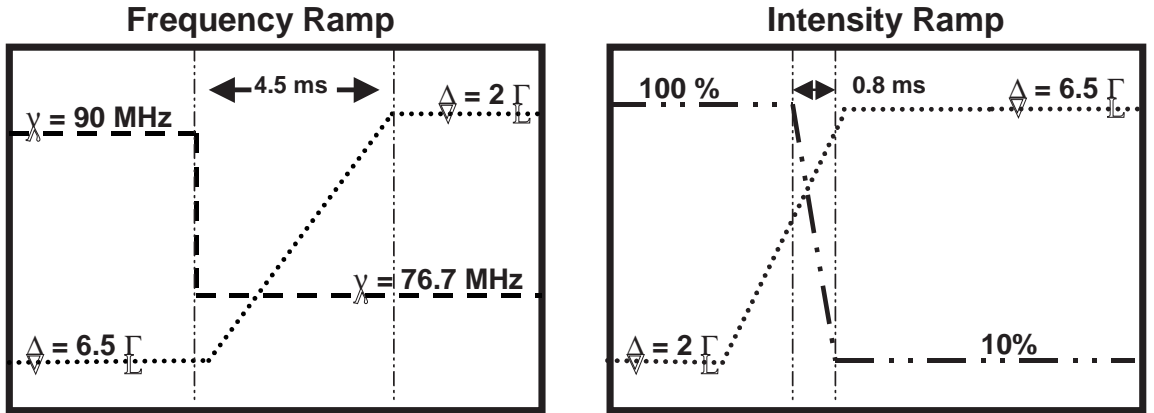


Figure 2.4 Compression and cooling ramps for the MOTs. The frequency ramp control is denoted by - - - line, the laser’s frequency response is the · · · line, and the intensity ramp is the - - - line. The frequency ramp is triggered first when the lock AO is digitally switched from 90 MHz to \sim 76 MHz. The dye laser’s responds is slow, and it ramps, roughly linearly, from the MOT detuning to near resonance, $\sim 2 \Gamma$. The intensity ramp occurs after the laser frequency has moved closer to resonance. The intensity is then reduced to $\sim 10\%$ in under 1 ms.

proportional to the kinetic energy: since the faster an atom is moving, the larger the Doppler shift, and the greater light scattering force. In the low intensity limit the Doppler cooling temperature is given by [28]

$$k_b T = \frac{\hbar \Gamma}{4} \left(\frac{1}{2\Delta} + 2\Delta \right). \quad (2.4)$$

In order to minimize the temperature, we want to be in the low intensity limit and make Δ small. For this reason, the laser frequency is ramped near resonance and the intensity of the MOT light is ramped down, decreasing the intensity by nearly a factor of 10. Figure 2.4 shows a timing diagram for the frequency and intensity ramps. The values given are the typical values used for ${}^7\text{Li}$. All the ramp parameters are adjustable by the operator, and vary depending of the output power of the dye laser, the laser lock stability, and gain settings. The ${}^6\text{Li}$ ramps are nearly identical to the ${}^7\text{Li}$ ramps, however, the ${}^6\text{Li}$ lasers are ramped from 4.5Γ to 1.5Γ , and the intensity is only reduced about 30%.

The results of the compression and cooling are shown in Fig. 2.3. The data was

taken using the Spectra-380D dye laser to perform fluorescence imaging of the MOT and compressed MOT at a detuning of 6Γ . From the images we see that the peak signal has increased, and the size of cloud is reduced. In section 2.1.3 we will analyze the data in Fig. 2.3, summarize the performance of the MOTs and compare the results to the compressed MOT.

Characterizing Compression and Cooling

The images in Fig. 2.3 were taken using an Electrim ECD-1000N CCD camera. It has $7.4 \mu\text{m}$ square pixels on a Texas Instruments TC-237 progressive scan CCD chip. The camera was mounted looking into the chamber through the top view-port. The image is collected using a Nikon 50 mm lens with a homemade C-mount to bayonet adapter. The magnification was measured by imaging a ruler, which gave $60 \mu\text{m}/\text{pixel}$, which is a magnification of 0.12. The vacuum view port is the limiting aperture in the imaging system. The geometric collection efficiency of the imaging system is given by;

$$\gamma = \frac{\pi D^2}{4\pi r^2} \quad (2.5)$$

where D is the clear radius of the view-port, and r is the distance from the atoms to the view-port. The atoms are illuminated with light for a time τ and a detuning Δ , the number of photons scattered per atom is

$$R \cdot \tau = \tau \cdot \frac{\Gamma}{2} \left(\frac{2 \frac{I}{I_{sat}}}{1 + 2 \frac{I}{I_{sat}} + 4\Delta^2} \right). \quad (2.6)$$

The total number of photons at the camera is then $R\tau\gamma N$, where N is the total number of atoms. Each photon has energy $h\nu$, so the total power incident on the camera is given by P , where

$$P = R\tau\gamma N h\nu. \quad (2.7)$$

The total number of counts on the camera, C , is given by;

$$C = R\tau\gamma N h\nu / Q, \quad (2.8)$$

where Q is the quantum efficiency of the CCD. The measured quantum efficiency for the Electrim CCD, at a gain of 180, is $1.2 \cdot 10^{-18}$ Joules/count. The total number of counts is collected by summing up the counts on the CCD array. Rearranging Eq. 2.8 we can solve for the total number of atoms, which is given by,

$$N = \frac{Q}{R\tau\gamma h\nu}. \quad (2.9)$$

The peak density for a Gaussian distribution is given by [15],

$$n_0 = N/\pi^{\frac{3}{2}} w^3, \quad (2.10)$$

where w is the 1/e Gaussian waist of the cloud. We can apply this analysis to the data presented in Fig. 2.3 and determine the effects of the compression on the number and density. For the ${}^7\text{Li}$ MOT, we get $N = 5.15 \cdot 10^{10}$ and $n_0 = 1.1 \cdot 10^{11} \text{ cm}^{-3}$. For the compressed ${}^7\text{Li}$ MOT we get $N = 1.9 \cdot 10^{10}$ and $n_0 = 2.0 \cdot 10^{11} \text{ cm}^{-3}$. The compression has lost a factor of 2.7 in number, and gained a factor of 2 in density.

In order to determine the effects of the cooling ramp, we must measure the temperature of the atoms. To determine the temperature of the atoms, we look at time-of-flight images of the MOT. This involves releasing the atoms from the MOT, allowing them to ballistically expand for a some time, t , and imaging the distribution. For time-of-flight imaging of a Gaussian distribution, the 1/e waist of the cloud as a function of time is given by [15],

$$w(t) = w_0 \sqrt{1 + \frac{2k_B T t^2}{m w_o^2}}, \quad (2.11)$$

where w_0 is the initial 1/e waist of the cloud and t is the expansion time. Using Eq. 2.11 and the data in Fig. 2.5, we calculate the temperature to be $\sim 600 \mu\text{K}$. If we repeat this process on the uncompresses MOT, we find the temperature to be $\sim 1.2 \text{ mK}$.

The parameter of greatest interest is the phase space density, ρ . This is the measure of how quantum degenerate the gas is, as $\rho \rightarrow 1$ the gas enters the quantum

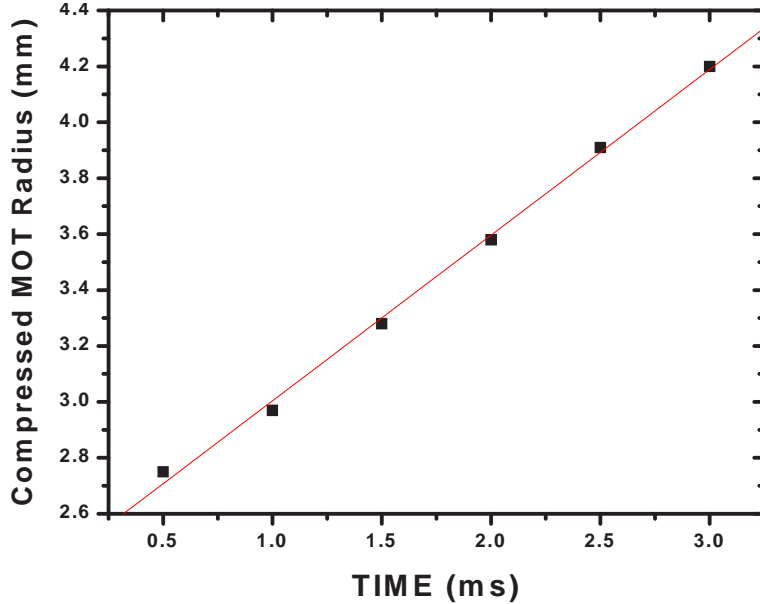


Figure 2.5 Time-of-flight temperature measurement for the compressed MOT. By releasing the atoms and observing the change in the waist versus time we can use Eq. 2.11 to extract the temperature. The data is fit to a line with a slope of 5.93 mm/ms.

degenerate regime. ρ is given by,

$$\rho = n_0 \left(\frac{2\pi\hbar^2}{mk_b T} \right)^{\frac{3}{2}} \quad (2.12)$$

where T is the temperature of the gas.

Table 2.2 lists typical number, density, temperature, and phase space density of both ${}^6\text{Li}$ and ${}^7\text{Li}$ in the MOT and in the compressed MOT. It should be noted that very little characterization of the ${}^6\text{Li}$ compressed MOT has been done. The characterization of the ${}^6\text{Li}$ has focused on maximizing the total number transferred and not maximizing the phase space density on transfer. In addition, the ${}^6\text{Li}$ characterization was performed with only ${}^6\text{Li}$ in the MOT.

Optical Pumping

As suggested above, the optical pumping is critical to ensure the highest phase space density on transfer. After the compression and cooling stage, most of the atoms

	^7Li MOT	^7Li CMOT	^6Li MOT	^6Li CMOT
N	$5.15 \cdot 10^{10}$	$1.8 \cdot 10^{10}$	$2 \cdot 10^9$	$\sim 9 \cdot 10^8$
n_0	$1.09 \cdot 10^{11} \text{ cm}^{-3}$	$2 \cdot 10^{11} \text{ cm}^{-3}$	$2.2 \cdot 10^{10} \text{ cm}^{-3}$	$1 \cdot 10^{10} \text{ cm}^{-3}$
T	1.2 mK	$600 \mu\text{K}$	1.2 mK	$400 \mu\text{K}$
ρ	$7.7 \cdot 10^{-7}$	$3.8 \cdot 10^{-6}$	$1.4 \cdot 10^{-7}$	$3.5 \cdot 10^{-7}$

Table 2.2 MOT and compressed MOT parameters for both ^6Li and ^7Li . The Fig. of merit for the compression and cooling stage in the nearly factor of five increase in the ^7Li phase space density.

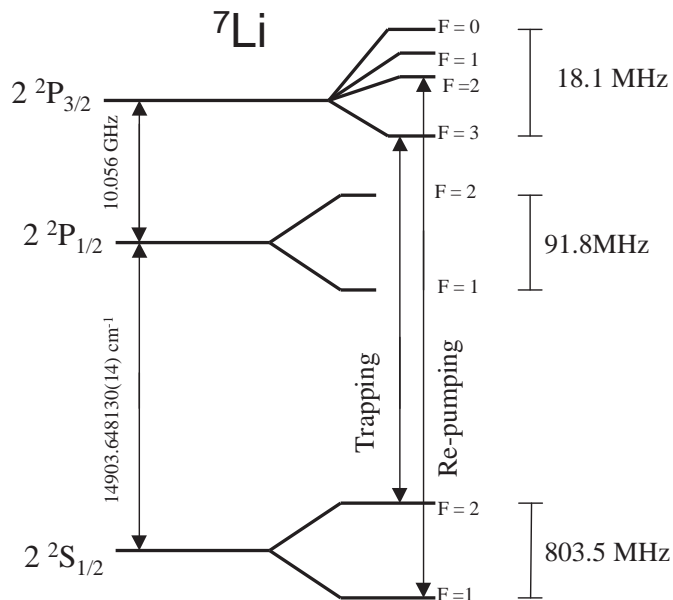


Figure 2.6 Shows the ground and upper states of ^7Li with the trapping and repumping transitions indicated.

are left in the $F = 1$ manifold, see Fig. 2.2. The first stage of the optical pumping is to pump the atoms out of the $F = 1$ manifold into the $F = 2$. This is done with the “F” pump. An 812 MHz electro-optical modulator, which produces the light that drives the $2^2S_{\frac{1}{2}}, F = 1$ to $2^2P_{\frac{3}{2}}, F = 2$ repump transition, is overdriven to nearly extinguish the carrier (which drives the trapping transition) and then the MOT beams are pulsed on for 200 μs . This pumps the atoms into the $F = 2$ manifold. However there are still 5 states in the $F = 2$ manifold in which the atoms can exist, and two of the states, $F = 2, m_F = 2$ and $m_F = 1$, can be magnetically trapped. For this reason, an on axis m_F optical pump pulse is applied.

The concept behind the m_F optical pump is that we want each atom to scatter around 10 photons, on the $\Delta m_F + 1$ transition. This gives enough scatters for all the atoms to cycle to the $F = 2, m_F = 2$. The number of scattered photons is given by the product of the pulse duration and the scattering rate

$$N_{scatter} = \frac{\Gamma\Omega^2}{2\Omega^2 + 4\Delta^2} \cdot \delta T, \quad (2.13)$$

where Ω is the Rabi frequency, and δT is the pulse duration. In order to ensure the atoms are always cycling towards the correct m_F state, the light propagates along a small (3 G) bias field and is circularly polarized, giving it a σ^+ projection onto the quantization axis. Since we do not want to push or heat the cloud, there are two counter-propagating beams. There is one additional issue to deal with, which is the same problem that leads to the density limiting effects in a MOT: re-radiative absorption. When the optical density gets too high, and an atom absorbs a photon, that atom can spontaneously emit a photon with a range of directions and polarizations. If that photon gets absorbed by another atom, that atom can lose its optical pumping. Therefore, optical pumping must be performed at a detuning where the optical density of the atoms is low. The EMtrap optical pumping is done with a detuning of 40Γ , 130 mW of total optical power, with a beam waste of 1.53 cm, a Rabi frequency of $\Omega = 2.66 \Gamma$, and a pulse duration of 250 μs . This yields about 10 scatters. The

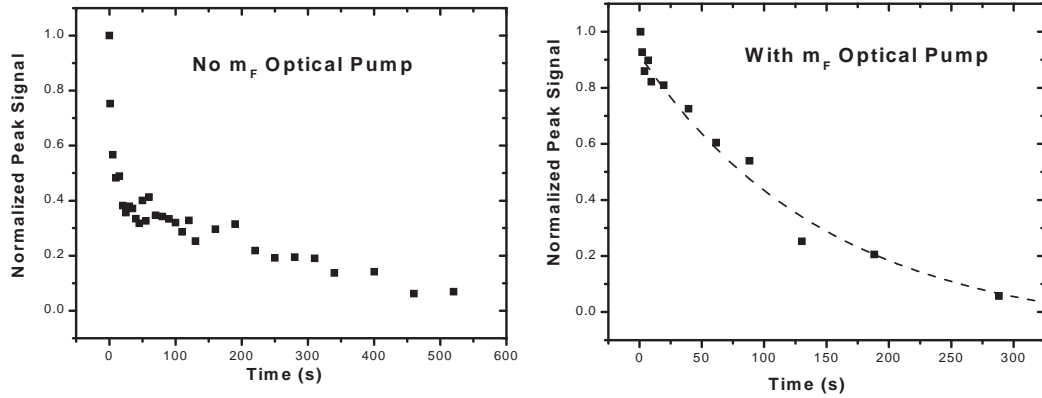


Figure 2.7 Comparison of $F = 2$, $m_F = 2$ lifetime with and without optical pumping. The non-optically pumped lifetime shows a spin purity of the $m_F = 2$ state at only 50%. The optically pumped lifetime shows a spin purity over 90%. With proper alignment of the optical pumping beams we are able to achieve > 95% spin purity in the $m_F = 2$ state.

pulse time δT is a variable experimental parameter and gives a high degree of optical pumping at time exceeding $500 \mu\text{s}$, or 20 scattered photons. Figure 2.7 shows the ${}^7\text{Li}$ lifetime in the magnetic trap with and without optical pumping. The rapid loss observed is not due to loss of $F = 2$, $m_F = 2$ state, but to the loss of atoms in the $F = 2$, $m_F = 1$ state. There are only two magnetically confinable ${}^7\text{Li}$ states in the $F = 2$ manifold, $m_F = 2$ and $m_F = 1$. Due to the total m_F conservation during a spin exchange collision, there is no combination that can lead to spin exchange loss of the $m_F = 2$ state, while the $m_F = 1$ state has a self spin exchange rate of $\sim 2 \cdot 10^{-10} \text{ cm}^3/\text{s}$ [15].

2.2 Electro-Magnetic Trap

Here we will discuss the theory behind the electromagnetic coils, their design and general construction, and how to operate the coils. The majority of this section is a review of material discussed in McAlexander's Ph.D. thesis [15], however, several significant modifications have been made to both the coils and the switch, while the general principles remain the same.

2.2.1 Clover Leaf Trap

The design of the clover leaf trap has been modified from the MIT design discussed in M. O. Mewes Ph.D. thesis [29]. The idea is adapted from the Ioffe-Pritchard trap [30]. The idea is to create a set of coils that provides tight electromagnetic confinement and maximizes optical access to the center region of the magnetic field. To do this we employ four D-shaped sets of alternating anti-Helmholtz coils which provide confinement in the radial dimension. These coils are called the quadrupole coils, since they produce a nearly linear quadrupole field in the radial dimension. The axial confinement comes from the sum of the bias and curvature coils. The bias coil is in Helmholtz configuration, while the curvature coils have the same separation as the bias coils, they have a smaller diameter which causes them to produce a bias field with curvature. The field from the curvature coils counters the flat bias field from the bias coils to create the axial confinement. The bias coil is actually an anti-bias coil, it cancels nearly all the bias contribution from the curvature coils, leaving only a small bias field. For hot atom clouds ($T > \sim 100 \mu\text{K}$) the radial gradient, B'_R provides the radial confinement and the axial confinement is always given by the curvature field B''_z . However, as the trapped gas cools, its size shrinks and only samples the center of the trap. In this case the trapping potential can be expanded about its minimum and we find [15]

$$U(r, z) = ((\mu B'_r)^2 r^2 + (\mu B_0 + \frac{1}{2} \mu B''_z)^2)^{\frac{1}{2}} + \mu B_0 \quad (2.14)$$

where B_0 is the residual bias field and μ is magnetic moment of the atom. We can solve this expression to find out what the harmonic radial frequency depends on at the bottom of the trap. The radial curvature is given by [29];

$$B_r'' = \frac{B_r'^2}{B_0} - \frac{B_z''}{2}. \quad (2.15)$$

Equation 2.15 shows that the radial harmonic trapping frequency actually decreases as the bias field increases. This tells us that the goal is to construct an electromagnetic trap with as low of a bias field as possible. It should be noted that due to Majorana spin flops [31] if the bias field goes through a zero the atoms loose their m_F projection and can be lost from the trap.

To calculate the trapping fields we simply use the Biot-Savart law. The bias and curvature sets are simple loops, while the quadrupole fields can be dealt with by breaking each section into a line current with finite extent and summing up the results. The finite extent of each track in the coil form is tackled by assuming that the wires are uniformly distributed throughout the track and summing over the different wires. The code for this has been converted from a *c* program into Matlab for ease of use and displaying the graphical results. The code was written by A.G. Truscott and is located in lab/source/emtrap/mag/...

2.2.2 Coil Construction

The general design of the coils is described in [15], however, one major modification has been made. The original design utilized the tightest confinement possible. Since the quadrupole coils are responsible for the radial confinement, which accounts for two of the three dimensions, the quads were placed closest to the atoms. As a result, the bias coils could not be exactly in Helmholtz configuration. In our latest design, the most critical issue is the flatness of the high field bias field. Therefore, the bias coils have been placed closest to the atoms, and in Helmholtz configuration, placing the quads behind the bias curvature stack. Figure 2.8 shows the current bias-curvature

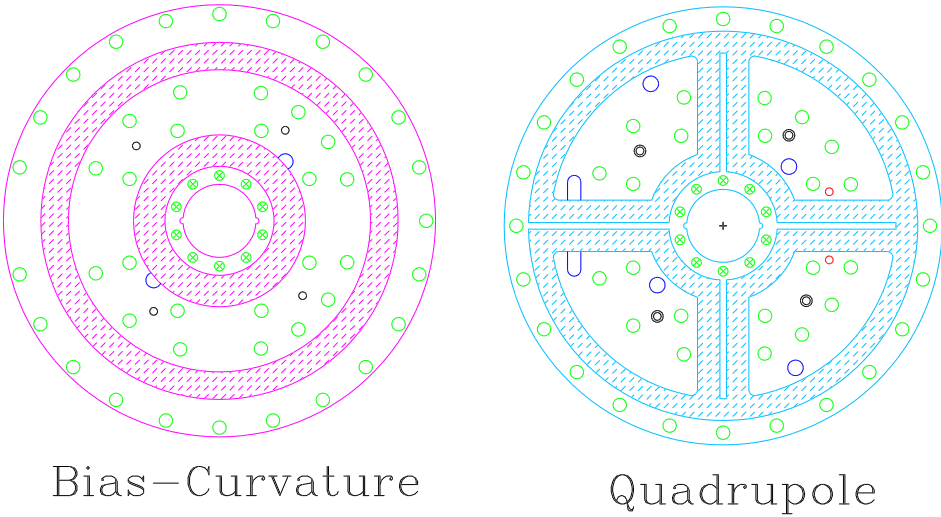


Figure 2.8 Schematic diagrams for the electro-magnetic trap coils, showing the bias-curvature set along side the quadrupole coils.

and quadrupole coil designs. Full schematics and machine drawings are located in appendix 5.2.

Construction

The real trick to the coils lies in their construction. It is a difficult process. Here we will outline a set of procedures: wrapping, assembling, and testing the coils.

The coils are made using an 18 gauge heavy armored copper-ETP magnet wire made by the California Fine Wire Company. The armor on the wire can handle temperatures exceeding 200 °C. The coil forms are constructed from a plastic made of Poly Ether Ether Ketone (PEEK) which can stand temperatures up to 250 °C and has a melting point of 348 °C.

Wrapping

There are six total coils: two bias, two curvature, and two quadrupoles. Each coil is wrapped independently. To wrap the bias coils, there is a white delrin form that has the same shape and volume as the coil form. The coils have 30 total turns

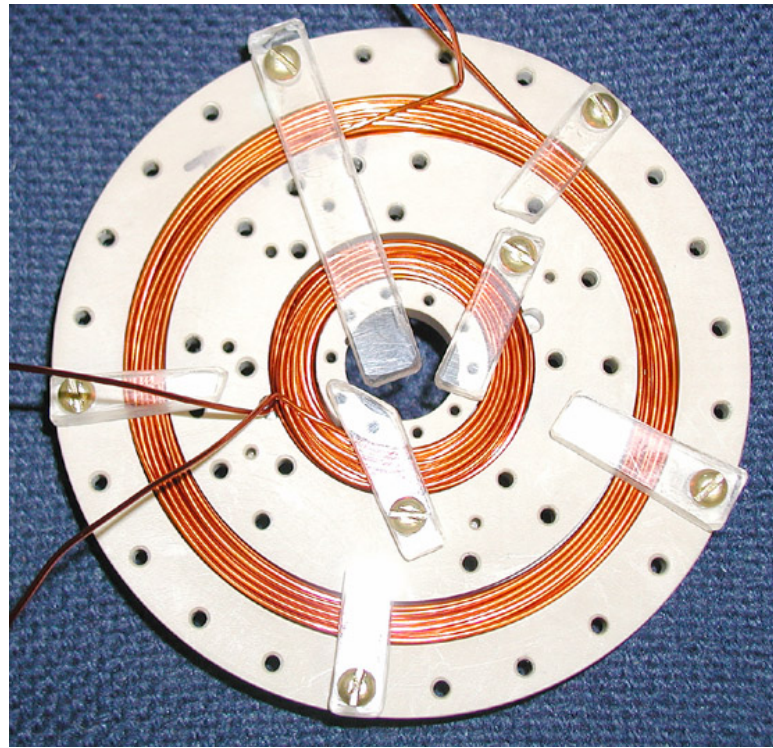


Figure 2.9 The shows the bias-curvature set under construction.

which must be wrapped carefully to insure uniformity of each wrap, and one half of a meter of spare wire should be left on the input and output of the coil for making the electrical connections. Once the wire is wrapped onto the delrin form, the top can be removed, and the coil can be slipped into the coil form. Once in the form, the coils will naturally spring out, so there are some high precision handcrafted coil holders that keep the coils in place. Figure 2.9 shows a photograph of the bias-curvature set during construction. The clear plastic bars are coil holders, and the lead wires have been twisted together. Since the coil holders must be removed to assemble the coil forms, we must ensure the coils do not pop out of the forms when the holders are removed. To do this we placed Elmer's wood glue into the coil tracks. The glue takes 12 to 24 hours to dry, but once dry, the coil holders can be removed and the coils will stay in place. This same process is repeated for the curvature coils but with 34

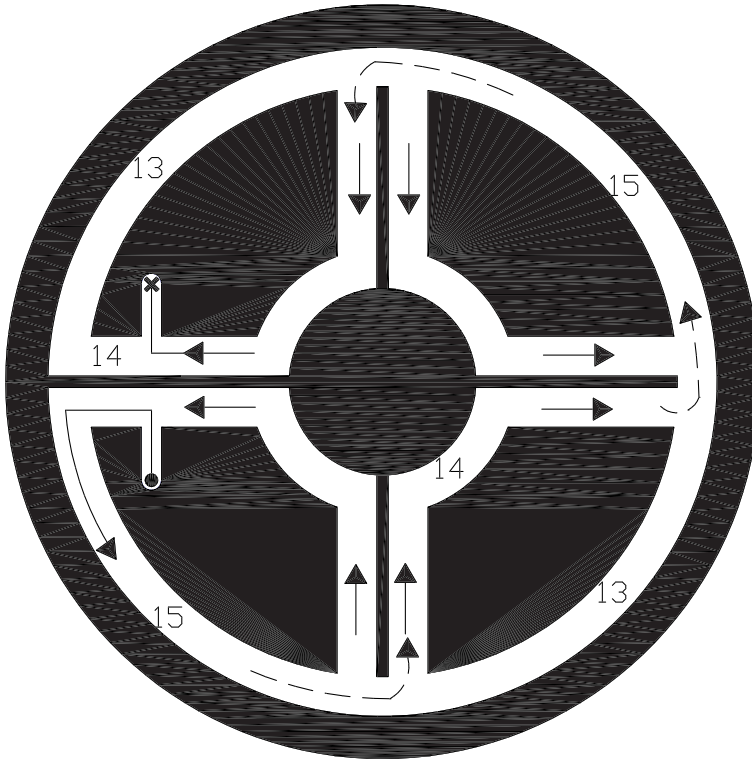


Figure 2.10 this Fig. illustrates the the direction of the wire for wrapping the quadrupole coils.

wraps. It should be noted that the bias and curvature sets can be made in parallel, so only one glue drying period is required. Figure 2.9 was taken during the glue drying phase for the bias-curvature set.

The quadrapole coils are somewhat more tricky to wrap. Figure 2.10 illustrates the flow of the wire around the quadrupole coil form. The wire enters at the dot and proceeds around the form as indicated by the arrows. Each “D” is wrapped following the flow of the solid arrows until the indicated number of wraps is achieved. The wire then progresses to the next “D” following the dashed arrows. This continues until the last “D” is wrapped, then the wire leaves the form at the “X”. There are two experimental methods for wrapping the quads; one is to take a scale printout of the coil form and place it onto a piece of plywood. Finishing nails are hammered

into the plywood, outlining the path of the wire, and the wire is wrapped around the nails, making the coil. The wire is then bundled with twist ties, and removed from the plywood form. The coils can be placed into the coil form (with the twist ties removed) held in place with the coil holders, and glued. This method is the “safest” since the number of turns in each coil can be counted (and re-counted) before being placed into the coil forms. However, there is one major drawback to this method: the points on the coils where the wire goes from the outer diameter to the bar, are tight corners. When the coils are wrapped around the nails, it is difficult to fill the corner properly with wire. Often, the corners are wrapped too tight, which causes a higher density of wire at the corner, and can lead to a burnout. The second method of wrapping the coils is more straight forward, but it takes more skill and a second set of hands. The second method involves wrapping the wire directly into the coil form. With the coil holders in place, each subsection of the coil can be wrapped. Once the coil is wrapped it can be glued. Figure 2.11 shows the quadrupole coils during the glue drying stage.

Assembly

While the glue is drying, the gaskets must be made. The gaskets come from Texas Gasket and Packing, part T722 Gasket. They are viton gaskets $\frac{1}{32}$ " thick, 5" OD, and $\frac{3}{4}$ " ID. The procedure is to print a scale drawing of the top and middle layers of the coils, and tape them each to a gasket. Using the punch tool, available from the machine shop, punch out the screw holes with the smallest punch. The water holes should be punched out with third smallest punch or larger where possible. Punching larger water holes helps to ensure that when the gaskets are compressed they will not occlude the flow of water.

Once the gaskets are punched, they are greased up with a sparing amount of cock-stop grease. Once the coil holders are removed, it is important to make sure there

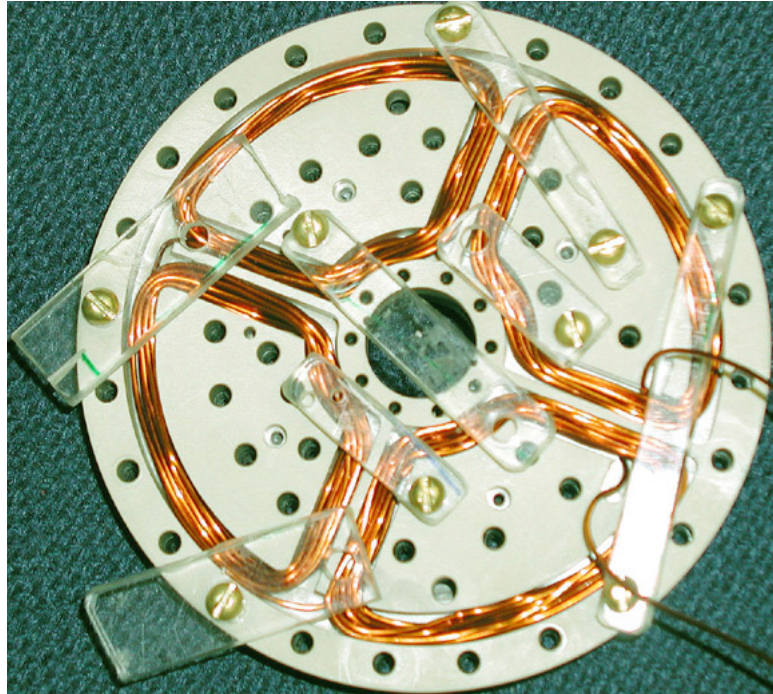


Figure 2.11 Photograph of the quadrupole coils during construction.

is no hardened wood glue on any of the sealing surfaces. The gaskets are then put in place and the forms are bolted together in the same fashion as a vacuum flange. The “star” pattern is not critical, but it is critical that the coil be tightened down gradually and uniformly to avoid stressing the threaded holes on the bottom layer of the form.

Once the coils have been assembled, they should be placed in hot water to soak (preferably overnight). Then, one at a time, each coil should have hot water flowed through it to remove all of the wood glue. The water will flow milky white at first but will run clear once the residual glue is removed.

The next step is to check the coils for leaks. The coils should be mounted on a test bench and plumbed, utilizing flowing water to identify any leaks. At this point, if the form is leaking, it is okay to tighten down the screws. (Prior to this step, the screws should not be excessively tight.) If leaking, the troubled area(s) should be

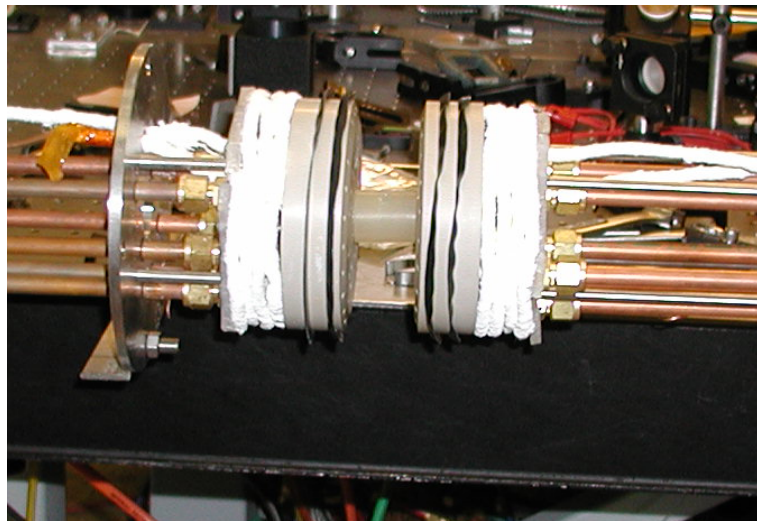


Figure 2.12 Photograph of the assembled coils.

marked, the water should be drained from the coils, and the leaks patched using a “wet surface epoxy”. The epoxy can be purchased from the chemistry stock-room. This process is repeated until there are no leaks.

Testing

Next, the coils should have their flow checked. With the coils plumbed, and the two bias coils in parallel, the two curvatures in parallel, and the two quadrupole coils in parallel, remove the return line from one coil at a time and measure the amount of water that flows out in 30 seconds. Repeat for each coil. Typical values for the bias coils are 85 mL/s, curvature 100 mL/s, and quadrupoles 110 mL/s.

The final step is to wire up the coils. The electrical connections are made by drilling a .05” hole in the copper plumbing, and pulling the wire out through the hole. The wires are braised to the outside of the pipe, an electrical connection to the pipe is made and the drill hole is sealed. The only cautions are: (1) do not accidentally drip solder into the hole and have it clog the coil, and (2) do not have any plumbing attached to the coil form while the plumbing is hot, as the PEEK could melt. Figure

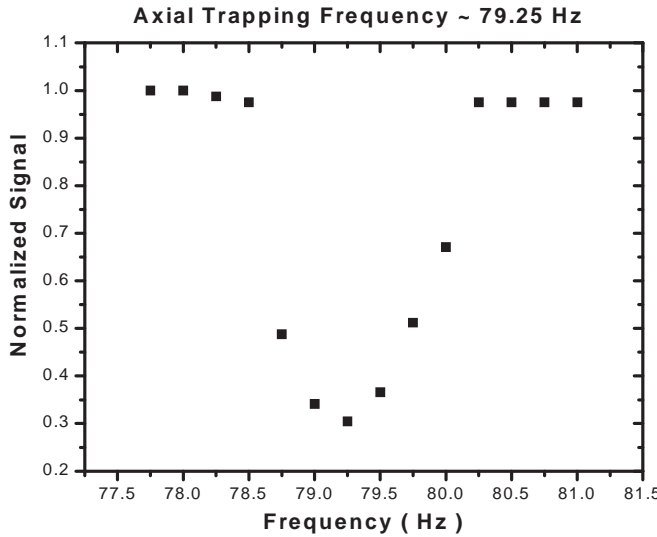


Figure 2.13 Axial trap frequency. Each point is obtained by diving the external coil at the specified frequency and recoding the peak signal after evaporation.

2.12 shows a photograph of the fully assembled coils.

Once the coils are installed the final characterization is to find the trapping frequencies. The calculations for our coils, gives the trapping frequencies at 80 Hz axially and 800 Hz radially for ${}^7\text{Li}$. To measure the trap frequencies we apply an external magnetic field oscillating near the trap frequency and look at the number of atoms after an evaporation. To drive the external field we use a hand-wound magnet that consists of ~ 100 turns of 22 gauge magnet wire. The drive signal is produced by an Agilent 33120A waveform generator and amplified by a TIP120/125 push-pull transistor pair. The coil is constructed on the end of a two foot Delrin rod. Shortly after the atoms are loaded into the magnetic trap and the evaporation is underway, the external coil is placed into the center hole of one of the magnetic trap coil forms. The results for the axial frequency is shown in Fig. 2.13. The axial frequency was found to be ~ 79.25 Hz, within 1% of the calculated value. Due to the geometry of apparatus, it is difficult to drive the radial component of the trap. Our best measurement of the radial frequency gives it at ~ 790 Hz, within 1.25 % of its calculated value.

2.2.3 The Switch

Once the electro-magnetic coils are in place, the next step is to switch them on and off. The basic idea is that the atoms are trapped in a MOT made by the MOT coils. Those coils must be de-energized, then at some time Δ later, the electro-magnetic coils must be energized. To accomplish this, we employ pairs of matched high power FETs controlled by optically buffered digital TTL lines from our control computer. Figure 2.14 shows the circuit diagram for the high current switch.

In order to test the performance of the switch, two non-grounded X100 high impedance scope probes are hooked up across sets of coils and fed into a Tektronix TDS200 digital scope. The scope is triggered by the switch's TTL control line and the scope's MATH function subtracts the two input signals, giving a signal proportional to the current. Since the time scale for these measurements is typically 10 ms, we can neglect any thermal effects on this measurement. Figures 2.15 and 2.16 show the turn on and off of the bias-curvature and quadrupole coils respectively.

The only thing to be careful of with the turn on of the coils is to make sure that the voltage limits are set correctly, otherwise during the turn on too much current can instantaneously flow, which will over compress the trap for a few ms, and then relax back to the proper steady-state value. Having the voltage limit set too high has the effect of heating the atoms during transfer, Fig. 2.17 shows the turn on in this case.

Next, we will discuss the turn off of the magnetic trap. The biggest issue with the turn off of the magnetic trap is that it must be done fast compared to the trapping frequencies. The reason for this is that if the ratio of currents between the quads and the bias-curvature set is not kept relatively constant, the center of the magnetic trap can move. This motion of the trap center seems to stem from non-perfect cancellation of the axial fields produced from the quadrupole coils. This problem has not been fully studied, but some initial testing suggests that if the bias/curvature coils and the

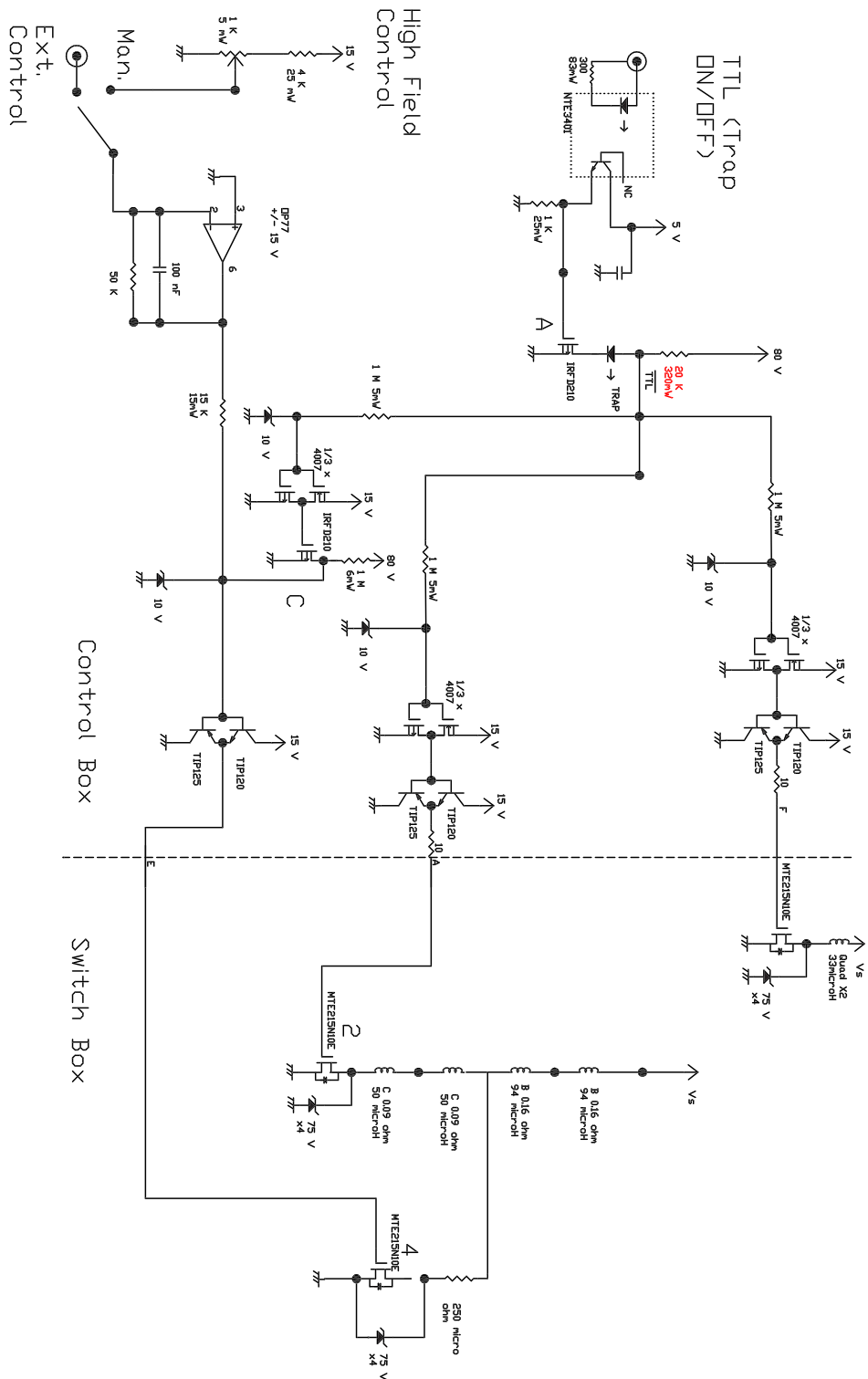


Figure 2.14 Circuit diagram for the electro-magnetic trap high current switch.

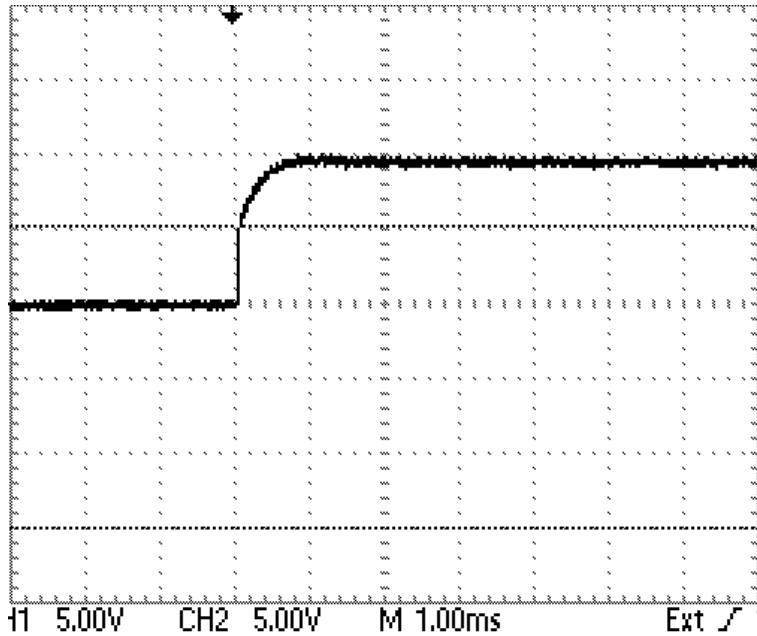


Figure 2.15 Trace of the bias-curvature coils switching on.

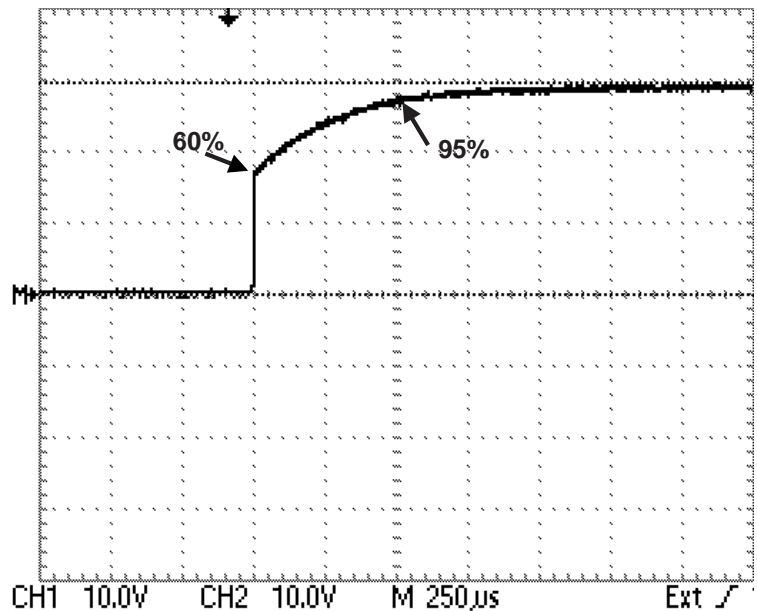


Figure 2.16 Trace of the quadrupole coils switching on.

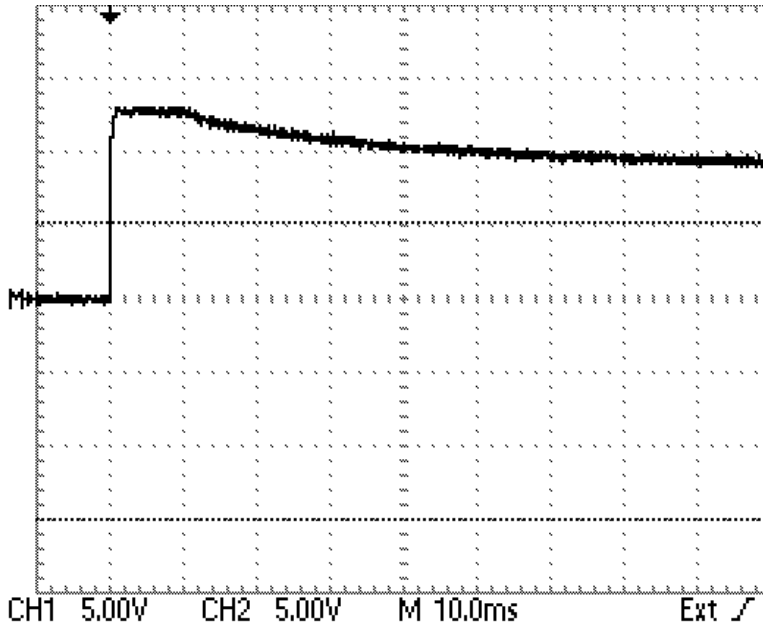


Figure 2.17 Trace of the bias-curvature coil switching on when the voltage limit is incorrectly set too high.

quadrupole coils were relaxed with a fixed current ratio, the fields could be turned off smoothly. However, currently it is sufficient to simply turn off both sets of coils as quickly as possible, so that the atoms do not have time to respond to the changing field. Figure 2.18 shows the turn off of both the bias/curvature set and the quads. The fields turn off in under $10\ \mu\text{s}$, except for some inductive ringing on the bias/curvature set which is on the 1 ms time scale.

2.2.4 High Field Control

The high field is defined to be the condition when the magnetic trap is off and only the bias coils are energized, producing a bias field that can be tuned from 0 G to ~ 1000 G. Since this condition requires the magnetic trap to be off, we confine the atoms using an optical trap, which is described in section 2.3.

The high field control is somewhat more involved than the EMtrap control. There are two main issues: the first is that in our magnetic trap configuration the bias coils

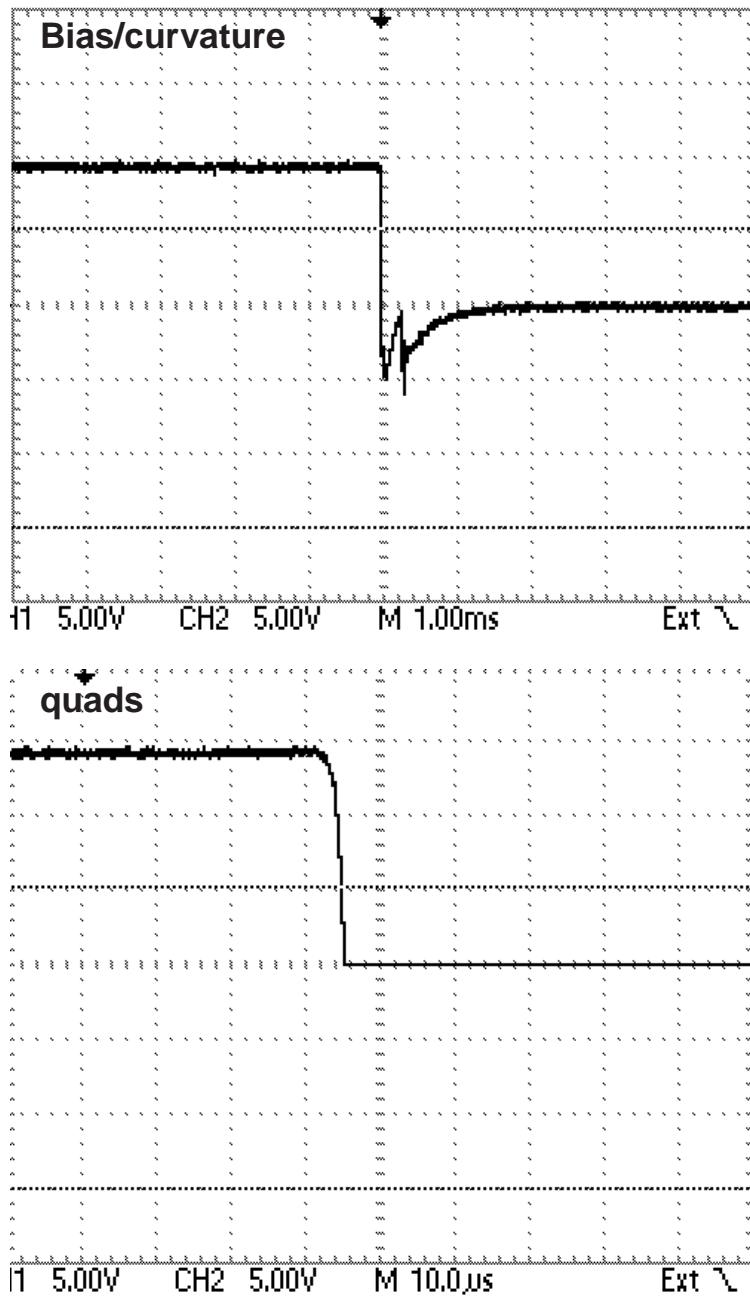


Figure 2.18 Traces of the bias-curvature and quadrupole coils turning off.

are actually “anti-bias” coils. This means they produce a field that points against the magnetic traps bias field ($-\hat{z}$ direction). Therefore, to keep the gas spin polarized when we go to the high field condition, we must adiabatically rotate the spins from the \hat{z} direction to the $-\hat{z}$ direction. The second is that we do not just want to turn on the high field, we want the ability to actively control the high field, i.e., the ability to ramp the field down and back up again with differing time scales.

The first problem is easily overcome using the “nulling cage”. The nulling cage is described in [15]. It consists of three pairs of roughly Hemholtz coils in the \hat{x} , \hat{y} , and \hat{z} directions. The \hat{z} (along the magnetic trap bias field) coils form the optical pumping bias field (~ 3 G) and magnetic trap bias field (0.7 G), described in section 2.1.3. The \hat{y} (vertical direction) cage is unused, while the \hat{x} coil provides a sideways field. Experimentally, the magnetic trap is switched off and the optical trap is switched on. This causes the atoms to be polarized along the \hat{z} direction. The sideways field is ramped up to nearly 3 G, and the atoms are now polarized along the $\frac{1}{2}(\sqrt{2}\hat{z} + \sqrt{2}\hat{x})$. After the sideways field is on, the bias coils are energized and the atoms rotate from the $\frac{1}{2}(\sqrt{2}\hat{z} + \sqrt{2}\hat{x})$ direction to the $-\hat{z}$ direction. By adding in the magnetic field from the sideways cage, the atoms avoid going through a zero in the magnetic field when the bias coils are energized.

The second issue essentially comes down to how do we control the high field (also called the bias field). The power supplies used are manufactured by Electronic Measurements Inc., model ESS 60-165-11-D. They have a 24 pin programming connector on the rear panel. They have the option for remote programming of both the current limit (I_{limit}) and the voltage limit (V_{limit}) using external voltages. Figure 2.20 shows the connection on the J1 connector for remote control of both I_{limit} and V_{limit} . The important thing is that the remote voltage is not applied between ground and a control pin, rather it is a voltage difference between two pins, so a floating voltage source must be used for stable operation.

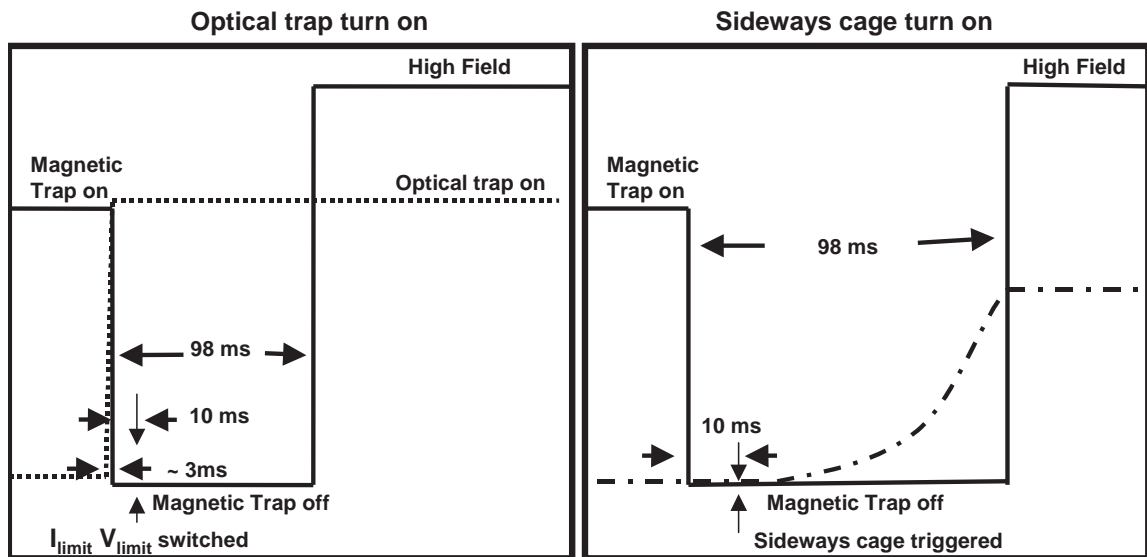


Figure 2.19 Timing diagram for the turn on of the optical trap and the turn on of the sideways cage with respect to the magnetic trap turn off and the high field turn on. The ■■■ line is the optical trap, the - - - is the sideways cage, and the solid line is a measure of the voltage across the bias coils.

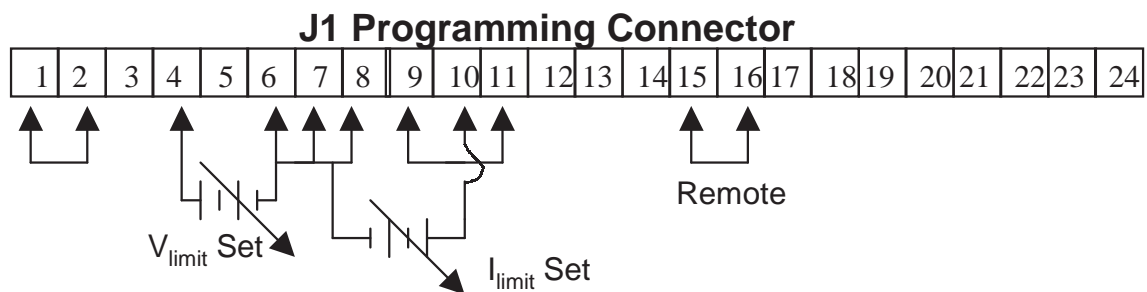


Figure 2.20 Diagram of the J1 remote programming connector for EMI ESS series power supply.

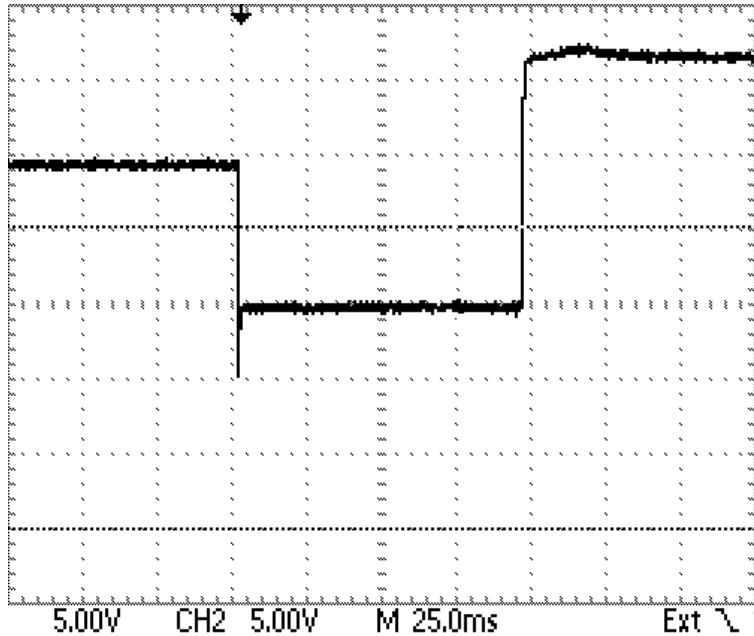


Figure 2.21 Trace of the bias-curvature coils switching off and the bias coils switching on to form the high field. The measurement was made by looking at the voltage across the bias coils. The plateau on the right corresponds to 50 A flowing through the bias/curvature set in magnetic trap mode, while the other plateau corresponds to 80 A in the high field mode.

The experimental sequence is as follows: once the magnetic trap is switched off, such that FET 2, 4, and 6 from Fig. 2.14 are non-conducting, the I_{limit} and V_{limit} are switched from the magnetic trap values to the high field values. Once the sideways cage is fully up, the bias field is ramped on, in 1 ms, by a 0 to 5 volt ramp applied to the external control in Fig. 2.14, which makes FET 4 conduct (see Fig. 2.19). If the ramp is much slower than 5 ms, the control circuit can oscillate, while if the ramp is much faster than 1 ms, the response will be limited by the power supply. Once the bias field is on the I_{limit} , it can be varied to ramp up and down the bias field.

The control electronics are designed around an electronic component called a precision CMOS analog switch. Figure 2.22 shows the functional block diagram for this switch. It is a single pull double throw (make before you break) switch. The benefit of this chip is that the voltages at $SW1$ and $SW2$ can be within $\pm .3$ V of

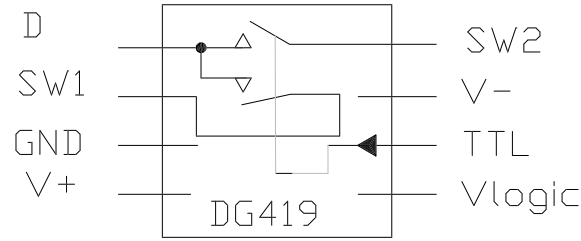


Figure 2.22 The functional block diagram for the DG419 precision CMOS analog switch.

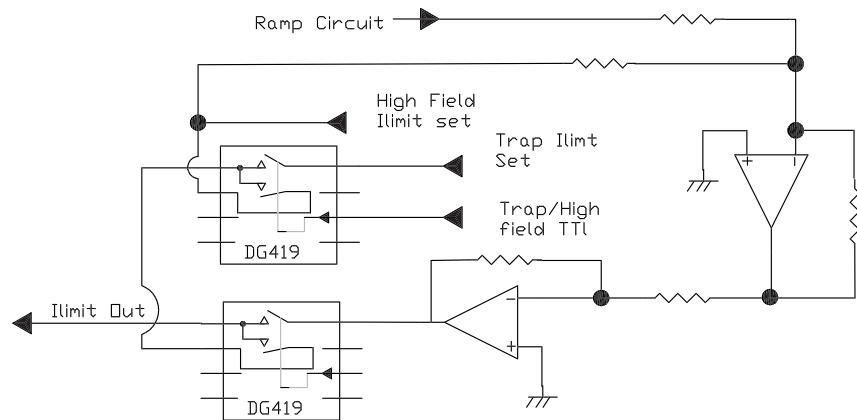


Figure 2.23 The functional diagram for the high field control circuit. All resistors are 10K and the operational amplifiers are OP177.

the supply, and completely independent. By employing several different DG419s and a regulated DC/DC converter with differential floating grounds, we can build a high field control circuit that switches between several highly stabilized floating voltages. Further, we can also add in linear and RC ramps. Figure 2.23 shows schematically how the high field is controlled. The analog switches are controlled using TTL lines to switch the voltage controlling I_{Limit} between various user-specified values. The circuit is powered by a floating DC/DC converter model WPC03R by C and D Technologies. There is a similar circuit in order to switch the V_{Limit} control when going into the high field mode as shown in Fig. 2.19. All the circuits, product data sheets, and chip layout schematics are located in [32], which is a grey 3-ring binder, labelled “EMTRAP Switch Book”.

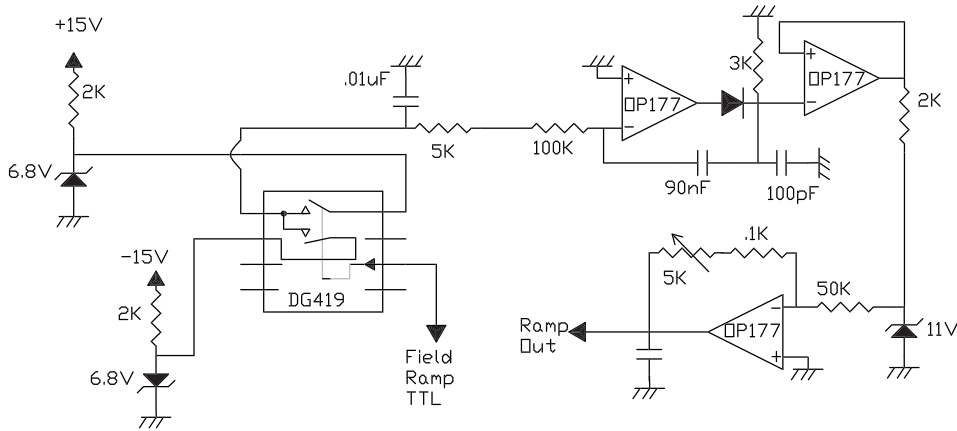


Figure 2.24 Schematic of the linear ramp circuit used to ramp down and up the bias field.

The ramp referred to in Fig. 2.23 has two possible states. The first is the ramp used in the soliton experiments. In this case, the two OP-AMPS are not present, and the high field I_{Limit} line is hooked to an RC circuit which ramps down the control voltage with an RC decay. The second rendition was used in the experiments for forming molecules. In this case, a linearized ramp circuit was used. The general schematic is given in Fig. 2.24. In the second case, the user can select the magnitude of the ramp and the time constant. The ramp is summed in with the I_{limit} set value to control the field.

Danfysik

Recently, an alternative means of controlling the external field has been added, which involves the use of a high precision DC current transducer, Manufactured by Danfysik. The current transducer puts out a current that is proportional to the current in the coils. That signal can be processed and fed back to the control of FET 4 in Fig. 2.14. Then, with the power supply in constant voltage mode, FET 4 can be used to both stabilize the bias field and to move the bias without having to adjust I_{limit} or V_{limit} . This method offers the ability to make changes to the external field on

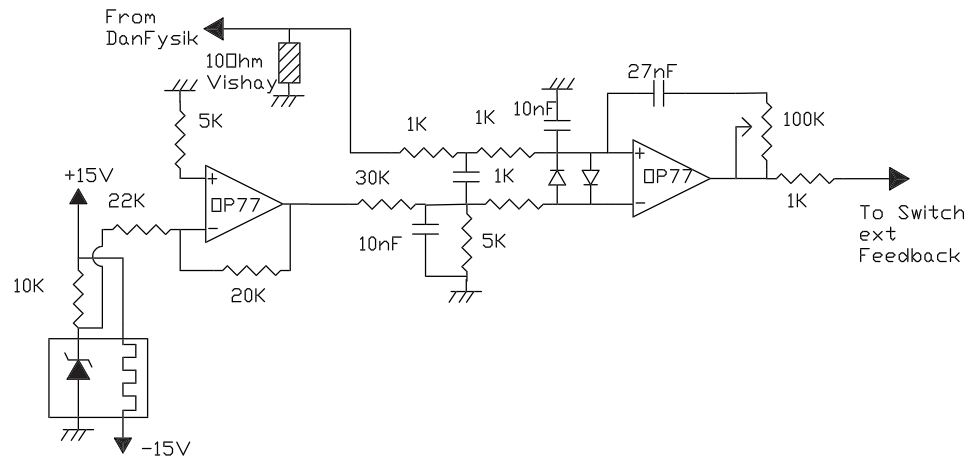


Figure 2.25 The functional diagram for the Danfysik high field control circuit.

a much faster time scale than can be achieved by adjusting the power supply. When we control the magnetic fields through the power supply the current can be reduced on the μs time scale, however, to increase the current the supply must charge up. This time scale varies with the magnitude of the increase in current, and can take as long as 500 ms for the field to stabilize. Using the current transducer, the output of the supply does not change, the field is controlled by a FET, and can respond as fast as the feedback bandwidth. The feedback circuit is shown in Fig. 2.25. The circuit is housed in a box mounted on top of the bias-curvature power supply stack. The current transducer is hooked up to the return line from the bias-curvature power supplies, and is mounted just behind them. The transducer is powered from the feedback loop and must always be powered when current is flowing through it to avoid damaging the transducer.

2.3 Optical Trap

The optical trap is the most versatile atom trap we employ. It allows us to trap any hyperfine state, and any mixture of hyperfine states. Since its potential does not rely on magnetic fields, an external magnetic field can be applied with any arbitrary magnitude. The principle behind the operation of an optical trap is quite simple. The atoms are attracted or repelled from the focus of a laser beam by the interaction of the atom's electric dipole moment with the laser field. If the laser is tuned to the red (longer wavelength) of the atomic transition, the atoms are attracted to the high intensity region (the focus) of the beam. Conversely, atoms are repelled by a blue detuned laser.

In this section we will discuss the theory behind the optical trapping potential, trap depth requirements, and loss rates. We will also look at our first implementation of an optical trap using a single focused infrared laser and two cylindrically focused green laser beams. We will look at our improved optical trap, formed by a crossed pair of focused infrared laser beams, and will conclude by reviewing some common experimental issues involved in aligning and transferring atoms to the optical trap.

2.3.1 FORT

There are two main types of optical traps, the first type is the QUEST, or quasi-electro-static trap. This type of optical trap occurs when the detuning of the trapping laser is so large that the rotating wave approximation is no longer valid, and both waves have comparable amplitudes. The laser is now interacting with the electric dipole moment of the entire atom [33]. For alkali atoms the most common type of laser for making a QUEST is a CO₂ laser at 10.6 μm . In the experiments described in this thesis, the laser frequencies are near 1.064 μm . In this frequency region a second type of optical trap exists: the FORT, or far off resonance trap [34]. For the FORT, the light interacts with the electric dipole moment between two internal states. The

trapping potential from the laser depends on the detuning, Δ , of the trapping laser and the Rabi frequency, Ω of the transition. The potential, in units of temperature, is given by:

$$U_{optical} = \frac{\Omega^2}{4 \cdot \Delta} \cdot \frac{\hbar}{k_B} \quad (2.16)$$

To put some numbers with this, if we have a 1 W Nd:YAG laser at 1.064 μm focused to a 50 μm spot size, we get a peak trap depth of approximately 13 μK . The other figure of merit for an optical trap is the trapping frequencies.

We can estimate the trapping frequencies by assuming the atoms make only small amplitude oscillations about the center of the potential. The potential can then be expanded about the origin, and we keep only the harmonic term in the expansion. We can equate the harmonic term with the classical energy of a particle in the harmonic well, as given by Eq. 2.17, where m is the mass of the particle, ω is the trapping frequency, T is the temperature, k_B is the Boltzman constant, and r is the excursion of a particle from the center of the trap:

$$U(r) = \frac{1}{2}m\omega^2r^2. \quad (2.17)$$

The difference between the axial and radial frequencies derives from the way a focused Gaussian beam diverges in two different dimensions. Equation 2.18 gives the familiar radial divergence of a Gaussian beam, where w_0 is the $1/e^2$ radius of the beam.

$$I_{radial} = I_0 \cdot e^{\frac{-2r^2}{w_0^2}} \quad (2.18)$$

$$I_{axial} = I_0 \left(1 + \frac{z^2}{R_l^2}\right)^{-\frac{1}{2}} \quad (2.19)$$

The axial beam divergence is given in Eq. 2.19, where $R_l = \frac{\pi w_0^2}{\lambda}$ and λ is the wavelength of the trapping laser. Now we can eliminate I_0 with the relation $I_0 = 2P/\pi\omega_0^2$. To estimate the radial trapping frequency, we must substitute Eq. 2.18 into Eq. 2.16 by rewriting the Rabi frequency as $\Omega = \gamma\sqrt{\frac{I}{I_{sat}}}$. Next we expand the exponential

and equate the harmonic term with the left hand side of Eq. 2.17, and solve for the trapping frequency ω . The result is given in Eq. 2.20.

$$\omega_{radial} = \sqrt{\frac{2\gamma^2 P}{\Delta I_{sat}\pi\omega_0^4 m}} \quad (2.20)$$

If we put in our numbers (1 W, 1.064 μm , and $\omega_0 = 50 \mu\text{m}$) we get a $\omega_r \simeq 764 \text{ Hz} \cdot 2\pi$. Figure 2.26 shows the radial trapping potential for these parameters.

The axial frequency is estimated in the same fashion, and the result is given by

$$\omega_{axial} = \frac{\gamma\lambda}{\pi^2\omega_0^3} \sqrt{\frac{\pi P}{\Delta I_{sat}m}}. \quad (2.21)$$

If we plug in our numbers, we get $\omega_a = 3.7 \cdot 2\pi \text{ Hz}$. Figure 2.27 shows the axial trapping potential for these parameters. We can then calculate the aspect ratio by dividing Eq. 2.20 by Eq. 2.21, yielding Eq. 2.22:

$$\omega_{radial}/\omega_{axial} = \sqrt{2} \frac{w_0\pi}{\lambda}. \quad (2.22)$$

These equations can be used to estimate the requirements to mode match to a magnetic trap, where the magnetic trap frequencies were given in section 2.2 as $\omega_a \simeq 80 \text{ Hz}$, and $\omega_r \simeq 800 \text{ Hz}$. Then for the optical trap, we want $\omega_{radial} \simeq 800 \text{ Hz}$, with an aspect ratio of about 10. The radial frequency is mode matched for $w_0 \simeq 47 \mu\text{m}$ at 1 W. If we wish to mode match axially, Eq. 2.22 shows that $\lambda \simeq 20 \mu\text{m}$. However, this would be in the QUEST regime, so the above analysis would not apply. In order to mode match using an $\sim 1 \mu\text{m}$ laser, the beam waist would have to be reduced by a factor of 20, giving $w_0 \simeq 2.35 \mu\text{m}$ for our system. When deciding on the beam waist, one must concede that if the beam is focused too tightly, the extent of the beam could be smaller than the atom cloud, resulting in low transfer efficiency. Equation 2.22 illustrates the difficulties in mode matching a single beam trap to a magnetic trap with such a small aspect ratio. For this reason, we have developed two different means of providing axial confinement greater than that from a single

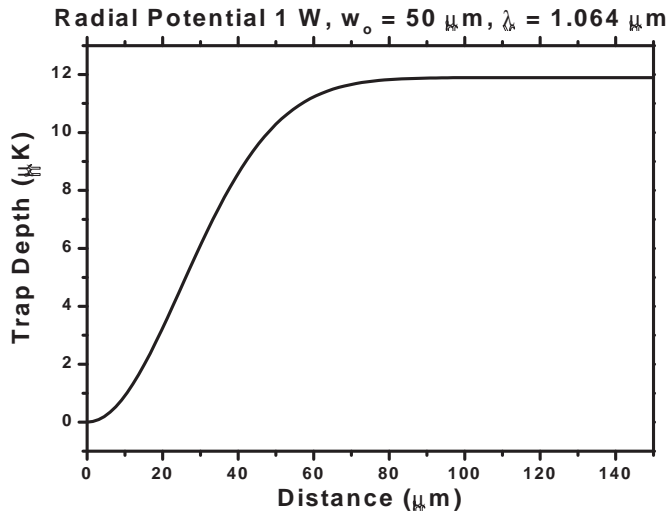


Figure 2.26 Calculation of the radial confining potential from a single focused Nd:YAG laser at 1064 nm. The beam waist, $w_0 = 47 \mu\text{m}$ at a power of 750 mW.

focused beam. The first is what we call the “end caps” and the second is a crossed beam trap, both of which will be discussed in the following sections.

2.3.2 End Caps

The first incarnation of our optical trap used a 1 W Nd:YAG laser at 1064 nm for radial confinement. Due to the severe miss-match between the axial and radial potentials, as described in section 2.3.1, we added two cylindrically focused 532 nm beams to act as “endcaps” shown schematically in Fig. 2.29. The beam is split off from a commercial frequency doubled YAG system (10-W Verdi laser, produced by Coherent). A beam sampler splits 30% of the Verdi power into the endcap beam. The beam is then sent through a $\lambda/2$ waveplate, and into a polarizing beam splitting cube (PBS). This allows us to vary the power in the endcaps between zero and full on without disturbing the 70% that is not reflected. (Which is crucial since this power is used to pump a Spectra-Physics 380-D dye laser.) After being sent through the PBS, the beam is coupled into a single-mode optical fiber (Thor Labs model FS-SN-4213 (discontinued 2001)). The far end of the optical fiber is collimated into

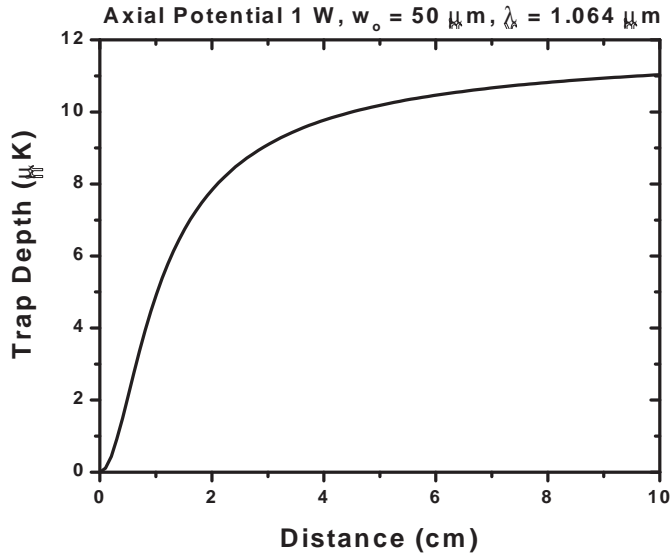


Figure 2.27 Calculation of the axial confining potential from a single focused Nd:YAG laser at 1064 nm. The beam waist, $w_0 = 47\mu\text{m}$ at a power of 750 mW.

free space by a Thor Labs FC connectorized collimating package (# F220FC-B). The beam then passes through a cylindrical telescope, giving it an aspect ratio near 10. The cylindrical beam is passed through an $f = 400$ mm doublet, and is separated into two co-propagating beams by a CVI energy separator cube (# ESC-25.4-532-S). The cube works as shown in Fig. 2.28, where the separation between the two beams is dependent on the incident angle, θ . The beam is then reflected into the chamber by a gimbal mounted dichroic beamsplitter (CVI model # LWP-45-RS532-TP670). The entire setup is shown in Fig. 2.29. The use of the dichroic beamsplitter is for alignment, and it will be further discussed in section 2.3.5.

The trapping potential is identical in form to that discussed in section 2.3.1, except that the potential is now repulsive, meaning that the atoms are expelled from the region of high intensity. The upshot of this is that the atoms spend their time in the dark, which greatly reduces the heating due to off-resonant scattering. However, the main draw back to using the endcaps derives from the shape of the endcap potential, which is shown in Fig. 2.30. The maximum depth of the endcap potential occurs

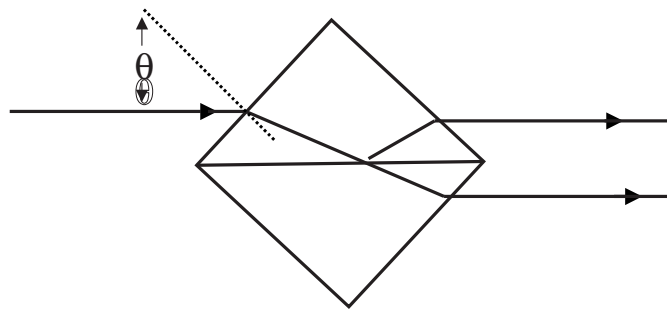


Figure 2.28 Diagram of the beam separator cube used to split the endcap beam into two co-propagating beams

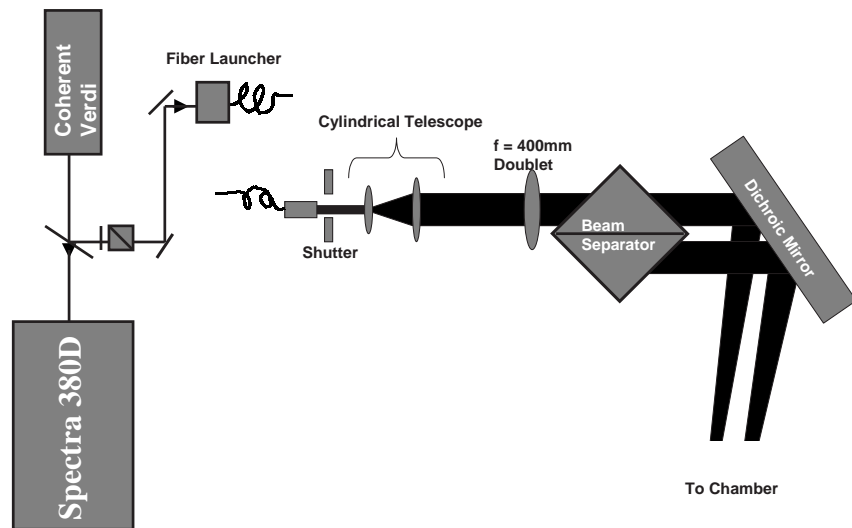


Figure 2.29 Optical layout of the endcap beams.

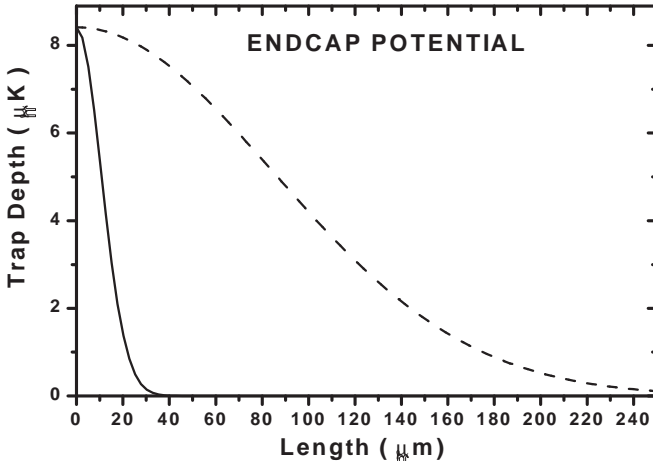


Figure 2.30 Optical potential formed by the endcap beams. The two curves show both foci of the cylindrical endcap beam. The tight axis is perpendicular the axial dimension while the other axis is perpendicular to the radial dimension.

at the center of the beam, however, the atom cloud has a finite radial extent, some fraction of the focused endcap beam. For example, a $1 \mu\text{K}$ cloud has a radial $1/e$ waist of $\sim 12 \mu\text{m}$, while the endcap beam has a $1/e^2$ waist of $120 \mu\text{m}$. The atoms are about 10 % the size of the endcap beam. Therefore, the trap depth of the endcaps is more accurately given by the maximum of the endcap potential at the edge of the radial confinement. This typically reduces the endcap potential by 10%.

2.3.3 Cross Beam Trap

The cross beam trap is the ideal optical trap since it can most closely mode-match a magnetic trap. The cross trap is formed by crossing a single focused beam optical trap (discussed in section 2.3.1) with a second focused red detuned laser beam. The resulting potential has three different frequencies, two radial frequencies and an axial frequency. The potential is shown in Fig. 2.31, for reasonable parameters. In our design of the crossed beam trap, we have added a new laser: an IPG fiber laser, Model YLR-20-LP, which is a 20 W Ytterbium doped fiber laser. The wavelength is centered at 1080.7 nm and has a FWHM of 1.6 nm. With the added optical power of this new

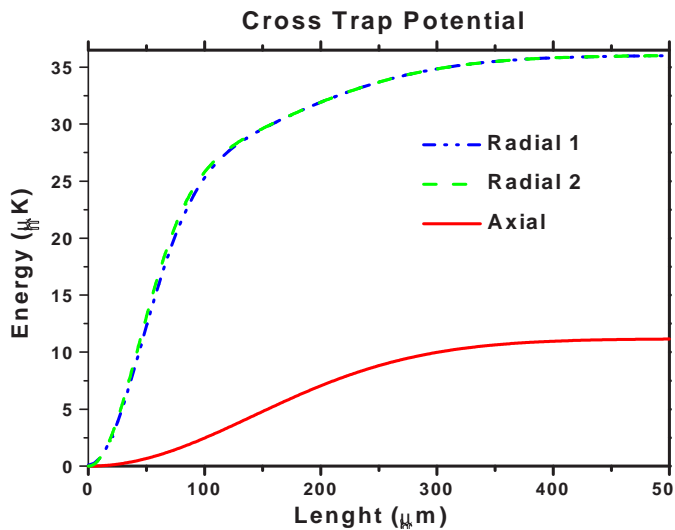


Figure 2.31 Calculation of the cross trap optical potential for all three dimensions.

laser, we designed the cross trap to have a trapping frequency of 80 Hz axially and 800 Hz radially (for ${}^7\text{Li}$), with a trap depth of 24 μK radially and 6 μK axially. To achieve this, we utilize 16 W at a 300 μm focus for the axial confinement and use either 700 mW at 30 μm focus or 3W at 60 μm focus for the radial confinement. As mentioned previously, this configuration over-confines one of the radial dimensions, but because of our choice of frequencies this effect is small.

The optical potential produced by the cross beam trap provides reasonable harmonic axial confinement, which allows us to extract temperatures from the axial profile. Figure 2.32 shows an axial cut of a ${}^7\text{Li}$ cloud that was held in the cross trap for just over 1 s. The atoms are held for 1 s to allow the ${}^7\text{Li}$ atoms time to thermalize. Fitting the axial profile, we extract a temperature of 830 nK for this cloud.

The optical layout for the cross beam trap is somewhat cumbersome. Currently, the axial beam can be produced by either the 1 W Crystal laser, or 4 W from the 20 W IPG laser, while the cross beam is formed using the remaining 16 W from the IPG laser. Figure 2.33 shows a schematic of the optical trap layout. The dichroic beam splitters are present to allow both the optical trap beams and the MOT laser

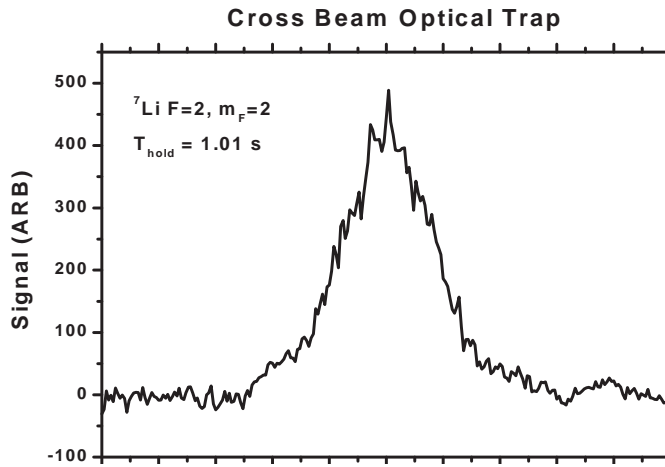


Figure 2.32 Image of ${}^7\text{Li}$ atoms in the cross trap. The atoms are confined for 1s with a calculated harmonic trapping frequencies of 800 Hz and 880 Hz radially and 110 Hz axially.

beams to propagate down the same axis. The acousto-optical modulators (AOs) in the diagram are all made by Crystal Technology and are centered at 110 MHz. The model number utilized is 3110-125, and they are rated for 90% efficiency with 4% optical insertion loss at 2 W of RF drive. The maximum efficiency occurs for an input beam waist between 500-600 μm . The lenses in the IPG setup are used to take the IPG output beam with a 2.25 mm waist and shrink it down for the AO, but then re-expand the beam to the appropriate size for focusing into the chamber. The Crystal laser output beam diameter is 300 μm and is slowly diverging, so the AO is placed where the beam diameter maximizes the diffraction efficiency. There is a final lens pair to magnify the beam before it is focused into the chamber.

2.3.4 Optical Trap Loss Rates

For atoms in an optical trap there are only three effects which limit the lifetime of the atoms: the background pressure, off-resonance scattering, and heating. Heating can arise from: either pointing instability or intensity fluctuations in the trapping laser. We will discuss each of the three loss mechanism as they pertain to our optical trap.

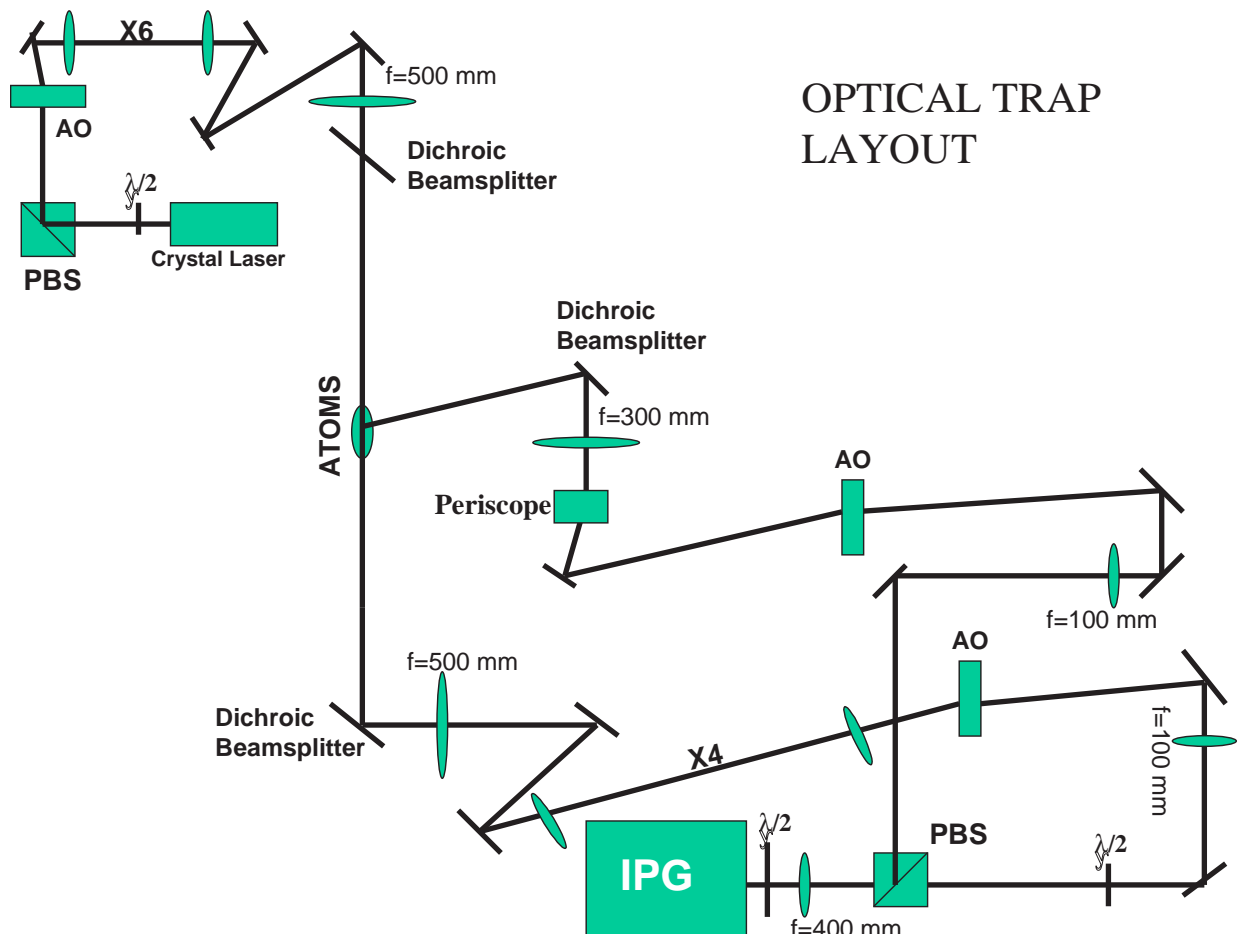


Figure 2.33 A schematic of the optical trap setup.

Background Losses

The first type of background loss comes from the vacuum pressure. Since the vacuum is not perfect, there are some contaminant molecules (mostly H₂) flying through the chamber at room temperature. If one of these molecules collides with a trapped atom, the kinetic energy transferred is sufficient to eject the cold atoms from the trap. The atom loss rate seems to be relatively independent of the trap depth, since the range of our trap depths (1 μK to 2 mK) is insignificant compared to the energy of the room temperature (300 K) molecules. The background lifetime has been measured to be between 100 s and 600 s in the magnetic trap (the lifetime can decrease following an oven change) while the optical trap lifetimes are between 3 s and 20 s (depending on the trap). Therefore, the effects of background gas collisions can be neglected when dealing with the optical trap loss rates.

Another source of background loss in an optical trap is from off-resonance scattering of light. Since the the detuning, | Δ |, is much larger than the Rabi frequency, Ω, the scattering rate Eq. simplifies into Eq. 2.23,

$$R = \frac{\Omega^2}{4\Delta} \quad (2.23)$$

where R^{-1} gives the time for an atom to scatter a photon. Since the photon recoil energy of lithium is about 6 μK [14], which is close to our optical trap depth, an atom that scatters a photon is heated, and lost from the trap. Typical time scales for the cross beam trap with conditions specified in section 2.3.3, Eq. 2.23 shows that the lifetime due to scattered photons is ∼ 10 s. This calculation is for atoms at the peak intensity of the laser. Since the atoms are constantly moving, sampling different laser intensities, we use the time to scatter a single photon as an estimate of the 1/e lifetime of the trap.

Heating

Heating from both intensity fluctuations and pointing instability has been discussed in great detail in [35] and [36]. Here we will briefly review these papers, and summarize the most pertinent information.

The rate of heating by intensity fluctuations can be calculated classically by finding the rate of change of the energy, which is given by Eq. 2.24 [35]:

$$\dot{E} = \Gamma \cdot E. \quad (2.24)$$

Γ^{-1} is defined as the time to increase the energy of the gas by a factor of e . The energy increases exponentially in time [35]. This type of resonance is a parametric resonance, and we can expect noise at twice the trapping frequency to be the largest contributor to the heating [37]. The heating rate Γ is calculated in [35] and given by Eq. 2.25.

$$\Gamma = \pi^2 \cdot \nu^2 \cdot S(2\nu) \quad (2.25)$$

The quantity $S(2\nu)$ is the square of the fractional intensity noise over a given frequency band. It has units of $1/\text{Hz}$. Our SRS spectrum analyzer has the option to plot the power density spectrum in power^2/Hz . Measuring the laser power with a photodiode allows the power density to be normalized by the DC component, and one can extract $S(2\nu)$.

For the radial trapping frequency of 800 Hz, we need $S(1600 \text{ Hz})$. The measurement (Fig. 2.34) gives $S(1600 \text{ Hz}) = 2.3 \cdot 10^{-12}$. This gives an e-folding time of approximately $3.9 \cdot 10^4 \text{ s}$, and is therefore not a significant source of heating. The axial trapping frequency set by the cross beam is currently 110 Hz. The quantity of interest then is $S(220 \text{ Hz})$, which we find to be $4.5 \cdot 10^{-12}$, as shown in Fig. 2.35. This corresponds to an e-folding time of $1.3 \cdot 10^4 \text{ s}$. The conclusion from the intensity spectrum is that any noise arising from intensity instabilities in the IPG laser has a negligible contribution to the heating rate in the trap.

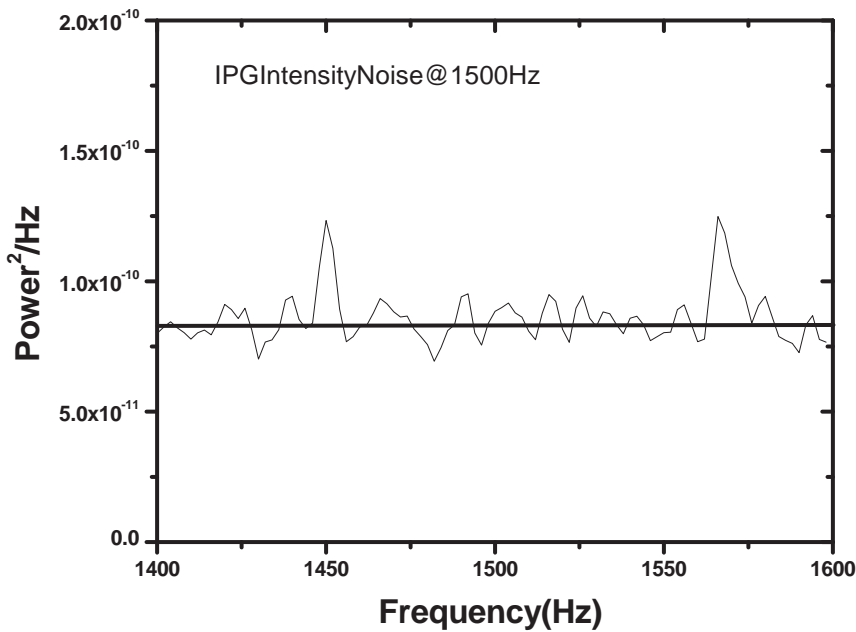


Figure 2.34 Noise spectrum at 2ν for the radial trapping frequency using the IPG laser.

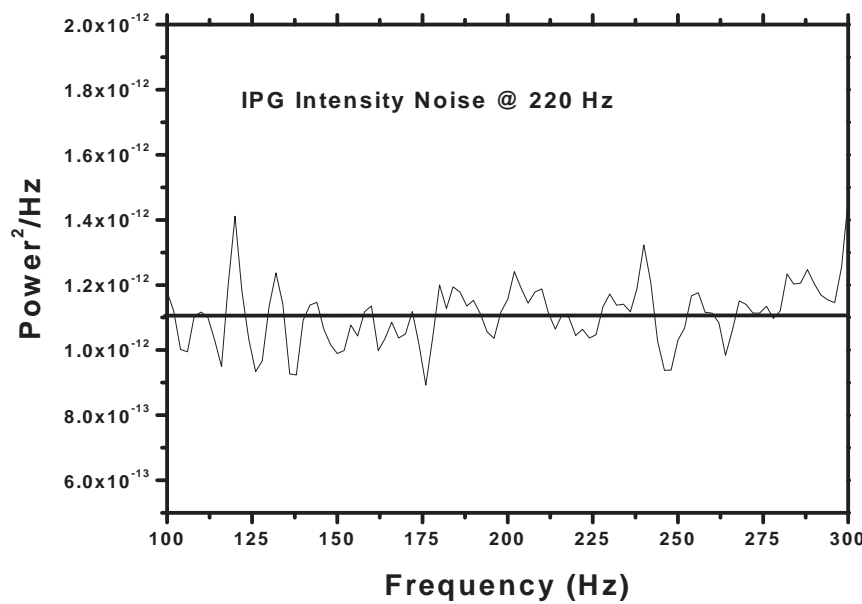


Figure 2.35 Noise spectrum at 2ν for the axial trapping frequency using the IPG laser as the cross beam.

The other type of heating comes from pointing instabilities in the laser. As the beam moves, it shakes the trap, which can heat the atoms. Heating from pointing instability translates to a constant heating rate given by Eq. 2.26 [36]:

$$\dot{Q} \cdot k_B = 4\pi^4 m \nu^4 S_p(\nu). \quad (2.26)$$

$S_p(\nu)$ is the position noise in units of cm^2/Hz , m is the atomic mass in grams, and \dot{Q} is in $\mu\text{K}/\text{s}$. This implies that for our radial confinement, a motion of $10^{-7} \mu\text{m}$ at 800 Hz would cause a heating rate 40 nK/s.

The suggested method for making this measurement is described in [35]. The basic idea is to utilize two photodiodes: one to monitor the laser intensity from a pick-off mirror or beam sampler, and one to monitor the intensity of the primary beam. The first photodiode is used to normalize out intensity fluctuations. On the primary beam, a razor blade is translated about half way into the beam at the focus (where the atoms would be). The second photodiode is placed after the razor blade to monitor the intensity in the primary beam. Subtracting the two signals removes the intensity noise, and the residual noise is a result of the pointing instabilities. Figure 2.36 shows the intensity noise spectrum at the radial trap frequency due to the pointing instabilities in the IPG laser. The power²/Hz is approximately $2.5 \cdot 10^{-12}$. Figure 2.37, shows the intensity noise spectrum at the axial frequency due to the pointing instabilities in the IPG laser. The power²/Hz in this case is approximately $8.5 \cdot 10^{-12}$. To convert from intensity fluctuations to spatial fluctuations, we need to calculate the effect of the razor blade, which means we must integrate the intensity profile in both dimensions, integrating over all \hat{y} and up to the edge of the razor blade in \hat{x} . The intensity is then given by;

$$I(x) = I_0 \int_{-\infty}^{\infty} dy \cdot e^{\frac{-2y^2}{w_0^2}} \int_b^{\infty} dx \cdot e^{\frac{-2x^2}{w_0^2}} \quad (2.27)$$

where w_0 is the beam waist at the razor blade. The solution to Eq. 2.27 is given by:

$$I = I_0 \frac{\pi w_0^2}{2} (1 - \text{erf}(b)), \quad (2.28)$$

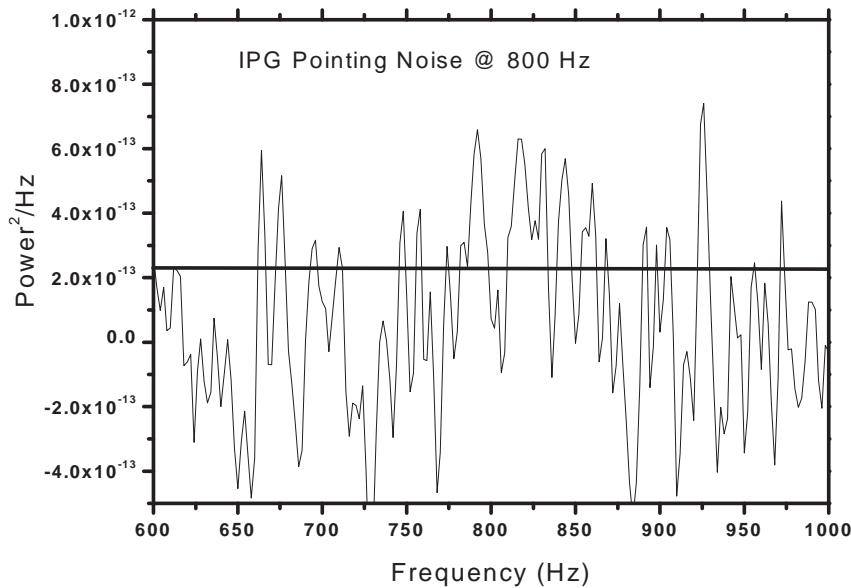


Figure 2.36 Pointing noise spectrum at 2ν for the radial trapping frequency using the IPG laser as the cross beam. The beam waist at the razor blade was measured to be $76 \mu\text{m}$ with a peak power of 2.63 W

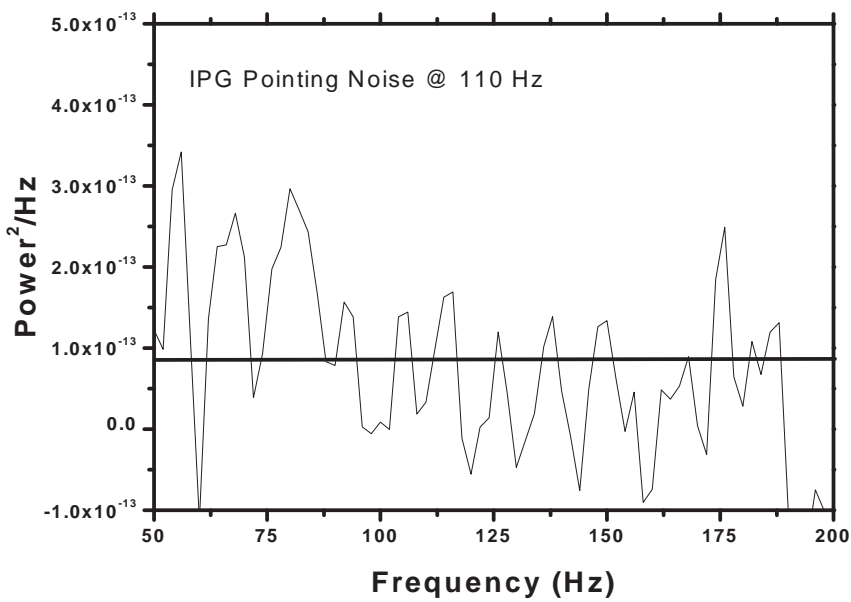


Figure 2.37 Pointing noise spectrum at 2ν for the axial trapping frequency using the IPG laser as the cross beam. The beam waare the same as Fig. 2.36.

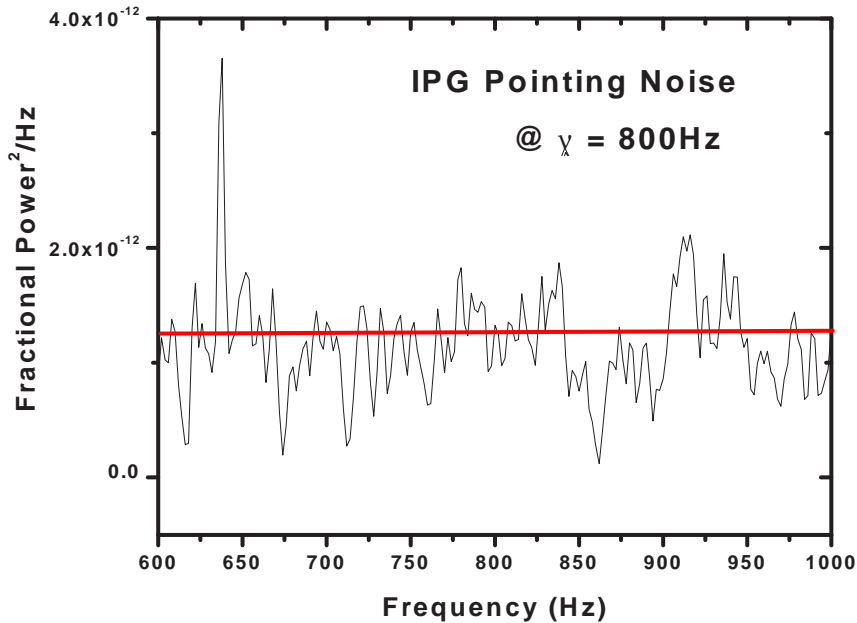


Figure 2.38 Pointing noise spectrum at 2ν for the axial trapping frequency using the IPG laser as the cross beam, with the fiber in its old mount. The beam waist at the razor blade was measured to be $76\text{ }\mu\text{m}$ with a peak power of 2.63 W

where $1 - \text{erf}(b)$ is the complementary error function evaluated at b . Now the pointing jitter, ΔI , can be quantified by determining the δb needed to give ΔI . We find $S_p(800\text{ Hz}) = 10^{-16}\text{ cm}^2/\text{Hz}$ gives a heating rate of 1.2 nK/s . For the axial confinement, we get $S_p(110\text{ Hz}) = 10^{-15}$, giving a heating rate of approximately 10 pK/s . These heating rates should have a negligible effect on the atoms at the temperatures we work at. The storage time in the optical trap is limited to approximately 10 s by off-resonant light scattering, so we can expect the atoms to be heated by 12 nK , while their average temperature is approximately $1\text{ }\mu\text{K}$.

The above results were achieved through a bench test performed using two glass plates, two photodiodes, a razor blade on a translator, and holding the output end of the IPG fiber in a specially-made mount. When the IPG fiber is placed back into our original mount, the pointing noise spectrum changes to that shown in Fig. 2.38. Performing the same analysis described above, we get a heating rate of $6.7\text{ }\mu\text{K/s}$,

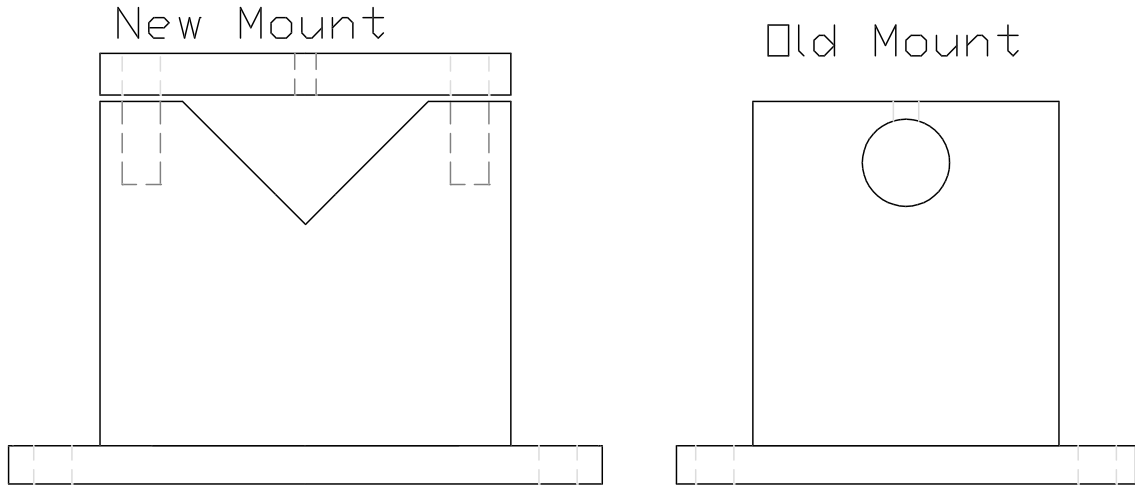


Figure 2.39 Schematics of both the original (old) IPG mount and the new IPG mount. They are both constructed out of Al. The primary difference between the mounts is how the IPG fiber is held.

giving a lifetime of ~ 2 s. Schematics for the both the new and old IPG fiber mounts are shown in Fig. 2.39. In the old mount, the IPG fiber has a compression fit into the center hole, and four nylon-tipped 8-32 set screws held the fiber in place. On the new mount, the fiber rests on the “V” shaped groove, the lid is bolted on and two 8-32 nylon-tipped set screws hold the IPG fiber in place. The main advantage of the new mount is that it ensures three points of contact, while the old mount does not.

The heating rate can be extracted experimentally by measuring the temperature of the atoms as a function of time (see Fig. 2.40). However, this gives us a lower bound for the heating rate, since the temperature is limited by evaporation and re-thermalization out of the shallow optical trap. The measured pointing instabilities with the old mount imply heating rates as high as $6.7 \mu\text{K/s}$ (as in Fig. 2.38) and as low as 400nK/s . The spread in the heating rate is believed to be due to variances in mounting the fiber rather than errors in the measurements.

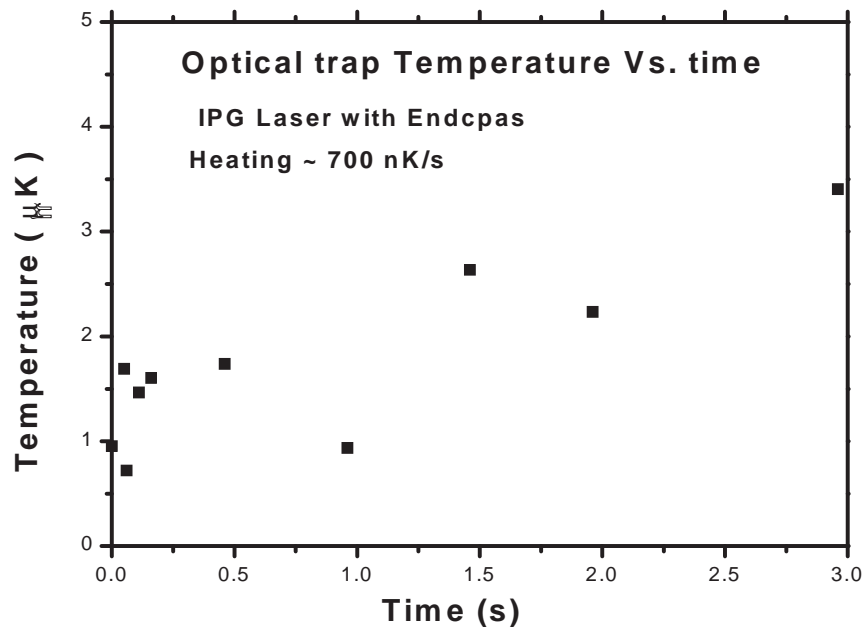


Figure 2.40 Heating rate of the optical trap formed with the IPG laser and the green beams. Since the axial profile is flat, due to the endcaps, the temperature is extracted from the waist of the radial profile. The heating rate is measured to greater than 700 nK/s.

2.3.5 Aligning and Transferring

For this last section, we will look at the two different optical (endcap vs. cross beam) traps separately. We see very different behaviors between the two traps.

ENDCAP TRAP

The ENDCAP trap uses two separate laser systems: a single infrared YAG laser beam for radial confinement, and two frequency doubled-YAG (“Green”) beams for axial confinement. Experimentally, it has been found that the maximal transfer efficiency into the single infrared beam occurs when the intensity is ramped on slowly over a 20 ms period and at 70% maximum power or greater when the magnetic trap is switched off. On the other hand, transfer efficiency is maximized when the endcap beams are simply turned on before the magnetic trap is switched off. This most likely occurs because the endcap beam separation is typically set to be $\sim 480 \mu\text{m}$, and the

axial 1/e diameter of a 2 μK atom cloud is $\sim 300 \mu\text{m}$, which is less than the endcap separation. The infrared laser intensity is controlled using an analog RF attenuator driven by an arbitrary waveform generator (Agilent 33120A), with a 1 V amplitude. The green beams are controlled by a shutter, which was constructed from a small, 1 cm long solenoid with a razor blade fragment glued to the solenoid post. The shutter has an open-close time of ~ 2 ms after a 15 ms inductive delay.

The procedure for aligning the ENDCAP trap from scratch begins by aligning the infared laser. First a “tracer” beam is overlapped with the infrared beam. The tracer beam is a near-resonant red beam picked off from the Spectra-380D dye laser. The beam is coupled into an optical fiber (Thorlabs P1-3224-FC-5 patch cable). The output of the optical fiber is caught, but not collimated, by a THOR Labs FC connectorized collimation package F230-FC-B. The beam is collimated to a waist of ~ 2 mm using an $f = 100$ mm lens. The tracer is overlapped with the infrared beam on the penultimate mirror (CVI YD-1037-45) in the axial beam setup (see Fig. 2.33). It reflects $>99\%$ at 1064 nm and transmits $\sim 30\%$ at 670 nm. Once the tracer beam is overlapped with the infrared beam, the frequency of the dye laser is tuned near the ${}^7\text{Li}$ resonance, and directed through a near resonance ($< 1\Gamma$) ${}^7\text{Li}$ MOT. The final focusing lens in the infrared beam setup is mounted on a Newport Ultra-Stab 3-D translator. The translator is used to direct the tracer beam. With this coarse alignment, the infrared beam should be within a 1 mm^2 area of the magnetic trap center. The tracer beam is then blocked and the hunt for the optical trap begins. We first evaporatively cool the atoms down to $\sim 3 \mu\text{K}$ and then allow the cloud to expand for 3 ms before imaging. This produces a roundish cloud $\sim 200 \mu\text{m}$ in diameter. The infrared beam is translated using the 3-D translator in $200 \mu\text{m}$ steps. The 1 mm square can be covered in just 25 pictures. With this method we are about 70% certain of finding the optical trap within the first 25 shots. When this method fails, the overlap of the tracer and the infrared beam should be rechecked and the overlap between the MOT

and the magnetic trap should be verified. The procedure is repeated until the optical trap is located.

To align the green beams from scratch, a similar procedure is followed. The final mirror on the green beams (see Fig. 2.29) is a CVI dichroic beamsplitter (LWP-45-RS532-TP670-PW1225-C) which reflects 532 nm and transmits 670 nm. The tracer beam is moved from the infrared setup and overlapped with one of the green beams. The same procedure as above is followed until the tracer hits the MOT. Once the tracer has hit the MOT, the dye laser is once again blocked and the atoms are cooled down $\sim 3 \mu\text{K}$. This time, we allow the atoms to expand axially in the infrared trap for 10 ms, and translate the gimbal mount knobs until the green beams are found. There is one further adjustment for the green beams, which is to adjust their separation. The separation of the green beams is adjusted by changing the angular rotation of the high energy beam splitting cube shown in Fig. 2.28. The rotation also translates the green beams slightly, so only small adjustments should be made in order not to lose the green beam alignment completely.

Cross Beam Trap

To align the cross beam, the tracer beam is first overlapped with the cross beam using the last mirror before the periscope (CVI YD-1037-45 mirror). The same procedures described above are used to locate the beam.

The cross beam trap alignment is the same as that used for the single infrared beam trap, but the turn on is slightly different. It was observed that after turning on the crossed beams, that the beams moved on a thermal time scale. Upon talking with the Crystal Technology technician, we learned that this is a common problem when switching AOs. As the RF is switched on, the AO crystal acquires a thermal gradient vertically across the crystal. The gradient has a tendency to displace the beam. The solution is to always keep the AO RF drive power on, and to change the

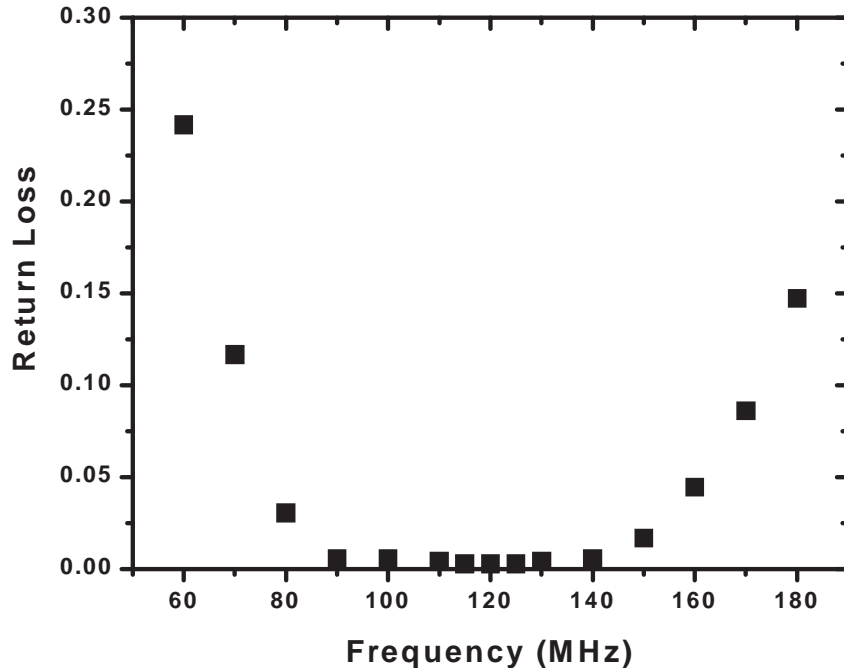


Figure 2.41 A sample return loss spectrum for Crystal Technology Model 3110-125 acousto-optical modulator.

drive frequency to switch the beam off. When the drive frequency is shifted to the edge of the AO modulation bandwidth, the sideband is not only weak, but separated enough to be blocked with a beam dump. This keeps a nearly constant RF heat load on the AO crystal. Figure 2.41 shows the measured RF return loss of the AOs used for the IPG laser setup. The AO bandwidths are centered around 110 MHz but still have a reasonably low return loss at 140 MHz. A schematic of the AO driving electronics is shown in Fig. 2.42. The switchable voltage control toggles between two control voltages, corresponding to 110 MHz and 140 MHz. The attenuation control voltage, which is normally high, corresponding to low attenuation, is suddenly switched off and then ramped up slowly using two separate Agilent 33210A arbitrary waveform generators. So far, the best experimentally-determined ramp rate for the axial beam is to ramp it up in 12 ms and to ramp up the cross beam in 20 ms, all 250 μ s before the magnetic trap is switched off.

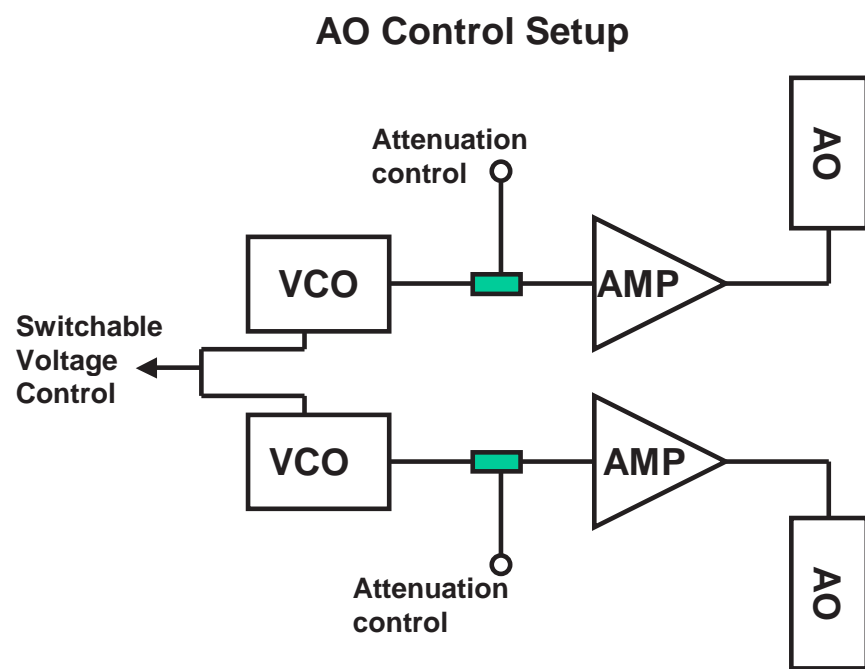


Figure 2.42 A schematic of the control layout for the Crystal Technology AO modulators.

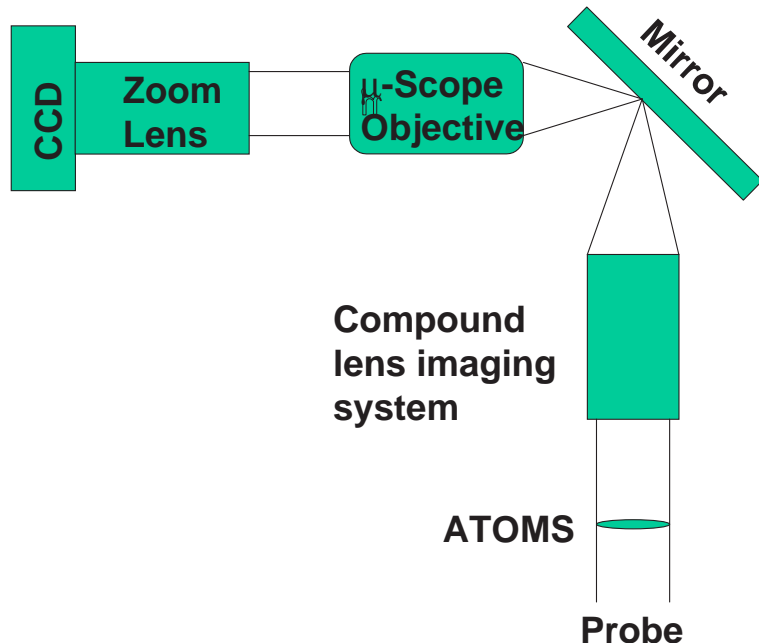


Figure 2.43 A block diagram of the imaging system setup. The details are presented in the text.

2.4 Imaging

2.4.1 Overview

The imaging system for the EMtrap was designed by B. Ghaffari with the intention of having diffraction limited performance, both on and off axis, with minimal spherical aberrations. A block diagram of the imaging system is shown in Fig. 2.43. This imaging system consists of a compound lens which relays the image of the atoms from inside the vacuum chamber to a place where the image can easily be accessed. Figure 2.44 is a CAD drawing of the compound lens system. The front working distance is 81.8 mm and the back is 139.7 mm. The image is magnified by a X10 infinite conjugate Mitutoyo microscope objective and then focused onto the CCD array using a plano-convex tube lens. In this design, the magnification is set by the ratio of the tube lens focal length divided by 20. For example, a 200 mm tube lens gives the microscope system a magnification of 10. This system is inherently difficult

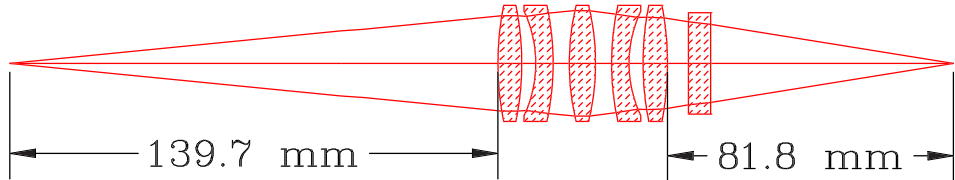


Figure 2.44 Compound lens system with front and back working distances labelled in mm.

to focus, since both the distance of the objective to the image and the distance of the tube lens to the CCD can be varied to focus the image. This is problematic because if the objective is slightly out of focus and the image is corrected by changing the distance of the tube lens to the CCD, the actual magnification will differ from the predicted magnification. As a result, a modification was made in which the tube lens was replaced by a Nikon zoom lens. The zoom lens has two benefits: first, the back focal length of the zoom lens is set to 50 mm, the Nikon standard, which is what the CCD camera was designed to accept. This eliminates the need to focus this particular portion of the imaging system. Second, the zoom capability allows the magnification of the Mititoyo microscope objective to be changed from 3.5 to 12.5 without requiring the imaging system to be refocused.

The specific details of the construction of the imaging system are in two theses [12] and [15]. The only addition that will be discussed here is that the Photometrics CCD was replaced with an Andor DV4-37-BV CCD camera, containing a frame transfer Marconi CCD57-10 array. The array is 512×1024 with $13 \mu\text{m}^2$ pixels and has a 512×512 pixel area masked for frame transfer operation. Also, the camera has an electronic shutter, which allows us to take two pictures separated by less than 20 ms. The Marconi is back-thinned, which gives it a quantum efficiency of 91% at room temperature and 97% at -40°C at 671 nm. It has a maximum read out rate of 1 $\mu\text{s}/\text{pixel}$. We have incorporated a $50 \mu\text{m}$ phase spot, described in [15], which allows us to perform phase contrast (dispersive) imaging at both high and low magnetic

fields.

The remainder of this section is dedicated to discussing the performance of this imaging system. We will cover both dispersive and non-dispersive imaging, and take a detailed look at our imaging analysis.

2.4.2 Imaging System Performance

As described in [12] the imaging system consists of a custom compound imaging lens, described in reference [15], a commercial Mitutoyo BD Plan 10X extended focal length microscope objective, and a NIKON 75-240 mm f/4.5-5.6 zoom lens which images onto the air-cooled Andor CCD described above.

The main obstacle in characterizing this imaging system has been in testing the custom compound lens system. Since 2002, at least four graduate students have dedicated considerable time to investigating, characterizing, and testing this system. The real problem was first discovered while attempting to image matter wave solitons. The solitons are predicted to be only $\sim 2.5 \mu\text{m}$ in size [38]. Image 2.45 shows what was observed. A fit to the axial profile gives the smallest solitons a waist of nearly $6 \mu\text{m}$, which is much larger than expected. Following these experiments, we removed the imaging system and briefly attempted a diagnostic. Two main test were performed on the imaging system: the first was to look at the minimum resolvable lines using a Melles-Griot USAF 1965 test target. The target is back illuminated with 670 nm light hitting a diffuser. The target is imaged using the highest magnification of the system, which is approximately X25. The results can be seen in Fig. 2.46. Group #7 and element #6 has 228 lines per mm, which is $4.3 \mu\text{m}$ per line. This test verifies that we can resolve objects $4.3 \mu\text{m}$ apart, but it does not tell us our imaging resolution. The second test was to measure the point spread function of a pseudo point source. To do this, we focused the imaging system onto a single mode optical fiber. The optical fiber was a 3M silica single mode optical fiber, Thorlabs part# FS-SN-3224. The optical

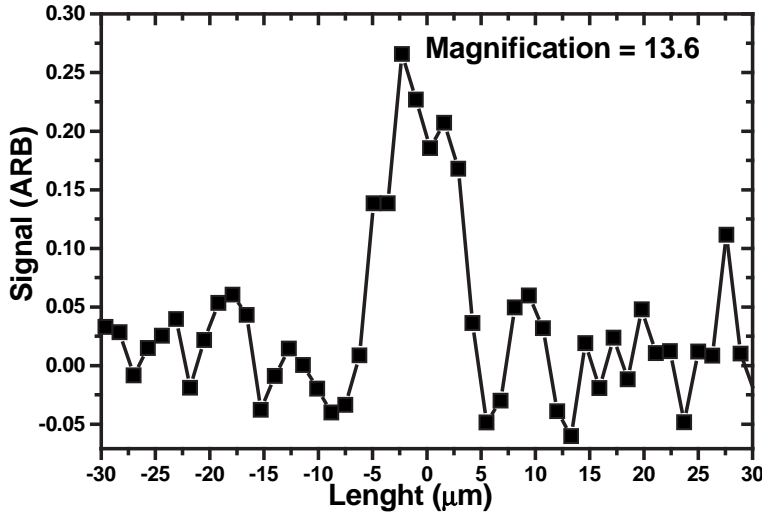


Figure 2.45 A high resolution image of a matter-wave soliton taken with a Photometrics CCD with 19 μm pixels and a magnification of 13.6.

fiber has a mode field diameter (MFD) of 4 μm , at 630 nm, where the MFD is defined as the diameter in which the intensity is reduced to $1/e^2$ of its maximum at the design wavelength of the optical fiber. At 671 nm the MFD $\simeq 4.24 \mu\text{m}$, approximated by the ratio of wavelengths. Figure 2.47 shows an image of the light emitted from the optical fiber. A Gaussian fit to the center gives a waist of 2.4 μm . The conclusion from these tests was that nothing was seriously wrong with the imaging system. However, these were not extensive tests, and the discrepancy between the predicted size of the soliton data and the observed 6 μm minimum waist of a soliton suggests there is a problem with the imaging system. This prompted an in-depth and currently on-going study of the imaging system.

A second compound lens system was constructed for testing purposes. The idea was to test the performance of the system and compare it with a theoretical model built by an optical engineering program, OSLO LT. The results are in the report entitled “Diffraction Limited Imaging System” [39] which can be found in lab\docs\imaging.

Experimental test showed that the imaging system is capable of diffraction lim-

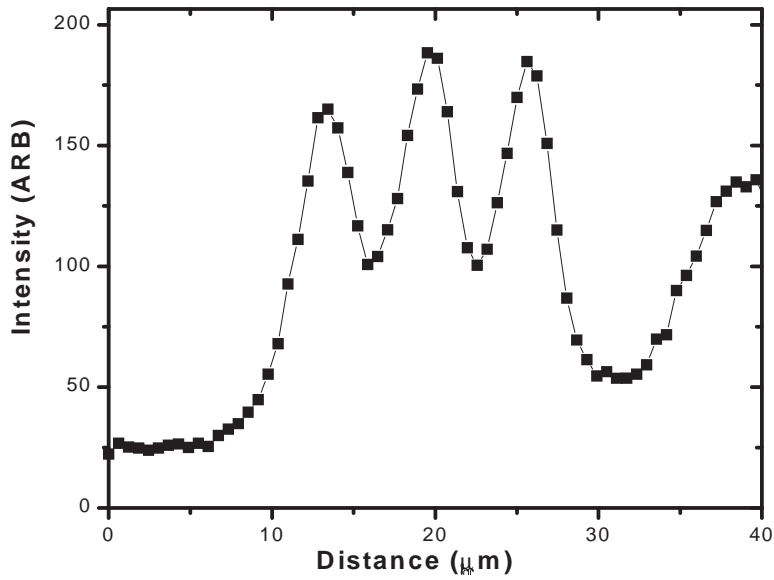


Figure 2.46 Cross section of $4.3 \mu\text{m}$ lines on a USAF test target, group #7 and element #6.

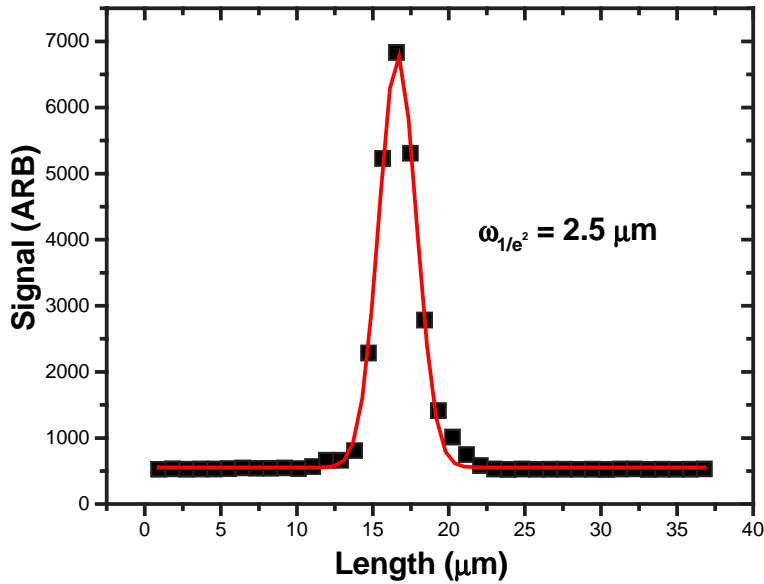


Figure 2.47 Cross sectional profile of the core of single mode optical fiber Thorlabs part# FS-SN-3224. Image was taken using the Andor CCD at a magnification of $\sim 16 \mu/\text{pixel}$.

ited performance at a specific working distance, however, if the working distance is changed, the imaging system will no longer provide diffraction limited performance. Suggesting that the problem with our current imaging system is that the compound lens is not at the optimal distance from the atoms to achieve diffraction limited performance.

2.4.3 Dispersive and Non-dispersive Imaging

In this section we will discuss the two types of imaging used on this apparatus and how to calculate the expected signals from each.

The dispersive and non-dispersive imaging refers to either phase contrast or absorption imaging, respectively. In phase contrast imaging, the signal is proportional to the dispersive phase, while in absorption imaging, the signal is proportional to the optical density. The dependance of the optical density and phase on the laser detuning Δ , where σ_0 is the on-resonance light scattering cross-section and n is the density, is given by

$$n_{OD} = \frac{\sigma_0 \cdot n}{4 \cdot \Delta^2 + 1} \quad (2.29)$$

$$\varphi = \frac{\sigma_0 \cdot n \cdot \Delta}{4 \cdot \Delta^2 + 1}. \quad (2.30)$$

Where we have assumed that $\Omega \ll \Gamma$, Δ is in units of Γ , and Γ is set equal to 1. Figure 2.48 shows plots of Equations 2.29 and 2.30 as a function of laser detuning. This illustrates the key difference between working with the phase versus working with the optical density: the optical density drops like $1/\Delta^2$ while the phase scales like $1/\Delta$.

If the off-resonant optical density gets too large, the atoms act like a lens and diffract the probe beam. Therefore, we want to keep the off-resonant optical density low, or equivalently, $\varphi \ll 1$. When the on-resonant optical density is low, the best images occur using near-resonant absorption, however, as the optical density grows the detuning of the probe must be increased in order to satisfy $\varphi \ll 1$. As the detuning

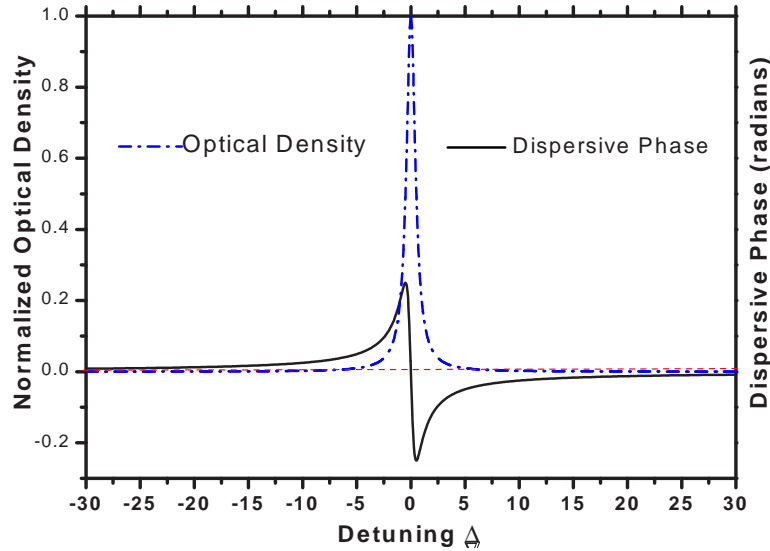


Figure 2.48 Plot shows the dispersive phase and optical density as a function of laser detuning.

increases the absorption signal decreases as $1/\Delta^2$, while the phase contrast signal is only decreasing as $1/\Delta$. In the limit of large detuning the signals are maximized using phase contrast imaging.

In order to calculate the expected image for a given cloud of atoms at a given laser detuning, one must consider just how the light is interacting with the atoms. This has been done in great detail in Curtis Bradly's thesis [40], reference [41] derives the following

$$\text{Signal} = I_0 \cdot [1 + t^2 + \tau^2 + 2t(\tau \cos(\varphi - \gamma) - \cos(\varphi)) - 2\tau \cos(\gamma)]. \quad (2.31)$$

Here $t = \exp\{-n_{OD}/2\}$, I_0 is the peak intensity, the phase spot factors are τ^2 , the transmittance factor of the phase spot, and γ is the retardation of the phase spot. For phase contrast imaging in our system, we utilize a phase spot with $\gamma = \pi/2$ and $\tau^2 = 0.09$. Then, for a dilute gas with small optical density and a small phase shift, $t \rightarrow 1$, $\varphi \rightarrow 0$ we can simplify Eq. 2.31 to

$$S_{pc} = I_0[1 + t^2 - 2t + 2t\tau\varphi + \tau^2] \quad (2.32)$$

As the detuning is increased, the absorption becomes negligible and Eq. 2.32 simplifies,

$$S_{pc} = I_0[2\tau\varphi + \tau^2] \quad (2.33)$$

For absorption imaging, $\tau^2 \rightarrow 1$, and $\gamma \rightarrow 0$, Eq. 2.31 simplifies to,

$$S_a = I_0[t^2]. \quad (2.34)$$

Using Equations 2.33 or 2.34, and the appropriate density distribution for the atom clouds, we can extract the atom number and temperature from the measured images. These images are a direct measurement of n_{OD} or φ , depending on the imaging method.

2.4.4 Imaging Analysis

The main components of the imaging analysis are discussed in detail in Strecker's masters thesis [12], since it was the analysis used for most of our experiments. The drawback to this method is that when fitting highly degenerate Fermi gases, the summations used to calculate the optical density fail to converge and a full integration must be employed. This can be skirted, however, by use of a polylogarithmic function which has been named the polylog, Li_n . The polylog, in its simplest form, is a series solution to an integral of the form of the Fermi distribution, as seen in Eq. 2.35.

$$\int dx \frac{x^n}{a^{-1}e^{bx} + 1} = (b^{-1})^{n+1}\Gamma(1+n)Li_{n+1}(-a) \quad (2.35)$$

We can follow the analysis presented in reference [42], using the standard definition of a Fermi distribution from Huang "Statistical Mechanics" [43] and the definition of the polylog. This allows us to form a column density distribution without the need to fully integrate the Fermi distribution.

We start with the Hamiltonian for a harmonic trap:

$$H(k_{x,y,z}, x, y, z) = \frac{\hbar^2}{2m}k(x, y, z) + \frac{m\omega^2}{2}(x^2 + y^2 + (\lambda z)^2) \quad (2.36)$$

where λ is the ratio of the two trapping frequencies, such that $\lambda = \frac{\omega_z}{\omega_r}$, and $k_{x,y,z}$ is the momentum in the \hat{x} , \hat{y} , and \hat{z} directions. Then from Huang Chapter 8, we use the Hamiltonian in Eq. 2.36 to get the phase space distribution:

$$W(x, y, z, k_{x,y,z}) = (2\pi)^{-3} \frac{1}{\xi^{-1} e^{\frac{H(k_{x,y,z}, x)}{k_B T}}}, \quad (2.37)$$

where ξ is the fugacity. The density distribution is then given by

$$n(x, y, z) = (2\pi\hbar)^{-3} \int d^3k W(x, y, z, k_{x,y,z}). \quad (2.38)$$

In order to use the polylog, we can change the variables in Eq. 2.38 until it has the form of the left-hand-side of Eq. 2.35. The trick is to switch the k integral into spherical coordinates, integrate out θ and ϕ , then redefine k , such that $k^2 = \frac{2m}{\hbar^2} \varpi$. Equation 2.38 can then be rewritten as 2.39

$$n(x, y, z) = (8\pi^2\hbar m)^{-1} \int d\varpi \frac{\varpi^{1/2}}{\varsigma^{-1} e^{\frac{\varpi}{k_B T}} + 1}. \quad (2.39)$$

The integral in Eq. 2.39 is just the polylog with $n = \frac{1}{2}$. Noting that $\Gamma(\frac{3}{2}) = \frac{2}{\sqrt{\pi}}$ the density distribution becomes

$$n(x, y, z) = \frac{(k_B T)^{\frac{3}{2}} \pi^{\frac{3}{2}}}{4\pi^3 \hbar m} Li_{\frac{3}{2}}(-\varsigma), \quad (2.40)$$

where $\varsigma = \xi e^{-(\frac{m\omega^2}{2k_B T}(x^2+y^2+(\lambda z)^2))}$.

To get the column density, we must integrate Eq. 2.40 over one of the dimensions. Our CCD camera images along the long axis (z) and one radial axis (y) so we must integrate along the x axis to form the column density distribution that our camera records. To do this we must employ one more relation

$$Li_n(-\varsigma) = \sum_{i=1}^{\infty} \frac{(-\varsigma)^i}{i^n}. \quad (2.41)$$

By substituting the series expansion for the polylog into Eq. 2.40, one can write out the first few terms of the series. Integrating through the first few terms and

simplifying, it can be shown that the solution to Eq. 2.40 is simply a polylog with $n = 2$. The column density is given by

$$OD(y, z) = -\sigma_L \frac{m(k_B T)^2}{2\pi\hbar^3\omega_r} Li_2 \left(-\xi e^{-\frac{m\omega^2}{2k_B T}(y^2 + (xz)^2)} \right) \quad (2.42)$$

where σ_L is the light scattering cross-section. This form of the polylog, with $n = 2$, is known as the dilogarithm and is solvable by an integral over the unit circle. The numerical integration of this function is fast. In a benchmark of this function versus our old method, generating a column density distribution of a cloud at $T/T_F = .18$, the old method took nearly 22 s/distribution while the new method took approximately .65 s/distribution.

The final task is to actually fit experimental data to the column density distribution. This is done using MatLab file PCFermi.m, which is described in detail in Appendix 5.3. The program reads the raw data files in FITs format, which is the current standard for high quality scientific images. The data gives three images: first is the “atoms” image containing the signal, second is the “noatoms” containing only the probe beam, and third is a “background” containing nothing but the dark counts on the array and any stray room noise. To fit the experimental data the background is first subtracted off, and the intensities of both the “atoms” and “noatoms” are normalized to a patch in their respective images. This is done to remove any intensity fluctuations. Finally, the “atoms” and “noatoms” are subtracted, yielding the signal picture. The program then locates the center and long axis of the cloud, and performs an angle average of $+/- 5^\circ$ about the major axis. This profile is then fit to a Gaussian distribution, which gives a rough estimate of the number and temperature of the atoms. N and T are then passed to Eq. 2.42 to find n_{OD} . The calculation constructs a profile that is compared to the profile of the processed image. A MatLab function “FMINS” then minimizes the difference between the calculated profile and the experimental profile by varying N and T . The variable T can also be fixed if it is determined from a fit to a Bose cloud.

Chapter 3

Experiments

This chapter will discuss our major experimental achievements. The experiments will be divided into three categories: bosons, boson-fermion mixtures, and fermion mixtures. First we will discuss the optical trapping of ^7Li and the production of a large stable lithium BEC in the $F = 1$, $m_F = 1$ state using a Feshbach resonance. Next we will discuss the production of matter-wave solitons using a Feshbach resonance. We will then move on to the production of a large degenerate Fermi gas (DFG) using dual evaporation. We will then discuss a set of experiments that includes coherent Rabi-oscillations in a DFG, observation of a long coherence time in a spin mixture of fermions near a Feshbach resonance, RF spectroscopy of the coherent spin mixture, observation of de-coherence, and an attempt at spectroscopy with a de-coherent spin mixture. To conclude, we will discuss the production of ultra-cold bosonic lithium dimers from a quantum degenerate Fermi gas and direct imaging of the molecules.

3.1 Bosons

The cornerstone of the entire experiment is the ^7Li , as it is the starting point of all of our experiments, and it must work well and repeatedly in order for any other experiment to be performed. Our initial goal was to evaporatively cool as much ^7Li to near the BEC critical temperature, T_C , as possible, and transfer it to an optical trap. With this experimental setup, many new experiments can be performed. The evaporation of the ^7Li is described elsewhere [15], along with the methods for constructing optimized evaporation trajectories [44] for a cloverleaf type trap [15].

3.1.1 Optical Trapping

The construction of the optical trap, electronic controls, and the general alignment procedures are outlined in the apparatus section. Here we will discuss “what to look for” when aligning an optical trap, and the details regarding the lifetime of the Crystal laser-greenbeam optical trap, which was used in all the experiments thus far.

Figure 3.1 shows the three different alignments of the single infrared axial beam of the optical trap. The atoms are initially cooled to approximately $1 \mu\text{K}$. The optical trap is turned on ~ 2 ms before the magnetic trap is switched off and then the atoms are imaged after 5 ms of ballistic expansion. The first frame shows the axial beam with an approximate $200 \mu\text{m}$ misalignment in the plane of the image. As the atom cloud expands, the atoms get stopped by the potential created by the laser beam. As a result, the expanded cloud looks like it has a hard edge caused by the presence of the laser beam. The second image corresponds to a $120 \mu\text{m}$ misalignment perpendicular to the plane of the image. In this case, the atoms expand and once again get sucked into the potential created by the optical trap. However, instead of a hard edge, we observe a minimum in the signal. The minimum signal is attributed to the optical trap being out of the focal plane of the imaging system. The third image shows the axial beam aligned. Images such as this occur when the optical trap alignment is

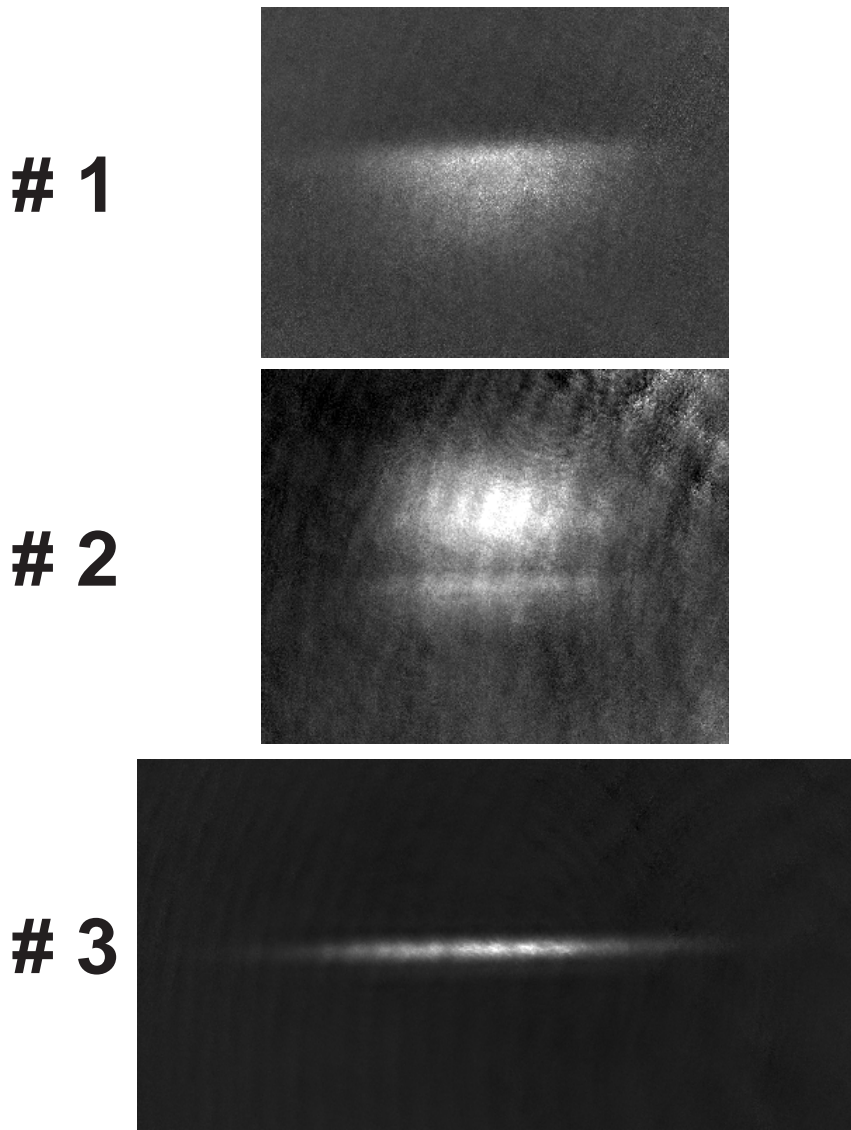


Figure 3.1 Three stages of the alignment of the axial laser beam after 5 ms of free expansion from the magnetic trap. # 1 corresponds to a $200 \mu\text{m}$ misalignment in the plane of the image. #2 corresponds to a $120 \mu\text{m}$ misalignment perpendicular to the plane of the image. # 3 shows the axial laser beam aligned.

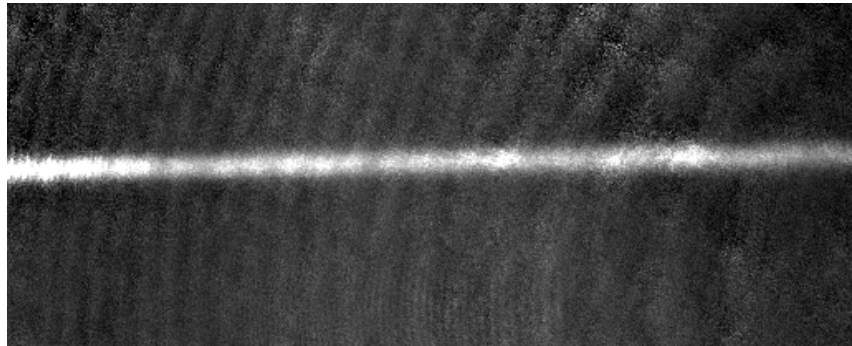


Figure 3.2 Picture of the axial beam after a 40 ms expansion. The atoms signal fills up the screen with a nearly uniform profile. The screen is 1.7 mm in width.

within 10 μm of the optimal alignment.

If we allow the optical trap to expand further (greater than 40 ms) then the optical trap fills the viewable area as seen in Fig. 3.2. Because of the relatively flat profile across the 1.7 mm viewable area, it is impossible to determine the axial beam focus, which means that this alignment procedure can only ensure that two of the three dimensions are aligned. To determine the focus of the axial beam, we form a BEC and allow it to oscillate in the optical trap. If the focus of the laser and the center of the magnetic trap overlap, the BEC will expand, but its center will not move. The only drawback is that this requires us to be at a large magnetic field (see section 3.1.2) and field inhomogeneities can interfere with this process.

Once the axial beam is aligned, the endcaps must be aligned. To do this, we allow the atoms to expand for 40 ms in the axial beam, as shown in Fig. 3.2, and look for asymmetries. Figure 3.3 shows this process with one green beam on the screen. The green beam simply stops the atoms from expanding in the axial beam. Once a green beam has been found, it is a simple matter of adjusting the gimbal mount in steps of 5 ticks to align the green beams. Once they are coarsely aligned, the best way to peak the alignment is to hold the atoms for 1 s and maximize the optical trap signal by adjusting the gimbal mount in steps of 2 ticks. Figure 3.4 shows a picture of the fully aligned optical trap.

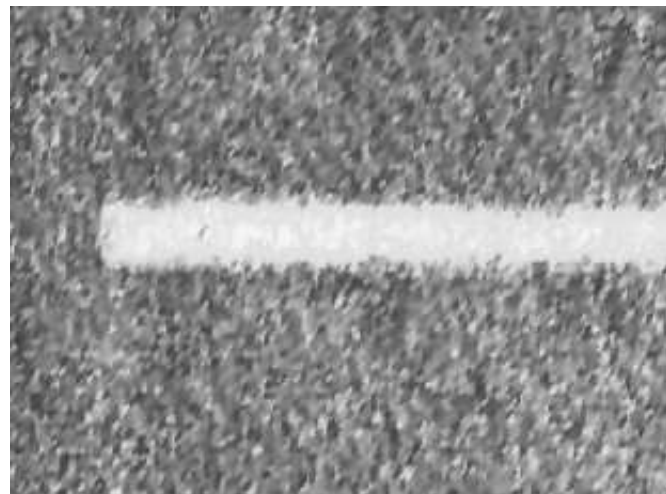


Figure 3.3 Picture of the axial beam after a 40 ms expansion with one green beam present. The screen is 1.7 mm in width.

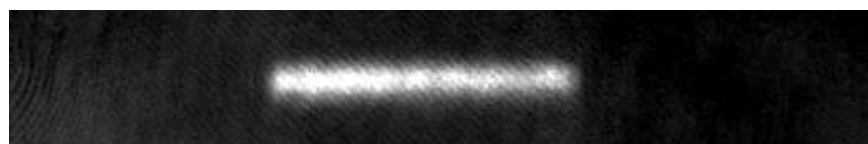


Figure 3.4 A picture of ${}^7\text{Li}$ in the optical trap after 1 s.

In this configuration, the optical trap is roughly mode-matched to the radial dimension of the magnetic trap, with a trapping frequency $\omega_r = 2\pi \cdot 800$ Hz for ${}^7\text{Li}$, while the axial dimension is box-like. Plugging in some numbers, if we had a ${}^7\text{Li}$ atom cloud at 1 μK , it would have a 10 μm radial waist and be 230 μm in axial length, determined by the endcap spacing. A 2 μK cloud would be $\sqrt{2}$ larger radially. Our typical magnification gives us 2 $\mu\text{m}/\text{pixel}$, so the difference in radial waist between the two clouds is less than 2 pixels, while the axial profiles are identical. This makes it very difficult to obtain quantitative temperature measurements in the green beam optical trap. However, a quantitative measure of the number can be made. By summing the signal over an area of interest, and knowing the amount of light, detuning, and duration of the imaging pulse, the number can be accurately determined. This method was employed in several of the experiments that will be discussed. Plotting the number versus time, we can determine the lifetime of the ${}^7\text{Li}$ atoms in the optical trap (Fig. 3.5). The ${}^7\text{Li}$ lifetimes are often bi-modal, showing a rapid decay on the thermalization time scale (less than 1 s) and then decaying slowly with time.

${}^7\text{Li}$ in the $F = 2, m_F = 2$ state can not form a large condensate due to the attractive interactions [2, 45]. Therefore, only a small fraction of our sample (less than 1%) can cool below T_C , the critical temperature for BEC. The critical temperature scales like $T_C \propto N^{1/3}$. Once the gas reaches T_C , it will remain at T_C and further cooling only results in the loss of atoms. Since this is inefficient, the atoms are transferred to the optical trap when the critical temperature is reached. If the actual temperature of the gas is greater than approximately 10% of the optical trap depth, we observe rapid initial loss of atoms from the optical trap (Fig. 3.5), otherwise we observe only the exponential decay of atoms.

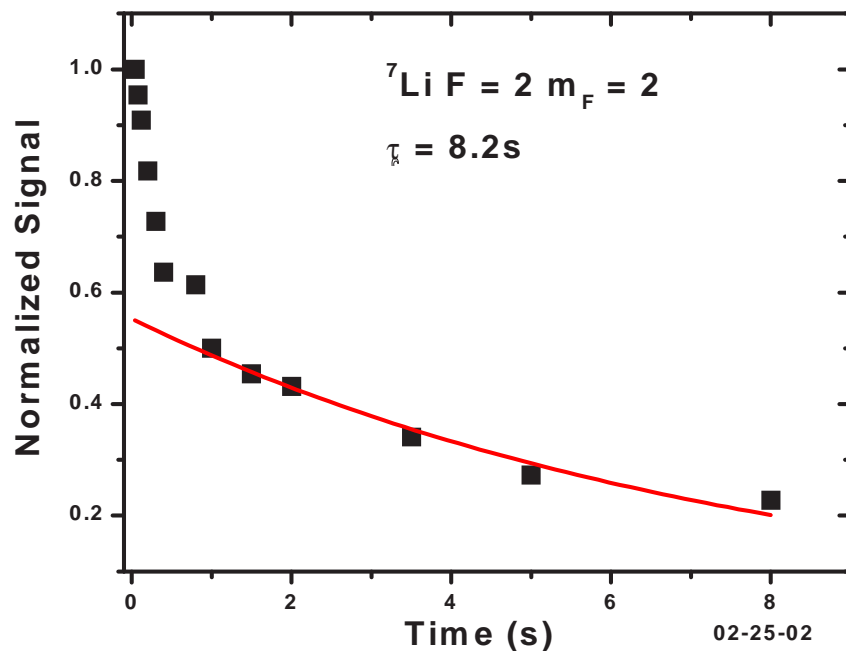


Figure 3.5 Plot of the lifetime of ${}^7\text{Li}$, $F = 2$, $m_F = 2$ state in the optical trap on 02-25-02. The lifetime is bi-modal. The first rapid contribution is due to evaporation out of the optical trap. The tail is fit to an exponential decay with a time constant, $\tau = 8.2$ s.

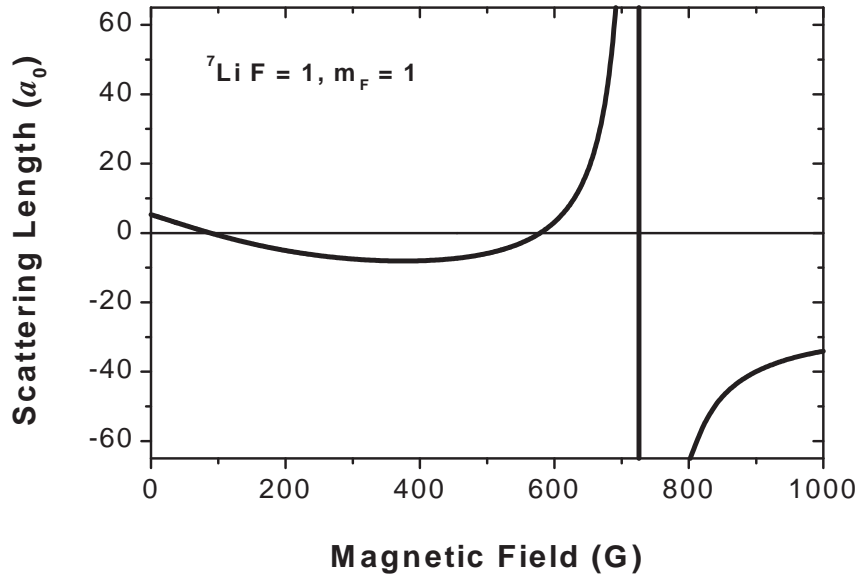


Figure 3.6 Coupled channel calculation of the ${}^7\text{Li}$ Feshbach resonance corrected using the experimentally corrected peak of the resonance [10].

3.1.2 ${}^7\text{Li}$ Feshbach Resonance

The motivation behind confining the atoms with an optical trap is to study the atoms both as a function of an applied external bias field, and also in any spin state or mixture of spin states. For the bosons, the spin state we are interested in studying is the $F = 1, m_F = 1$ state. Not only is this state stable against spin exchange on itself and on our initial state $F = 2, m_F = 2$ state [15], it has a positive scattering length at zero field of $5a_o$ and it has a Feshbach resonance, originally predicted near 800 G [15]. This resonance goes through zero and becomes attractive between zero field and the resonance (Fig. 3.6).

The peak of the resonance can be experimentally determined by looking at the rate of loss of atoms from the optical trap as a function of magnetic field [8]. To determine the position of the Feshbach resonance, we need to determine both the magnetic field and atom loss rate. The magnetic field can be found by microwave spectroscopy. We maintain the atoms in $F = 2, m_F = 2$ until we are at the desired magnetic field.

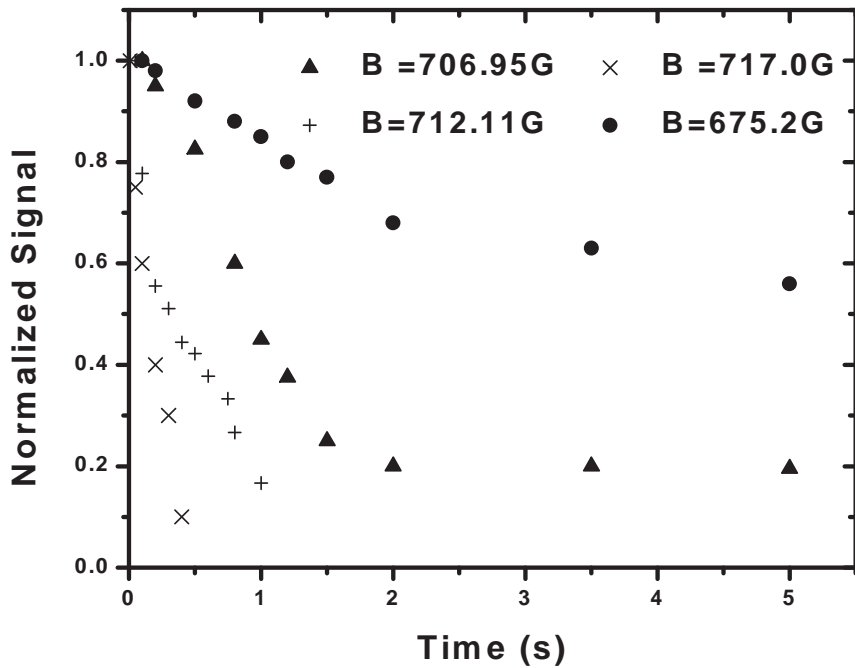


Figure 3.7 Selected lifetimes at various magnetic fields, both near and far from the $F = 1, m_F = 1$ Feshbach resonance.

Then, by applying a microwave frequency sweep, the atoms are transferred to the $F = 1, m_F = 1$ state. The microwave sweep is a 20 ms, 1 MHz sweep. The magnetic moment difference between the two states is $2\mu_B$ or 2.8 MHz/G. In order for the sweep to be adiabatic and to transfer all the atoms to the $F = 1, m_F = 1$ state, the transition frequency must be in the center of the sweep. A 250 KHz deviation in the sweep center will result in an 80% or less transfer efficiency. This gives a magnetic field resolution of 100 mG.

The loss rate of atoms can be determined by measuring the time it takes for the number of atoms to drop to $1/e$ of the $t = 0$ value. Time $t = 0$ is defined as the point at which the microwave sweep ends and all the atoms are transferred to the $F = 1, m_F = 1$ state. Figure 3.7 shows some sample loss lifetimes near the Feshbach resonance. Far from the resonance, the lifetime fits to a $1/e$ rate of 10 s, while near the resonance the lifetime is reduced by over an order of magnitude. These measurements

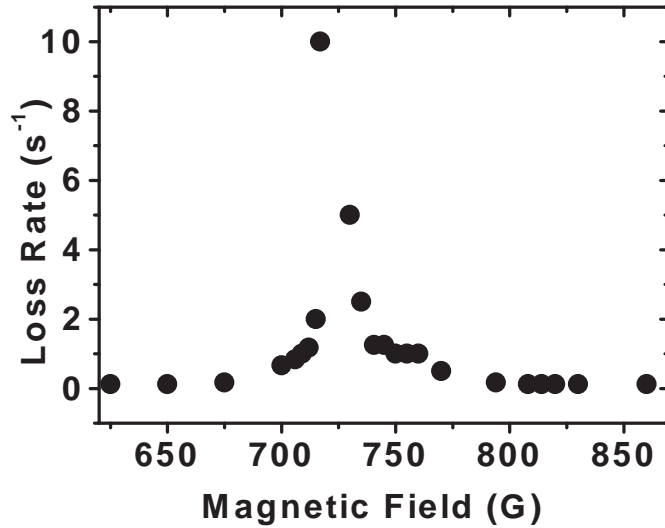


Figure 3.8 Loss rate as a function of magnetic field near the $F = 1$, $m_F = 1$ Feshbach resonance.

were made at several different magnetic fields. The lifetimes were converted to loss rates and plotted in Fig. 3.8. Figure 3.8 shows the peak of the loss to be near 725 G. Since the loss is expected to be due to three body recombination and to scale as a^4 [46], we expect the peak of the loss to correspond to the peak of the Feshbach resonance.

As mentioned above, Fig. 3.6 was corrected using the data from Fig. 3.8. The coupled channel calculations use spectroscopic data obtained from photoassociation experiments [22, 25] along with theory. Slight errors in the construction of the potential and uncertainty in the disassociation energy of the ground state, shift the position of the resonance. Using the experientially determined peak of the Feshbach resonance we have shifted the peak of the calculated Feshbach resonance to align with the loss peak.

3.1.3 Large Lithium Bose Einstein Condensate

After the peak of the Feshbach resonance was determined and the calculation adjusted, the next experiment was to actually use the resonance to Bose condense

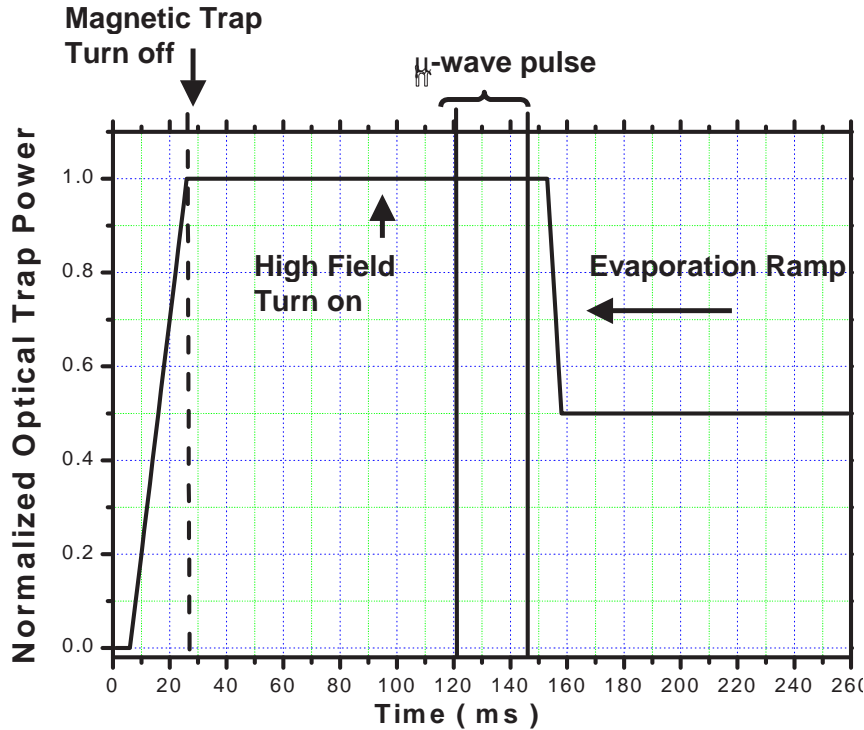


Figure 3.9 Timing diagram for the YAG laser. The laser is ramped on, the atoms are transferred to the $F = 1$, $m_F = 1$ state, and held for 5 ms. The YAG intensity is then halved. The atoms thermalize during the variable hold time and form a BEC.

^7Li . To form the BEC, the atoms were taken to the high field, where $B = 705.3$ G, in the $F = 2$, $m_F = 2$ state. At this field, Fig. 3.6 shows that $a = 200 a_0$. A 25 ms microwave sweep from 2628.6 MHz to 2629.6 MHz transfers the atoms from the $F = 2$, $m_F = 2$ to the $F = 1$, $m_F = 1$ state. There is a 5 ms delay, and then the intensity is ramped down to 50%, which allows the atoms to thermalize, as illustrated in Fig. 3.9. The formation of the condensate occurs on the 10 ms to 20 ms time scale, after the reduction of the trapping intensity. Due to the box-like axial potential, the formation of the condensate does not significantly change the axial spatial distribution of the atom cloud but is accompanied by sudden drastic increase in optical density of the cloud (Fig. 3.10). The radial radial dimension decreases in width, but due to heavy distortions in the images we can not be quantitative about

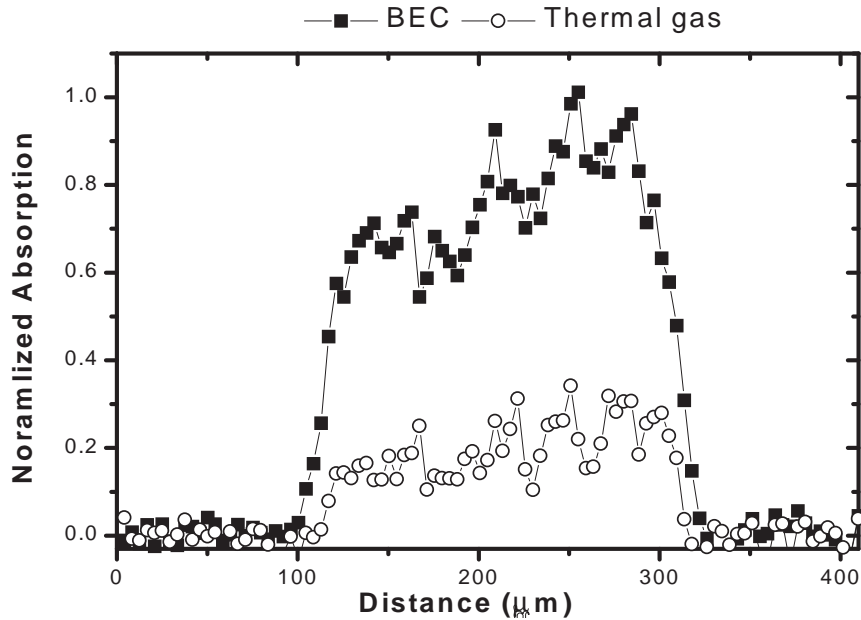


Figure 3.10 Images of a thermal gas and a BEC of ${}^7\text{Li}$ in the $F = 1$, $m_F = 1$ state in the end cap trap. The images were taken with near resonance absorption, the thermal gas was probed at a detuning of 3Γ , while the BEC was probed at 10Γ .

the radial distribution. The axial distribution does not change because the axial condensate diameter, approximately $260 \mu\text{m}$ with $1 \cdot 10^6$ atoms at a scattering length $a \sim 200 a_0$, is larger than the $230 \mu\text{m}$ spacing of the end caps. These images have $\sim 2.3 \cdot 10^6$ atoms in the BEC image and $\sim 1.2 \cdot 10^6$ atoms in the thermal gas image.

3.1.4 Bright Matter Wave Solitons

As a wave propagates, dispersion causes the localized wave to spread out. However, under the proper circumstances, non-linear effects can cause a self-focusing of the wave that exactly counters the dispersion. As a result, the wave can propagate without dispersion. These waves are known as solitons. Two types of solitons have been studied with Bose-Einstein condensates. The first type is the “dark” soliton. Dark solitons are formed in BECs with positive scattering length, such that $a > 0$. In this case the soliton is a localized absence of atoms, or density notch [47], that can

propagate through the condensate due to an applied phase gradient [48]. The dark solitons are similar to optical solitons in that both require the medium they propagate through to provide the non-linearity, and they do not exist outside of the non-linear medium. Bright solitons, on the other hand, are localized spikes, or maxima, in the density distribution. Bright solitons form because of the non-linearity of the atomic interactions. Atomic bright solitons are themselves individual BECs; wave packets that can propagate without dispersion, which are not limited to exist only in a condensate, like dark solitons. The experiments we conduct are with bright solitons, so from this point we shall refer to “bright solitons” as “solitons” and “dark solitons” as “dark solitons”.

The soliton we will consider is stable only in 1-D. In higher dimensions the soliton is unstable and will undergo collapse, similar to catastrophic self-focusing in optical solitons [38]. The collapse of the condensate in 3-D has been studied in ${}^7\text{Li}$, in the $F = 2$, $m_F = 2$ state, when the condensate number exceeds a critical value it suddenly implodes [45, 49, 50]. In the 1-D limit, a condensate with attractive interactions has been shown to have a solution stable against collapse [51], which is a soliton.

In order to form stable solitons, the atoms must be in a 1-D or what is called a quasi-1-D trap. A BEC in a cylindrically asymmetric potential has only four length scales; the radial trap length, $l_r = \sqrt{\frac{\hbar}{m\omega_r}}$, the axial trap length, $l_a = \sqrt{\frac{\hbar}{m\omega_a}}$, the scattering length, a , and the healing length, ξ , where $\xi = (8\pi\hbar n a)^{-\frac{1}{2}}$ [52]. For a 3-D gas, $l_r, l_a \gg \xi$, for 2-D $l_r > \xi > l_a$, and for 1-D $l_a > \xi > l_r$. The condition for 1-D can be restated as the radial energy spacing $\hbar\omega_r$, must be greater than the mean field energy, $U_0 = \frac{4\pi\hbar^2 n_0 a}{m}$, where

$$\hbar\omega_r > \frac{4\pi\hbar^2 n_0 a}{m}. \quad (3.1)$$

The axial waist of a soliton has been derived [38],

$$W_a = \frac{\sqrt{3}\pi a_{ho}}{aN} \quad (3.2)$$

where $a_{ho} = l_r$ is the ground state harmonic oscillator length for the radial dimension, and N is the number of atoms. From Eq. 3.2 we see that as N increases, the axial waist decreases. As the soliton shrinks the density increases, decreasing ξ taking the gas from the 1-D regime into the 3-D regime where the soliton collapses. To estimate the critical number of atoms in a soliton, we can substitute $n = N/l_r^3$ into Eq. 3.1, using the relation that $l_r = \sqrt{\frac{\hbar}{m\omega_r}}$, we get that

$$N_c < \eta l_r / |a|, \quad (3.3)$$

where η is a constant on the order of 1.

Solitons are general solutions of the 1-D non-linear Schrödinger equation (NLSE) [38]. The NLSE is given by

$$i\hbar \frac{\partial \psi}{\partial t} = -\frac{\hbar^2}{2m} \nabla^2 \psi + V(r+z)\psi + g|\psi|^2\psi \quad (3.4)$$

where $g = 4\pi\hbar^2 a/m$, and a is the scattering length. $V(r+z)$ is the trapping potential. This equation becomes 1-D in the limit that the trapping potential in the z dimension becomes much less than the trapping potential in r . The ψ^3 term in Eq. 3.4 is the non-linear term that gives rise to the solitons, and for $a < 0$ is called a Kerr non-linearity [53]. The strength and sign of the non-linearity is determined by g and hence by the scattering length. If $a > 0$, the non-linear term aids in the dispersion and diffraction of the wave packet, while if $a < 0$ the non-linear term gives rise to self-focusing that compensates dispersion.

Experiment

In the experiments described here, we used the optical trap composed of the 1 W Crystal laser for radial confinement and the green beams for axial confinement. The resulting potential is cylindrically symmetric in the radial dimension and box-like along the axial dimension, such that $V = \frac{m}{2}(\omega_r^2(x^2 + y^2)) + V_z$ where V_z is the optical box potential [54]. In these experiments, the Crystal laser beam was focused down

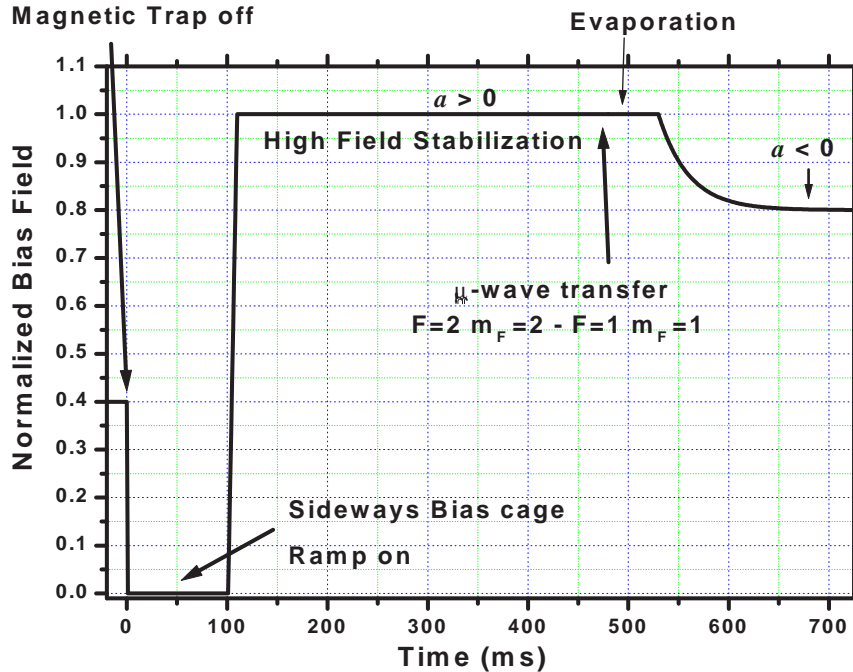


Figure 3.11 Timing diagram of the magnetic field for the formation of solitons. The actual scale of the magnetic field is arbitrary, and only requires that field be ramped to a value where a is positive, held until a BEC is formed, then ramped to a magnetic field where a is negative. It should be noted that the time from the microwave transfer until the formation of the BEC is magnetic field dependent. The timing diagram is drawn for $B_{max} = 710$ G.

to a $\frac{1}{e^2}$ waist of $47 \mu\text{m}$ with 750 mW of power, giving a radial frequency of $\omega_r = 2 \pi \cdot 800 \text{ Hz}$ and an axial frequency of $\omega_a = 2 \pi \cdot 4 \text{ Hz}$ for ${}^7\text{Li}$. The green beams were cylindrically focused to a $\frac{1}{e^2}$ waist of $100 \mu\text{m}$ by $22 \mu\text{m}$ with 350 mW of power per beam and a separation of $230 \mu\text{m}$ [10]. This gave a trap depth of $12 \mu\text{K}$ radially and $10 \mu\text{K}$ axially. With the end caps removed, this optical trap had an aspect ratio $l_r/l_z \sim 200$.

In order to form solitons, we must first form a BEC, as described in section 3.1.3. Figure 3.11 is a representative timing diagram for forming solitons. First, the magnetic trap is turned off, and there is a 100 ms delay while the sideways magnetic field cage (section 2.1.3) is ramped on. The bias field is quickly ramped on to its

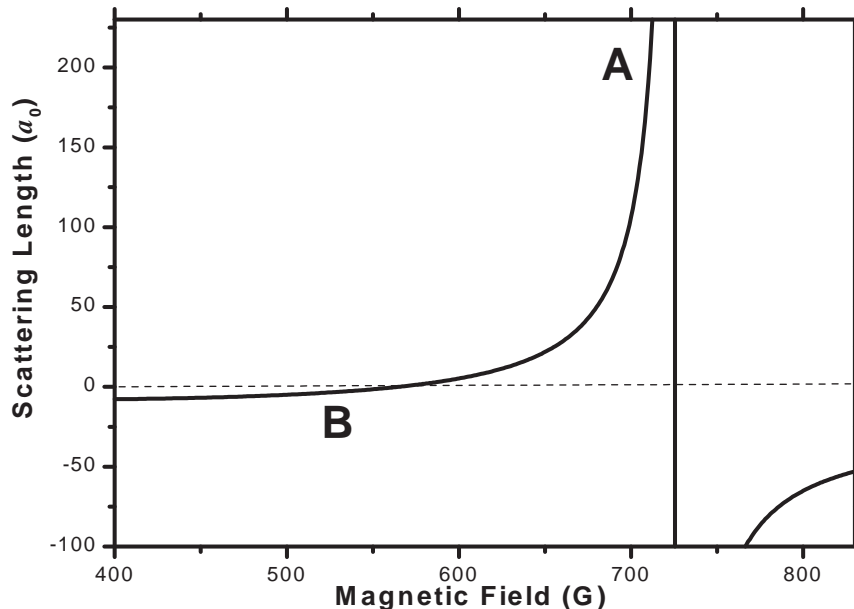


Figure 3.12 ${}^7\text{Li}$ $F = 1, m_F = 1$ Feshbach resonance calculated by McAlexander [15] and shifted to agree with the experimentally observed peak in the loss rate (Fig. 3.8). This calculation gives the zero-crossing at 565 G.

maximum value (typically 710 G) where a further 400 ms is allowed for the magnetic field to stabilize. After the field stabilizes, a 25 ms linear adiabatic microwave sweep transfers the atoms from the $F = 2, m_F = 2$ state to the $F = 1, m_F = 1$ state. Here the $F = 1, m_F = 1$ scattering length is approximately $200 a_0$, and is represented as point “A” in Fig. 3.12, which shows the best known calculation of the Feshbach resonance at the time of the experiments. The peak of the resonances was originally calculated at 795 G, and shifted to 725 G to agree with the experimental observations in section 3.1.2. Figure 3.8 shows that the lifetime of the atoms near point “A” is reduced due to the proximity of the Feshbach resonance. We observe formation of the BEC within 50 ms of reducing the optical trap intensity, which is noted as “Evaporation” in Fig. 3.11. To avoid losing atoms from the losses near the Feshbach resonance, the magnetic field is ramped down, away from the resonance, within 10 ms of the formation of the BEC. The final magnetic field value is arbitrary, however, for the

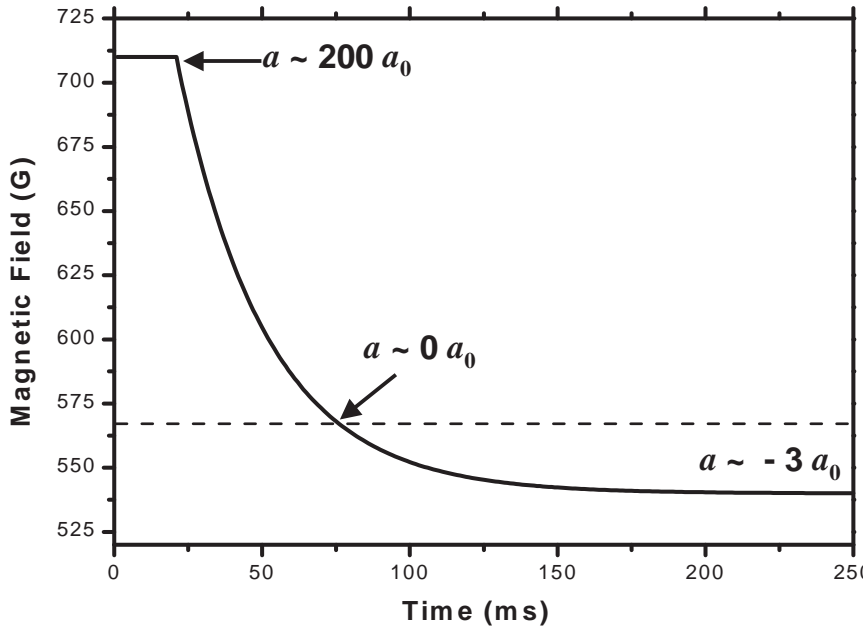


Figure 3.13 RC ramp down of the magnetic field used to form solitons. The field starts out near 710 G with $a \simeq 200 a_0$ and is ramped down to near 540 G with $a \simeq 3 a_0$.

experiments here, it was varied between 540 G ($a < 0$ see point “B” in Fig. 3.12) and 630 G ($a > 0$). Figure 3.13 shows a detailed diagram of the ramp down of the magnetic field.

The magnetic field values were determined using microwave spectroscopy between the $F = 2, m_F = 2$ state to the $F = 1, m_F = 1$ state. Figure 3.14 shows the field calibration for the bias shunt (see 2.2.4). After forming a BEC, the magnetic field is ramped down to various values. Figure 3.15 shows the BEC at several magnetic fields where a is predicted to be negative. We observed that the BEC fragment into several smaller BECs, and as the final magnetic field value is decreased the size of the BECs reduced. Figure 3.16 shows the axial cross-sections of the brightest solitons in select images from Fig. 3.15. As expected from Eq. 3.2, the axial waist shrinks as a function of increasing $|a|$. Choosing 540 G as our negative a point and extrapolating 610 G for positive a , where $a \simeq 10 a_0$, we performed the experiments. Recall that the definition of a soliton is an object that does not change shape as it propagates

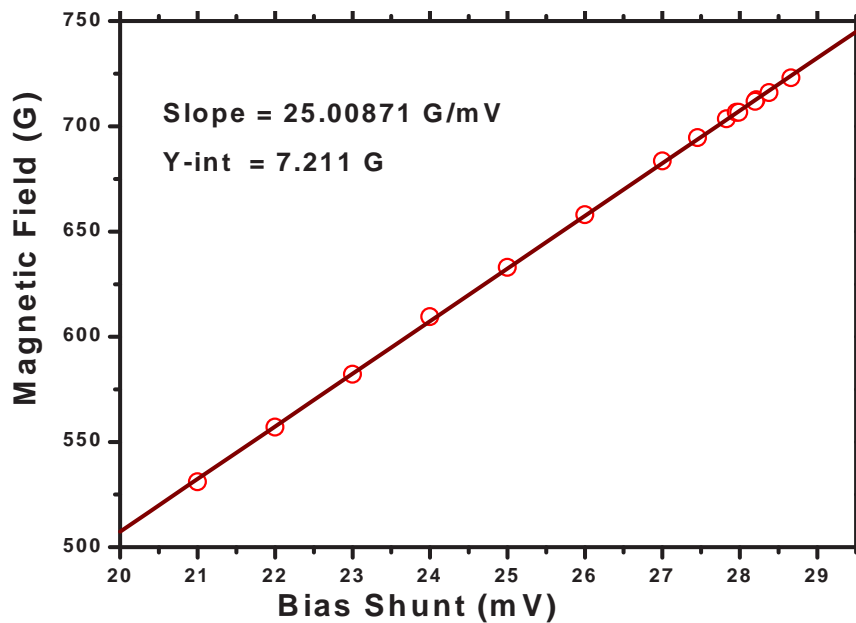
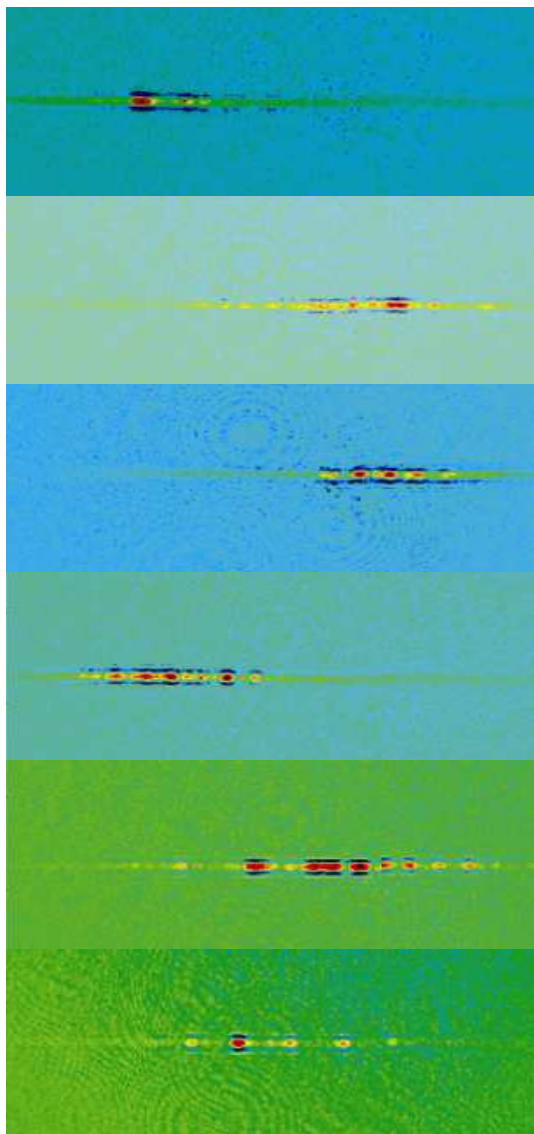


Figure 3.14 Plot showing the experimentally determined magnetic field calibration. Microwave spectroscopy between the $F = 2, m_F = 2$ state to the $F = 1, m_F = 1$ state was performed. The magnetic field was then determined using the Breit-Rabi formula to convert the transfer frequency into a magnetic field, which was plotted against the bias shunt value.

Released Solitons B-Field Calculated a



557.21 G $-0.7 a_0$

554.9 G $-1.0 a_0$

551.5 G $-1.5 a_0$

548.4 G $-2 a_0$

545.0 G $-2.5 a_0$

540.0 G $-3 a_0$

Figure 3.15 Formation of solitons as a function of ending magnetic field. The magnetic field is measured using Fig. 3.14, and the scattering length is determined by the coupled channels calculation of a vs. B , where the resonance was shifted to agree with the experimentally determined peak of the resonance (Fig. 3.12). As the magnetic field is decreased, the scattering length also decreases, as a result, the solitons decrease in diameter.

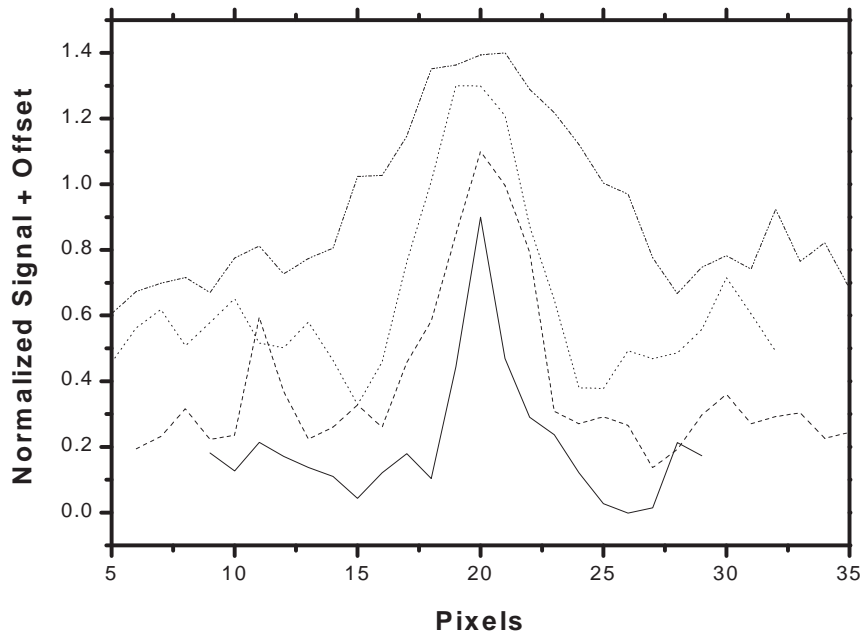


Figure 3.16 Axial size of solitons as a function of ending magnetic field. The profiles shown are the brightest solitons from the images in Fig. 3.15. The --- corresponds to 557 G and $a \sim -0.85 a_0$. The ··· line corresponds to 551 G and $a \sim -1.4 a_0$. The - - - line corresponds to 548 G and $a \sim -2 a_0$, and the solid line corresponds to 540 G and $a \sim -3 a_0$.

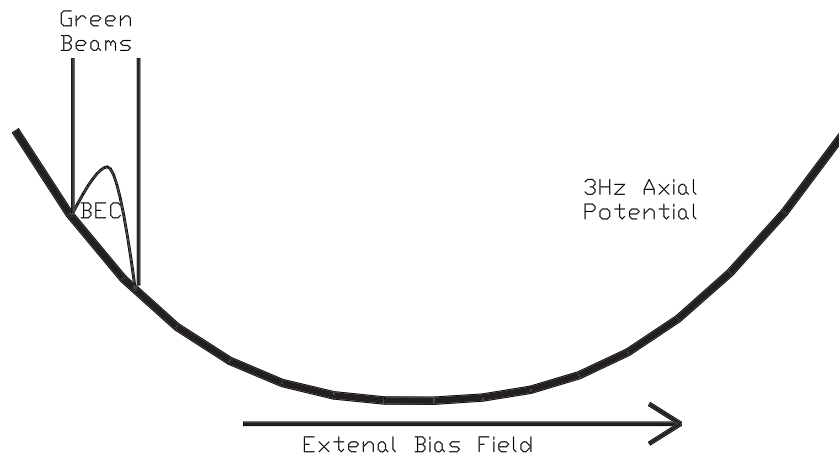


Figure 3.17 Diagram illustrates the experimental setup for forming solitons and setting them in motion. The focus of the infrared beam was displaced from the center of the magnetic trap potential. The BEC is then formed on the side of the axial potential formed from the single infrared beam. Once the green beams are removed, the BEC/solitons will oscillate in the harmonic potential.

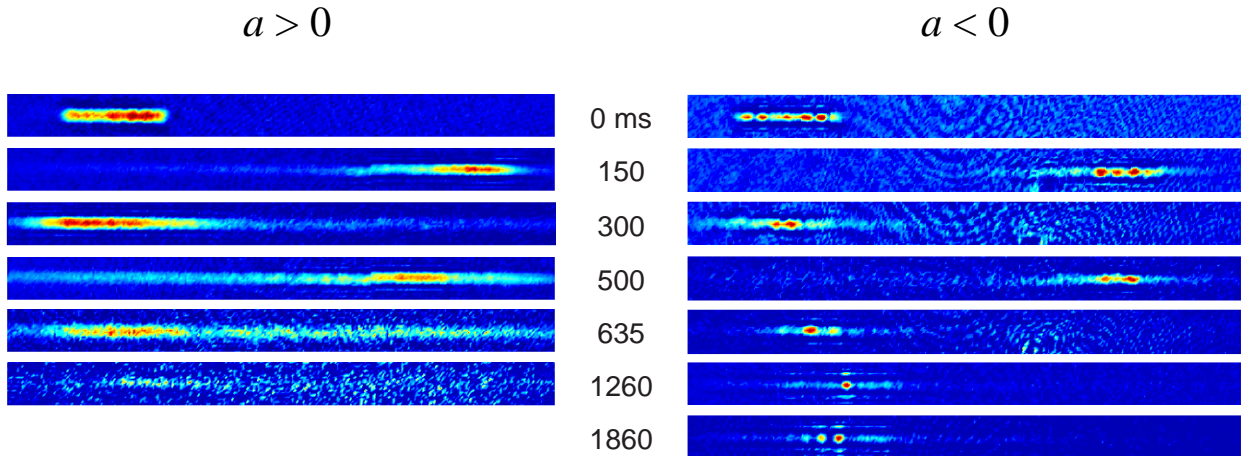


Figure 3.18 Images showing the observation of solitons, with $a < 0$ in contrast to a dispersive BEC with $a > 0$ from Ref. [10]. The $a < 0$ data was taken at $B = 540$ G, and $B = 630$ G for the $a > 0$ data.

[53]. We want to look at a propagating BEC at two distinct places, where a is either sufficiently negative or positive. To accomplish the propagation, the optical trap was aligned such that the focus of the infrared beam was displaced from the center of the of the magnetic trap potential by approximately $185 \mu\text{m}$ (see Fig. 3.17). The endcaps hold the atoms on the side of the weak axial potential formed from the single focused infrared beam. After the BEC is formed, the endcaps can be removed, leaving only the axial beam, allowing the BEC to oscillate in the axial potential. Figure 3.18 shows the propagation of both a dispersive BEC with $a > 0$ and a non-dispersive BEC with $a < 0$. The right hand side of Fig. 3.18 demonstrates clear evidence of the formation of solitons. We observed that the BEC broke into several smaller BECs, typically four or five. As they oscillated, we saw that they maintained their shape for times exceeding 1.8 s. The images were taken using absorption imaging with a 9Γ detuned probe beam. Since each image is destructive, each frame in Fig. 3.18 shows an independent experimental run. The variation in the number of solitons formed from shot to shot is $\sim 25 \%$. This variation may be due in part to variations in the number of atoms within the initial BEC.

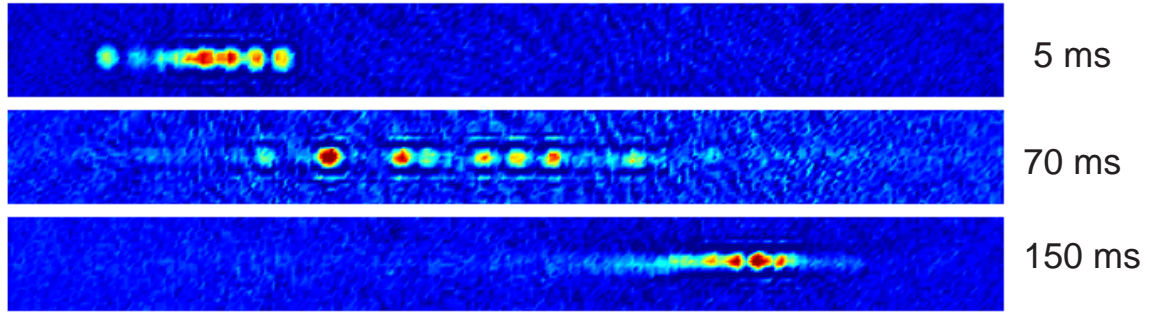


Figure 3.19 The propagation of a soliton train across the axial potential. The relative motion between adjacent solitons shows that the solitons actually repel each other, from Ref. [10].

Another experimental observation can be seen in Fig. 3.19. As the solitons propagate through the axial potential, they are observed to spread out at the minimum of the axial potential and bunch up at the turning points. The expectation for non-interacting objects is that they must end up at the same height in the potential as they started. In addition, for a harmonic potential, each object has the same oscillation frequency, so that non-interacting particles must cross the center of the well all at the same time. Here we observe the opposite effect: the soliton spacing is maximum at the center of the potential. From this we deduce that the individual solitons have repulsive interactions.

Discussion

There are two main points to discuss: the first point is how the solitons form, and the second is the observation of repulsive soliton-soliton interactions. We will also compare our results with an experiment done at Ecole Normale Supérieur (ENS) in Paris [55].

As discussed above, to form solitons we make a stable repulsive BEC near a Feshbach resonance and ramp the magnetic field down to a magnetic field corresponding to a small negative scattering length. The ramp down of the magnetic field is achieved by reducing the supply current with a 35 ms RC decay. With this procedure we typi-

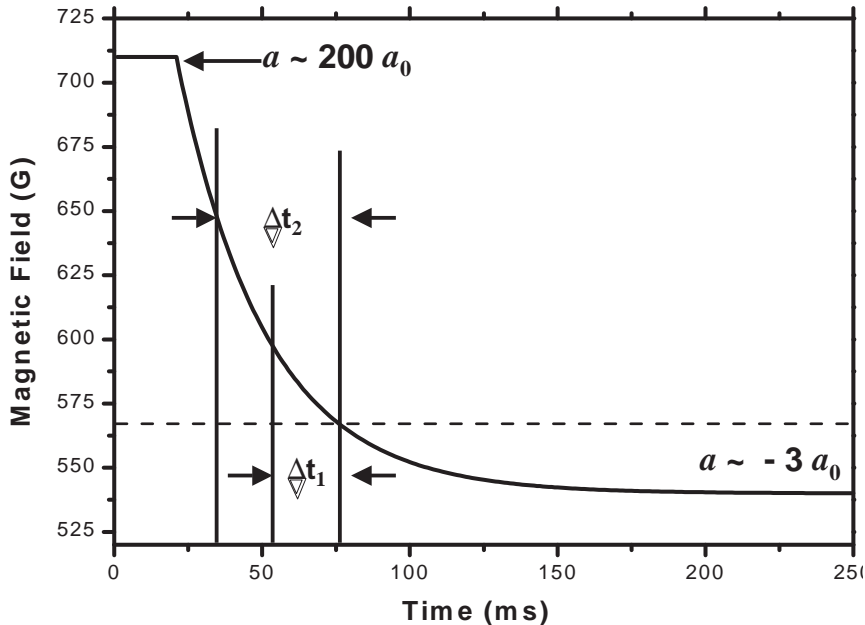


Figure 3.20 The timing diagram for studying the number of solitons formed versus release time. Δt_1 shows a sample delay time for removing the endcaps. In this case, the endcaps are removed at a scattering length of $\sim 6 a_0$, ~ 25 ms before the scattering changes sign. For Δt_2 , the end caps are removed at a scattering length of $\sim 20 a_0$, ~ 38 ms before the scattering length changes sign.

cally form four solitons. The number of solitons formed is related to the initial size of the BEC compared to the healing length $\xi = (8\pi n a_0)^{-\frac{1}{2}}$ [56]. The healing length is the length scale over which the condensates wave function can respond to a localized perturbation [20]. Since each soliton is a BEC, the number of solitons formed should vary with the ratio l_c/ξ , where l_c is the length of the condensate. In order to study how many solitons are formed, we want to vary the initial size of the condensate before the scattering length is changed from positive to negative. This is accomplished by removing the endcaps prior to sweeping the magnetic field across the zero crossing of the scattering length. Figure 3.20 shows the timing diagram for this experiment. There are two sample delay times shown: the first corresponds to $\Delta t = 25$ ms, and the second corresponds to $\Delta t = 38$ ms. The delay is defined to be the time between when the endcaps are removed and when the scattering length changes sign. Figure

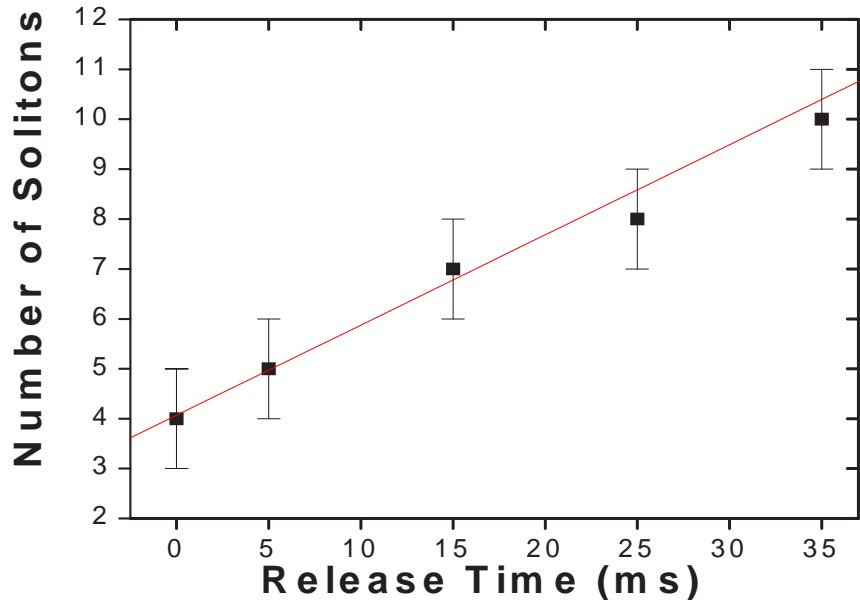


Figure 3.21 The number of solitons vs. release time. The release time is defined as the interval of time between the time the scattering length becomes negative and the time that the endcaps are removed. Therefore, the release time equals the amount of time the BEC expands before the scattering length changes sign.

3.21 shows the results. We observe a linear increase in the number of solitons versus the release time. The linear increase in soliton number versus time can be understood by looking at how the condensate size, l_c , changes in time. As the condensate grows, the density is reduced, the healing length increases as $\xi \propto l_c^{\frac{1}{2}}$. The number of solitons, $N_s \propto l_c/\xi \propto l_c^{\frac{1}{2}}$. There are three effects that can contribute to the change in l_c : first are the harmonic forces in the trap, second is the atom-atom interaction pressure, and third is the kinetic energy. For early release times, like those in Fig. 3.21, the harmonic forces tend to compress the condensate, while the interaction pressure and the kinetic energy tend to make the condensate expand. A further complication is that $\xi \propto a^{\frac{1}{2}}$ while $l_c \propto a^{\frac{1}{5}}$, and the scattering length is constantly changing while $a > 0$. From this analysis we conclude that if $l_c \propto v \cdot t^2$, then we expect a linear increase in N_s versus time. However, without further study we can not determine the dependence of l_c on v .

To calculate the number of solitons formed we can model the formation of the solitons using the dissipative time dependant Gross-Pitaevskii equation [54]. The model starts with a repulsive condensate, as the scattering length changes sign, such that $a < 0$, a modulation instability occurs. The instability is a result of phase fluctuations in the condensate caused by the non-linearity which grows due to self-focusing. These modulations grow into solitons [56]. The number of solitons can be estimated by [54],

$$N_s = \frac{\sqrt{Nal_c}}{\pi l_r} \quad (3.5)$$

where N is the number of atoms, $l_r = (\hbar/m\omega_r)^{\frac{1}{2}}$. If we use a to be the final value, such that $|a| = 3 a_0$, and $N = 5 \cdot 10^5$ atoms, we get that 14 solitons should be formed. However we only observe that typically ~ 4 solitons are formed. Reference [54] suggest that this disagreement between the expected number of solitons formed and the number observed might be due to the size of the solitons, either being large and too diffuse to identify as solitons or are too small to be able to distinguish between adjacent solitons.

The second point is to look at the soliton-soliton interactions. From the observations in Fig. 3.19 we see that adjacent solitons have repulsive interactions. Calculations for the interactions of optical solitons show that two optical solitons would have repulsive interactions if they had a π phase difference [57]. When two solitons with opposite phases overlapped they destructively interfere. This interference makes the slope of the wave function greater, increasing the kinetic energy term in the NLSE. The more they overlap, the higher the kinetic energy, which leads to a repulsive interaction. Figure 3.22 shows several pictures of the solitons repelling each other as they propagate across the axial potential. Figure 3.23 shows the separation of the brightest two adjacent solitons from each picture of Fig. 3.22 as a function of time, normalized to the axial trapping frequency. The line is a theoretical plot of the motion of two solitons with π phase difference [56]. The agreement between the experimental and the

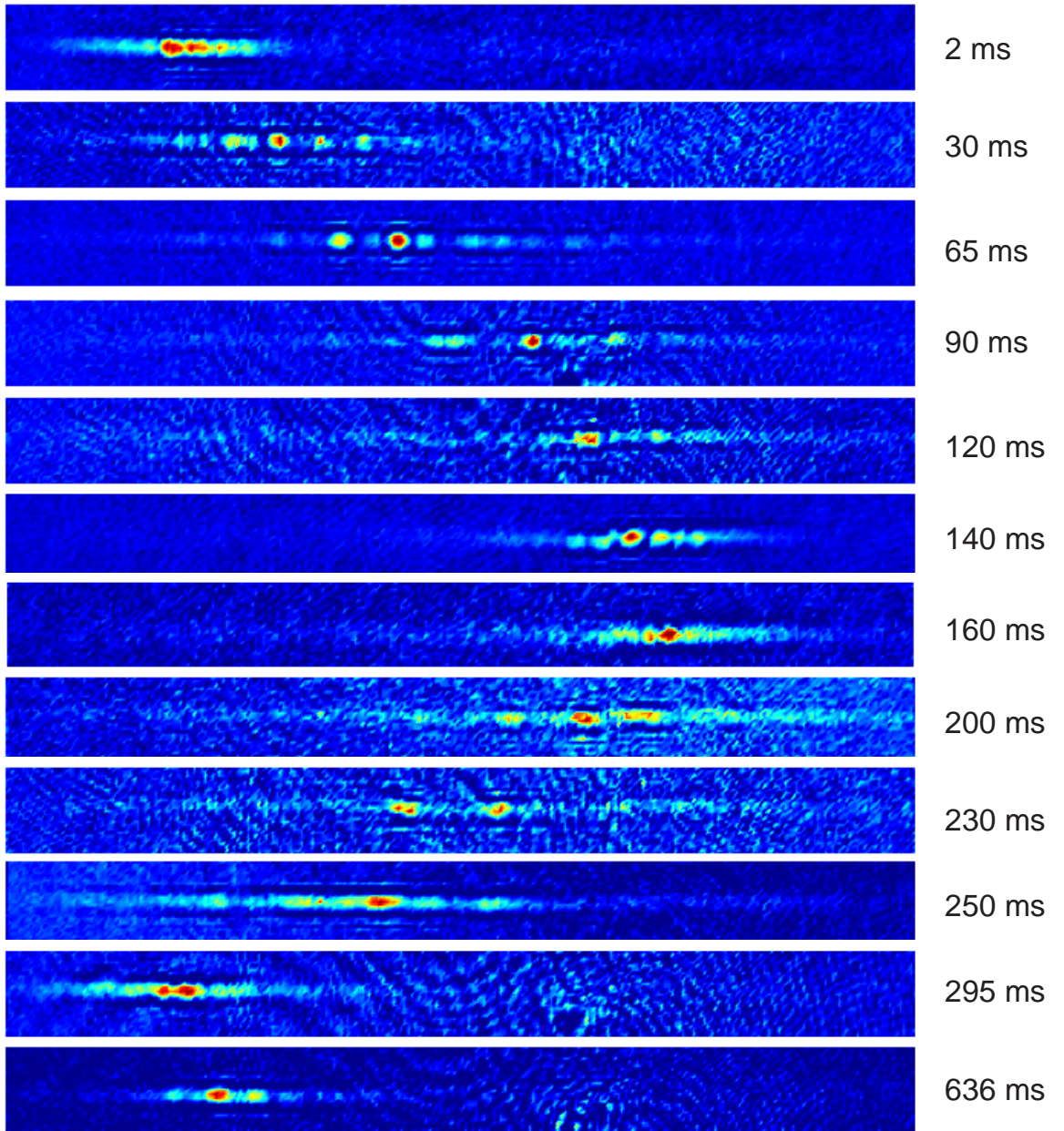


Figure 3.22 Several images of solitons oscillating in the axial potential. By estimating the distance between adjacent solitons, we can study their dynamics in the harmonic potential.

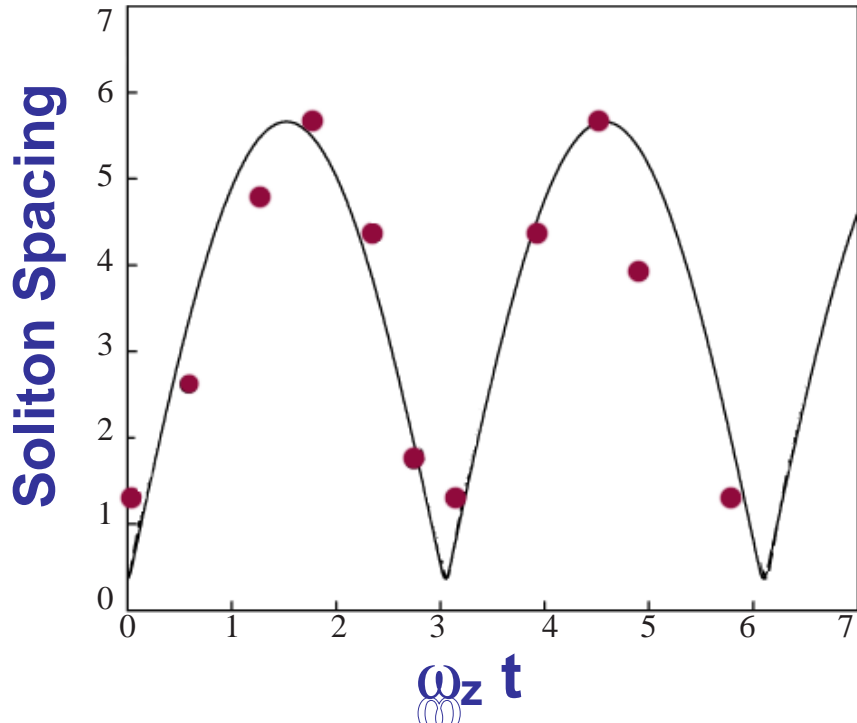


Figure 3.23 Comparison of theoretical calculations with experimental results for the relative motion of two adjacent solitons as a function of time [56].

theoretical data is good. Solving the time dependant Gross-Pitaevskii equation for the phase of the solitons shows that the solitons are produced with nearly a π phase differences [54]. As a result of the near π phase difference, the repulsively interacting solitons can exchange atoms during a collision, through tunnelling of atoms between adjacent solitons. While there is yet no experimental evidence suggesting a non- π phase difference, Ref. [54] suggests that the reason for the decay of the solitons with time in Fig. 3.18 could be explained by atoms tunnelling between adjacent solitons, causing the solitons to become unstable and collapse.

The final issue is to compare our results with the ENS experiment [55]. The main results of the ENS experiment is the formation of a single soliton of ${}^7\text{Li}$ in the $F = 1$, $m_F = 1$ state, and the propagation of the soliton compared to the propagation of a BEC. The two main differences between our results and the ENS results are: first,

the ENS produces only one soliton while we produce a train. Second, the ENS soliton is only observed to propagate for 8 ms while our solitons propagate for over 2 s.

The difference in the number of solitons formed can be argued that the ENS experiment simply did not have enough atoms to form multiple solitons. They report forming a condensate with $2 \cdot 10^4$ atoms, reducing the magnetic field to 420 G and observing a soliton with $6(2) \cdot 10^3$ atoms [55]. Their BEC is originally formed in a crossed-dipole trap with $\omega_x = 2\pi \cdot 710$ Hz, $\omega_y = 2\pi \cdot 1000$ Hz, and $\omega_z = 2\pi \cdot 710$ Hz. The axial frequency is then relaxed to $\omega_z \approx 2\pi \cdot 50$ Hz, the magnetic field is reduced to form a soliton, and the axial confinement is removed [55]. Using that the soliton is formed with $\omega_z = 2\pi \cdot 50$ Hz, Eq. 3.5 yields that only 1.18 soliton should form, while the similar calculation for our experiment gave 14 solitons.

In the ENS experiment the soliton is set in motion when the axial confinement is removed. Residual curvature in the magnetic bias field forms and expulsive potential with $\omega \approx 2\pi \cdot 78$ Hz [55]. The expulsive potential launches the soliton out of the trapping region in ~ 8 ms. However, in our data the solitons oscillate in a $2\pi \cdot 3$ Hz confining harmonic potential. Since our solitons experience a confining potential they are able to remain in the trapping region for several seconds.

3.2 Boson-Fermion Mixtures

Although many exciting experiments are waiting to be performed on Bose-Fermi mixtures, in our current experiments the Bose-Fermi mixture is merely a tool which allows identical fermions to incur thermalizing collisions necessary for evaporative cooling. In our original work on Bose-Fermi mixtures, we made a dual quantum degenerate sample of bosons and fermions using a technique called “sympathetic cooling” [6, 58–60]. This was the first ever observation of a quantum degenerate Bose-Fermi mixture in an alkali gas. However, as is frequently found in pioneering experiments, we learned much in doing the experiment that could lend to vast improvements over the original system.

The primary difficulty in the first Bose-Fermi experiments was to obtain consistent loading conditions for the ${}^6\text{Li}$. As described in [12], the experimental procedure was to fully load the ${}^7\text{Li}$ MOT, then pulse-load the ${}^6\text{Li}$ MOT for between 10 to 100 ms. Next we optically pumped both isotopes and turned on the magnetic trap. The aim is to load approximately 10^6 ${}^6\text{Li}$ atoms into the magnetic trap. After 120 s of evaporation we have around $7 \cdot 10^5$ ${}^6\text{Li}$ atoms remaining below 1 μK in temperature. The problem is that slight variations in the locking frequencies of the trap/re-pump laser and/or the Zeeman slower laser lock caused large variations in the final number of ${}^6\text{Li}$ atoms. To put this in perspective, our Bose-Fermi Science paper [6] has about 50 total data points showing the mixture cool from the classical regime into the quantum regime. Obtaining this data took nearly 1000 experimental runs, at 120 s per cycle to collect. The data was rejected if either the ${}^6\text{Li}$ or ${}^7\text{Li}$ signal was too weak, which resulted in a less than 10% collection efficiency. Since our goal was to utilize the dual quantum degenerate mixture for the starting point of many future experiments, our new primary objective for the Bose-Fermi system became to improve the repeatability, so that we can reproduce the quantum degenerate Bose-Fermi mixture every experimental run.

The first improvement, discussed in the apparatus section and further discussed in [13], was the implementation of a MOT for the ${}^6\text{Li}$ that was being repumped on the ${}^6\text{Li}$ D1 line. The D1 repumping scheme is necessary to avoid adverse effects on the ${}^7\text{Li}$ arising from competition between the ${}^7\text{Li}$ MOT and the ${}^6\text{Li}$ D2 repump laser frequency [12, 13]. The other goal was to construct the MOT solely using diode lasers, instead of using the Spectra-Physics 380D dye laser. Although the optical power would be significantly reduced from our original ${}^6\text{Li}$ MOT, we assumed that it would be possible to load the ${}^6\text{Li}$ MOT in steady state and trap $> 10^6 {}^6\text{Li}$ atoms. In this configuration, we would no longer be dependent on the ${}^6\text{Li}$ load rate, the MOT would load in steady state, achieving the necessary number of ${}^6\text{Li}$ atoms and solving the repeatability issue. However, there is an additional caveat. As mentioned in section 2.1.2, fine-structure-changing collisions between the ${}^6\text{Li}$ and ${}^7\text{Li}$ deplete the ${}^6\text{Li}$ atoms from the dual MOT. Using only diode lasers, we found that ${}^6\text{Li}$ are lost faster than they can be loaded, resulting in a complete loss of ${}^6\text{Li}$. To address this problem, we were compelled to re-introduce the Spectra-Physics 380D dye-laser, which provides much greater power, and consequently a greater ${}^6\text{Li}$ trap depth. The additional trap depth was found to be sufficient to suppress fine-structure-changing collisions [26]. This new ${}^6\text{Li}$ MOT is much more robust against fine-structure-changing collisions, and as a result of the increased trap depth, the MOT can capture $\sim 10^9 {}^6\text{Li}$ atoms, which is far more than can be sympathetically cooled using $2 \cdot 10^9 {}^7\text{Li}$ atoms. Therefore we load the the ${}^6\text{Li}$ MOT with fewer atoms by pulsing the lasers on for ~ 1 s.

In order to utilize all the ${}^6\text{Li}$ that can be trapped we needed to devise a cooling scheme that would work when the numbers of both species are nearly equal, that is $N_6 = N_7$. In this case, we simply have twice the number of atoms ($N_{total} = N_6 + N_7$). The increased number leads to a higher elastic collision rate, that should improve the efficiency of evaporative cooling, if we evaporate both species. A feature common with forced evaporation is that as long as there are more initial atoms then a given critical

number, the end result, after evaporation, will be less sensitive to fluctuations in the initial number of atoms. Dual evaporation eliminates the issues of being dependent on the load rate and exact number of ${}^6\text{Li}$ in the dual MOT, improving the repeatability of the evaporatively cooled Bose-Fermi mixture.

3.2.1 Dual Evaporation

In the previous section, we suggested dual evaporation as a solution to our problem when the number of trapped ${}^6\text{Li}$ atoms approaches the number of trapped ${}^7\text{Li}$ atoms. However, this is not valid for our initial conditions, which are around $2 \cdot 10^9$ ${}^7\text{Li}$ atoms and $2 \cdot 10^8$ ${}^6\text{Li}$ atoms confined in the magnetic trap. To obtain the desired condition for dual evaporation, we begin cooling the ${}^6\text{Li}$ sympathetically [6], and as the number of ${}^7\text{Li}$ atoms approaches the number of ${}^6\text{Li}$ atoms we begin to gently evaporate the ${}^6\text{Li}$. When $N_6 \simeq N_7$, ${}^6\text{Li}$ and ${}^7\text{Li}$ are evaporated at nearly the same rate. These three regions of evaporation are determined empirically to maximize the final phase space density of the ${}^6\text{Li}$.

Initially, two different dual evaporation methods were attempted before the best solution was attained. The first method, described in reference [13], used a mixer and a fixed local oscillator (LO) to generate a second evaporation frequency that followed the ${}^7\text{Li}$ evaporation frequency with an offset determined by the LO frequency. The LO was turned off in the initial stages of the evaporation to allow for sympathetic cooling, and was then turned on approximately 3/4 of the way through, at a frequency near 575 MHz (the difference between the ${}^7\text{Li}$ and ${}^6\text{Li}$ ground state hyperfine splitting). This method of dual evaporation did not work as a result of a difference in the curvature between the ${}^7\text{Li}$ $F = 1$, $m_F = 1$ state and the ${}^6\text{Li}$ $F = \frac{1}{2}$, $m_F = \frac{1}{2}$, which causes a changing non-linear difference between the two evaporation frequencies, as seen in Fig. 3.24.

The second method was to generate two independent microwave frequency ramps,

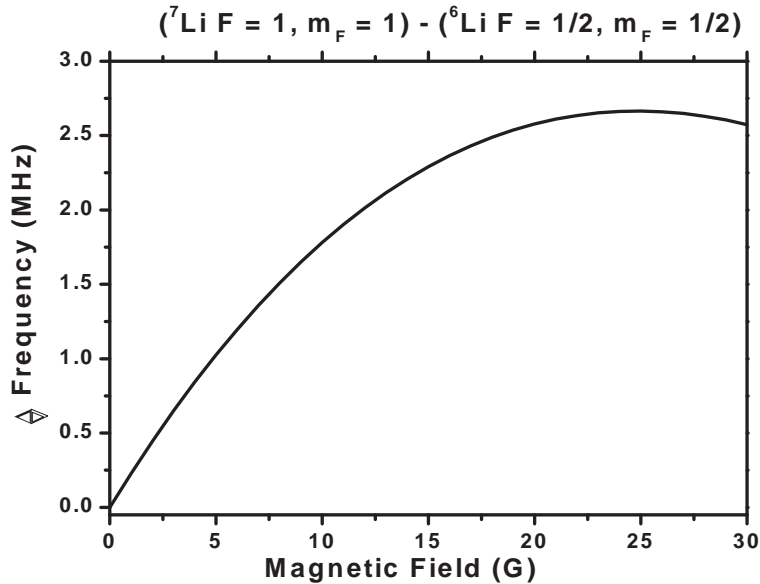


Figure 3.24 Difference in frequency between the ${}^7\text{Li } F = 1, m_F = 1$ state and the ${}^6\text{Li } F = \frac{1}{2}, m_F = \frac{1}{2}$ state. As a result of this changing difference between the two states, a second synthesizer is required to perform dual-evaporation.

or trajectories, using an optimized ${}^7\text{Li}$ trajectory [44], along with a modified version of the ${}^7\text{Li}$ trajectory used for the ${}^6\text{Li}$ (see Fig. 3.25). This method resulted in vast improvements in the consistency of creating quantum degenerate Bose-Fermi mixtures.

3.2.2 Optimized Evaporation

The optimization of ${}^7\text{Li}$ has been discussed elsewhere [13, 15, 16, 44], and reference [15] has dealt explicitly with producing optimizing evaporation trajectories for ${}^7\text{Li}$ in our Ioffe-Pritchard trap. Conceptually, the trajectories are optimized by taking a classical Boltzmann distribution for the atoms at some temperature T , and truncating the distribution by removing all the atoms with energy above some cutoff energy $E_{cut} = \eta \cdot \langle E \rangle$. Then, the distribution is allowed to thermalize through elastic collisions. The elastic collision rate is approximately

$$\dot{r}_{col} = n_7 \sigma_{77} V_7, \quad (3.6)$$

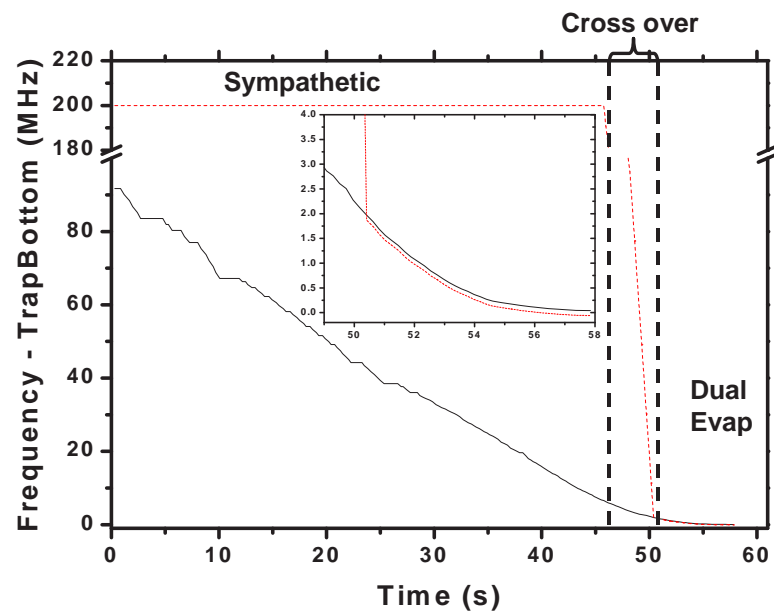


Figure 3.25 An optimized ${}^7\text{Li}$ trajectory with an empirically determined ${}^6\text{Li}$ trajectory. The premise is to divide the trajectory into three regions. A sympathetic region, a cross over region, and dual evaporation region. The cross over region is determined by the temperature of a ${}^6\text{Li}$ cloud after a full sympathetic evaporation.

where n_7 is the ${}^7\text{Li}$ density, $\sigma_{77} = 8\pi a_7^2$ is the scattering cross section, and V_7 is the velocity of the atoms. There is also atom loss that comes from dipolar collisions [61] and from collisions with the background gas. To make the optimization concrete, we must define what an optimized trajectory does. That is, an optimized trajectory maximizes the phase space density, ρ , at the end of the evaporation, where $\rho = n_0 \Lambda^3 \propto N/\langle \varepsilon \rangle^3$ and $\langle \varepsilon \rangle$ is the per particle energy. Sackett showed that maximizing the instantaneous phase space density at every point in the trajectory is equivalent to maximizing the phase space density at the end of the trajectory [16, 44]. The instantaneous optimization is found by determining the maximum value for the change in phase space density for a given change in the number of atoms, which defines the efficiency

$$\gamma = \frac{\partial \rho / \rho}{\partial N / N}. \quad (3.7)$$

After truncating the distribution we must determine how the atoms respond in time. The kinetic equation used to describe the evolution of the gas is the Boltzmann transport equation, which for a free (non-trapped) gas relies on the assumption that the momentum and spatial coordinates are independent [43]. For a trapped gas, this approximation is the ergodic approximation. The ergodic approximation states that the momentum of any two particles found inside a volume element ∂r are uncorrelated. For a trapped gas, this means the momentum and spatial coordinates are uncorrelated and that the gas can be described in terms of its energy. Then the Boltzmann transport equation for the energy distribution $f_7(E)$ is given by [44]:

$$g(E) \frac{\partial f_7(E)}{\partial t} = I_7(E) - \Gamma_7(E)g(E)f_7(E) \quad (3.8)$$

where $g(E)$ is the density of states, $I_7(E)$ is the elastic collision term, and $\Gamma_7(E)$ loss term. Equation 3.8 can be numerically solved, yielding the distribution function versus time. We then break up the evaporation into a time grid with step size ∂t . For each step, ∂t , we remove all the atoms with energy above E_{cut} , where E_{cut} is chosen

to maximize the efficiency given by Eq. 3.7, and allow the distribution to evolve according to Eq. 3.8. We iterate through this process until the final temperature is reached, giving us our optimized evaporation trajectory, $E_{cut}(t)$.

Optimizing evaporation trajectories for mixed Bose-Fermi gases is similar to the single species case, except the scattering integrals become more involved. The ${}^7\text{Li}$ elastic collision rate is

$$\dot{r}_7 \simeq V(n_7 \cdot \sigma_{77} + n_6 \cdot \sigma_{67}), \quad (3.9)$$

where σ_{67} is the ${}^6\text{Li} \leftrightarrow {}^7\text{Li}$ scattering length ($a_{67} = 40.1 a_0$) [25]. The ${}^6\text{Li}$ has no self interaction due to its fermionic nature, and its elastic collision rate is

$$\dot{r}_6 \simeq V(n_7 \cdot \sigma_{67}) \quad (3.10)$$

The elastic collision integrals for the ${}^7\text{Li}$ becomes [13]

$$I_7(E_1) = \frac{m_7 \sigma_{77}}{\pi^2 \hbar^3} \int dE_2 dE_3 dE_4 g(E_{min}) \delta(E_1 + E_2 - E_3 - E_4) \times [f_7(E_3) f_7(E_4) - f_7(E_1) f_7(E_2)] \quad (3.11)$$

$$+ 2 \frac{m_{67} \sigma_{67}}{\pi^2 \hbar^3} \int dE_2 dE_3 dE_4 g(E_{min}) \delta(E_1 + E_2 - E_3 - E_4) \times [f_7(E_3) f_6(E_4) - f_7(E_1) f_6(E_2)], \quad (3.12)$$

while the elastic collision integral for the ${}^6\text{Li}$ is

$$I_6(E_1) = 2 \frac{m_{67} \sigma_{67}}{\pi^2 \hbar^3} \int dE_2 dE_3 dE_4 g(E_{min}) \delta(E_1 + E_2 - E_3 - E_4) \times [f_6(E_3) f_7(E_4) - f_6(E_1) f_7(E_2)], \quad (3.13)$$

where $E_{min} = \min\{E_1, E_2, E_3, E_4\}$, and m_{67} is the reduced mass. The δ -function over the energies is a statement of conservation of energy in the collisions.

The loss rate, given by Γ , depends mainly on the background loss rate, G_1 , and the dipolar loss rate G_2 . There are two dipolar terms. The first is the ${}^7\text{Li} \leftrightarrow {}^7\text{Li}$ dipolar term, which is measured to be ${}^7\text{Li}-{}^7\text{Li} G_2^{77} = 1.05 \pm 0.10 \times 10^{-14} \text{cm}^3/\text{s}$ [61],

while the ${}^6\text{Li} \leftrightarrow {}^7\text{Li}$ dipolar rate $G_2^{66} = 2.35 \times 10^{-15} \text{cm}^3/\text{s}$ [62]. The ${}^7\text{Li}$ and ${}^6\text{Li}$ loss integrals are then given by

$$\Gamma_7(E) = \Gamma_1 + \frac{2(m_7)^3}{\nu^2 \zeta^{1/2} \pi^3 \hbar^6} G_2^{77} \int_0^\infty dE' [E_{<}^{7/2} h_1(x) + U_0 E_{<}^{5/2} h_2(x)] f_7(E') \quad (3.14)$$

$$+ \frac{2(m_{67})^3}{\nu^2 \zeta^{1/2} \pi^3 \hbar^6} G_2^{67} \int_0^\infty dE' [E_{<}^{7/2} h_1(x) + U_0 E_{<}^{5/2} h_2(x)] f_6(E'), \quad (3.15)$$

$$\Gamma_6(E) = \Gamma_1 + \frac{2(m_{67})^3}{\nu u^2 \zeta^{1/2} \pi^3 \hbar^6} G_2^{67} \int_0^\infty dE' [E_{<}^{7/2} h_1(x) + U_0 E_{<}^{5/2} h_2(x)] f_7(E'), \quad (3.16)$$

where $E_{<}$ is the lesser of $\{E, E'\}$, $E_{>}$ the greater, $x = E_{>}/E_{<}$. ν , ζ and U_0 characterize the Ioffe-Prichard trapping potential, where $\nu = \mu B'$, $\zeta = m\omega_z^2/2$, and $U_0 = \mu B_0$. $h(x)$ is the definite integral

$$h_1(x) = \int_0^1 dz z^{3/2} \sqrt{1-z^2} \sqrt{x-z^2}. \quad (3.17)$$

$$h_2(x) = \int_0^1 dz z^{1/2} \sqrt{1-z^2} \sqrt{x-z^2}. \quad (3.18)$$

Our goal is to produce the maximum number of ${}^6\text{Li}$ atoms at the Fermi temperature. To optimize the trajectories to accomplish this for the dual evaporation, there are three parameters to consider: ρ_7 , ρ_6 , and $\rho_{Total} = \rho_7 + \rho_6$. A simple Gedanken experiment tells us that if we attempt to maximize ρ_7 , the optimization would result in the removal of all the ${}^6\text{Li}$, since it is a thermal drag on the ${}^7\text{Li}$. If we instead maximize ρ_6 , the first cut would remove nearly all the ${}^7\text{Li}$ in an attempt to get the ${}^6\text{Li}$ slightly colder, which would leave too few ${}^7\text{Li}$ atoms to effectively cool the ${}^6\text{Li}$ further. If we try to optimize ρ_{Total} we have to add the condition that $\rho_6 \simeq \rho_7$, without this condition there would be no mathematical reason not to allow $\rho_6 \rightarrow 0$, then $\rho_{Total} \rightarrow \rho_7$ which would bring us back to the first scenario. However, this condition is too stringent for the entire trajectory. Since initially, $N_7 \gg N_6$, the first cut would remove most of the ${}^7\text{Li}$ in an attempt to satisfy $\rho_6 \simeq \rho_7$. In the single species evaporation, it was proven that optimizing the instantaneous phase space density was equivalent to optimizing the final phase space density. This is no longer the case

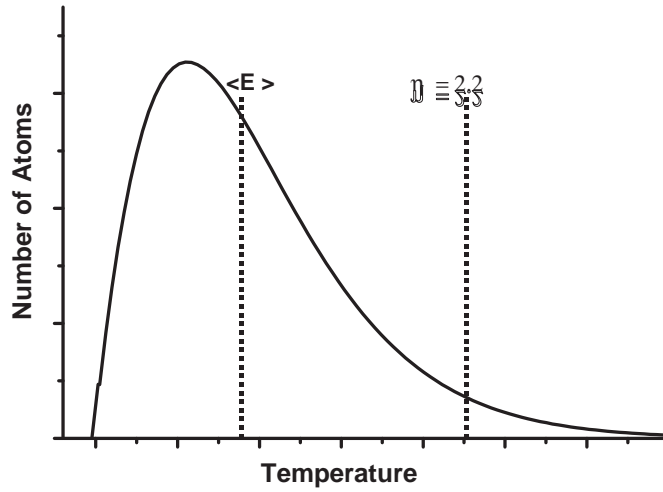


Figure 3.26 Cartoon depicting the the cut energy, η . η determines how far into the distribution the evaporation cuts, which is the number of atoms removed from the trap. The cartoon shows $\eta \approx 2.2$, which is a typical η for cooling ${}^7\text{Li}$.

for the dual evaporation. Therefore, we find an approximate optimized trajectory for ${}^6\text{Li}$, by assuming a trial trajectory and then by use of the Boltmann equation optimization, modify that trajectory until the maximum phase space density of ${}^6\text{Li}$ is achieved. The ${}^7\text{Li}$ trajectory, in the presence of the ${}^6\text{Li}$, is optimized as before for each ${}^6\text{Li}$ trajectory.

The procedure is to first compute the optimized trajectory for ${}^7\text{Li}$ in the presence of ${}^6\text{Li}$. In parallel, the distribution of ${}^6\text{Li}$ atoms is computed based on some simple guidelines for its trajectory, which are similar to those specified above for the non-optimized trajectory. We divide the trajectory into three regions: a sympathetic region, a transition region, and a dual evaporation region. For calculating the trajectories, the figure of interest is the parameter η , which is defined to be the cut energy divided by the average energy, such that $\eta = E_{cut}/\langle E \rangle$. Figure 3.26 shows a pictorial representation of the meaning of η . For a non-optimized trajectory, η would be constant, resulting in an exponential frequency dependence [63]. For the optimized ${}^7\text{Li}$ trajectories, η_7 is adjusted in time to maximize the phase space density. For the approximately optimized ${}^6\text{Li}$ trajectories, η_6 is set empirically for the three different

regions: for the sympathetic region, η_6 is set to be 5 and in this case, the ${}^6\text{Li}$ atoms are essentially not evaporated. For the transition region, η_6 is set to exponentially decreased until $\eta_6 = \eta_7$. In the dual evaporation region, $\eta_6 = \eta_7 - \alpha$, where α is a constant on the order of 0.05. The final phase space density is maximized by systematically adjusting the boundaries of the three regions and varying α . The boundary between the sympathetic region and the transition region is set by $N_6 = \beta \cdot N_7$, where β is found to be ~ 0.333 . The condition for the transition/dual evaporation boundary is similar: $N_6 = c \cdot N_7$, where $c \sim 0.667$. By iteratively varying α , β , and c while monitoring the final phase space density of ${}^6\text{Li}$, we can construct an optimized ${}^6\text{Li}$ trajectory. Figure 3.27 shows outputs for four different values of α with fixed initial conditions and fixed values of β and c . Using this technique we can arrive at an approximate optimized trajectory for the dual evaporation with a given set of initial conditions. Figure 3.28 shows the output from the optimization code. The parameters are given in the caption. According to the simulation of the optimized trajectory, we can achieve repeatable results. In addition, we can overcome the limitations of sympathetic cooling [12, 64] and achieve highly degenerate Fermi gases.

3.2.3 Large Degenerate Fermi Gas

We now put the idea of dual evaporation to the test, and find out if there is an improvement in both the repeatability and achievable phase space density. The results are summarized in Fig. 3.29.

While the results of the dual evaporation are impressive, and have lead to significant improvements in the repeatability of producing cold fermions, the data shown in Fig. 3.29 was taken with a trajectory that assumed only $5 \cdot 10^7$ ${}^6\text{Li}$ atoms initially, which is similar to the number observed after a 90 s evaporation. Several different evaporation trajectories were tried with more initial ${}^6\text{Li}$ atoms, however, none performed as well. Even though the dual evaporation seems to be working better, there

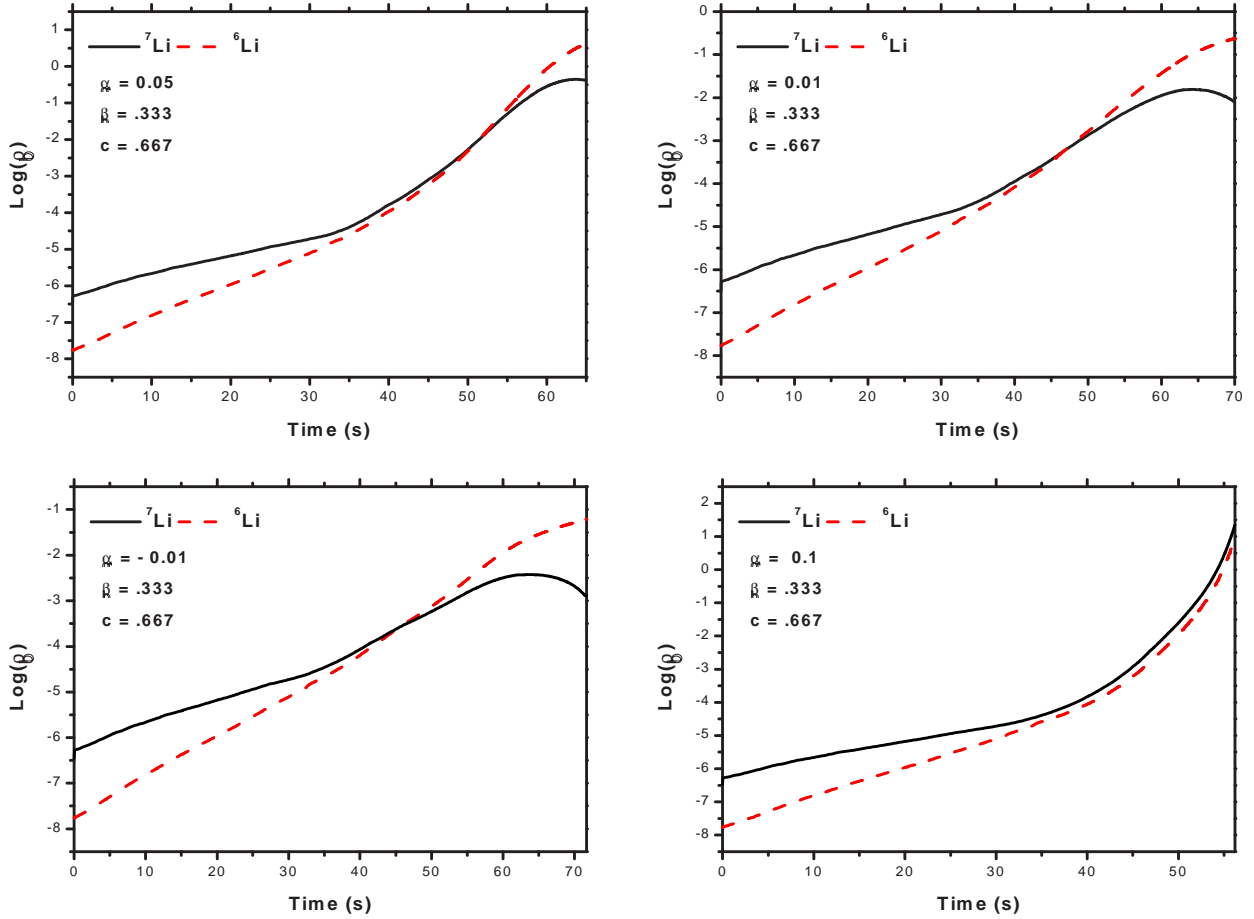


Figure 3.27 α is varied while the final phase space density of ^6Li is monitored. The initial conditions for each trajectory are; $N_7 = 2 \cdot 10^9$, $N_6 = 1 \cdot 10^8$, $T_i = 700 \mu\text{K}$, with a 140 s background lifetime. We find that if α is either too small or negative then the atoms never reach quantum degeneracy ($\log(\rho) = 0$). While an $\alpha > .05$ gives trajectories that reach quantum degeneracy.

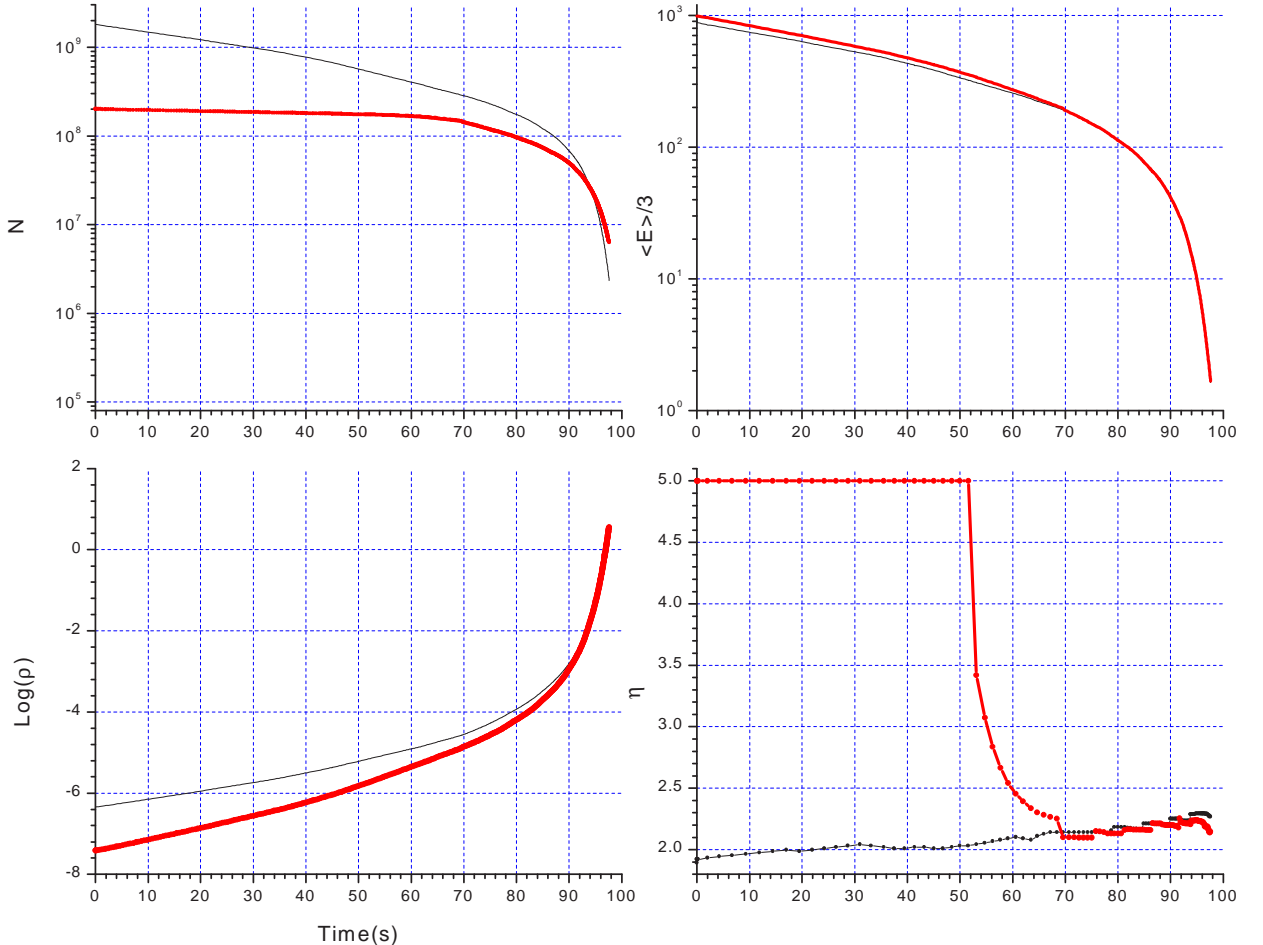


Figure 3.28 Optimized dual ${}^7\text{Li}/{}^6\text{Li}$ trajectories. Going clockwise, we plot the number, the average energy, η , and the log of the phase space density, all versus time. The thick lines correspond to ${}^6\text{Li}$ while the thin line corresponds to ${}^7\text{Li}$. The trajectories are calculated for $N_{7i} = 2 \cdot 10^9$, $N_{6i} = 2 \cdot 10^8$, with $\alpha = 0.98$, $\beta = 0.32$, and $c = 0.5$. This gives a final $N_6 = 7 \cdot 10^6$ at a temperature of $1 \mu\text{K}$, corresponding to $T/T_F = 0.162$.

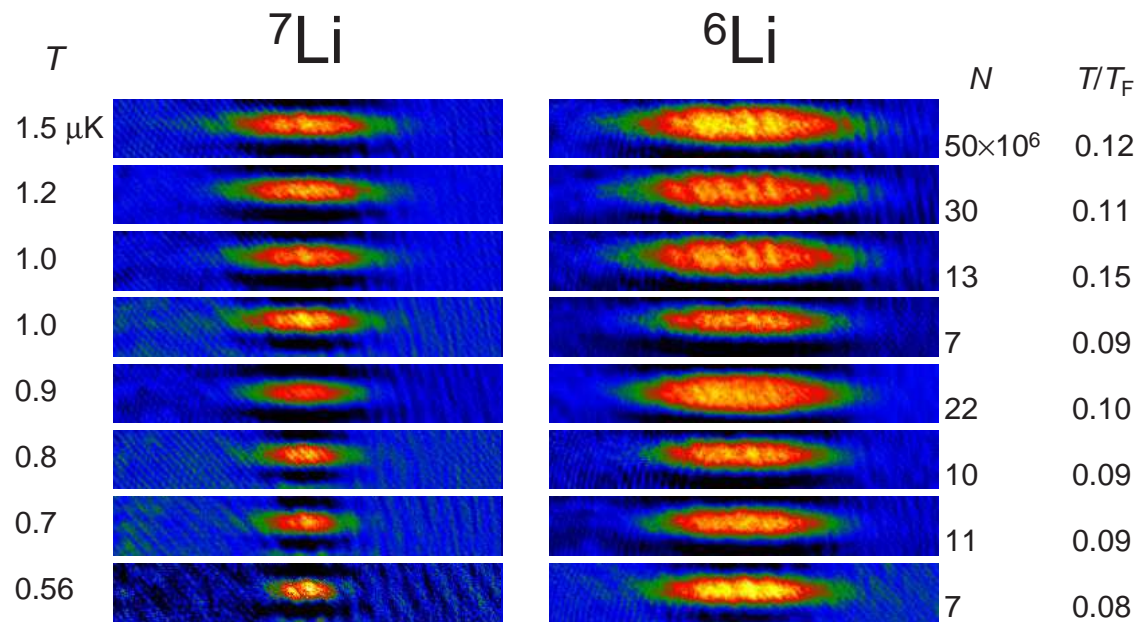


Figure 3.29 Eight successive runs of the experiment, each with a slightly lower final temperature for the evaporation. We are able to achieve degeneracy factors as low as 0.08 T/T_F . The data was collected using absorption imaging at a detuning of 9.1Γ for both isotopes.

is disagreement between the calculated trajectories and the experimental results, in contrast to the results observed for pure ^7Li [44]. We are currently modifying the dual evaporation code, as several simplifications have lead to the non-convergence of the collision integrals. The result is that the adjustments to the accuracy and time step size on the code, yield different answers. As soon as these problems are resolved, we should be able to better compare the calculated results with the experimental observations.

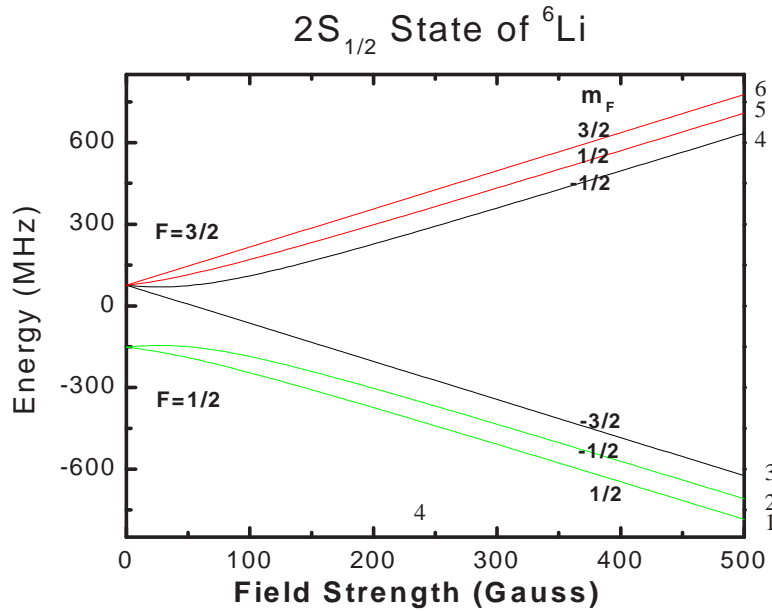


Figure 3.30 Calculation of the ${}^6\text{Li}$ $2\text{S}_{\frac{1}{2}}$ ground state structure. The states are labelled 1 through 6, in order of increasing energy. This provides a convenient method for referring to the different states.

3.3 Fermi-Fermi Mixtures

The starting point for all of the Fermi mixture experiments is an evaporatively cooled Fermi gas in the $F = \frac{3}{2}$, $m_F = \frac{3}{2}$ state. Due to spin exchange [15], there is no stable magnetically confineable ${}^6\text{Li}$ spin mixture. Thus, the atoms must be transferred into the optical trap. This is accomplished in exactly the same manner as with the bosons (see section 3.1.1).

For the experiments in this thesis, we focus on a spin mixture between the two lowest levels in ${}^6\text{Li}$ (see Fig. 3.30). This is done for two reasons. The first is that since they are the two lowest hyperfine levels, energy and spin conservation both forbid spin exchange between the states. Also, there is a large Feshbach resonance between the two states (see Fig. 3.31). On closer inspection of the resonance, there are actually two Feshbach resonances. The small resonance is centered near 540 G, while the large resonance is centered near 840 G.

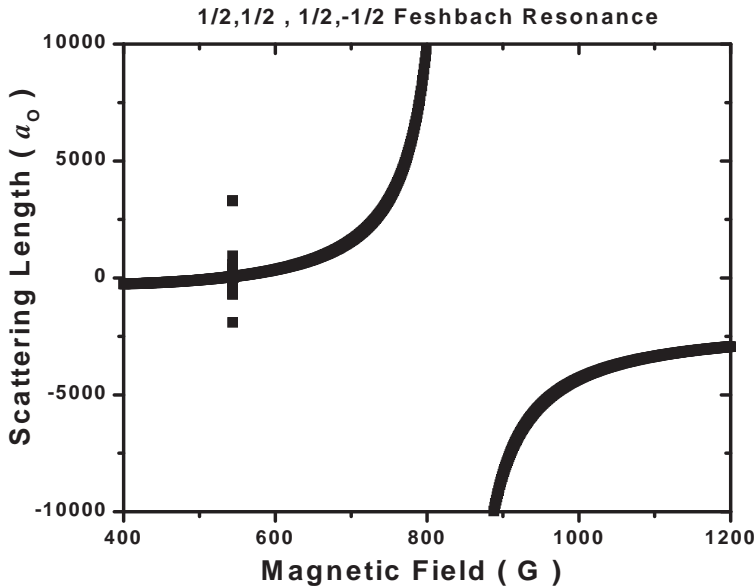


Figure 3.31 Coupled channel calculation of the ${}^6\text{Li}$ $F = \frac{1}{2}, m_F = \frac{1}{2}$ on the $F = \frac{1}{2}, m_F = -\frac{1}{2}$ scattering length versus magnetic field. Two Feshbach resonances can be seen in the calculation: a narrow resonance near 540 G and a large resonance centered near 840 G.

In order to get the atoms into the desired states, we must apply microwave transfers similar to those used in the ${}^7\text{Li}$ case. The first microwave transfer is from the 6 state to the 1 state (Fig. 3.30). Figure 3.32 shows the transfer frequency as a function of magnetic field. The slope of the line is $2 \cdot \mu_B$. Once the atoms are in the 1 state, they must be probed. As was discussed in section 2.4, our probe light is linearly polarized and perpendicular to the bias field axis. As a result, 50% of the probe light couples to σ^+ transitions and 50% of the light couples to σ^- transitions. The high field probing diagram is given in Fig. 3.33. Due to the proximity of the transition frequencies to our MOT lasers, we choose to probe the 6 state on a σ^+ transition and then to probe the 1 state on a σ^- transition. (For clarity's sake, recall that a σ^+ transition conserves m_i and increases m_j by 1, while an σ^- conserves m_i and decreases m_j .)

After the atoms are all transferred from the 6 state to the 1 state, the mixture is made by a second microwave transfer from the 1 to the 2 state. Figure 3.34 shows

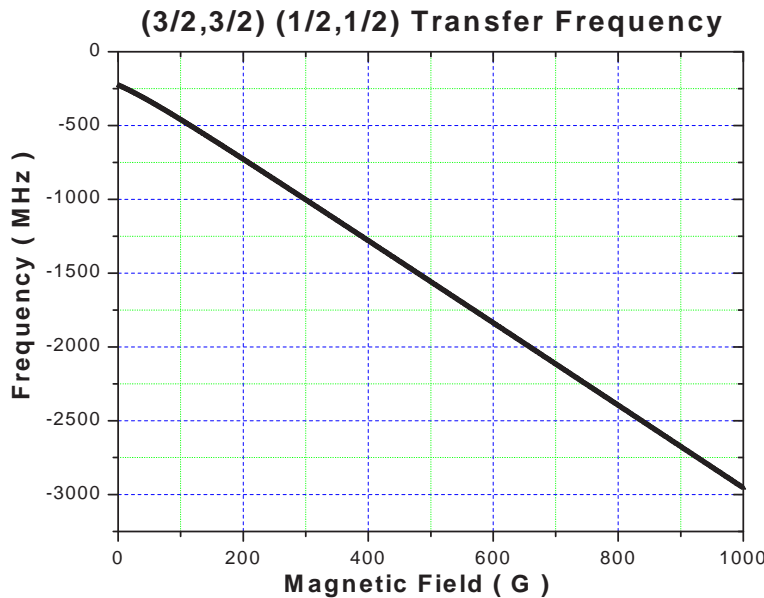


Figure 3.32 Transfer frequency for taking ${}^6\text{Li}$ atoms from the 6 state to the 1 state as a function of magnetic field.

the behavior of the 1 to 2 transition frequency verses magnetic field. At fields above approximately 450 G, the slope of the transition frequency is $\sim 3 \text{ KHz/G}$. The 2 state is probed on a σ^- transition, $m_i = 0$ $\Delta m_j = -1$, to the $2\text{P}_{3/2}$ $F = 5/2$, $m_F = -3/2$ state ($k = 8$ in Fig. 3.33). The difference in the optical transition frequencies between the $1 \rightarrow 8$ and the $2 \rightarrow 9$ transition is 75 MHz, the same as the difference in the $1 \rightarrow 2$ microwave transition frequency to within 1 MHz. The difference in frequency is due to the small frequency difference between the 8 and 9 states (see Fig. 3.33). The actual transition frequencies are calculated using Matlab. The file is called rkkr6.m and is located in /lab/source/acq/emtrap/imaging. The input is magnetic field in Tesla and the two desired states. The output is in units of Δ , which is 5.87 MHz.

3.3.1 Producing a Spin Mixture

There are two main ways that we construct a spin mixture. One method is to utilize a $\pi/2$ pulse to transfer 50% of the atoms from the 1 state to the 2 state.

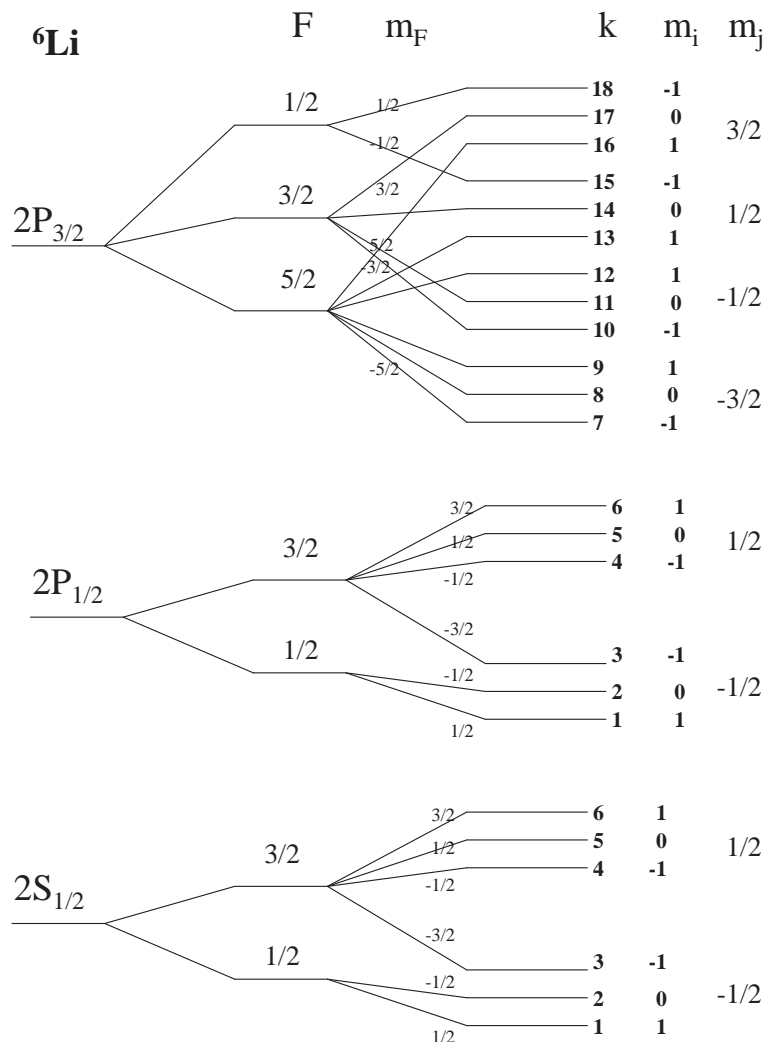


Figure 3.33 Diagram showing the $2S_{\frac{1}{2}}$, the $2P_{\frac{1}{2}}$, and the $2P_{\frac{3}{2}}$ states for both fields where F is a good quantum number and high fields where it is not.

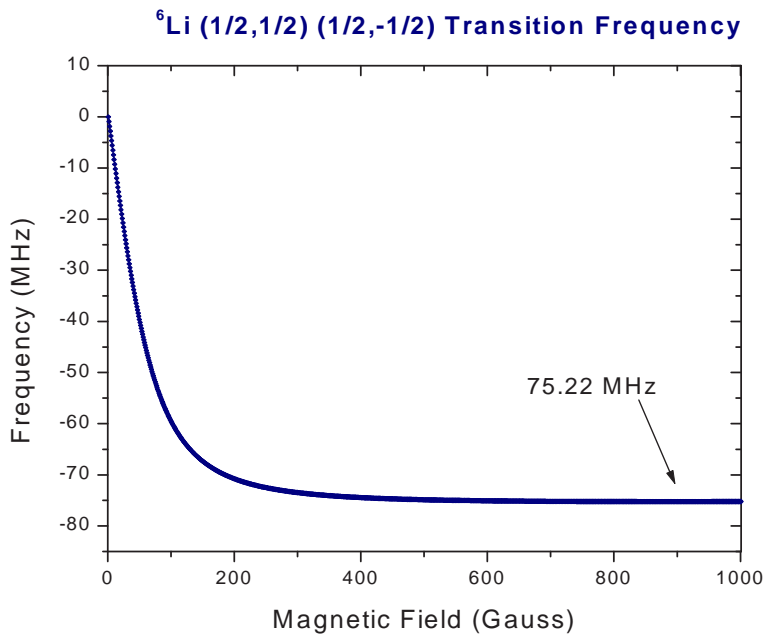


Figure 3.34 The transfer frequency for driving ^6Li atoms from the 1 state to the 2 state as a function of magnetic field.

Another method is to ramp the microwave frequency with the correct microwave power to give a 50% transfer efficiency. It had been experimentally determined that the most certain method for repeatedly producing a 50/50 spin mixture is to apply several of these ramps. If each ramp is nearly 50/50, then each successive ramp the mixture will converge towards an exact 50/50 mixture. For the experiments in this section, the spin mixture was formed either by a $\pi/2$ pulse or a series of 100 microwave sweeps.

The other important factor, as we shall see in section 3.3.2, is that in order for the atoms to interact they must be in an incoherent spin mixture.

3.3.2 Long Lived Coherence

The first attempts to make a Fermi spin mixture revealed a unique and interesting feature of our apparatus: the ability to produce long lived coherent mixtures of states 1 and 2. To drive a Rabi oscillation, a microwave pulse is applied for a specified

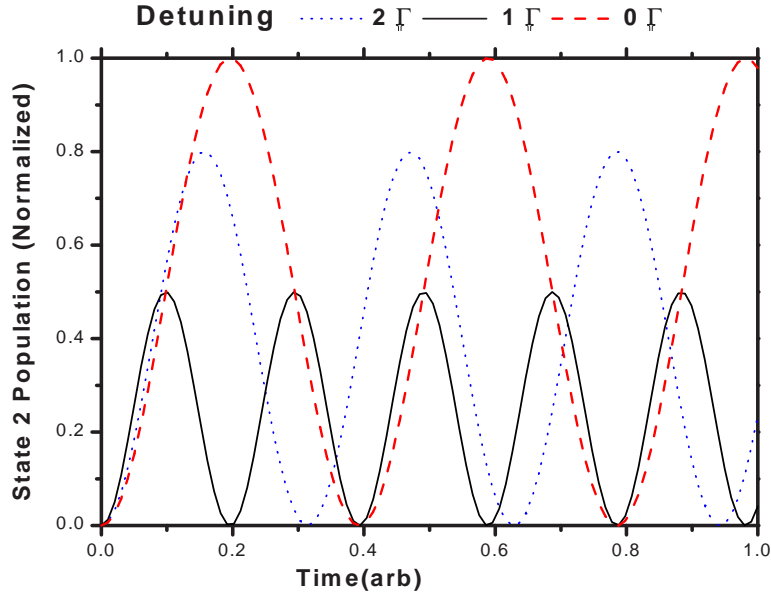


Figure 3.35 Calculation of several coherent Rabi oscillations for different detunings from resonance. Note that the oscillation frequency changes with detuning and that complete transfer only occurs for 0 detuning.

duration of time, and the resulting spin mixture is probed. The system is a simple, two level system consisting of states 1 and 2, which are coupled together by a microwave field with a coupling constant Ω (the Rabi frequency) and having some detuning, δ , from resonance. The probability of making the transition to the excited state is given by $|C_e(t)|^2$ where,

$$|C_e(t)|^2 = \frac{\Omega^2}{\Omega^2 + \delta^2} \sin^2((\Omega^2 + \delta^2) \cdot \frac{t}{2}) \quad (3.19)$$

Figure 3.35 shows calculated Rabi oscillations for three different detuning values. The main features to note are that the frequency of oscillation depends on both the Rabi frequency and detuning, and that 100% transfer is only achieved when the drive is on resonance. The data in Fig. 3.36 was collected by using absorption imaging to first image the 2 state and then the 1 state. The fractional signal was found by selecting a region of interest that includes the entire atom signal. The fractional signal is found by summing the region of interest, yielding a number proportional to the total number of atoms. The total signal is defined to be the sum of the fractional signals

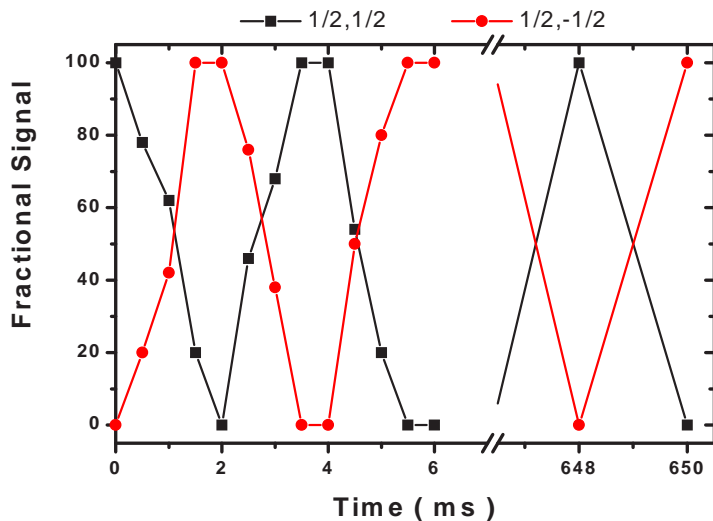


Figure 3.36 Rabi oscillations between the 1 and 2 state in ${}^6\text{Li}$ at 530 G. The data give an approximate 3.5 ms oscillation period.

from state 1 and state 2.

The scattering length at 530 G is calculated to be approximately $5 a_0$. In an attempt to de-cohere the gas, we measured the Rabi oscillations at 903 G where the scattering length is calculated to be $-8090 a_0$ (Fig. 3.31). Figure 3.37 shows some noisy Rabi oscillations. However, if the gas were truly de-cohering, the oscillations would damp out and would not revive. The most likely explanation for the shape of the oscillations is either due to fluctuations in the bias field causing the detuning of the microwaves to change, or power fluctuations in the microwave drive. Both of these effects would cause the oscillation frequency to change over time.

These oscillations at 903 G were then observed over longer intervals. This time we allowed the microwaves to drive the oscillations for over 1 s before measuring the relative occupation of states 1 and 2. Figure 3.38 shows that the coherence persists. If the mixture does not decohere then the atoms are in a coherent superposition of the 1 and 2 states, described by $\Psi_{12} = 1/\sqrt{2}(\Psi_1 + \Psi_2)$. Since Ψ_1 and Ψ_2 are both fermions, Ψ_{12} is also a fermion. Then, without decoherence, all the atoms are identical

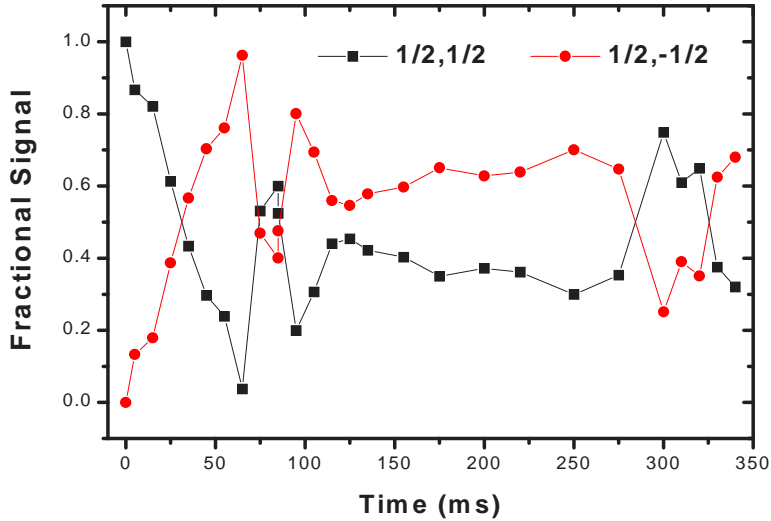


Figure 3.37 Rabi oscillations between the 1 and 2 state in ${}^6\text{Li}$ at 903.25 G. The oscillation time is not well-defined. The gas initially appears to be de-cohering, until 300 ms when the oscillations partially revive.

fermions in state Ψ_{12} , and they are Pauli-excluded from interacting. Another method we used to look for decoherence in our system was to drive a $\pi/2$ pulse and then allow the atoms to evolve on their own. Due to the shallow nature of our optical trap, we expect to see loss on the thermalization time scale, which is proportional to a^2 , after the atoms decohere.

We conduct the experiment at two different magnetic field values: the first region is where the scattering length is small, 530 G. Figure 3.39 shows these results. For a control we took lifetimes of the both the pure 1 state (squares) and the pure 2 state (circles). The mixture lifetime shows no evidence of decoherence. The mixture signal is shown at 50% of the signal of a pure state since half the atoms are in each state, and the resulting signal is thus reduced by 50%.

The second case is where we make the $\pi/2$ pulse at 530 G, ramp the field up to 903.25 G, and take a lifetime. Again, for a control we have also taken the lifetime of a pure state. Figure 3.40 shows the results. We see that even at a magnetic field where the $2 \leftrightarrow 1$ scattering length is calculated to be $-8090 a_0$ there is no evidence of

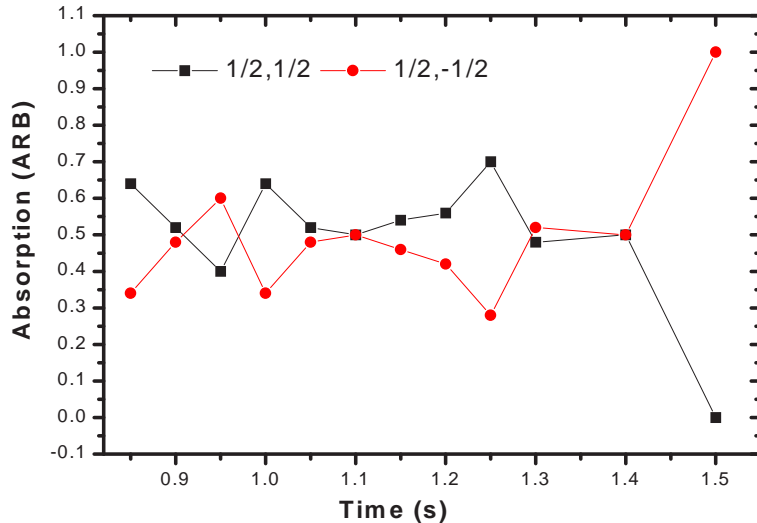


Figure 3.38 Rabi oscillations between the 1 and 2 state in ${}^6\text{Li}$ at 903.25 G. Following 1 s of driving the oscillations, we still observe full transfer to the 2 state at 1.5 s, suggesting no decoherence of the sample.

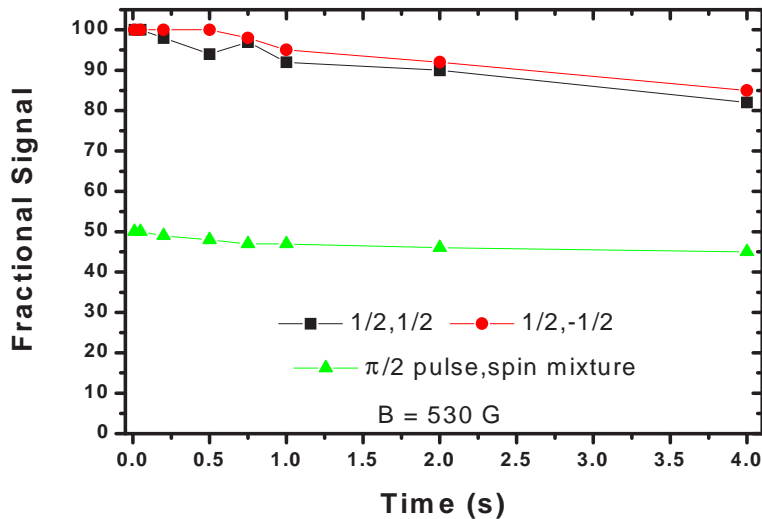


Figure 3.39 Trap lifetime at 530 G. The ■ and ● correspond to lifetimes of the pure states, while the ▲ data represents the spin mixture. There is no indication of decoherence from the trap lifetimes.

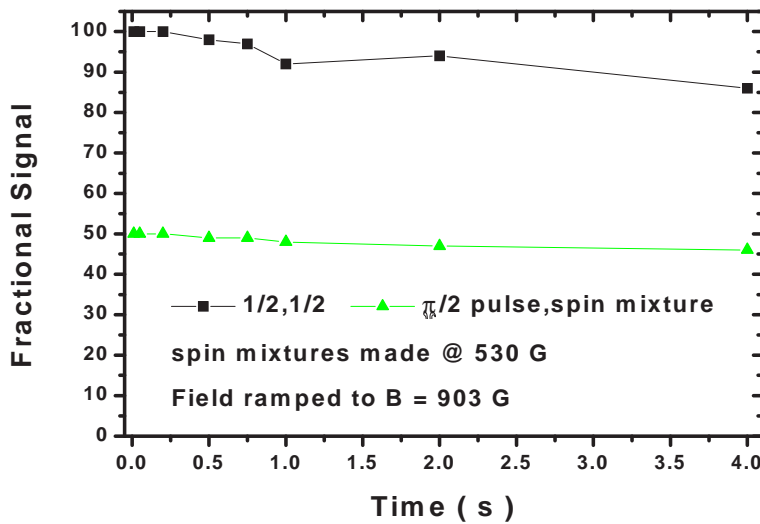


Figure 3.40 Lifetime at 903 G. The ■ correspond to a lifetime of the pure 1 state, while the ▲ data is the spin mixture. Again, there is no indication of decoherence from the atomic lifetimes.

enhanced loss from the optical trap due to decoherence followed by evaporation from the trap.

These tests show that the combination of our optical trap with a well-engineered bias field is capable of maintaining the coherence between two states that otherwise would have enormous elastic scattering rates. As we will see in section 3.3.3 this could have potential for eliminating cold collision shifts in atomic frequency standards.

3.3.3 Microwave Spectroscopy

Microwave, or RF (radio-frequency) spectroscopy is a powerful tool for exploring the mean field energy and cold collision shifts in ultra cold gases [65]. Current atomic frequency standards are based on making microwave transitions, called “clock transitions”. The clock transitions, however, are subject to cold collision shifts due to interactions between the initial state and the state being populated by the microwave pulse. The energy of the shift is given by;

$$\Delta E = \frac{4\pi\hbar^2}{m} \cdot n \cdot a \quad (3.20)$$

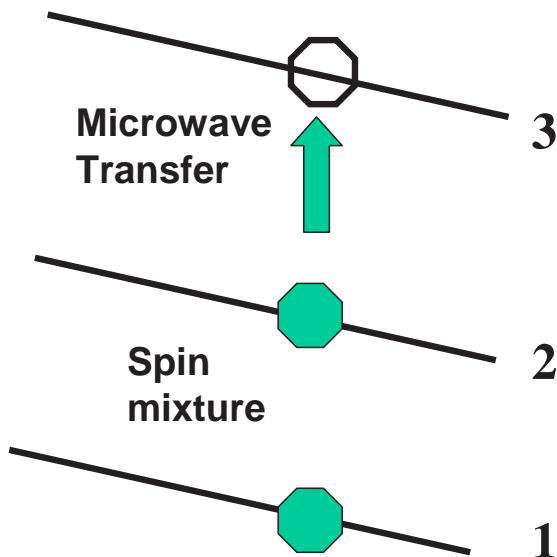


Figure 3.41 Schematic diagram of the hyperfine states and microwave transfers involved in performing RF spectroscopy on a spin mixture of ${}^6\text{Li}$.

where m is the mass, n is the density, and a is the scattering length between the two states.

In our system, we are interested in exploring a spin mixture of two different hyperfine levels in ${}^6\text{Li}$. This requires making a spin mixture between the two levels, and driving a microwave transitions to a 3rd level. Figure 3.41 shows a schematic of how the spectroscopy is performed. The atoms are prepared in a 50/50 mixture between states 1 and 2, and then some atoms are driven from state 2 to state 3.

The energy shifts are somewhat more complicated than what is described in Eq. 3.20, since there are now three states. There is one simplification that can be made if the microwave transitions are performed on a time scale that is faster than the decoherence time of the system: once the spin mixture is made between the 1 and 2 state, a microwave pulse drives the atoms into the 3 state, and during that transfer, the 2 and 3 states are in a coherent mixture. Thus, the frequency shift becomes

$$\Delta\nu = \frac{2\hbar}{m} \cdot n_1(a_{13} - a_{12}) \quad (3.21)$$

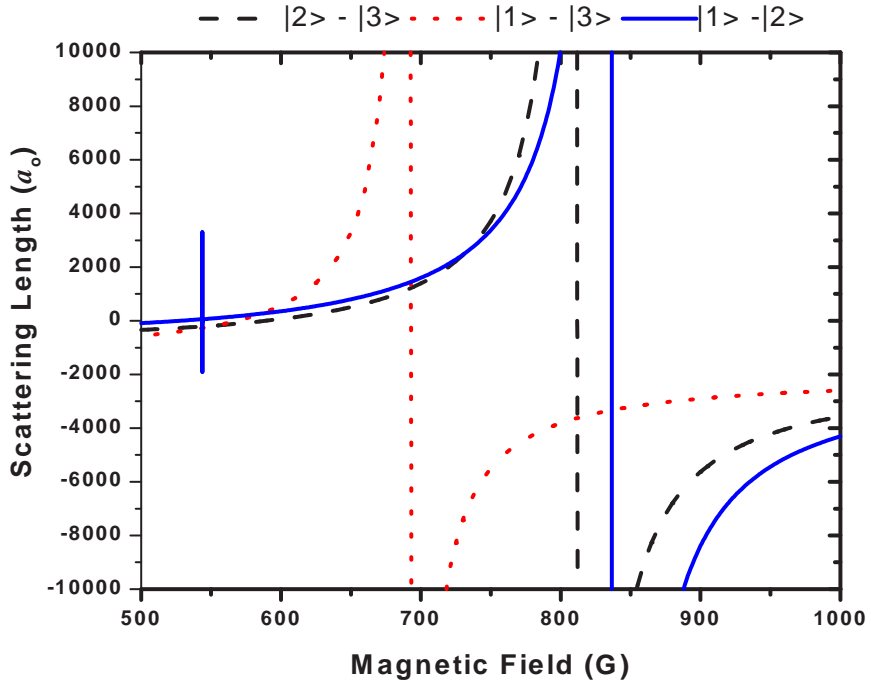


Figure 3.42 Coupled channel calculations of the scattering length as a function of magnetic field for three combinations of ${}^6\text{Li}$ hyperfine states. The \blacktriangle shows the scattering length between the 2 and 3 states. The \blacksquare shows the scattering length between the 1 and 3 states, and the \bullet shows the scattering length between the 1 and 2 states.

where a_{13} is the scattering length between the 1 and 3 states and a_{12} is the scattering length between the 1 and 2 states. The coherence between the 2 and 3 state during the transfer removes any effect of the scattering length between the 2 and 3 states.

For our system, the spin mixture we want to study is between the 1 and 2 states. We do spectroscopy to the 3 state since any other combination of three ${}^6\text{Li}$ ground hyperfine states have spin exchange. The rates are typically $9 \cdot 10^9 \text{ cm}^3/\text{s}$, with typical densities $\sim 10^{12} \text{ cm}^{-3}$ we get a lifetime of less than 1 ms. To calculate the expected energy shift for the $2 \rightarrow 3$ microwave transition, we need to determine a_{13} and a_{12} . Figure 3.42 shows the coupled channel calculations of the scattering lengths between these three states in the magnetic field range of interest. All three combinations show Feshbach resonances, but at slightly different magnetic fields. Putting some numbers into Eq. 3.21, we have a total density $n_{Total} = 5 \cdot 10^{12} \text{ cm}^{-3} = n_1 + n_2$, and a magnetic

field value of 550 G, giving $a_{13} = -212 a_0$ and $a_{12} = 84 a_0$, we get a shift of 775 Hz. In addition, it is well known that in the Feshbach resonance, the scattering cross section σ , where $\sigma = 4\pi a^2$, goes to the “unitarity limit”. In this limit, $\sigma = 4\pi/k_F^2$, where $k_F = (6\pi^2)^{\frac{1}{3}}$ is the Fermi wave vector. For our conditions, this gives a unitarity limited scattering length (k_F^{-1}) of approximately 3573 a_0 . If both a_{13} and a_{12} become unitarity limited, the shifts cancel [66].

The experiments we have performed thus far have been done by making a 50/50 mixture, then giving the mixture a fixed amount of time, typically 1 s, to evolve and decohere. We then drive a microwave transition between the 2 and 3 state using a square RF pulse. Some spectra at 567 G are shown in Fig. 3.43. The \bullet and \blacktriangle are spectra of a pure 2 state. The difference in the widths is due to the transit time broadening from the RF pulse, which is the only observable source of broadening. The \blacksquare data shows a spectrum of a spin mixture. The reduction in signal is due to 50% of the atoms being in the 1 state and not taking part in the spectroscopy. The slight shift in the spectrum is attributed to a slow thermal drift in the magnetic field of approximately 15 mG/s, and not to the mean field effects described above. No collisional broadening is observed. The conclusion from this data is that the 1-2 mixture has not decohered, and that the coherence is suppressing and collisional frequency shifts.

In order to verify that this coherence is not due to the particular magnetic field value utilized, the experiment was repeated at several different magnetic field values. Figure 3.44 shows spectra taken at 552 G. The \odot data is the spectrum of a pure 2 state, while the \blacksquare is the 1-2 mixture spectrum. Again there is no observation of any shift to the $2 \rightarrow 3$ transition due to the presence of the mixture.

To observe the coherence time, we significantly increased the hold time between the time when the mixture was initially formed, and the time the $2 \rightarrow 3$ transition was made.

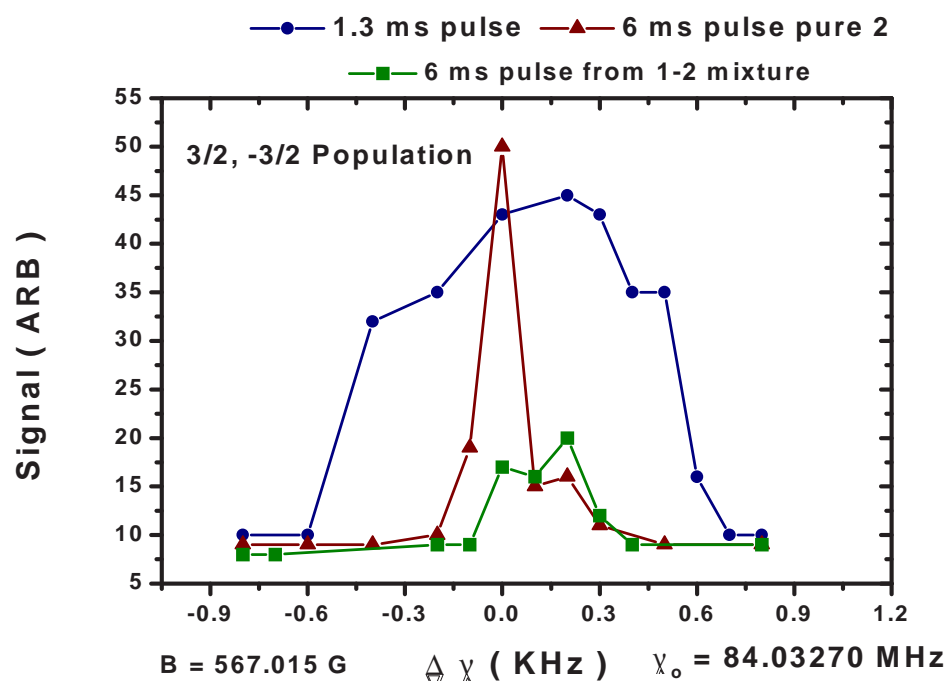


Figure 3.43 RF spectrum at 567 G, showing three different plots: the ● and ▲ show spectroscopy of the pure 2 state with different microwave pulse widths, and the ■ shows a spectrum of the spin mixture.

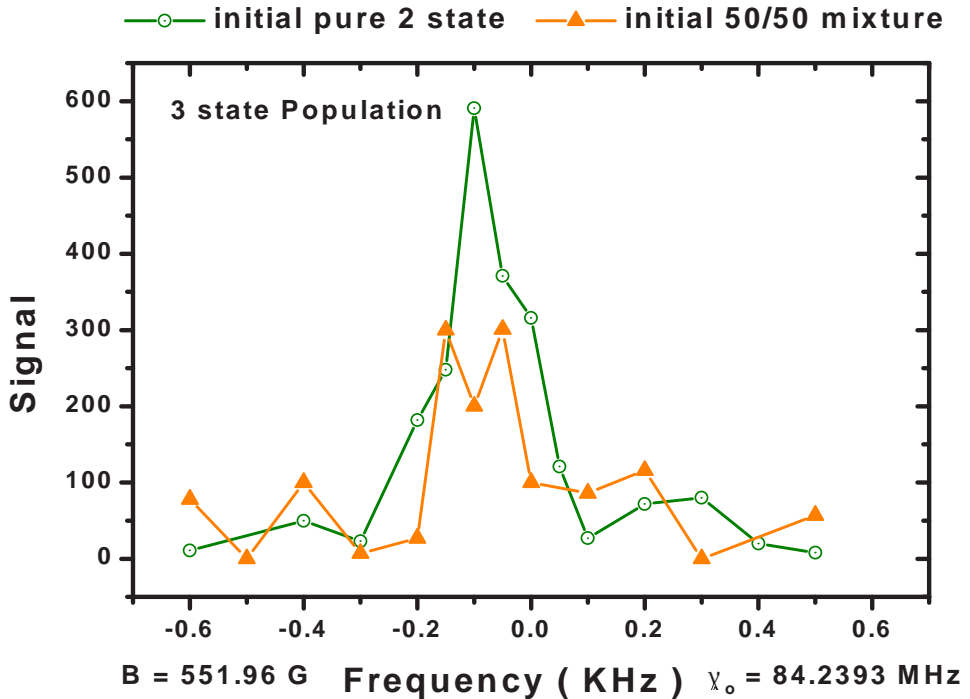


Figure 3.44 RF spectrum at 551 G, showing two different plots. The \odot shows the pure 2 state spectrum, while the \blacktriangle shows the 1-2 mixture spectrum.

Figure 3.45 shows these results, where the \odot is the control (the pure 2 state), while the \square is the spectrum of the mixture. Again, we observe no shift in the spectrum. In fact, the width of the spectrum is less than 200 Hz and the expected shift, from Equ. 3.21, is over 500 Hz. In addition, we expect collisional broadening from the 1-2 elastic interactions [66] which was not observed in the data.

As a final probe of the coherence, we added a magnetic field inhomogeneity by shorting one of the external bias coils, producing an approximately 3 mG/mm gradient across the cloud. In this instance, after a 1 s hold time, no transfer from the 2 to 3 state was observed. It has been suggested that the reason for the lack of transfer is that the 1-2 collisions have broadened out the 2 state's energy by several KHz. The 200 Hz broad probe would transfer too few atoms from the 2 to 3 state to detect. This postulation is supported by the finding in Gupta *et al.* [66] where these same

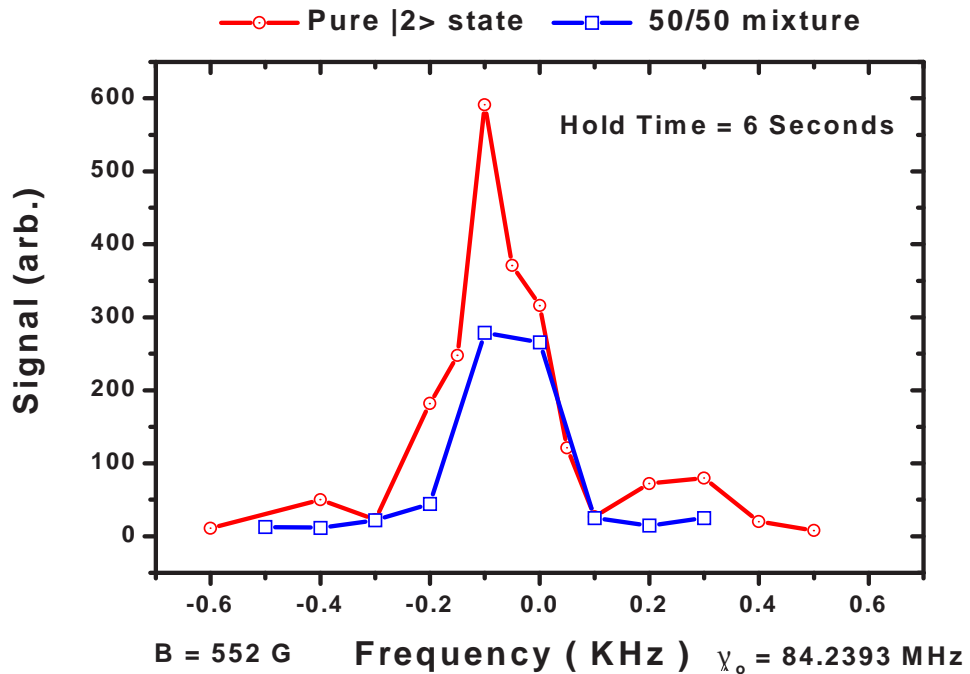


Figure 3.45 RF spectrum at 552 G after a 6 s hold. The hold time was increased to let the spin mixture decohere. The \odot shows the pure 2 state spectrum, while the \square shows the 1-2 mixture spectrum.

types of experiments were performed. They observed coherence times of 20 ms and a collisional broadening of over 20 KHz. In these experiments they reported a density of $3 \cdot 10^{13} \text{ cm}^{-3}$ and used microwave pulses on the order of $140 \mu\text{s}$, giving a transit time broadening of $\sim 600 \text{ Hz}$. Thus, we conclude that spectroscopy on the incoherent mixture with a shorter pulse is needed to determine the effects of the collisional broadening.

3.3.4 ${}^6\text{Li}$ Feshbach Resonance

In order to explore Feshbach resonances between the different spin states in ${}^6\text{Li}$ we must make the spin mixture discussed in section 3.3.3 decohere. We will discuss how to make an incoherent spin mixture. Then we will examine the experiment performed to locate the narrow ${}^6\text{Li}$ Feshbach resonance between the $F = 1/2, m_F = 1/2$ state

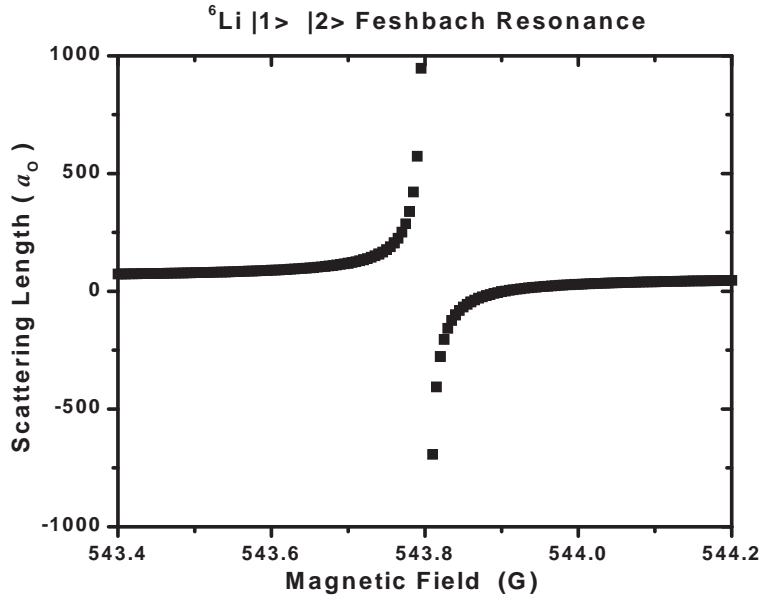


Figure 3.46 Coupled channel calculation of the the small ^6Li Feshbach resonance. The peak is seen near 543.8 G with a width of around 0.1 G.

and the $F = 1/2$, $m_F = -1/2$ state, seen in Fig. 3.31.

To decohere the spin mixture we must introduce some type of noise into the microwave transfer that is non-reversible. This is done by shorting one of the external bias coils (section 2.1), which provides a small, ~ 3 mG/mm, magnetic field gradient across the atoms. As the microwave transfer occurs, atoms on opposite ends of the trap experience different Rabi frequencies. Since the atoms are constantly moving in the trapping potential, any subsequent microwave pulse will be unable to reverse the effects of the first microwave pulse. This process initially forms a coherent spin mixture, however, as the spins evolve they decohere. With this technique we observe decoherence on the ~ 25 ms time scale.

To study the narrow ^6Li Feshbach resonance, we must first determine the magnetic field at which the resonance occurs. Figure 3.46 shows a blowup of the region around the small Feshbach resonance from Fig. 3.31. As with the ^7Li Feshbach resonance, we search for the ^6Li resonance by examining the lifetime of the spin mixture as a function

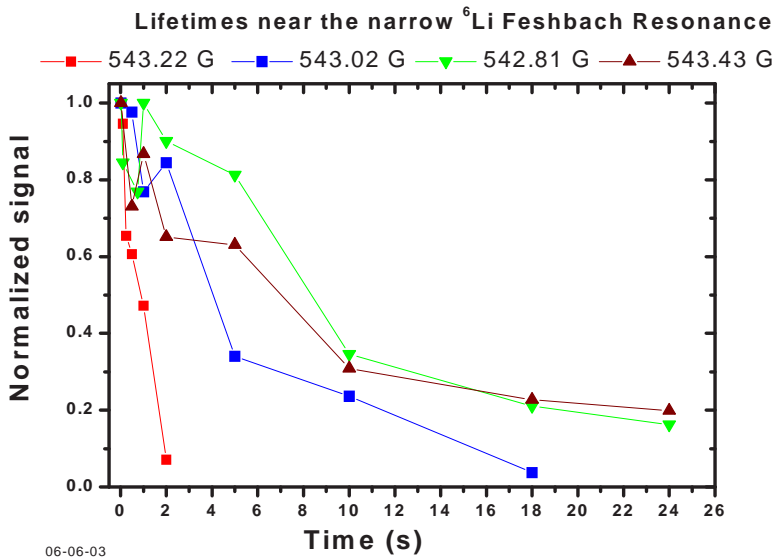


Figure 3.47 Plot of the fractional signal as a function of time for several magnetic field values near the small ${}^6\text{Li}$ Feshbach resonance.

of magnetic field. Figure 3.47 shows several sample lifetimes at magnetic field values near the ${}^6\text{Li}$ resonance. Re-casting the lifetime data as a loss rate, we can plot the loss rate versus magnetic field, which is shown in Fig. 3.48. From Fig. 3.48, we can identify the resonance by the peak in the rate. The loss rate is not well understood. In the case of the bosons, the loss is attributed to 3-body recombination to a bound molecular dimer. However, for fermions, 3-body recombination is suppressed by symmetry: in a two species spin mixture, two of the three colliding atoms are identical, which is suppressed for s-wave collisions. The primary theory is that the loss inducing collisions are still due to 3-body recombination, however, they are between a free atom and a bound molecule. From this interpretation, we infer that the observed asymmetry in Fig. 3.48 is due to the lack of molecules on the high magnetic field side of the Feshbach resonance, and that the peak in the loss is not the center of the resonance, but is instead shifted slightly to the low magnetic field side.

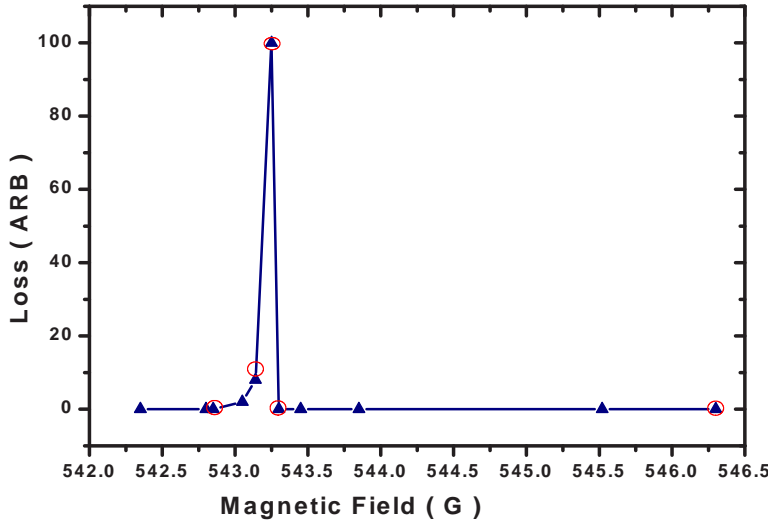


Figure 3.48 Loss rate verses magnetic field. As in the case of ${}^7\text{Li}$, we interpret the peak in the loss rate to be near the peak of the Feshbach resonance.

3.3.5 Formation of ${}^6\text{Li}_2$ Dimers

Now that we have determined the position of the Feshbach resonance, we can use it to vary both the strength and the sign of the interactions. Since the Feshbach resonance arises from the mixing between the atomic and molecular levels, we can utilize the resonance to convert cold atom pairs into bound variationally excited molecules.

Specifically, the Feshbach resonance couples the triplet $F = 1/2$, $m_F = 1/2$ $F = 1/2$, $m_F -1/2$ atom pair, to the $X^1\Sigma_g^+$ $v = 38$ state of ${}^6\text{Li}_2$. As brief explanation of the molecular notation: the first term is the (state designation) $^{2S+1}$. The X signifies the ground state and $2S+1 = 1$, since the total spin is zero. The second term is the projection of the electronic spin onto the axis defined by the two nuclei. The subscript indicates the parity of the wavefunction, and g equals even parity (“ g ” stands for “gerade” which is German for even [11]). The superscript is an indication of plane symmetry of the molecule about a plane bisecting the nuclei axis. Note, this superscript notation is only used for single diatomic molecules [67].

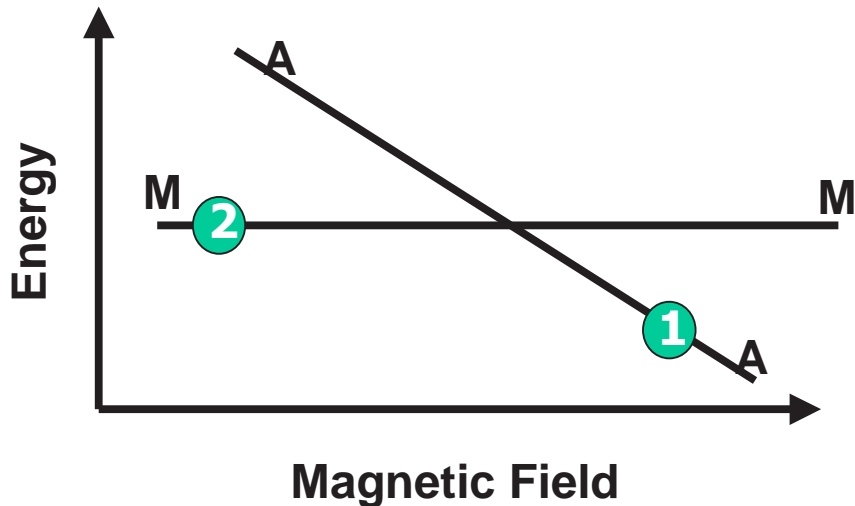


Figure 3.49 Illustration of the Landau-Zener model for the atom-molecule coupling from a Feshbach resonance. As the magnetic field increases, the atomic energies decrease and cross the least bound molecular level.

We begin by making an assumption of a two level system. One level consists of a free atom pair and the other consists of the bound molecule. The bound molecule is in a singlet state, so the energy is not shifted by the external magnetic field. The atoms are in a triplet state, and their energy decreases with increasing magnetic field. Figure 3.49 illustrates the atom-molecule crossing. Let us call the atoms state “A” and the molecules state “M”. At the energy crossing, the two states are coupled through the hyperfine interaction and the crossing of the two states becomes avoided. Figure 3.50 shows the avoided crossing picture. If we initially prepare the system in state A, then according to the Landau-Zener (LZ) model, the probability of not making a transition, that is, going from state A to A’ is given by $P_{AA'}$, where [68]

$$P_{AA'} = \exp\left(\frac{-2\pi |V|^2}{\hbar(\frac{\partial E}{\partial t})}\right) \quad (3.22)$$

where V is the coupling between states A and M, and $\frac{\partial E}{\partial t}$ is proportional to the magnetic field sweep rate. There are two limits to this equation, the first is if the quantity $|V|^2/\hbar$ is small compared to $\frac{\partial E}{\partial t}$, then $P_{AA'} \rightarrow 1$ and the transition is said to be diabatic. The second case is when $|V|^2/\hbar$ is large compared to $\frac{\partial E}{\partial t}$, then $P_{AA'} \rightarrow 0$.

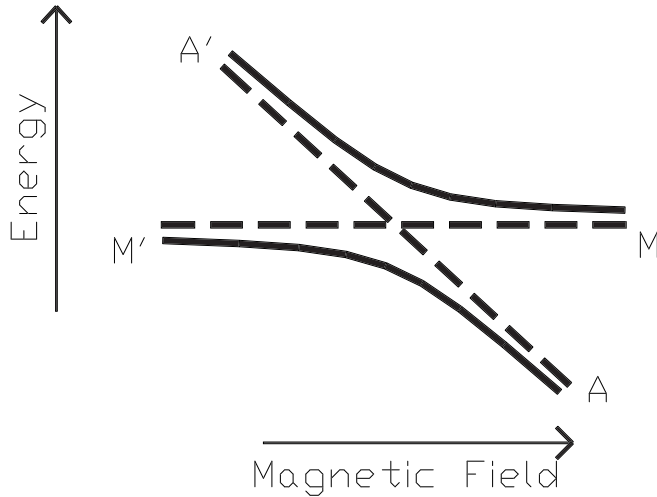


Figure 3.50 Illustration of an avoided crossing for the Landau-Zener model of the Feshbach resonance. The singlet-triplet coupling breaks the coupling at the crossing, making it an avoided crossing.

and the transition is adiabatic. In this latter case, as $P_{AA'} \rightarrow 0$ then $P_{AM'} \rightarrow 1$ and atoms in state A end up as molecules in state M'. In the adiabatic limit, if we start out with a sample of atoms (state A), and then ramp the magnetic field down through the Feshbach resonance, the atoms should be adiabatically transferred into molecules (state M') (Fig. 3.50).

The first experiment was to test the LZ model and to sweep the magnetic field through the Feshbach resonance at various approximately linear rates and look at the number of atoms remaining. We initially prepared our spin mixture at 549 G, approximately 6 G above the resonance. We then ramped the magnetic field down to around 350 G (nearly 200 G below the resonance), and then probed the remaining atoms. These results are shown in Fig. 3.51. Since the loss of atoms is due to $P_{AM'}$, we can rewrite Eq. 3.22 for $P_{AM'}$ in terms of the experimental variables

$$P_{AM'} = 1 - \exp(-2\alpha/\dot{B}), \quad (3.23)$$

where α is $\pi \cdot |V|^2 / \hbar$, and \dot{B} is the rate of change of the magnetic field. We can compare Eq. 3.23 to the results in Fig. 3.51. In Fig. 3.51 the horizontal axis is \dot{B}^{-1} .

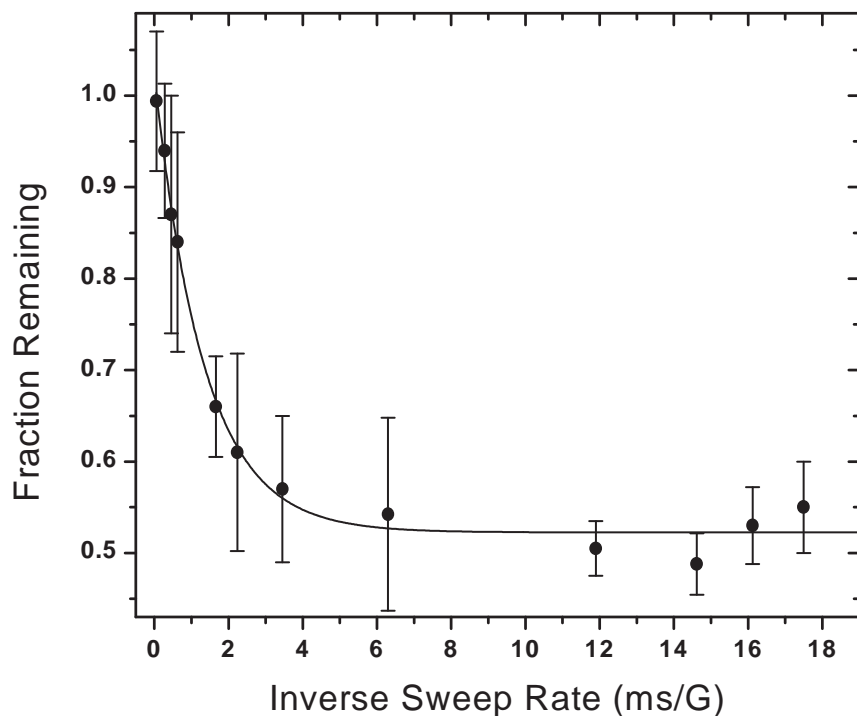


Figure 3.51 Atom loss as a function of sweep rate through the Feshbach resonance. For each sweep rate, we made between six and ten experimental runs. The error bars are the standard deviations of these measurements, and the solid line is an exponential decay fit to the data, giving a $1/e$ decay constant of 1.3 ms/G .

In this formulation the adiabatic criteria is that α must be large compared to \dot{B} , so as \dot{B} decreases (\dot{B}^{-1} increases) we go from diabatic to adiabatic. This is readily seen in Fig. 3.51, as our fastest ramp rate has no effect on the number of remaining atoms. This rate satisfies the diabatic condition and the atoms are transferred from state A to A'. In addition, for slower ramp rates we see up to 50% of the atoms lost from the sweep. While in the adiabatic limit we would expect $P_{AM'} \rightarrow 1$, we only observe a maximum conversion efficiency of 50% from sweeping sufficiently slowly through the resonance.

This observation is supported by a similar experiment at JILA done with ^{40}K [69]. The JILA group swept through a 9.7 G wide resonance located at 224 G and observed that for sufficiently slow ramp rates, they too achieved a maximal conversion efficiency of 50% [69].

The mechanism for the limiting conversion efficiency is still not understood and is a current matter of theoretical interest. Our current results support the idea that the conversion efficiency is somehow related to the nature of the Fermi gas.

In the second experiment we investigated the conversion efficiency of atoms to molecules for different final values of the magnetic field. Once again, we prepared the spin mixture at 549 G, and then ramped the magnetic field down to various ending field values between 546 G and 320 G. The large range of ending fields allows us to verify that the only magnetic field values which affect the atom signal are near the Feshbach resonance. In order to assure maximal conversion efficiency, we must keep our ramp rate sufficiently adiabatic. For all of the data presented below, the inverse ramp rate was greater than 12 G/ms.

The results of this experiment are shown in Fig. 3.52. We observe no loss of atoms for ending fields above the resonance and a 50% loss for all ending fields sufficiently below the resonance. The solid line in Fig. 3.52 is an empirical formula given by,

$$\frac{1}{2}[1 + 1/(1 + \exp((B_0 - B)/\Delta B))], \quad (3.24)$$

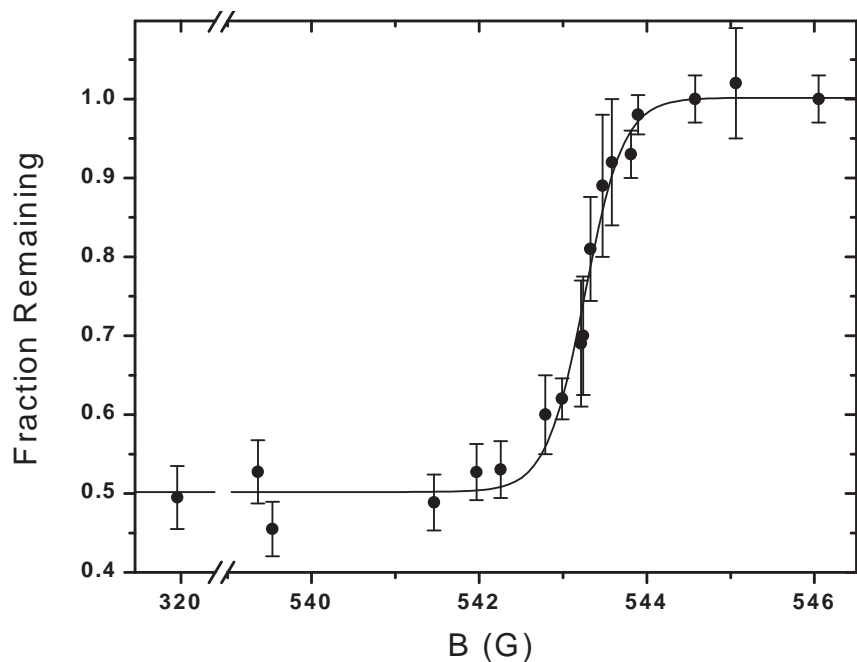


Figure 3.52 Atom loss as a function of ending magnetic field. For each sweep rate we made between 10 to 15 experimental runs. The error bars are the standard deviations of these measurements, and the solid line is a fit to an empirical equation given in the text.

where B_0 is the center of the resonance, and ΔB is the width. The resolution of our final ending field value was determined by measuring the voltage across the bias shunt (see section 2.2.3). This gives an uncertainty of 0.1 G in the ending magnetic field. The fit gives $B_0 = 543.26 \pm 0.1$ G, which is 0.6 G below the location of the Feshbach resonance predicted from the coupled channel calculation in Fig. 3.31. The width, ΔB , is found to be $\Delta B = 0.23$ G. From the coupled channel calculation, the resonance is expected to be approximately 0.1 G wide, which is over a factor of two narrower than the observed resonance. A portion of this discrepancy can be attributed to our 0.1 G resolution in the stopping field value. Also, whatever effects are limiting the conversion efficiency of atom pair to molecules may play a role in broadening out the observed resonance.

The last experiment was to look at the lifetime of the molecules by adiabatically reversing the ramp and converting the molecules back into atoms. The experiment was done in two separate fashions due to experimental details that will be explained below.

In the first experiments, the magnetic field down was ramped down to a set value past the resonance, as determined from Fig. 3.52, held for a set time, and then ramped back through the resonance. The atoms were then probed as usual. The experimental difficulty was that in order to ensure that the ramps were sufficiently adiabatic, the inverse sweep rate had to remain above 12 ms/G. Thus a 10 G sweep, down and back, from 549 G to 539 G, would take 240 ms. The time of interest is how long the molecules survive. The relevant experimental time is how long the field stays below the resonance. In this example, the relevant time is 96 ms ($((543-539) \times 12$ ms). Under these conditions, the minimum time that could be investigated was ~ 100 ms. To minimize this time, the inverse ramp rate was decreased to 7 ms/G and the final field was increased to 540 G. This gives a minimum probe time of 42 ms. In Fig. 3.53 we plot the fraction of atoms remaining as a function of time spent below

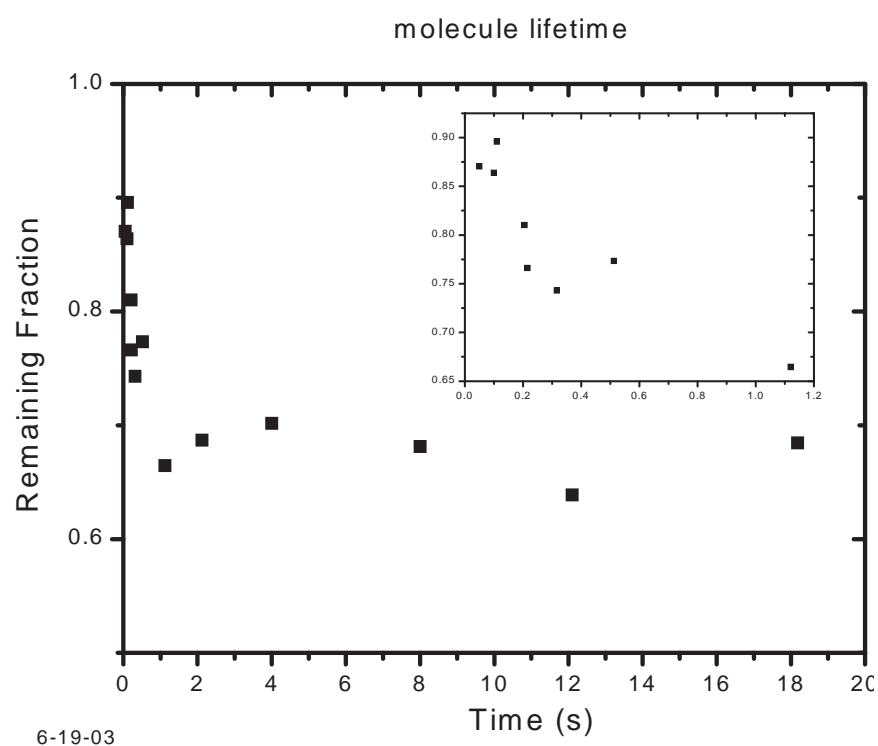


Figure 3.53 Number of atoms as a function of time spent with the magnetic field below the Feshbach resonance. The inset shows the early time behavior. We observed a rapid decay on the short time scale.

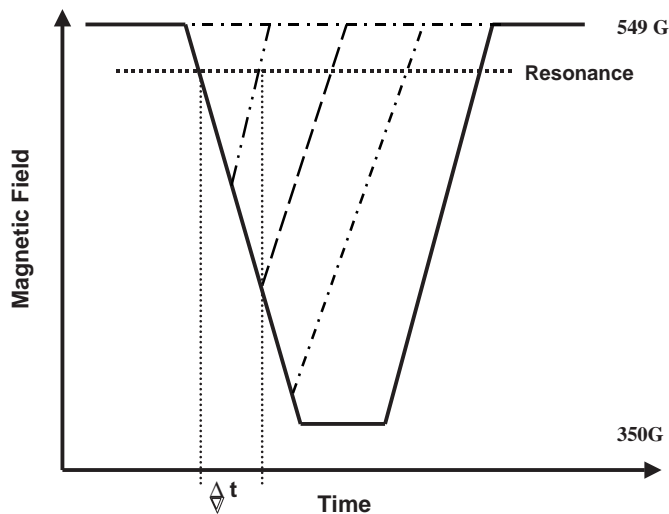


Figure 3.54 Schematic diagram of the timing involved in the ramp to measure the molecular lifetime. The dotted horizontal line shows the resonance. The relevant time for the molecule lifetime is the amount of time spent below the resonance, depicted as Δt .

the resonance. The fraction is given by the remaining number of atoms after ramping down and back up through the resonance as compared to a single ramp through the resonance. The non 50% conversion efficiency is attributed to a non 50/50 initial spin mixture. The early time behavior in Fig. 3.53 clearly shows a signature from the back conversion of molecules into atoms, decaying on the ~ 1 s time scale.

The second set of lifetimes were taken with a fast inverse sweep rate of 3.5 ms/G. The atom mixture was again prepared at 549 G and then ramped down to 369 G. To obtain early times, the ramp was reversed before it reached 369 G. Figure 3.54 shows a schematic for the magnetic field ramp. For short times, like $\Delta t = 40$ ms, the ramp is reversed at 538G. This is shown by the $- \cdots -$ line. For $\Delta t = 248$ ms, the final field is 508 G, which is depicted by the $- - -$ line, and so on. This method of ramping the magnetic field allows us the ability to both make short time measurements and to ensure the linearity of the ramp while the field is sweeping through the resonance. Figure 3.55 shows the results of measuring the molecular lifetime with this method. We observe a non-exponential initial shape to the lifetime, followed by an exponential

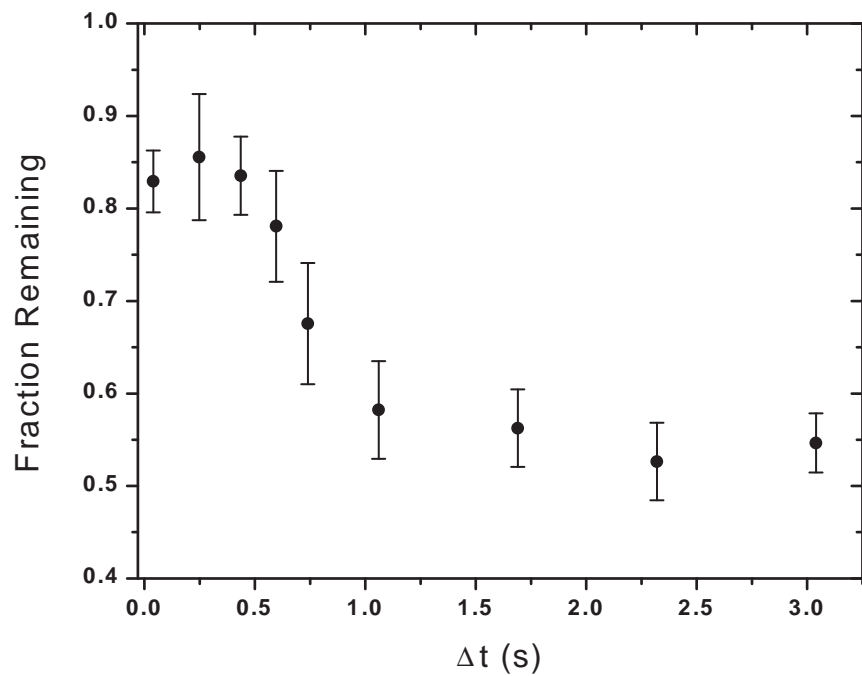


Figure 3.55 Molecular lifetime taken with the ramp as described in Fig. 3.54. Each data point is made up of an average 8 to 16 measurements. The error bars are the standard deviation of those measurements.

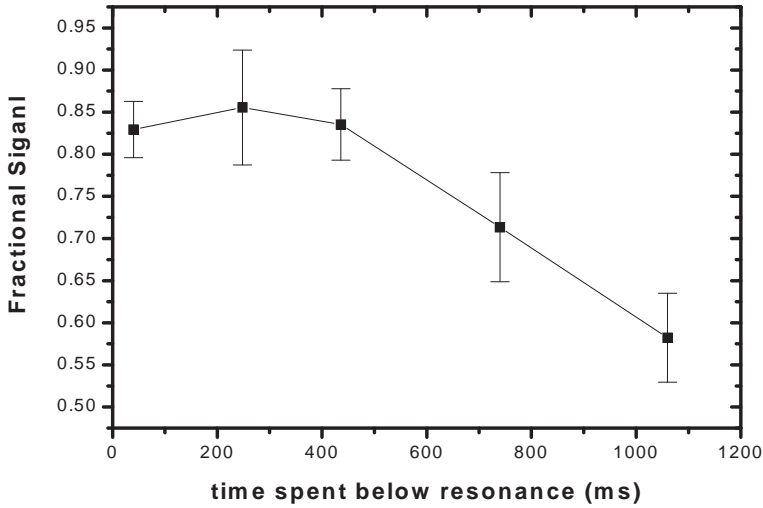


Figure 3.56 Molecular lifetime taken with the ramp as described in Fig. 3.54. Each data point is an average 10 measurements. The error bars are the standard deviation of those measurements.

tail. The molecules are observed to persist for over one second. Figure 3.56 shows another lifetime taken in a similar fashion to Fig. 3.55. The data here shows extreme non-exponential behavior for the lifetime.

The lifetime of these molecules is longer than expected. Since the molecules are in a vibrationally excited state, they are expected to rapidly vibrationally quench, as was seen with ^{87}Rb [70]. The quenching would lead to loss from the optical trap, since the energy difference between the $v = 38$ and the $v = 37$ levels is greater than 50 GHz [9].

Other notable observations are in the non-exponential decay of the molecules and the high back-conversion. In both our experiment and the first JILA experiment [69], the conversion efficiency to molecules is $\sim 50\%$, while the back-conversion, of molecules to atoms, is closer to 100% than to 50%. In our experiment, we see over 85% back conversion while the JILA group sees over 80% back-conversion [69]. This suggests that the explanation of the 50% conversion efficiency may rely on the properties of the Fermi gas. There can be only 1 fermionic atom pair per energy level in

the trap, this could cause the two level Landau-Zener picture break down resulting in the $\sim 50\%$ conversion efficiency. If this assumption is correct, the non-exponential decay of the molecules might be due to a convolution of an exponential decay of the molecules with increasing back-conversion efficiency due to the molecules attaining an equilibrium Bose-Einstein distribution, which allows for multiple molecules to occupy a given energy level.

3.3.6 Direct Detection of Molecules

Up to this point all detection of trapped molecules has been through back conversion of the molecules into atoms, and the standard detection of those atoms. We propose a method to phase contrast image the bare molecules, by driving a bound-bound molecular transition between the $X^1\Sigma_g^+ v'' = 38$ and a bound vibrational level of the electronically excited singlet potential. The transition is not a cycling transition, thus we only expect to be able to scatter 1 photon per molecule. We will employ phase contrast imaging, because it is more sensitive than absorption imaging.

There are two suggested experiments. The first experiment is to repeat the molecular production described in section 3.3.5, but instead of reversing the magnetic field ramp to detect the molecules, perform direct optical detection of the molecules. This could shed light on the non-exponential nature of the molecular lifetime and further serve to uncover the origins of the 50% conversion efficiency. The second experiment is to image the bare molecules inside of the large Feshbach resonance and to look for Bose condensation of the molecules. Both of these experiments are currently underway.

Chapter 4

Conclusion

Our main engineering goal was to build an apparatus that would allow experimenters to explore the fundamental quantum nature of bosons, fermions, or Bose-Fermi mixtures. However, unlike many of the original BEC apparatuses, we did not want to limit the spin states that could be explored. Therefore, we added an optical trap to confine any spin state, or mixture of spin states desired. In addition, we wanted the apparatus to be able to explore a large range, 0 G to 1000 G, of externally applied magnetic bias fields.

As the results of Chapter 3 suggest, we have accomplished these engineering goals. We have been able to cool a Bose gas to quantum degeneracy, change internal spin states, make a large BEC, and even form solitons by manipulating external magnetic fields in order to precisely tune the atomic scattering length. By adding fermions to the apparatus, we were able to make the first ever quantum degenerate Bose-Fermi mixture, and demonstrated their distinct quantum nature. We transferred the fermions to an optical trap where we studied a spin mixture of two internal states, and used microwave spectroscopy to investigate the coherence of the spin mixture. Finally, by using time-varying magnetic fields, we have produced samples of ${}^6\text{Li}$ dimers with extraordinary long lifetimes.

The remainder of this chapter will focus on portions of the apparatus that have been problematic. Specifically, we will discuss some of the commonly encountered problems and offer solutions in an attempt to make the apparatus more robust, and help to troubleshoot it when it is not functioning properly.

4.1 Trouble Shooting

One of the largest time sinks for this apparatus is troubleshooting why the evaporative cooling is not working. Evaporation can fail for many reasons: poor background lifetime due to high background gas pressure, poor optical pumping, poor transfer efficiency, too few atoms in the MOT, to name a few. The reason that troubleshooting the evaporation is so cumbersome is that there are very few diagnostics. Diagnostics that would be useful in troubleshooting include measurements of atom number and temperature at various points along the experimental cycle. Currently the only diagnostics the apparatus can perform include measuring the background lifetime and the spin purity of the gas. There is some ability to extract relative atom number from non-evaporatively cooled clouds, but it is not quantitative. To troubleshoot the apparatus, one would like to know the number and temperature of the atoms at several stages: in the MOT, just after the compression stage in the MOT, upon transfer to the magnetic trap, and after evaporation to a temperature of approximately $2 - 3 \mu\text{K}$. The final measurement (after evaporation) is currently the only measurement we can make quantitatively. For the other measurements, the size of the atom cloud is too large to image using our standard imaging system, which has a minimum magnification of 5.6. To make these other diagnostic measurements, an imaging system is needed that can image a magnetically trapped atom cloud 1.5 cm in length, which for a typical CCD with 512×512 pixels and $13 \mu\text{m}/\text{pixel}$, the required magnification is 0.44, over a factor of ten less than the current minimum magnification.

One proposed solution is to remount the gimbal mirror reflecting the green beams into the chamber (see section 2.3.2) with a 2 inch dichroic beamsplitter that reflects 532 nm and transmits 670 nm. A second CCD camera, with a commercially available lens, could be mounted to look down at the center of the chamber through the beamsplitter. This setup would be ideal for fluorescence imaging of the MOT and the magnetic trap. However, since the fluorescence imaging is accomplished by pulsing on

the MOT light, this will not give a quantitative result for diagnosing the compression and cooling stage, since the laser frequency is being swept as part of the compression and cooling stage.

A possible solution to get more quantitative images during the compression and cooling stage is to perform absorbtion imaging. To implement absorption imaging for the MOT, the absorption beam would have to be on the order of the size of the a MOT beam. The beam could be formed by adding a third optical fiber and second AO to the probe set up. The new fiber would then be collimated to a $\frac{1}{e^2}$ beam waist of 1 cm, using ~ 5 mW of optical power. With this setup, and by adjusting the new probe AO frequency, all the diagnostics mentioned above could be quantitatively performed, and would yield benchmarks for each step of the apparatus. With these benchmarks, the complexity of troubleshooting the apparatus could be greatly simplified, thus reducing the amount of time and effort needed to obtain peak performance from the apparatus.

4.2 Improvements

Although the construction of the experiment is finally complete, there are still a few improvements that could be made. The most important improvement to the apparatus would be to fix the vacuum window across from the re-entrant imaging window. This particular view-port has a defect in the AR coating which lenses and distorts the probing beam. As a result, there is structure on the imaging beam which can harm the image quality. There is one other view-port with the same defect, which is located on one of the radial MOT beams. It is unknown what effect this defect on the MOT beam has on the performance of the apparatus, but it would be best to simply replace the window. The final suggestion on the vacuum windows is that they all be replaced with windows that have AR coatings at all three wavelengths used in the experiment, 532 nm, 670 nm, and 1064-1080 nm.

Another improvement would be to remove the skimmer assembly. If the skimmer were removed, it would free up a view-port with optical access into the center of the chamber. Removing the skimmer would also enable a turbo-molecular pump and a rough-pump to be removed from the table that could be causing vibrations. In addition, with the skimmer gone, there would be more room on the apparatus table for aligning optics.

The final major improvement to the apparatus would be to have an in-vacuum microwave antenna. The reason for the new antenna would be to increase the coupling of the microwaves to the atoms. The current setup requires a 10 W amplifier with a 3 dB attenuator, providing 5 W to the antenna, just to perform the evaporation. In addition, when the optimized evaporation trajectories are shorter than 35 s, the evaporation seems to fail because of lack of microwave power, and not a lack of atoms. Significantly improving the antenna would allow us to evaporate faster, to transit time broaden the RF transitions making them easier to find, and would reduce the amount of RF broadcast into the laboratory.

The reason that these improvements have not already been undertaken is that they all require the apparatus to be brought up to atmosphere. While pumping out the chamber and baking it is only a two week process, in order to bake the apparatus, the MOT optics and the EMTRAP coils must be removed. Removing the coils requires removing the optical trap. Hence all three atom traps would have to be removed and reassembled after the bake, and this last step can be time consuming.

Chapter 5

Appendix

5.1 EMRTAP Control

In this appendix we will go over the EMTRAP1.c source code used to generate the experimental sequences from the EMACK command prompt. In particular, we will look at how to use the code to control the experiment. As it turns out, the source code itself is over 26 pages long, so we will not go through it line by line, but we will discuss the main areas important to both operating and understanding the code.

The timing card used is a LabPac multi-function card, by Scientific Solutions. It has 24 D/A TTL outputs, two A/D analog outputs, and two A/D analog inputs. The card contains 5 timers, whose values are given in the table below.

Timer	Speed
11	1 MHz
12	100 KHz
13	10 KHz
12	1 KHz
15	100 Hz

The timers are called by the TIST labpac command. Another important command is DORAW, or digital output write. This is the command that updates the DTOD TTL lines. The way in which the code works is that the TTL lines are updated by passing the variables TTLVAL0, TTLVAL1, and TTLVAL2 to the card through the DORAW command. Each variable stands for a binary address on either TTL banks 0, 1, or 2, respectively. As the code progresses, TTLs are taken either high or low depending on the experimental needs. To control the evaporation synthesizer(s) we simply send a string to the appropriate GPIB address, and issue the device standard GPIB/HPIB commands.

Figure 5.1 gives the layout for all the DTOD TTLs and their respective channels. In order to program channel 0 with the magnetic trap off, the MOT magnetic

Channel/ TTL	1	2	4	8	16	32	64	128
0	Trap on/off	7Li sw. AO	MOT on/ff	6Li 3/2 shutter	7Li Beam Dump	CCD	7Li EO RF SW	7Li EO step attn
1	High Field ramp up	RA	Zeeman shutters	7Li EO OD	Optical pump AO	7Li MOT Shutter	6Li CMOT	7Li EO Freq
2	Evap μ - waves	Optical trap On/off	High field On/off	Hv transf arb	6Li $\frac{1}{2}$ Shutter	High Field Ramp down	6Li SW AO	High Field Vset sdw cage

Figure 5.1 Map of the TTL values to their experimental actions. For example, channel 0 TTL 1 turns the magnetic trap on and off, while channel 2 TTL 64 switches the ^6Li MOT AO on and off.

field on, the ^7Li AO switch on, the beam dump open, and the others all low, we need channels 0 TTLs 2, 4, 16 high and 1, 8, 32, 64, 128 low. The code would go as follows;

1. `ttlval0 = 2+4+16;`
2. `labpac(DORAW,0,255-ttlval0);`

The TTLVAL0 variable is assigned the numeric value for all s TTLs going high, and when that number is passed through the DORAW command to channel 0, and the TTLs follow.

Now if we want to turn on the optical pump for 200 μs and then turn it off again, we must take TTL channel 1 TTL 16 high, wait 200 cycles of counter 11 then take it low. The code goes as follows;

1. `ttlval += 16;`
2. `labpac(DORAW,1,255-ttlval1);`

3. labpac(TIST,4,11,0);
4. labpac(TISTAT,4,200);
5. ttlval -= 16;
6. labpac(DORAW,1,255-ttlval1);

This sequence takes TTL channel 1 TTL 16 high, then calls timer 11 with the TIST command, then the TISTAT command waits for 200 cycles of timer 11, then the TTL is taken low again.

This last sequence is used throughout the EMTRAP code to control all the pulse sequences. There are two things to note: first is that the timer can only count to 64000, so if we wanted to wait 200 ms instead of 200 μ s, we would have to change from counter 11 to counter 12. The second is that the TISTAT command has a delay on the order of 10 μ s. This time is random about 10 μ s with a 4 μ s window. The delay is due to the multi-function card interfacing with the software. To skirt this issue, anything that requires pulses on the scale of 100 μ s or less is performed with external pulse delay circuits.

The final portion of the code that should be discussed is communicating with the synthesizers via the GPIB. If we want to update the frequency and amplitude of the synthesizer we would send it the following commands;

1. sprintf(strg,"FREQ:CW %.5lf MHz",850MHz);
2. send(SYNTHADDRESS,strg,&stat_f);
3. sprintf(strg,"POW:AMPL %.1lf DBM",powA);
4. send(SYNTHADDRESS,strg,&stat\$_ \$f);

Here line 1 constructs a string with the GPIB command FREQ:CW, to set the CW frequency with a frequency of 850 MHz. Then sprintf writes the command to the

GPIB device with the address SYNTHADDRESS. A similar task is done to set the amplitude in lines 3 and 4. These commands are used for the computer controlled evaporation and microwave transfers. For the dual evaporation scheme, a second synthesizer is added on a new GPIB address. The program can communicate with it in the same method as shown above. However the GPIB takes an average of 200 ms to communicate between the control program and the synthesizer. To minimize the talk time, we communicate with one synthesizer as described above and use an external application to program a “list sweep” into an Agilent ESG E4400 signal generator. The list sweep is a list of frequencies and amplitudes. Each point in the sweep is triggered using the GPIB bus, however, since no real information is sent to the signal generator, the GPIB responds in under 10 ms. To summarize, the dual evaporation is carried out by sending individual frequencies across the GPIB to the primary synthesizer. Each time a new frequency is sent, the GPIB triggers a pre-programmed list sweep on the secondary signal generator, causing the two generators to sweep together in time with a accuracy of approximately 10 ms.

The external application for programming the signal generator is called SYNTH.EXE. It is a DOS-based program compiled with MS Quick C. It can be compiled using MS Visual C/C++, however, EMACK is currently run under a DOS environment and it is useful to keep all the programs in the same environment. The source code and the program are located on atomcool lab drive /acq/emack/agilent/... The program takes an evaporation trajectory for ^7Li , stored in the file *evapdat.dat*, along with a command line input of the trap bottom in MHz and the final frequency in MHz. The programs then sends the information to the signal generator.

Once the .c file for EMACK has been altered, the current file must be named *emtrap1.c*. The code is then complied using Microsoft Quick C, at the command prompt (DOS). The file is compiled by recompiling the entire *EMACK.EXE* program using a “make” file. The make file is executed by typing c:\ *make emack.mak* at the

DOS prompt. To run *EMACK.EXE* that file is copied to the C:\BIN directory, and the operator can go to the current directory on the atomcool data drive and run EMACK.EXE by simply typing: emack. Now all the modifications made to the *emtrap1.c* file are incorporated into the EMACK program.

A diagnostic program has been complied that only performs fluorescence imaging called *EMACKFR.EXE*. It can be run instead of EMACK when the MOT to magnetic trap transfer needs to be measured, or when a lifetime of the magnetic trap needs to be taken. All the files and source code are stored in /lab/source/acq/emack/.

Vacuum Chamber and Coils

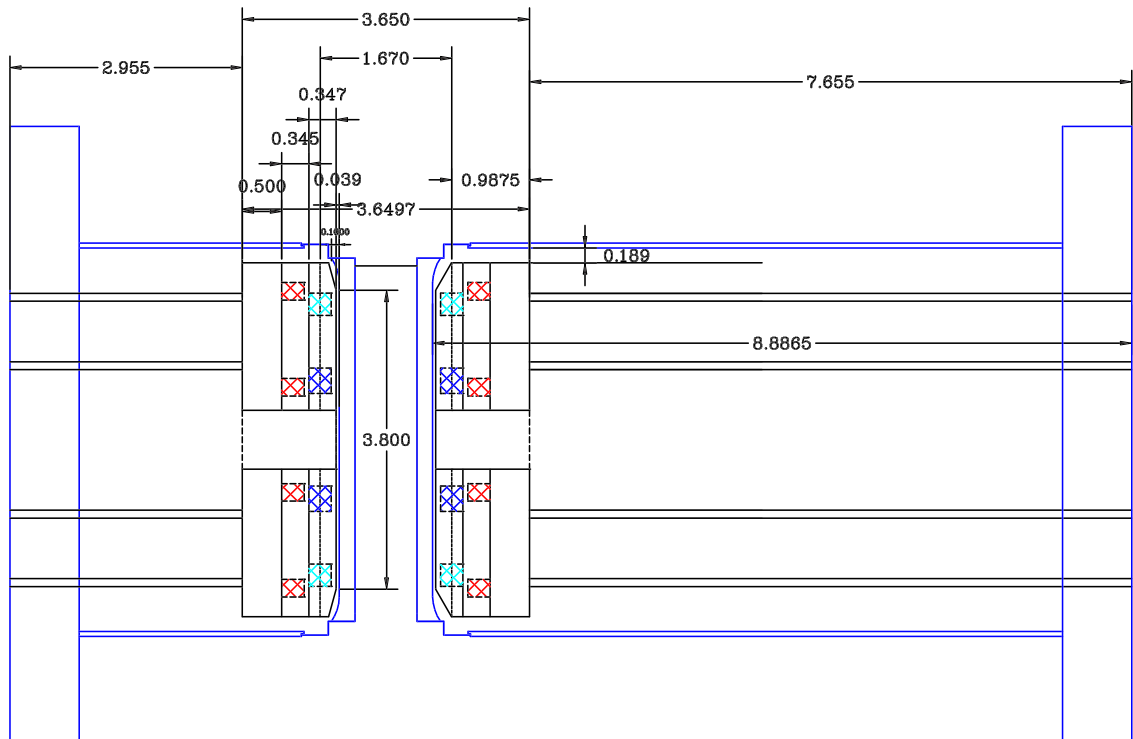


Figure 5.2 A view of the re-entrant coil design. With the orientation of the chamber in the laser lab, the “short side” faces the laser table. All dimensions are in inches.

5.2 EMTRAP coil design

In this section we will document the design of the current EMTRAP coils. They have been designed based on the coils described in [15]. The concept, modifications and general design criteria are explained in [15] and discussed in section 2.2.1 of this thesis. Here we will present the machine drawings of each component of the EMTRAP and its use.

Figure 5.2 shows a cross-sectional view of the re-entrant portion of the chamber with the coils in place. The re-entrant windows are the same un-coated windows as described in [15], made by Larson Electronic Glass.

After the glass window, the first part of the coil we encounter is the bias curvature

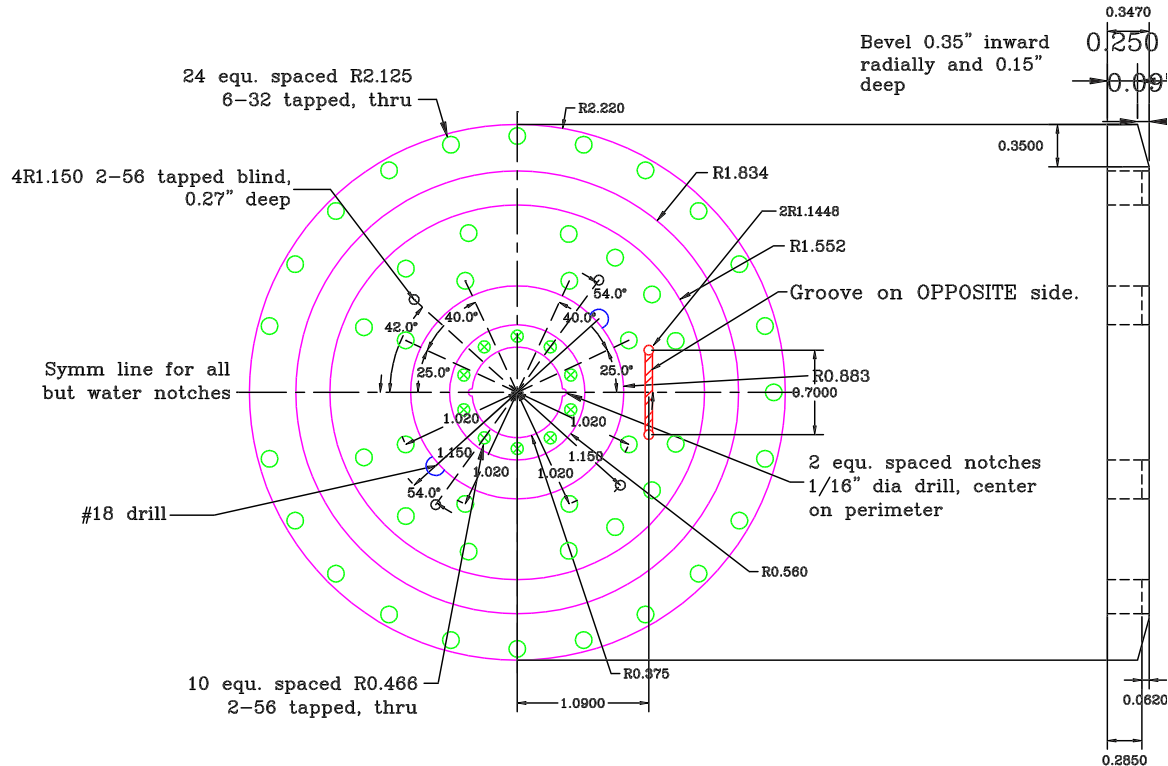


Figure 5.3 Top and side view of the bias-curvature coil set. All dimensions are in inches.

set, shown in Fig. 5.3. The important part of the bias-curvature set is the beveled edge on the front face. This is due to a ridge in the re-entrant window where the glass-to-metal seal is formed, see Fig. 5.2. The 2 equally spaced notches on the center perimeter along with the groove are no longer needed. They were originally used for a microwave antenna that never actually worked.

The next layer of coils is the quadrupole coils, or quads, shown in Figure 5.4. Few modifications have been made to the quad layer. The tracks have been made wider, and deeper (see Fig. 5.4).

The final layer of the coils is the lid, shown in Fig. 5.5. The only major modification to the lid is that more screw holes have been added to allow for better compression of the gaskets, to stop water leaks. An important note is that the R1.600 hole and

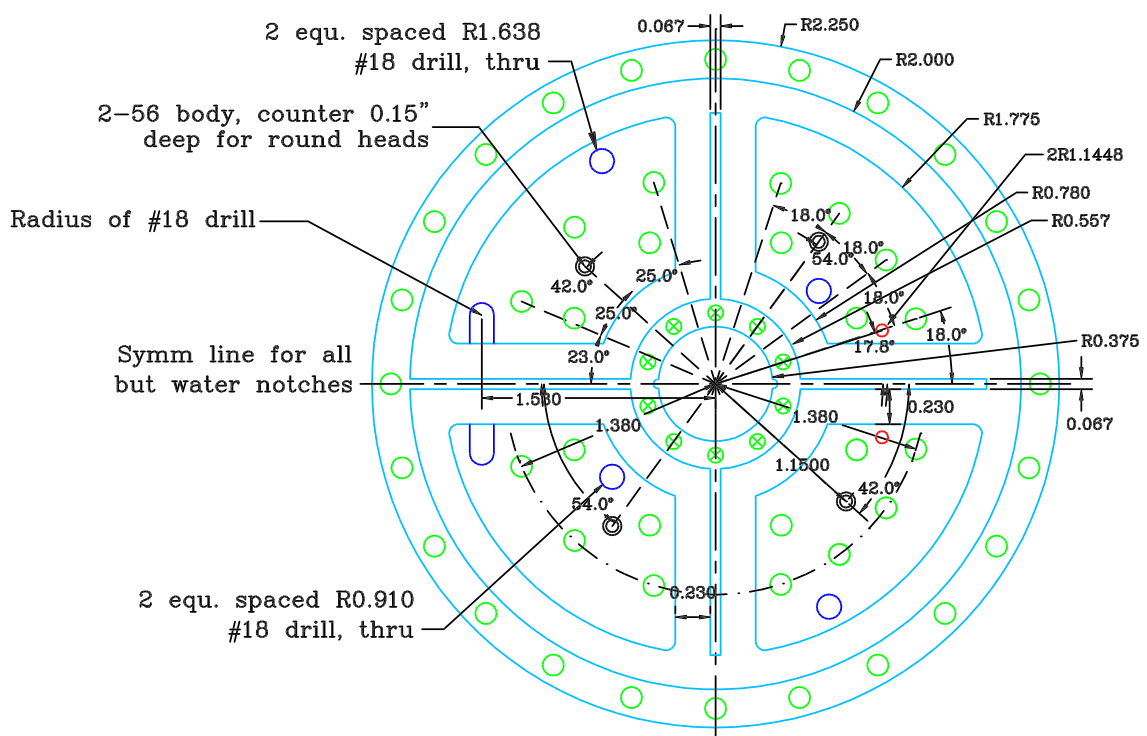


Figure 5.4 Top view of the quadrupole layer. All dimensions are in inches.

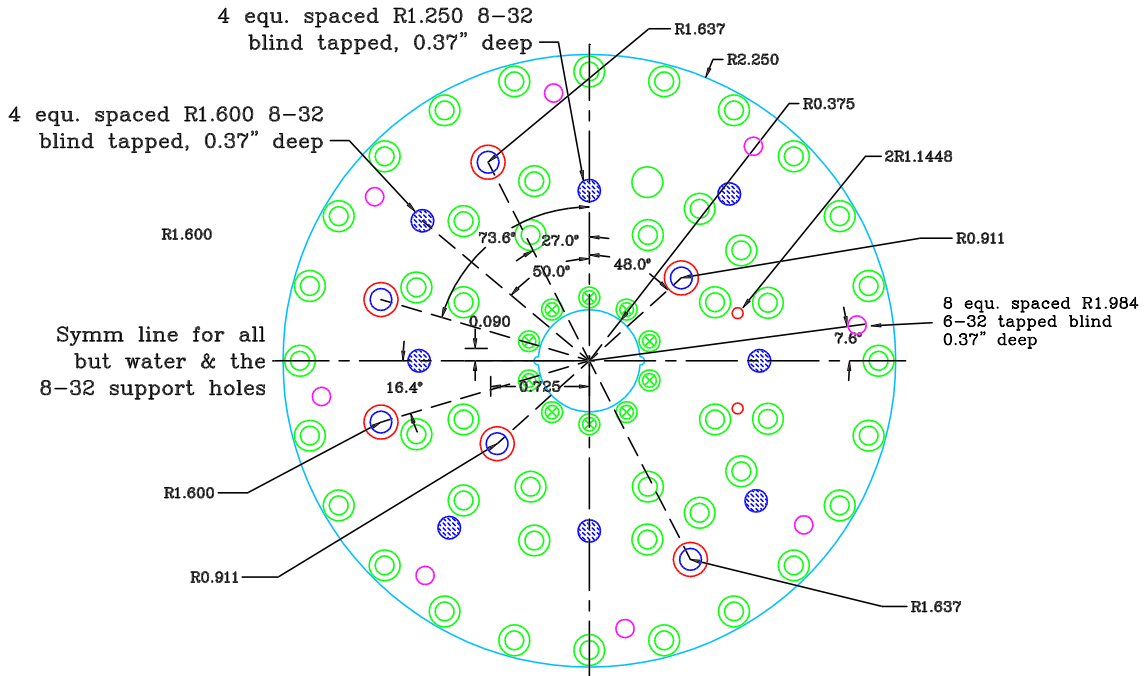


Figure 5.5 Top view of the lid for the EMTRAP coils. All dimensions are in inches.

its mirror image about the water symmetry line are quite close. While this caused no problems in the construction of the EMTRAP coil set, a duplicate set for the new EMT2 experiment was made and the thin wall between these two holes cracked, causing water to leak from the coil forms.

Figure 5.6 shows a semi-transparent view of the assembled coils. This gives an idea of the orientation and available space on the coil form. Figure 5.7 shows the steel plates for attaching the coils to the chamber. The steel plate bolts onto the flange of the re-entrant window, via a bolt circle custom-designed into the flange.

To attach the coil forms to the steel plate, there are four hybrid stainless steel/titanium rods, shown in Fig. 5.8. The reason for the hybrid stainless/titanium rods was partly for their strength and rigidity, but also an attempt to match the thermal expansion of the chamber and coils. Since the chamber is asymmetric, if the chamber expands from a change in the temperature of the lab the coils could move relative to

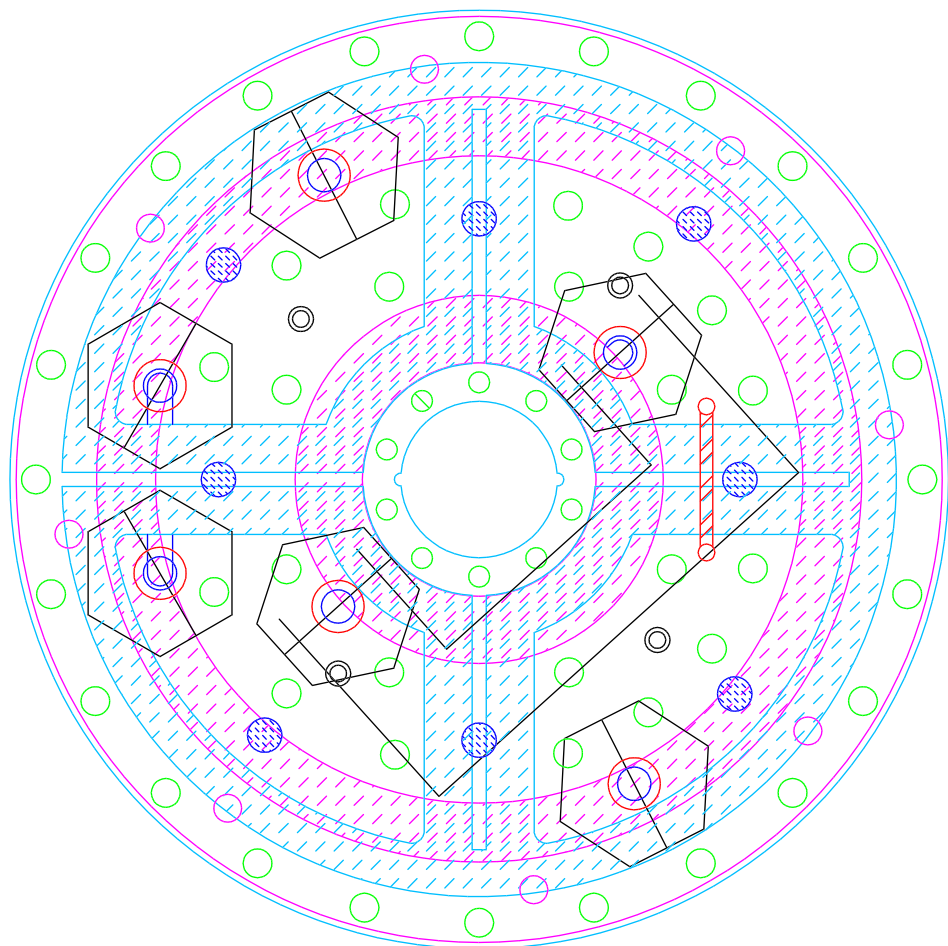


Figure 5.6 Shows a top view of the assembled coils with the Swagelok water connectors in place.

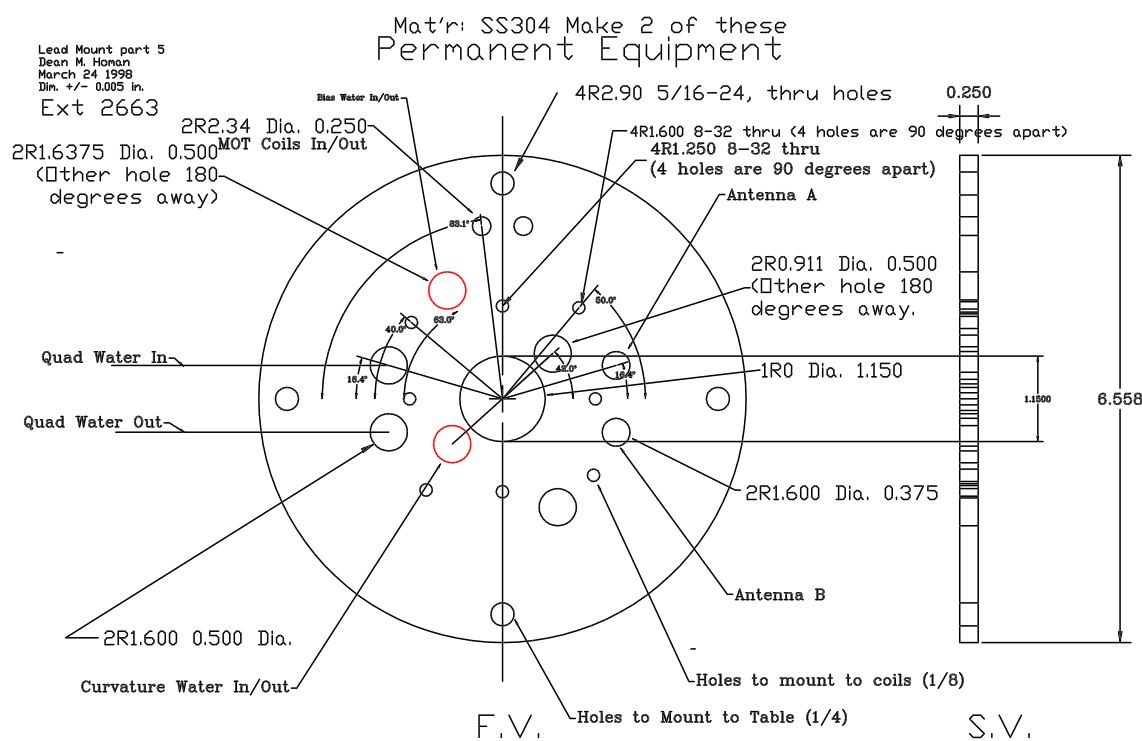


Figure 5.7 The coil holder plate. This plate bolts to the re-entrant window flange and supports the coils. All dimensions are in inches.

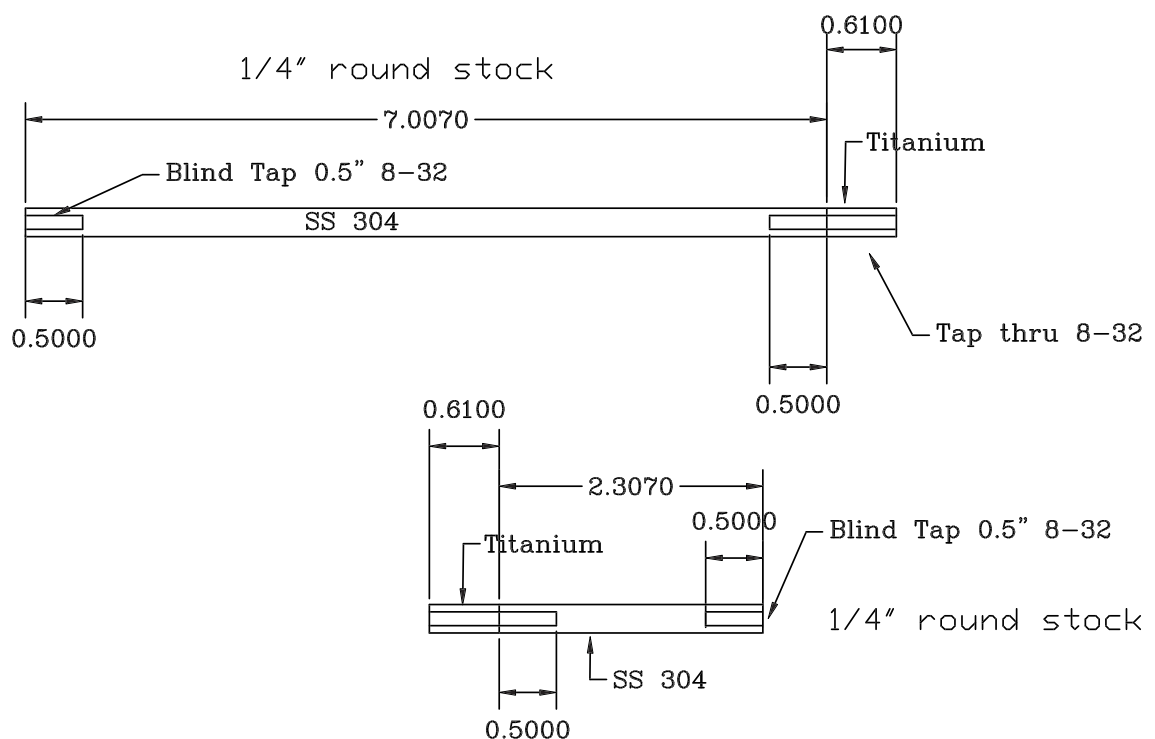


Figure 5.8 CAD drawing of the stainless steel/titanium standoffs that attach the coil forms to the steel holding plate. All dimensions are in inches.

each other changing the magnetic trap potential and the flatness of our bias magnetic field. The standoffs were constructed to expand and counter the motion of the chamber, keeping the coils a fixed distance apart.

In this new coil design, with the bias/curvature coils closer than the quads, we have observed a double well forms in the magnetic trap potential when the bias/curvature current is within 50% of the quadrupole current. This limits the maximum axial frequency to ~ 80 Hz. We have not explored this effect fully, rather we have just reduced the operating current of the bias/curvature coils in the magnetic trap configuration.

Further, about two years after these coils first went into operation, one of the coils burned out. Upon inspection of the coil, the failure was due to erosion of a wire in the quadrupole coil. Some type of reaction had occurred between the chilled water and the copper wire. Several places on the coils showed signs of fatigue from this process.

Upon replacing the coil, the side of the coils which the current leads of the bias/curvature coils were on was switched. It was observed that the magnetic trap bias field was reduced ~ 0.25 G, and that the high field bias magnetic field slightly inhomogeneous. It is unclear if this is due to the swapping of the bias/curvature leads, the uniformity of the bias coil wrappings, or subtle change in the position of the coils after being removed and remounted.

All the machine drawings are stored electronically on atomcool on the lab drive /lab/cadd/emtrap/... The particular file used for the construction of the current EM-TRAP coil set is /lab/cadd/ben-coils/new-ben-everything-v1.dwg. The file contains all the CAD drawings necessary to construct a set of these coils.

5.3 Image Analysis

In this section we are going to look at the imaging analysis program written to fit both classical and quantum degenerate Bose or Fermi distributions. The programs are written in MATLAB due to its ease in manipulating large matrixes, like our data. In addition, MATLAB can be programmed to have a complete graphical interface. There are four separate programs, PCBOSE.M, PCFERMI.M, ABOSE.M, and AFERMI.M that are used. The programs are for Bose or Fermi distributions and either phase contrast imaging or absorption imaging. The programs are very similar, and only exist as four separate files due to the simultaneous evolution of the experiment and the code. As with most of the code we use, it is long, nearly 23 pages. The source code is available in /lab/source/acq/emtrap/imaging... The goal of this section is to provide an overview of how these programs work. We will provide a description of the task to be accomplished and follow the description with the relevant excerpts from the source code.

The section below first reads in the data as .fit, called a FITS file. FITS stands for Flexible Image Transport System. It is the current NASA standard for astronomical data. The FITS format is widely supported, it consists of a header file and 2-dimensional array of ascii data. In our program, data is read into three matrices using the Fitsread function in MatLab: atoms, noatoms, and the reference. The data is then manipulated to normalize out intensity fluctuations between the atoms and noatoms image by comparing patches of the data in a portion where there is no signal from the atoms. Then the image is constructed and plotted. The program displays a single plot with three windows containing the atoms, noatoms, and the processed image.

```
atoms=fitsread(filea); noatoms=fitsread(filena);
ref=fitsread(fileref);
%%%%%%%%%%%%% subtract off reference picture%%%%%%%%%
%%%%%%%%%%%%% atoms=atoms-ref;
```

```

noatoms=noatoms-ref;
%%%%%%%%%%%%%%%
%%%%%%%normalize out intensity fluctuations%%%%%%
%%%%%%%nominate patch
colcent=480;
rowcent=20;
side=15;
patchatoms=atoms(((rowcent-(side/2):rowcent+(side/2)),((colcent-(side/2):(colcent+(side/2))));;
patchatoms=sum(sum(patchatoms));
patchnoatoms=noatoms(((rowcent-(side/2):rowcent+(side/2)),((colcent-
(side/2):(colcent+(side/2))));;
patchnoatoms=sum(sum(patchnoatoms));
%%%%%%%make a patch in the noatoms picture%%%%%
%%%%%%%noatomspatch=noatoms;
noatomspatch(((rowcent-(side/2):rowcent+(side/2)),((colcent-(side/2):(colcent+(side/2))))=0;
% ok now divide by the patch noatoms=noatoms*(patchatoms/patchnoatoms);
%%%%%%%Calculate phase shift %%%%%%
%%%%%%%diffmat=(1/6.324)*((atoms./noatoms)-1); % THIS IS THE PHASE SHIFT
subplot(3,1,1)
surf(atoms)
grid off
colormap('default')
shading interp
view(2)
subplot(3,1,2)
surf(noatomspatch)
grid off
colormap('default')
shading interp
view(2)
subplot(3,1,3)
surf(diffmat)
grid off
colormap('default')
shading interp
view(2)
colorbar
toc

```

After the data is displayed, the user can crop down the image to remove any edge effects from the data. The user simply clicks on the center of the cloud, and the computer finds the global maxima around the region specified by the user and calls that the center. The program then finds the major and minor axis of the cloud and

checks with the user. This step is often skipped, since the angle does not change, and thus it is simply hardwired into the code. Next, the program does an angle average of the data for a $\pm 5^\circ$ angle about the major axis. The important parameters are then specified, such as magnification, detuning and trapping frequency. These can all be changed in the pop-up dialog box during the fitting routine. However, if they need to be changed they are in the section of code below:

```
%%%%% Define input parameters to use %%%%%%
%%%%% Define input parameters to use %%%%%%
unmagpixsize=13e-6;
mag=6.375;
pix=unmagpixsize/mag;
sig0=6*pi*(671e-9/(2*pi))^2;
det=33;
wa2=79.8*2*pi;
wr2=800*2*pi;
mass=6/6e23/1000;
kb=1.38e-23;
hbar = 6.626e-34/(2*pi);
```

The averaged data is now fit to a Gaussian function. This is accomplished by passing a 1-D matrix containing the axial profile of the data and a parameterized Gaussian function to a MatLab function called fmins. The fmins function adjusts the Gaussian parameters until it minimizes the difference between the data and the function. This is shown in the code below:

```
%%%%%Now fit the averaged curve%%%%%
%%%%%
axparam(2)=0;
axparam(3)=bestwast;
global avp xbest
fitax=fmins('guassfunave',axparam,options);
x=xbest;
y=fitax(1)*exp(-((x-fitax(2))/fitax(3)).^2)+fitax(4);
plot(x,y,'r',x,avp,'b')
pause
```

The next portion of the code reads back the Gaussian fit parameters and calculates the number, temperature, density, and phase space density. While this is only a classical fit, these numbers give us initial guess for the quantum degenerate fit.

```
%%%%%%%
%%%%%% Relevant fitted parameters %%%%%%
%%%%%%%
peakphase=fitax(1)-fitax(4);
axialwaist=fitax(3)*pix;
radiwaist=(wa2/wr2)*axialwaist;
T=(.5*mass*wa2^2*axialwaist^2)/kb
n0=(peakphase/(sig0*sqrt(pi)*radiwaist))^(4*det));
N= (n0*pi^(3/2)*radiwaist^2*axialwaist)
debrog=((2*pi*hbar^2)/(mass*kb*T))^(1/2); phase=log10(n0*debrog^3); n0=n0/1e6;
```

The last step is to again use the fmins function, however this time we pass it the axial distribution and a Fermi optical density distribution. The Fermi optical density distribution is formed from the fermifunpc.m function. This function follows the fitting process discussed in section 2.4. It reads in the initial guess of number and temperature, and constructs a chemical potential. The chemical potential is then used to calculate the Fermi density distribution, which is integrated in the \hat{z} direction, creating an optical density distribution. The process is iterated through until fmins minimizes the optical density function with respect to the data, yielding N, T, and T_F . The process is identical for the bosons, except the function that the data is fit to is called bosefunpc.m.

```
%%%%%%%
%%%%%% Now lets fit the a Fermi Dist to avprof %%%%%%
%%%%%% %%%%%% (which is the phase of the signal)%%%%%
%%%%%% %%%%%% %%%%%% %%%%%% %%%%%% %%%%%% %%%%%%
%%%%%% options for fmins%%%%%
options(1)=0;
options(2)=1e-3;
options(3)=1e-3;
options(14)=60;
%%%%% Use classical numbers as first guess%%%%%
fg(2)=T*1.5;
fg(1)=N;
fitfermi=fmins('fermifunpc',fg,options,[],x,avprof,error,wa2,wr2,det,sig0);
T= fitfermi(2)
N=fitfermi(1)
Tf=hbar/kb*(6*fitfermi(1)*wr2^2*wa2)^0.33;
rat=fitfermi(3)/Tf
```

References

1. M. H. Anderson, J. R. Ensher, M. R. Matthews, C. E. Wieman, and E. A. Cornell. “Observation of Bose-Einstein condensation in a dilute atomic vapor.” *Science* **269** 198 (1995).
2. C. C. Bradley, C. A. Sackett, J. J. Tollett, and R. G. Hulet. “Evidence of Bose-Einstein condensation in an atomic gas with attractive interactions.” *Phys. Rev. Lett.* **75** 1687–1690 (1995).
3. K. B. Davis, M.-O. Mewes, and W. Ketterle. “An analytic model for evaporative cooling of atoms.” *Appl. Phys. B* **60** 155 (1995).
4. H. T. C. Stoof, M. Houbiers, C. A. Sackett, and R. G. Hulet. “Superfluidity of spin-polarized ^6Li .” *Phys. Rev. Lett.* **76** 10 (1996).
5. B. DeMarco and D. S. Jin. “Onset of Fermi degeneracy in a trapped atomic gas.” *Science* **285** 1703 (1999).
6. Andrew G. Truscott, Kevin E. Strecker, William I. McAlexander, Guthrie B. Partridge, and Randall G. Hulet. “Observation of Fermi pressure in a gas of trapped atoms.” *Science* **291** 2570 (2001).
7. E. Tiesinga, B. J. Verhaar, and H. T. C. Stoof. “Threshold and resonance phenomena in ultracold ground-state collisions.” *Phy. Rev. A* **47**(5) 41144122 (1993).
8. S. Inouye, M. R. Andrews, J. Stenger, H.-J. Miesner, D. M. Stamper-Kurn, and W. Ketterle. “Observation of Feshbach resonances in a Bose-Einstein condensate.” *Nature* **392** 151 (1998).

9. Kevin E. Strecker, G.B. Partridge, and Randall G. Hulet. “Conversion of an atomic Fermi gas into a long-lived molecular Bose gas.” *Phys. Rev. Lett.* **91**(8) 135–138 (2003).
10. Kevin E. Strecker, Guthrie B. Partridge, Andrew G. Truscott, and Randall G. Hulet. “Formation and propagation of matter-wave soliton trains.” *Nature* **417** 150–153 (2002).
11. S. Svanburg. *Atomic and Molecular Spectroscopy*. Springer-Verlag, New York, second edition (1992).
12. K.E. Strecker. *Sympathetic Cooling of a Bose/Fermi Mixture of Lithium to Quantum Degeneracy*. Masters thesis, Rice University (2002).
13. G.B. Partridge. *An Improved System for Creating Ultra Cold Fermi Gases of ⁶Li*. Masters, Rice University (2003).
14. H. J. Metcalf and P. van der Straten. *Laser Cooling and Trapping*. Springer-Verlag, New York (1999).
15. W. I. McAlexander. *Low Energy Collisional Interactions in Magnetically Trapped Lithium*. Ph.d. thesis, Rice University (2000).
16. C. A. Sackett. *Dynamics of Bose-Einstein Condensation in ⁷Li*. Ph.d. thesis, Rice University (1999).
17. L. I. Schiff. *Quantum Mechanics*. McGraw-Hill, New York, third edition (1968).
18. G. B. Arfken and H. J. Weber. *Mathematical Methods for Physicists*. Academic Press Inc., San Diego, fourth edition (1995).
19. D. J. Griffiths. *Introduction to Quantum Mechanics*. Prentice-Hall Inc., Englewood Cliffs (1995).

20. C.J. Pethick and H. Smith. *Bose Einstein Condensation in Dilute Gases*. Cambridge University Press, UK, 1st edition (2002).
21. C. J. Joachain. *Quantum Collision Theory*. Elsevier Science Publishers B. V., Amsterdam, third edition (1975).
22. Eric R. I. Abraham, Nicholas W. M. Ritchie, W. Ian McAlexander, and Randall G. Hulet. “Photoassociative spectroscopy of long-range states of ultracold ${}^6\text{Li}_2$ and ${}^7\text{Li}_2$.” *J. Chem. Phys.* **103**(18) 7773–7778 (1995).
23. E. R. I. Abraham, W. I. McAlexander, H. T. C. Stoof, and R. G. Hulet. “Hyperfine structure in photoassociative spectra of ${}^6\text{Li}_2$ and ${}^7\text{Li}_2$.” *Physical Review A* **53**(5) 3092 (1996).
24. E. R. I. Abraham, W. I. McAlexander, J. M. Gerton, R. G. Hulet, R. Cote, and A. Dalgarno. “Singlet s-wave scattering lengths of ${}^6\text{Li}$ and ${}^7\text{Li}$.” *Phys. Rev. A* **53**(6) R3713 (1996).
25. E.R.I. Abraham, W.I. McAlexander, J.M. Gerton, R.G. Hulet, R. Cote, and A. Dalgarno. “Triplet s-wave resonance in ${}^6\text{Li}$ collisions and scattering lengths of ${}^6\text{Li}$ and ${}^7\text{Li}$.” *Physical Review A* **55**(5) R3299–R3302 (1997).
26. N. W. Ritchie, E. R. I. Abraham, Y. Y. Xiao, C. C. Bradley, , and R.G. Hulet. “Trap-loss collisions of ultracold atoms.” *Phys. Rev. A* **51**(2) R890 (1995).
27. W. Ketterle, K. B. Davis, M. A. Joffe, A. Martin, and D. E. Pritchard. “High densities of cold atoms in a dark spontaneous-force optical trap.” *Phys. Rev. Lett.* **70**(15) 2253 (1993).
28. W. D. Phillips. “Laser cooling and trapping of neutral atoms.” *Rev. MOD. Phys.* **70**(3) 729 (1998).

29. M.-O. Mewes. “Bose-Einstein condensation of sodium atoms.” Ph.d., Massachusetts Institute of Technology (1997).
30. D.E. Pritchard. “Cooling neutral atoms in a magnetic trap for precision spectroscopy.” *Phys. Rev. Lett.* **51** 1336 (1983).
31. E. Majorana. “Atomi orientati in campo magnetico variable.” *Nuovo Cimento* **9** 43 (1932).
32. K. E. Strecker. “Electromagnetic trap switch.” . Laboratory binder containing diagrams, schematics, and component specifications.
33. T. Takekoshi, J.R. Yeh, and R.J. Knize. “Quasi-electrostatic trap for neutral atoms.” *Optics Comm.* **114** 421–424 (1995).
34. Steven Chu, J. E. Bjorkholm, A Ashkin, and A Cable. “Experimental observation of optically trapped atoms.” *Physical Review Letters* **57**(3) 314–317 (1986).
35. T.A. Savard, K.M. O’Hara, and J.E. Thomas. “Laser-noise-induced heating in far-off resonance optical traps.” *Phys. Rev. A* **56**(2) R1095 (1997).
36. K.M. O’Hara, S.R. Granade, M.E. Gehm, T.A. Savard, S. Bali, C. Freed, and J.E. Thomas. “Ultrastable CO₂ laser trapping of lithium fermions.” *Phys. Rev. Lett.* **81**(21) 4204 (1999).
37. L. D. Landau and E. M. Lifshitz. *Mechanics*, volume 1 of *Course of Theoretical Physics*. Pergamon, London, 3rd edition (1960).
38. V.M. Pérez-García, H. Michinel, and H. Herrero. “Bose-Einstein solitons in highly asymmetric traps.” *Phys. Rev. A* **57**(5) 3837–3842 (1998).
39. M. Junker. “Diffraction limited imaging system.” , (2003).

40. C. C. Bradley. *Bose-Einstein condensation of Lithium.* Ph.d., Rice University (1996).
41. M. Inguscio, S. Stringari, , and C.E. Wieman. *Bose-Einstein Condensation in Atomic Gases, Societa Italiana Di Fisca.* IOS Press, P.O. BOX 10558, Burk,Va, 1st edition (1999).
42. B. DeMarco. *Quantum Behavior of an Atomic Fermi Gas.* Ph.d. thesis, University of Colorado (2001).
43. K. Huang. *Statistical Mechanics.* John Wiley & Sons, New York, second edition (1987).
44. C. A. Sackett, C. C. Bradley, and R. G. Hulet. “Optimization of evaporative cooling.” *Phys. Rev. A* **55** 3797 (1997).
45. C. C. Bradley, C. A. Sackett, and R. G. Hulet. “Bose-Einstein condensation of lithium: observation of limited condensate number.” *Phys. Rev. Lett.* **78**(6) 985–989 (1997).
46. P. O. Fedichev, M. W. Reynolds, and G. V. Shlyapnikov. “Three-body recombination of ultracold atoms to a weakly bound s level.” *Phys. Rev. Lett.* **77** 29212924 (1997).
47. S. Burger, K. Bongs, S. Dettmer, W. Ertmer, K. Sengstock, A. Sanpera, G. V. Shlyapnikov, and M. Lewenstein. “Dark solitons in Bose-Einstein condensates.” *Phys. Rev. Lett.* **83** 5198–5201 (1999).
48. J. Denschlag, J. E. Simsarian, D. L. Feder, C. W. Clark, L. A. Collins, J. Cubizolles, L. Deng, E. W. Hagley, K. Helmerson, W. P. Reinhardt, S. L. Rolston, B. I. Schneider, and W. D. Phillips. “Generating solitons by phase engineering of a Bose-Einstein condensate.” *Science* **287** 97 (2000).

49. C. A. Sackett, J. M. Gerton, M. Welling, and R. G. Hulet. “Measurements of collective collapse in a Bose-Einstein condensate with attractive interactions.” *Phys. Rev. Lett.* **82** 876–879 (1999).
50. J.M. Gerton, D. Strekalov, and I. Prodan R.G. Hulet. “Direct observation of growth and collapse of a Bose-Einstein condensate with attractive interactions.” *Nature* **408** 692–695 (2000).
51. P. A. Ruprecht, M. J. Holland, K. Burnett, and Mark Edwards. “Time-dependent solution of the nonlinear Schrodinger equation for Bose-condensed trapped neutral atoms.” *Phys. Rev. A* **51** 4704–4711 (1995).
52. A. Gorlitz, J.M. Vogels, A.E. Leanhardt, C. Raman, T.L. Gustavson, J.R. Abo-Shaeer, A.P. Chikkatur, S. Gupta, S. Inouye, T. Rosenband, and W. Ketterle. “Regimes of quantum degeneracy in trapped 1-D gases.” *Phys. Rev. Lett.* **87**(13) 130402–1–130402–4 (2001).
53. George I. Stegeman and Mordechai Segev. “Optical spatial solitons and their interactions: Universality and diversity.” *Science* **286** 1518–1523 (1999).
54. L. Salasnich, A. Parola, and L. Reatto. “Modulational instability and complex dynamics of matter-wave solitons.” *Phys. Rev. Lett.* **91**(8) 080405–1–4 (2003).
55. L. Khaykovich, F. Schreck, G. Ferrari, T. Bourdel, J. Cubizolles, L.D. Carr, Y. Castin, and C. Salomon. “Formation of a matter-wave bright soliton.” *Science* **296** 1290–1293 (2002).
56. U. Al Khawaja, H.T.C. Stoof, R.G. Hulet, K. E. Strecker, and G. B. Partridge. “Bright soliton trains of trapped Bose-Einstein condensates.” *Phys. Rev. Lett.* **89**(20) 200404–1–4 (2002).

57. J. P. Gordon. "Interaction forces amoung solitons in optical fibers." *Opt. Lett.* **8**(11) 596–598 (1983).
58. J.J. Bollinger Wayne M. Itano D.J. Larson, J.C. Berquist and D.J. Wineland. "Sympathetic cooling of trapper ions: A laser-cooled two-species nonneutral ion plasma." *Phys. Rev. Lett.* **57**(1) 70–73 (July 1986).
59. F. A. van Abeelen, B. J. Verhaar, and A. J. Moerdijk. "Sympathetic cooling of ^6Li atoms." *Phys. Rev. A* **55** 4377 (1997).
60. R.W. Ghrist E.A. Cornell C.J. Myatt, E.A. Burt and C.E. Wieman. "Production of two overlapping bose-einstein condensates by sympathetic cooling." *Phys. Rev. Lett.* **78**(4) 586–589 (January 1997).
61. J. M. Gerton, C. A. Sackett, B. J. Frew, and R. G. Hulet. "Dipolar relaxation collisions in magnetically trapped ^7li ." *Phys. Rev. A* **59**(2) 1514–1516 (1999).
62. Bruce Johnson. Personal communication.
63. K. B. Davis, M.-O. Mewes, M. A. Joffe, and W. Ketterle. "Evaporative cooling of sodium atoms." . In *Fourteenth International Conference on Atomic Physics*, page 1M, University of Colorado Boulder, Colorado (1994).
64. A.G. Truscott. "Emtrap imaging system." , (2000). Internal laboratory report.
65. D.M. Harber, H.J. Lewandowski, J.M. McGuirk, and E.A. Cornell. "Effect of cold collisions on spin coherence and resonance shifts in a magnetically trapped ultracold gas." *Phys. Rev. A* **66** 053616 (2002).
66. S. Gupta, Z. Hadzibabic, M.W. Zwierlein, C.A. Stan, K. Dieckmann, C.H. Schunck, E.G.M. Kempen, B.J. Verharr, and W. Ketterle. "Radio-frequency spectroscopy of ultracold fermions." *Science* **300** 1723–17226 (2003).

67. G. Herzberg. *Molecular Spectra and Molecular Structure, I. Spectra of Diatomic Molecules*. Krieger Publishing, Flordia (1950).
68. J.R. Rubbmark, M.M. Kash, M.G. Littman, and D. Kleppner. “Dynamical effects at avoided level crossings: A study of Landau-Zener effect using rydberg atoms.” *Phys. Rev. A* **23** 3107–3117 (1981).
69. C.A. Regal, C. Ticknor, J.L. Bohn, and D.S. Jin. “Creation of ultracold molecules from a Fermi gas of atoms.” *Nature* **424** 47–50 (2003).
70. Roahn Wynar, R. S. Freeland, D. J. Han, C. Ryu, and D. J. Heinzen. “Molecules in a bose-einstein condensate.” *Science* **287** 1016–1019 (2000).